The influence of machine thermal design and operating conditions on scuffing failure

by

Melanie P. Finnis

Thesis submitted to the University of Leicester
for the degree of Doctor of Philosophy

NOVEMBER
1989

Acknowledgements

The work reported in this thesis was carried out in the Department of Engineering at the University of Leicester and the author wishes to thank Professor G.D.S. MacLellan for making the research facilities available.

The project was funded by the Science and Engineering Research Council with a CASE Studentship Grant and by the Petroleum, Chemistry and Technology Division of the Royal Aeronautical Establishment at Farnborough.

I wish to thank my Supervisor, Dr. D.A. Kelly, for his guidance during the project and my Industrial Supervisor, Mr. Norman Hopkinson.

The instrumentation for the test machine was developed by Mr. Peter Williams. This, and particularly his 'comradeship' during the experimental work is much appreciated.

My thanks also go to Mrs. Helen Townsend for typing the thesis.

This thesis has taken six years to complete. I am certain that without the guidance, encouragement and friendship shown to me by Mrs. Pat Baglin I would have given up the task long ago.

Finally, I wish to thank my parents for their encouragement in the early stages and for consoling me in the latter.

The influence of machine thermal design and operating conditions on scuffing failure

ABSTRACT

Scuffing is a severe form of surface damage which limits the performance of lubricated sliding machine components. Empirical work has shown that failure either occurs under relatively mild elastohydrodynamic conditions with barely modified surfaces or under severe conditions with the surfaces well run-in. Two hypotheses exist which may explain these experimental differences. This thesis examines their relevance.

The first hypothesis is that, under elastohydrodynamic lubrication, the surface asperities either remain rigid or become elastically deformed - micro-elastohydrodynamic lubrication. A non-dimensional plot, developed by Baglin, predicts the occurrence of the regimes. An experimental study of running-in and scuffing for tests initially operating in the different regimes is described. Tests were run on a two disc machine with incremental loading. Running-in occurred both when tests started in the micro-ehl regime and when they apparently entered it during operation. High sliding prevented entry into micro-ehl; scuffing occurred with barely modified surfaces. This hypothesis discriminates between failure types but cannot alone predict scuffing.

The second hypothesis, by Crook and Shotter, is that scuffing represents an inbalance between the rate of film thinning with increasing load and the rate of running-in. Increasing load increases the temperature which, due to its effect on viscosity, controls film thinning. Knowledge of the machine's thermal behaviour is required. A model is developed to predict temperature in a finite length cylinder subject to a discrete rotating heat source and convective cooling. Steps to apply the theory to a two disc machine are detailed and the results compared to previous experimental temperatures. Methods of changing thermal response are considered and preliminary tests with the discs insulated to increase the temperature rise are described. A marked reduction in scuffing load emphasises the importance of thermal design. Further experimentation is necessary to determine whether the Crook and Shotter hypothesis can quantify scuffing failure.

Contents

Notation

Symbols used only once are defined in text. Notation specific to Chapters 5, 6 and 7 is given at the beginning of Chapter 5.

b	-	half Hertz contact width	- m
B	-	non-dimensional group $\frac{b}{\sqrt{2Rh^*}}$	
d_o	-	asperity amplitude for sinusoidal roughness model	
E	-	Young's modulus	- N/m
E'	-	combined Young's modulus $\frac{1}{E'} = \frac{1}{2}\left(\frac{(1-\nu_1)^2}{E_1} + \frac{(1-\nu_2)^2}{E_2}\right)$	ν = Poisson's ratio
$E(\ )$	-	expectation value	
h	-	general term for film thickness (between mean levels with rough surfaces)	- m
h^* ,	-	film thickness in e.h.l. contact at p_{max}	- m
h_{min}	-	minimum film thickness in e.h.l. contact	- m
h_a	-	compliance - average film thickness for rough surfaces	- m
h_o	-	minimum film thickness in classical lubrication	- m
H	-	local gap with rough surface lubrication	- m
$I, I_a, I_{a\tau}$	-	integrals in solution of Reynolds equation	
L	-	half wavelength of sinusoidal surface roughness	- m
p	-	general term for pressure	- N/m^2
p_o	-	maximum pressure in e.h.l. contact	
P	-	αp - non-dimensional pressure	
P_{max}, P_{min}	-	pressure at ripple peak, trough	
ΔP	-	$P_{max}-P_{min}$ - size of pressure ripple	
P_{asp}	-	maximum asperity pressure in dry contact configuration	
q	-	reduced pressure $= \frac{1}{\alpha}\left(1 - e^{-\alpha p}\right)$	
R	-	disc radius	- m
R'	-	effective disc radius for two discs $\frac{1}{R'} = \frac{1}{R_1} + \frac{1}{R_2}$	- m
R_a	-	average surface roughness (c.l.a)	- μm
R'_a	-	combined surface roughness $= \sqrt{R_{a_1}^2 + R_{a_2}^2}$	- μm
ΔR_a	-	difference in pre/post test R_a value	- μm

t	-	time	
T	-	bulk temperature	- °C
T_{int}	-	initial disc temperature	
u_1, u_2	-	speed of surfaces 1,2	- m/s
u_s	-	sliding speed = $u_1 - u_2$	
$\bar{u}$	-	rolling speed = $\frac{u_1 + u_2}{2}$	
w	-	load/unit length	- N/m
x	-	rolling direction	
y	-	$\perp$ to flow	
z	-	cross film direction	
α	-	pressure coefficient of viscosity	- m^2/N
γ	-	temperature coefficient of viscosity	- 1/°C
$\delta(y)$	-	random roughness element = $h_1 + h_2$	
η	-	dynamic viscosity of lubricant	- Ns/m^2
η_o	-	dynamic viscosity of lubricant at atmospheric pressure	
σ	-	root mean squared surface roughness	
τ	-	non-dimensional distance in x-direction in terms of prevailing film thickness	
τ_i	-	non-dimensional inlet distance	
Ψ	-	non-dimensional distance in x-direction in terms of ideal film thickness	

<u>Subscripts</u>

a	-	denotes value with rough surfaces
τ	-	value for a starved contact
i	-	value at inlet

<u>Superscripts</u>

—	-	value at x = 0

CHAPTER 1

INTRODUCTION

1.1 Scuffing Failure

Scuffing is a severe form of surface damage which can occur between non-conforming lubricated components such as meshing gear teeth or a cam and tappet. It is characterised by the plucked, torn appearance of the surface (Fig.1.1). Scuffing has been defined by the Institution of Mechanical Engineers (1957) as "gross damage characterised by the formation of local welds between the sliding surfaces".

Scoring is a milder form of damage which does not noticeably affect the machine performance. It was defined by the Institute of Petroleum (1968) as "scratching across the rubbing surfaces without modification of the general form". Confusion can arise between the two terms because, in the United States, the word "scoring" is often used to describe "scuffing". Barwell and Milne (1957) found that scoring, if it did occur, was closely followed by scuffing, but it was by no means a prerequisite.

Scuffing does not often occur in practice but if it does take place a scuffed part may render a machine inoperable by total seizure between the components. If the failure is not catastrophic and operation continues, the scuffed part may suffer from rapid wear and pitting which can cause secondary performance problems, for example:-

severe pitting may eventually cause gear teeth to break,

the wear of a cam alters its profile, which in turn reduces the engine performance, and wear of piston rings causes 'blow back' which again reduces efficiency.

As an economic and performance factor it is therefore essential that scuffing failure is avoided.

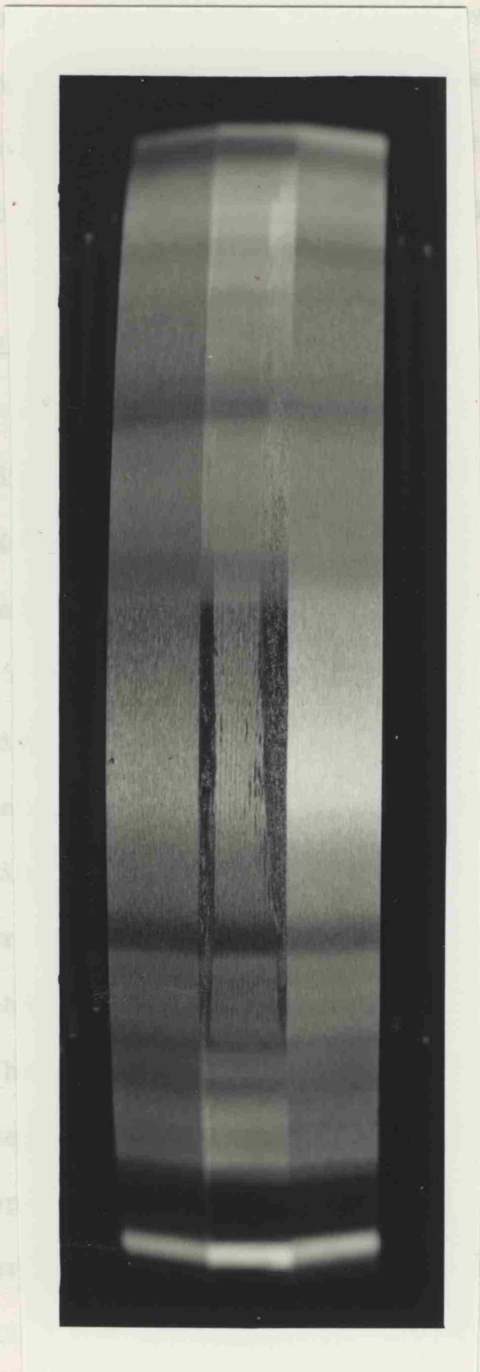

Figure 1.1 A scuffed surface.

Investigations over the last 50 years or so have attempted to understand the nature of the scuffing and to add to the development of design criteria. Many of these investigations have been carried out on two disc, four ball or other such machines. These simplify the study of lubrication phenomena as they run at steady conditions. Two disc machines can be used to replicate the conditions at a particular point in the operating cycle of gears.

These investigations have highlighted factors which influence scuffing conditions, some of which are outlined here. (For further details one of the many excellent reviews of subject, for example those by Dyson (1972) and by Neale (1971), should be consulted.)

Scuffing is a sudden type of failure and its onset in test machines is accompanied by an immediate rise in the levels of noise and friction, and by a sharp rise in the temperature of the scuffed parts.

Various operating and environmental factors are known to influence scuffing. High sliding speed, high temperature, high load and rough surfaces, in general, promote scuffing failure, whilst high rolling speeds, high viscosity and the use of certain oil additives enhance successful running. However, the exact influence of each of these factors is not known and much of the experimental evidence produced is contradictory.

Material properties of the surfaces can influence scuffing. With ferrous surfaces there is a change in the composition of a thin layer of the surface material of the scuffed part. These layers are hard, white and etch resistant.

Rodgers (1969, 1970) identified two such layers with different physical properties on the surfaces of scuffed piston rings. Campany and Wilson (1977) associated the first of these layers WI, - a form of iron carbide, with scoring and the second WII , - a mixture of austenite and martensite, with scuffing. The presence of this transformed layer and an underlying tempered layer indicated that the contacting surfaces had been subjected to very high temperatures followed by rapid cooling, a hypothesis confirmed by Padmore and Ruston (1964/65) with a hardness relaxation method and Sakmann (1947) with heat flow calculations.

Scuffing can vary in severity. It is possible for small scuffs to occur which 'heal' themselves with continued operation and have no prolonged effect. Such scuffs are sometimes only recognised by visual examination of the surfaces.

Tallian (1972) suggested that scuffing was an accumulative process and this was demonstrated by Carper, Ku and Anderson (1973). They compared the results from tests which were identical except that in one batch the discs were coupled by gears and driven by one motor, and in the other the discs were driven independently by separate motors. Synchronisation would not be so exact by the second method, consequently there would be less frequent contacts between any two locations. The second batch of tests ran to more severe conditions. This implies that repeated contacts between the same points somehow aggravate the surface. This concept is also shown in practice by the more successful operation of hunting tooth gears, where there is no simple ratio of the gears (e.g. 21:60). This reduces the frequency of contact between any two teeth, compared to simple ratio gears (e.g. 20:60=1:3). Running-in of the surfaces also increases scuffing resistance. In this respect demands on marine gears are particularly arduous due to the practice of checking the maximum ship speed during the first trial.

Although there is an appreciation of the many factors which effect scuffing there is still a lack of fundamental understanding of the scuffing mechanism, and so the design of components where there is a risk of scuffing failure is based on empirical knowledge. Consequently these components may be over-designed and testing of prototypes is necessary to ensure that they do not fail within normal operating conditions.

There are many examples of the way in which scuffing influences design. In gears, a balance must be struck between the tooth load and sliding speed in determining the number and the size of the teeth. Larger teeth produce a higher sliding speed which is known to promote scuffing.

With smaller teeth the sliding speeds are reduced but the loads are increased. Valve train systems in cars may be positioned and the materials of the cams chosen primarily to avoid scuffing failure. Many motor vehicle manufacturers have adopted overhead valve trains to reduce the weight borne between the cam and tappet. The cams themselves are often made of cast iron as this is a more scuff-resistant material than steel, and in this application the better strength and ductility of steel is not essential.

1.2. Scuffing failure criteria

Many criteria have been proposed to predict when scuffing failure will occur, but as yet no criterion has proved successful over a wide range of operating conditions. This section outlines some of these criteria and the experimental evidence for and against each. Many of these criteria were empirically derived by observing conditions at failure. That which has gained most attention and use was first introduced by Blok in 1939.

'Total contact temperature criterion'

The 'total contact temperature' is the sum of the bulk or body temperature and the flash temperature which is the transient temperature rise at the surface as it passes through the contact. Blok (1939) proposed that for any material and lubricant combination there was a critical total contact temperature at which the surfaces would scuff. He came to this conclusion from the study of gear rig test results. The bulk temperatures were found experimentally. An expression was derived by Blok (1937) to estimate the flash temperatures from the load, friction and surface speeds. The critical total temperature for a specific material and lubricant combination could only be found by experiment. Blok gave no physical justification for this criterion. Grew and Cameron (1972) suggested that it was related to a failure of boundary lubrication due to the physical desorption of surface active materials from the surface.

The 'total contact temperature' failure criterion has met with various degrees of acceptance. The most positive evidence in support of the total critical temperature concept was reported by Leach and Kelley (1965), and by Ku and Li (1977) - both groups working with disc machines. O'Donahue, Manton and Askwith (1967-68) found agreement but only over a narrow range of speed and bulk temperature. Bell, Dyson and Hadley (1975), found that although the total temperature at failure was approximately constant over a narrow range of rolling and sliding speeds, there was a large variation in the total temperature over a wider range of speeds.

Contradictory evidence was produced by Fein (1967), using the same machine and lubricant as Leach and Kelley but more varied conditions. He found that the total temperature at failure varied by up to 550°F (200°C), compared to $\pm$ 20°C found by Leach and Kelley. Bell and Dyson (1972) noted the factors that increased the bulk temperature at failure also increased the flash temperature and so their total could not be constant.

The variability of results in terms of the total contact temperature has led to the formulation, from test results, of various modifications to the original criterion. Meng (1960), Niemenn and Lecher (1967) and Niemenn and Seitzenger (1971) all showed the average tooth temperature in gear tests to be constant at failure. Bailey and Cameron (1973), using discs, showed the total contact temperature to be constant at low bulk temperature and the flash to be constant at higher bulk temperatures. Carper, Ku and Anderson (1972) and Staph, Ku and Carper (1973) found a reasonable correlation between the total contact temperature and a parameter, ξ , which included the viscosity, surface speeds, disc radius and the load. It was suspected that the line of failure conditions was, in fact, the operating line of the test machine. The same criticism can be made of the correlation, reported by Fein (1960), between the reciprocal of the absolute bulk temperature and a parameter including the load and the sliding speed. The relationship was later shown by Fein (1965 and 1967) to vary with operating conditions.

'Frictional power intensity criterion'

Another criterion which has received attention is that of constant generation of frictional power intensity in the contact at scuffing. There is again much evidence for and against this suggestion. Matveesky (1965) analysed test results of various other authors, including those of Matveesky (1965) for a two disc machine, Remezova (1959) for a cross cylinders machine and Vinogradov and Podolsky (1960) for a high speed four ball machine. He showed that for any machine/oil combination both the frictional power intensity and the total contact temperature at failure was almost constant.

However, Carper and Ku (1974) showed that the frictional power intensity often fell during a test so the proposal that scuffing would occur at a critical maximum value could not hold. Again, others have shown agreement over limited ranges of conditions - for example, Bell, Dyson and Hadley (1975). Several variations on the theme have again been reported. For example, Meng (1960) referred to the total frictional power in the contact, and Carper and Ku (1974) related the total frictional power to their parameter ξ. The above criteria are of an empirical nature and do not take into account any aspect of the lubrication in the contact. Other failure criteria have been evolved which relate to lubrication.

' λ ratio criterion'

Originally it was assumed that heavily loaded non-conforming contacts were not hydrodynamically lubricated as the film thicknesses, calculated from the classical lubrication theory of Osborne Reynolds (1886), were less than the roughness of the surfaces. However, it was often found that machining marks persisted, even after prolonged periods of running. The introduction of an elastohydrodynamic lubrication solution to Reynolds' equation by Grubin (1949) was a large step forward in explaining the successful operation of these heavily loaded components. The high pressures generated in the contact had been shown to have two effects, to elastically deform the surfaces and to increase the viscosity of the lubricant. Grubin was the first to include both of these effects in a single analytic solution. The calculated film thicknesses using this new theory were greater than those from the classical solution at the same conditions, thus maintaining the separation of the surfaces - hence the successful operation of such systems.

Perhaps the most obvious scuffing criterion follows on from the successful use of elastohydrodynamic theory to explain the operation of heavily loaded contacts. With increasing severity of conditions the film thins, bringing the surfaces closer together until contact or interaction of the surface asperities occurs. It seemed reasonable to suggest that failure would occur either at first contact of the asperities or at some critical degree of interaction. This condition is expressed in terms of the λ ratio, the ratio of the film thickness to surface roughness. Some workers, Bodensiek (1967) for example, found the film thickness between gear teeth to be a useful criterion. Others, such as Bell and Dyson (1972) found no relation between this parameter and failure. Christensen (1965), by measuring the electrical resistance between the discs in a two-disc machine, showed that there could be significant surface contact between running discs without distress. The λ ratio may therefore be useful in showing the limit at which contact will occur, but cannot be used as a failure criterion.

'Dyson criterion'

A complete change of tack was made by Dyson (1976). He was the first to consider the failure of elastohydrodynamic lubrication from first principles. The elastohydrodynamic problem requires the simultaneous solution of the elastic and hydrodynamic equations. Dyson included the roughness of the surfaces in both elastic and the hydrodynamic parts of the analysis and predicted the temperature at which the system would fail to generate sufficient pressure to maintain elastohydrodynamic lubrication.

This temperature is that of the bodies at the entry to the conjunction, since it is this temperature which controls the viscosity of the oil and hence film thickness. This temperature is different to that previously used in the other criteria and care is needed to avoid confusion.

Comparison with scuffing test results of Bell and Dyson (1972) showed an encouraging similarity between the temperatures predicted by the Dyson theory for the breakdown of the lubrication, and the measured bulk temperatures at which the discs scuffed. Rossides at Cardiff University (Snidle, Rossides and Dyson (1984), Rossides (1980)) set out to test this correlation. His discs similarly scuffed at bulk temperatures approximately equal to, or slightly greater than, those predicted for the breakdown of the lubricating film.

Story, at Leicester, (Story, Archard and Baglin (1980), Story (1984)), also explored Dyson's theory. In contrast she found that her discs scuffed at temperatures less than those predicted for the breakdown of the lubricant film, so in this case the Dyson criterion was not obeyed. This difference in results stimulated further investigations, of which this thesis forms a part.

1.3. Further developments

Comparison, by Story, of the test results of Story, Rossides and Bell and Dyson, gave rise to two possible causes for the early failure of the Story tests. These were (a) the role of the operating conditions, in particular the initial oil supply temperatures and the loading sequence, and (b) the thermal response of the two disc machines which were of different designs.

(a) Experimental work by Fein (1967) had shown that altering the operating conditions in two disc scuffing tests, the total contact temperature at failure could be varied by as much as 550°F. Baglin (1986a and b) explored theoretically the way in which operating conditions may be important. It was shown that as surfaces approach there are at least two modes of elastohydrodynamic lubrication in which the system could run, depending on the operating conditions.

It was proposed that the conditions of the tests of Bell and Dyson (1972) and Rossides (1980) on the one hand and Story et al (1980) on the other, were such that the tests ran in different regimes of lubrication and that this was in some way responsible for the different observed results of the tests.

(b) An experiment reported by Crook and Shooter (1957) led them to suggest that the rate of change of the temperature following the application of the load and the ability of the surfaces to run-in, is of importance in determining failure conditions. The rate of change of temperature in a two disc machine will depend on the thermal characteristics and hence design of the test machine. Story (1984) began an investigation into this role of temperature changes in disc tests by developing thermal analysis to predict the temperature changes in two disc machine tests. Further work was needed to produce an applicable form of this analysis.

The aim of the present project follows on from both these lines of investigations - to further explore the role of operating conditions and machine thermal characteristics on the history of two disc scuffing tests.

1.4 Thesis outline

Chapter 2 reviews the various pieces of work which are responsible for the present investigation, that is the Dyson criterion, the tests of Story, of Rossides and of Bell and Dyson. The work of Crook and Shotter, and of Fein, is also outlined. The chapter concludes with a review of Baglin's model of regimes of elastohydrodynamic lubrication and how these can be related to operating conditions in two disc tests.

Chapter 3 begins with an introduction to a two disc, designed by Kelly and constructed in Leicester University Engineering Department Workshops. Instrumentation to monitor test conditions developed mainly by Williams (Williams, Finnis and Kelly (1988)) is described. A test programme, designed to explore the role of operating conditions in relation to Baglin's model, and the results of the test series are detailed. The results are finally discussed with reference to the Baglin model of regimes of lubrication.

Some of the results detailed in Chapter 3 indicate values of film thickness less than those calculated from film thickness formulae. Although not an original aim this discrepancy was thought to warrant further investigation and this is the subject of Chapter 4. The chapter reviews some of the factors which could be responsible for this discrepancy. Analytical modelling shows the combined effect of two such factors, surface roughness and lubricant starvation, on the film thickness compared to that found from ideal formulae. It is shown how these factors might alter the results of Chapter 3.

The second of the suggested reasons for the different failure types (discussed in Section 1.3) was the effect of the thermal response of the test machine. Chapters 5, 6 and 7 report the results in this line of the investigation.

A model is developed which can be used to predict temperatures in a two disc machine. Chapter 5 outlines the various temperatures which exist in such a system, and their role in elasto-hydrodynamic lubrication and in failure. Various attempts to model the temperatures in cylinders and in discs are reviewed and the most appropriate approach to the problem is extended to find the temperature changes in finite length cylinders. The results, in appropriate non-dimensional form, are presented for a range of conditions.

Chapter 6 applies the theory of the previous chapter to predict the temperatures in a two disc machine. Expressions are given for the size and strength of the heat source and the division of heat between the two discs.

Difficulties in finding the correct heat transfer coefficients for the environment of the discs and experiments devised to determine working values are discussed. A comparison of calculated and measured temperatures for some of the tests reported in Chapter 3 is made. The analysis is used to show the extent to which the thermal response of the Story and Rossides tests (Section 1.3) could be due to the machine design.

Preliminary experimental work on the effect of the machine thermal response is reported in Chapter 7. The possible methods by which the machine thermal response can be changed and the problems in implementing these changes on the present two disc machine are discussed. The results of an exploratory series of tests using two of the methods are reported and compared to the results of the test series described in Chapter 3.

The discussion of Chapter 8 re-examines some of the results in more detail and with respect to recent work by other authors.

CHAPTER 2

REVIEW OF RELEVANT WORK

2.1 Introduction

The review of scuffing failure in Chapter 1 highlighted some of the contradictory evidence on the subject and subsequent confusion that has arisen over the years. Most of this work has been of an empirical nature with little consideration of, or relation to fundamental lubrication principles. Work by Dyson (1976) into the lubrication of rough surfaces opened a new approach to the subject. The present project does not relate directly to the Dyson criteria for failure, but to several pieces of work which stemmed from Dyson's work. The salient points from these investigations (including that of Dyson) and how they led to the work presented in this thesis, are discussed in this chapter. It begins with an outline of the principles of elastohydrodynamic lubrication and the solution of the problem first reported by Grubin (1949).

2.2. The Grubin Solution

2.2.1. Principles of elastohydrodynamic lubrication

The pressure build-up generated between convergent moving surfaces is governed by Reynolds equation. With conforming surfaces such as in journal bearings, the load is spread out over a relatively large area. The pressures generated in the system are found by the integration of Reynolds' equation between the appropriate limits using the film shape of the two surfaces. With non-conforming surfaces, as in gears or rolling bearings, the load is concentrated onto a small area. At low pressures the film shape is that of the undeformed surfaces, separated by the lubricating film. This is termed 'classical' hydrodynamic lubrication, Fig.2.1. As the load increases, high localised pressures are formed in the fluid

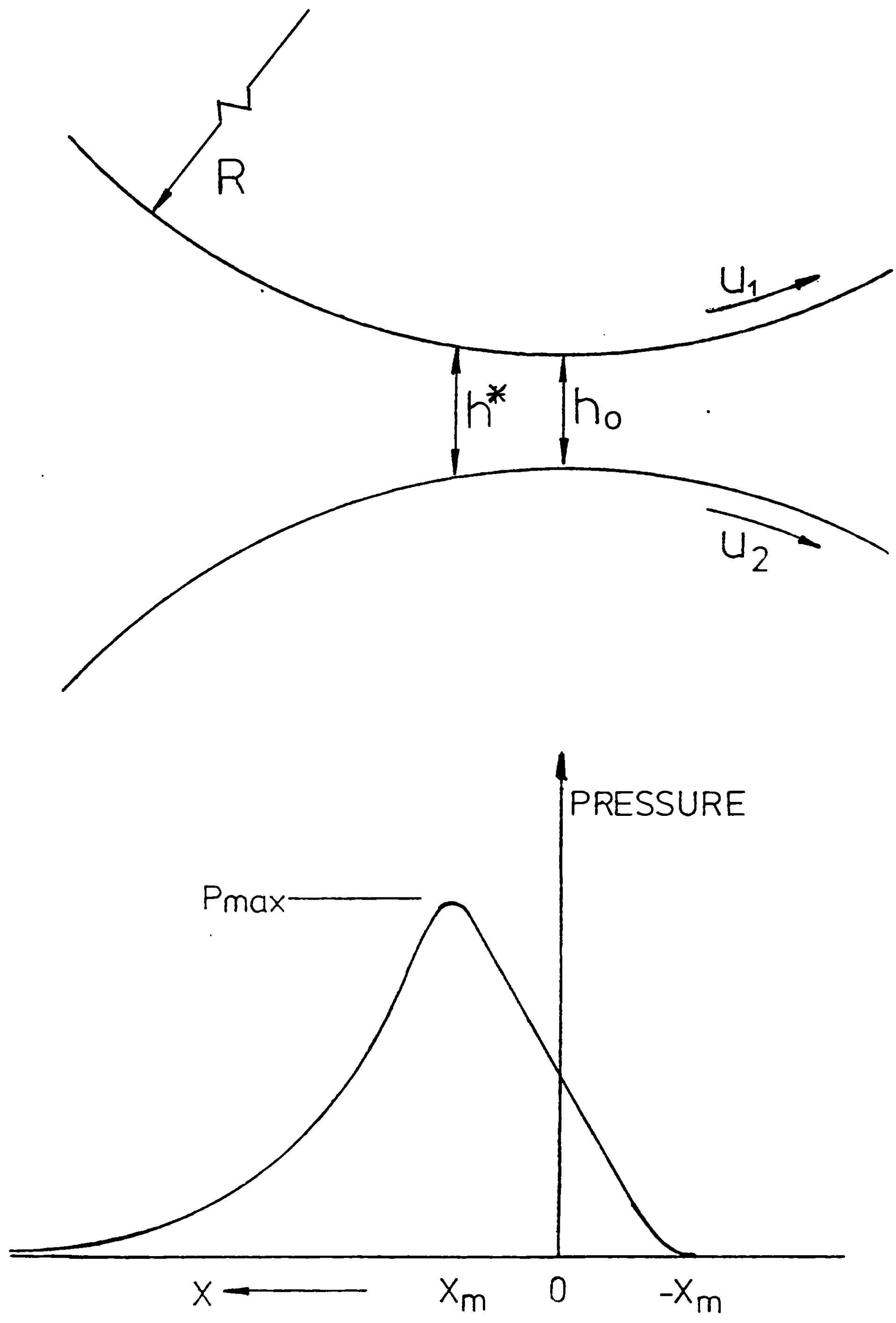

Figure 2.1 Classical lubrication - film shape and pressure distribution.

film and these have two serious effects:

1) The viscosity of the oil changes with the pressure.

2) The surfaces are elastically deformed around the high pressure regions.

When these effects act in tandem the system is said to be operating with elastohydrodynamic lubrication - ehl. At high pressures both the viscosity and the film shape are functions of the pressure. The hydrodynamic pressure generated by the unknown deformed film shape must simultaneously match the elastic pressures causing the deformation.

For line contacts, with smooth surfaces, the form of Reynolds equation for one dimensional isothermal flow is

$$\frac{dp}{dx} = -12\,\eta\bar{u}\left(\frac{h-h^*}{h^3}\right). \tag{2.1}$$

where h^* is the unknown film thickness at the position of maximum pressure.

Various relationships have been used for the dependence of viscosity, η, on pressure, p. In this thesis it is assumed that the fluid is Newtonian with a viscosity dependence on pressure given by the Barus relationship:

$$\eta = \eta_o e^{\alpha p} \tag{2.2}$$

where α is the pressure viscosity enhancement coefficient and η_o is the viscosity at ambient pressure. The viscosity also varies with the temperature by, for example,

$$\eta = \eta_o e^{-\gamma T} \tag{2.3}$$

Using the relationship given in eqn.(2.2), Reynolds' equation becomes

$$\frac{dp}{dx} = -12\,\eta_o e^{\alpha p}.\bar{u}\left(\frac{h-h^*}{h^3}\right) \tag{2.4}$$

or $$\frac{dq}{dx} = -\ 12\ \eta_o \bar{u}\ \left(\frac{h-h^*}{h^3}\right) \tag{2.5}$$

where $$\frac{dp}{dx} = e^{-\alpha p}\frac{dq}{dx}\quad . \tag{2.6}$$

q, the reduced pressure, is the pressure that would be generated by the system if there was no pressure/viscosity enhancement. On integrating, eqn.(2.6) gives

$$q = 1/\alpha\ (1 - e^{-\alpha p}) \tag{2.7}$$

Reynolds equation (eq.(2.5)) can be solved, for a known film shape, to give q , from which the real pressure p can be found using eqn.(2.7).

2.2.2. Grubin approximation to film shape

The problem of the elastic deformations at the heavy load asymptote was very much simplified by Grubin. He assumed that with lubricated non-conforming contacts at heavy loads the elastic deformation of the surfaces would be the same as that produced under dry contact by the same load, Fig.2.2a, but the deformed surfaces in the contact region would be separated by a very thin parallel fluid film, Fig.2.2b. Under dry contact conditions the elastic deformation and the pressure distribution are given by the Hertz equations. By using the film shape given by the Hertz equations in the Reynolds' equation, the need for simultaneous solution of the elastic and hydrodynamic parts of the problem is removed. Reynolds equation, using the Hertz shape, can then be solved directly to give the reduced pressure q . The expression for the real hydrodynamic pressure p , is then found from q using eqn.(2.7).

These expressions for the real and reduced hydrodynamic pressure are in terms of the thickness of the parallel region of the fluid film, h^*, which is still unknown. The following argument was used by Grubin to find this film thickness.

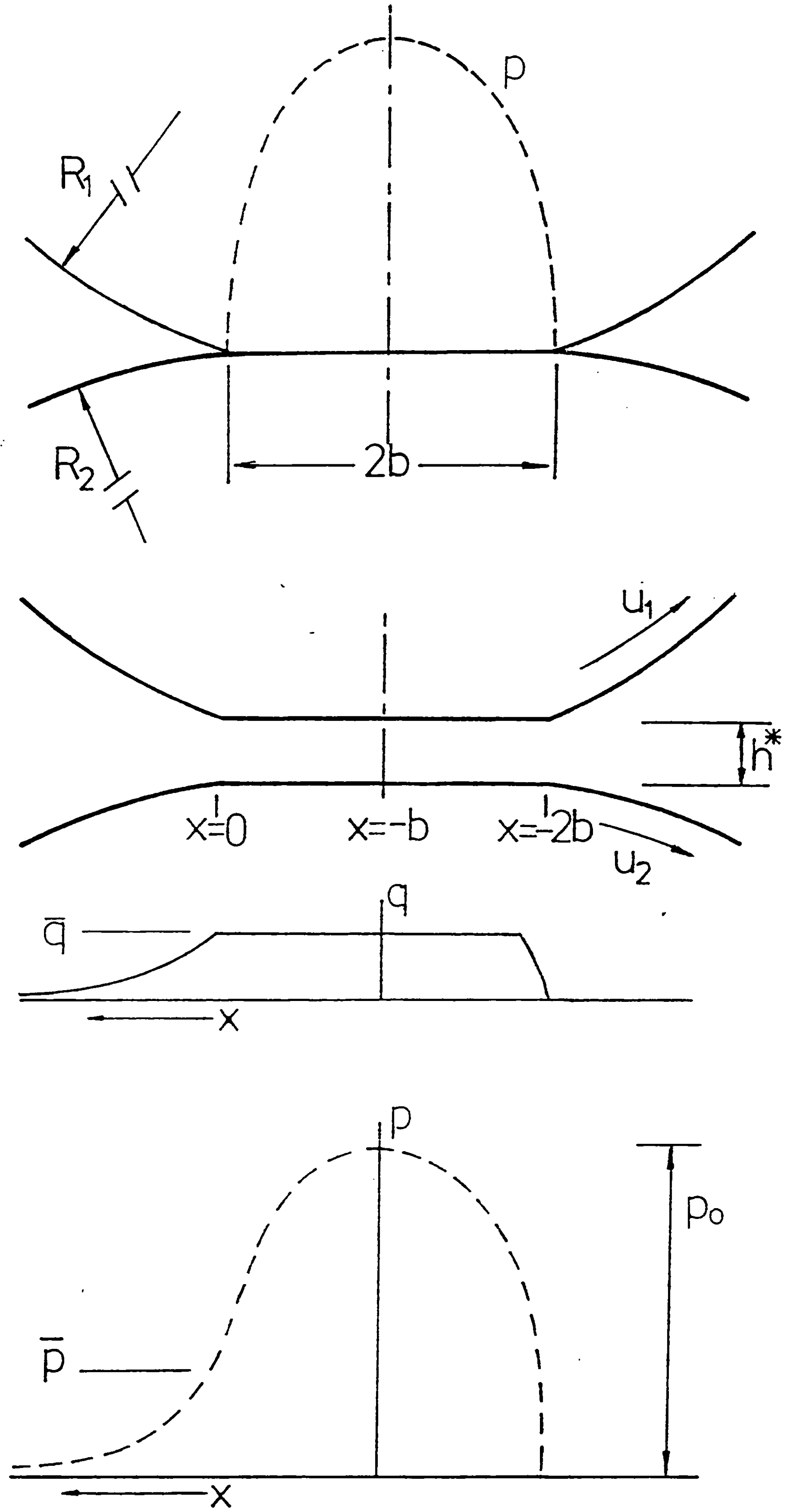

Figure 2.2 Elastohydrodynamic lubrication
a/ Hertz dry contact configuration
b/ film shape
c/ reduced pressure distribution
d/ real pressure distribution.

2.2.3. To solve for h^*

The elastic and hydrodynamic pressures and pressure gradients should match over the contact region. In the contact region the Hertzian pressure distribution is elliptic, i.e. $p = p_o\ (1-x^2/b^2)^{\frac{1}{2}}$ as shown in Fig.2.2a. dp/dx is moderate at all but the very edges of the parallel region. The hydrodynamic pressure gradient is given by the Reynolds equation (eqn.(2.4)).

Since the pressures over the contact region are high, giving αp typically of the order of 10, the $e^{\alpha p}$ term is very large. For the hydrodynamic pressure gradient to be moderate over most of this region $(h-h^*)$, must be very small. This means that the film tends to parallel over the contact region, as originally assumed by Grubin. With a parallel film, the reduced pressure q, over the contact region will be constant (eqn. (2.5)) as shown in Fig.2.1c. The real hydrodynamic pressure, p, in the contact, must still match the elastic pressures and this is achieved by the pressure/viscosity enhancement effect. In the Hertzian elastic pressures distribution, $p = 0$ at the edges of the parallel region, $x = 0$, Fig.2b. For the enhancement of the viscosity to occur over the parallel region, the hydrodynamic pressure cannot be zero at the inlet edge but must be large enough to produce the enhancement of viscosity, Fig.2.1d.

The relationship between p and q is shown in Fig.2.3. The pressure viscosity enhancement becomes significant at larger q, towards the limiting value of $q = 1/\alpha$. Grubin took the limiting condition, $\bar{q} = 1/\alpha$, where $\bar{q}$ indicates the value of q at $x = 0$, as a prerequisite value which ensures that the pressure/viscosity enhancement takes place in the near parallel contact region. This pressure must be generated by the converging inlet zone. This limiting value for $\bar{q}$ can be used as a boundary condition with the integrated form of the Reynolds equation, to find the central film thickness, h^*.

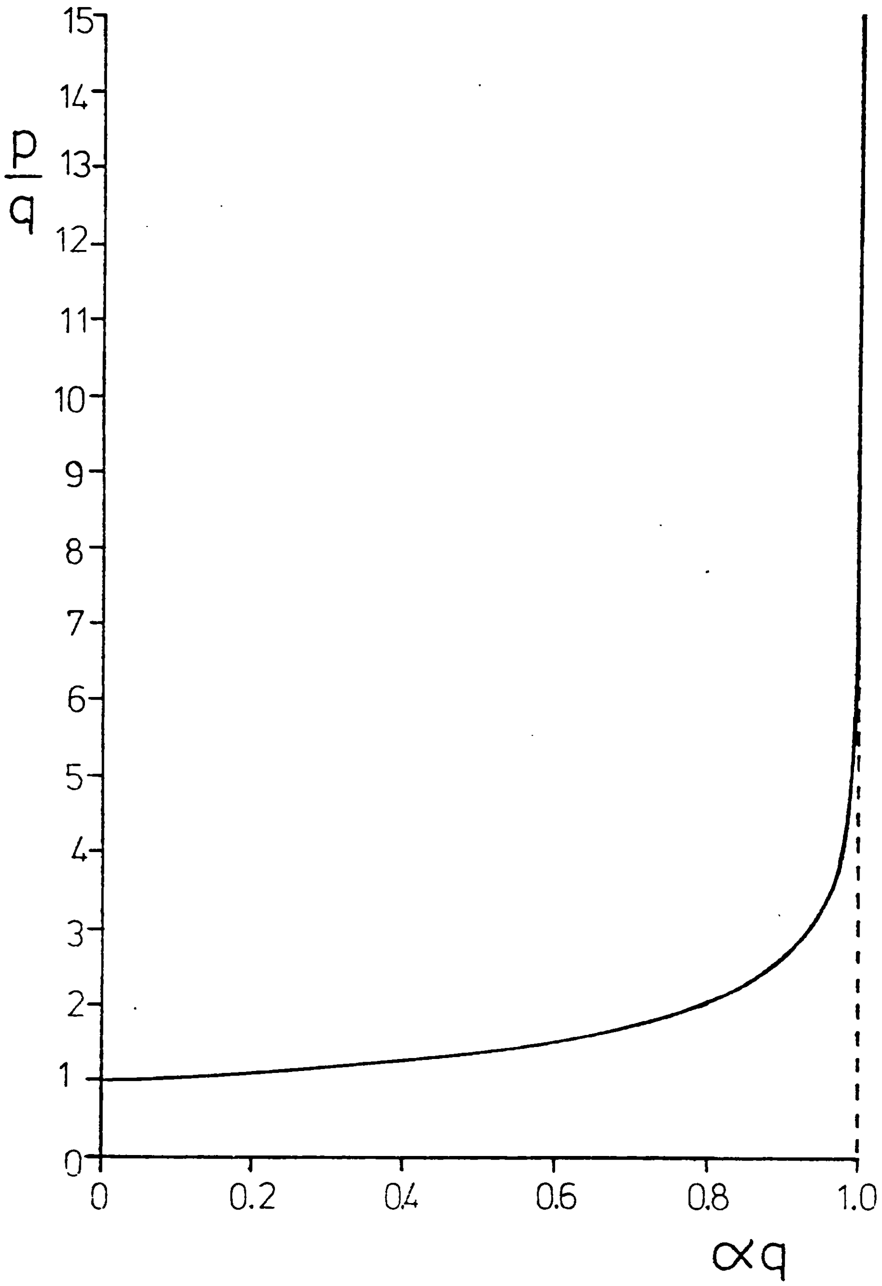

Figure 2.3 Relationship between enhanced and reduced pressure.

2.3 Dyson's Failure Criterion

2.3.1. Failure of rough surfaces

Most surfaces used in lubrication practice are prepared using finishing techniques which involve random contacts between grits and the surface. The resultant texture consists of a more or less random roughness superimposed on a more or less periodic structure termed waviness, Fig.2.4. Smooth surface solutions for the e.h.l. problem often result in λ ratios, which predict a high degree of surface interaction. This suggests that the effects of the surface roughness cannot always be ignored. Two types of solution to Reynolds equation have evolved to deal with roughness effects. Averaged solutions of Reynolds equation smooth out the variations due to individual asperities and show the effect on the macro behaviour, for example, Christensen (1969). Deterministic solutions show the effect of the individual roughness features which are usually represented by a simplified surface form such as a sine wave - for example Dowson and Whomes (1971).

Dyson explored the failure of the lubrication of rough surfaces. He considered the effects of surface roughness on both the contact mechanics and on the hydrodynamics of the system.

The high degree of surface interaction which occurs at severe conditions in e.h.l. line contacts does not necessarily lead to failure. Dyson argued that surfaces can only survive a high degree of asperity overlap or interaction if a high viscosity fluid is present between the sliding asperities - so protecting them. With very thin films, at heavy loads, most of the load is carried between deformed asperities. If the high viscosity fluid is present then the asperities are not necessarily in dry contact but separated by a very thin highly viscous film.

The condition used by Dyson to show that sufficient pressure was being generated in the converging inlet wedge to enhance the fluid viscosity

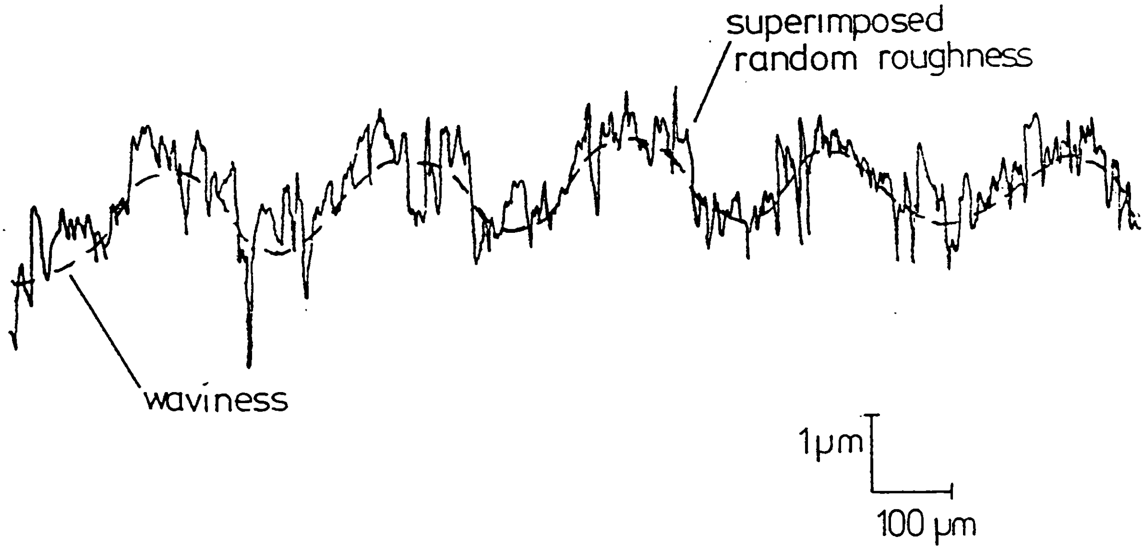

Figure 2.4 Surface profile of a ground surface.

by the required degree was that the maximum reduced pressure (q_{max}) tended to $1/\alpha$.

With increasing temperature, as in a two disc scuffing test, the viscosity and hence the reduced pressure generated in the inlet wedge is reduced. The mean lines of the opposing surfaces must move closer together to maintain the condition $q_{max} \to 1/\alpha$ and thereby ensure the enhancement of the viscosity with the pressure. With rough surfaces there is a limit for a given load to the approach of the surfaces due to asperity contact and interaction. Dyson argued that if this limiting mean approach or gap was less than that required at the given temperature and load to meet the condition $q_{max} \to 1/\alpha$, then the system would fail to produce the high viscosity fluid film, the asperities would no longer have hydrodynamic protection and this could lead to failure.

2.3.2 Form of Reynolds Equation

Dyson considered the behaviour of circumferential ground surfaces in line contact. The asperity length is long compared to the Hertzian contact width and so the asperities in the solution of Reynolds equation can be considered as continuous ridges and grooves. The profiles of two such opposing surfaces at right angles to the direction of flow are shown in Fig.2.5 h - the compliance, is the distance between the mean levels of the surfaces. h_1 and h_2 are the local deviations from the mean level and H the local gap is given by

$$H = h - h_1 - h_2$$

The appropriate form of Reynolds equation was given by Christensen (1969-70) as

$$\frac{dp}{dx} = - 12\, \eta \bar{u} \,.\, \frac{E(H) - E(H_m)}{E(H^3)}$$

where E(H) is the expected or average gap between the surfaces. To solve this equation for a given pair of surfaces and to find the critical temperature for a given load at which $q_{max} = 1/\alpha$ requires a knowledge of

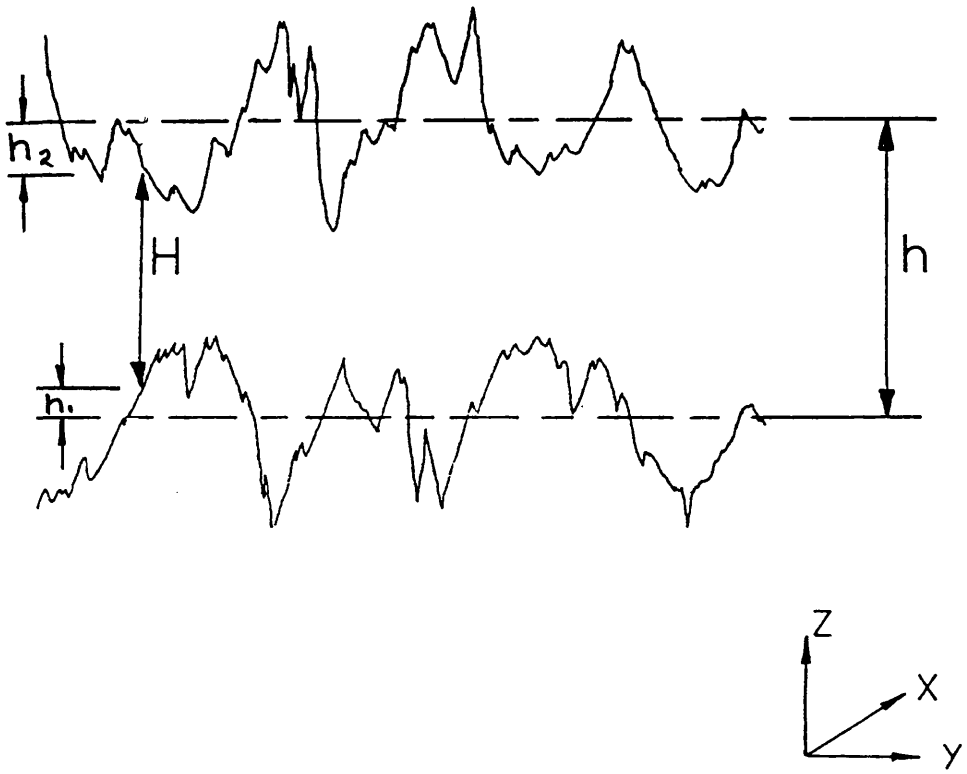

Figure 2.5 Opposing circumferential ground surfaces (section perpendicular to flow).

a) The relationship of the statistics of the surface heights to $E(H)$ and $E(H^3)$.

b) The distance to which two plane surfaces with the same superimposed roughness could approach under a given load, and

c) The macro shape of the deformed body.

2.3.2a. Surface heights distribution

The analysis was for a pair of circumferentially ground discs from a scuffing test by Bell and Dyson (1972). The surfaces in question are those just prior to failure which, as running-in had occurred, were different to the original surface. It was assumed that the unscuffed portions of the surface would have the same characteristics as the scuffed areas before failure. The surface profiles of the unscuffed areas were measured with a stylus instrument to find the surface height distributions to which approximate analytical surface height probability distributions were fitted

On bringing the surfaces together it was assumed that they could overlap without interference, Fig.2.6a. The expected film thickness, or the separation $E(H)$, is the average value of the remaining spaces between the overlapping asperities. At severe conditions the mean lines of the surfaces can overlap, i.e. a negative compliance. The average gap $E(H)$, decreases with the compliance but remains positive, Fig.2.6b. Expressions were found from the individual surface height probability distributions of the surfaces which related $E(H)$ and $E(H^3)$ to the compliance - the distance between the mean levels of the undeformed surfaces.

2.3.2b. Relationship between load and surface approach

Dyson assumed that at severe lubricated conditions all the load would be carried between deformed asperities. The relationship between the approach or compliance of the rough surfaces and the applied load

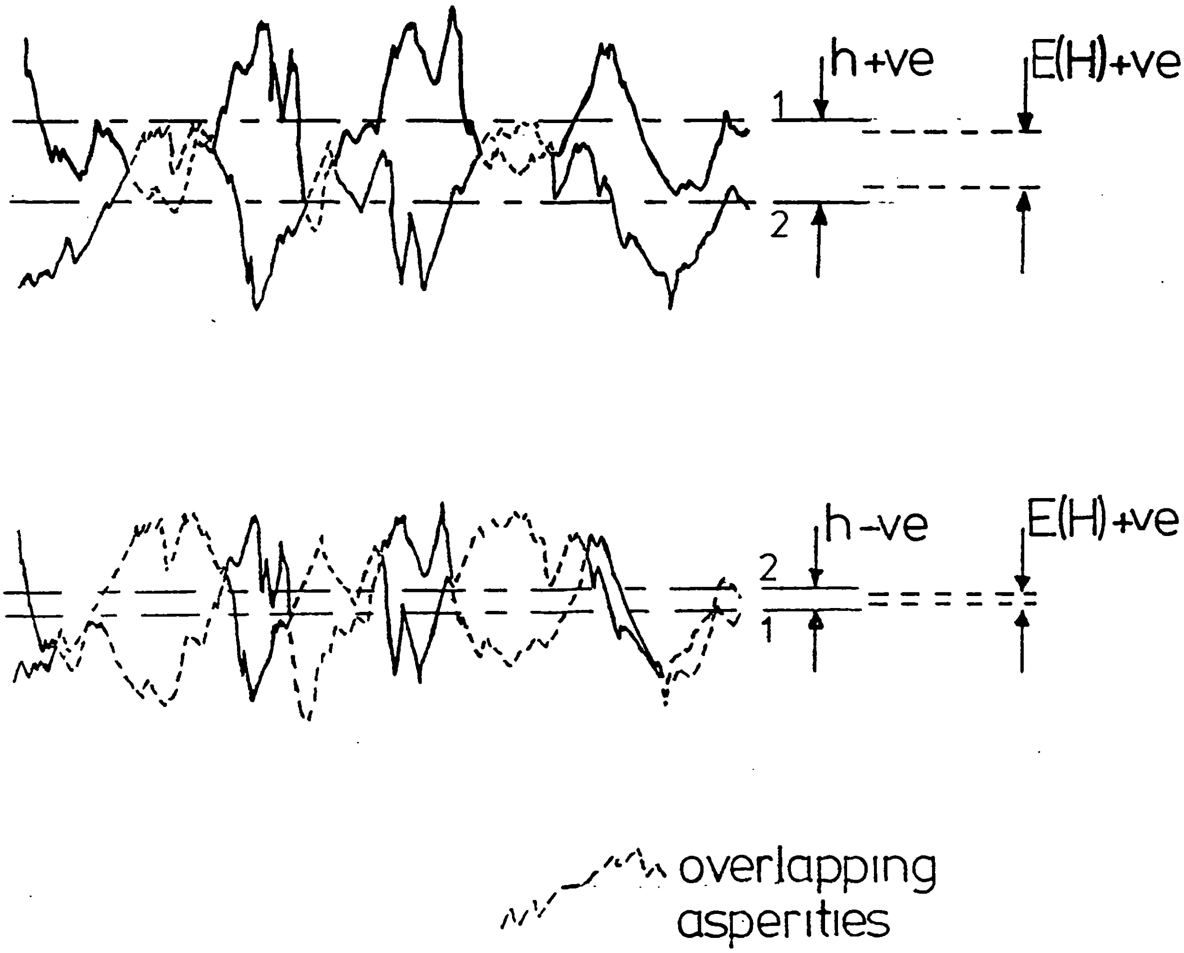

Figure 2.6 Separation of surfaces - E(H) with a/ positive and b/ negative compliance - h.

would therefore be the same as that for the dry contact configuration. This relationship was found using a computational method devised by Archard, Hunt & Onions (1975). A number of profiles of a portion of each of the disc were superimposed on a plane surface. The two opposing surfaces were brought together in a computer simulation and again it was assumed that they could overlap without interference. From the area and overlap of each asperity interaction, the elastic or plastic pressures which would be generated if the asperities deformed, as would be the case in practice, were found, Fig.2.7. Summing the asperities, pressures of all the overlapping asperity pairs gave the mean pressure for the apparent contact area. This was done for non-dimensional compliances, t, in the range $t = h/\sigma = 0.5 - 2$.

At severe conditions approaching scuffing failure, i.e. high temperature, there is a negative compliance, i.e. the original mean lines of the surfaces overlap. Dyson grossly extrapolated the load compliance relationship to higher loads and negative compliance, down to $t = -4$, to match the scuffing conditions of the test.

2.3.2c. Macro film shape

For two smooth surfaces loaded together in dry contact, the deformation, contact area and elastic pressures are given by Hertz equations. The effect of surface roughness is to increase the apparent contact area, which in turn alters the pressure distribution and the resulting deformation. Dyson assumed a pressure distribution of the form

$$p = \left(1 - \frac{x^2}{c^2}\right)\left(p_o + p_2 \frac{x^2}{c^2}\right)$$

where p_o, p_2 and c are unknown constants, and c is the half contact width. For rough surfaces the contact width is greater than that for smooth surfaces and the pressure distribution is more spread out than the Hertzian form.

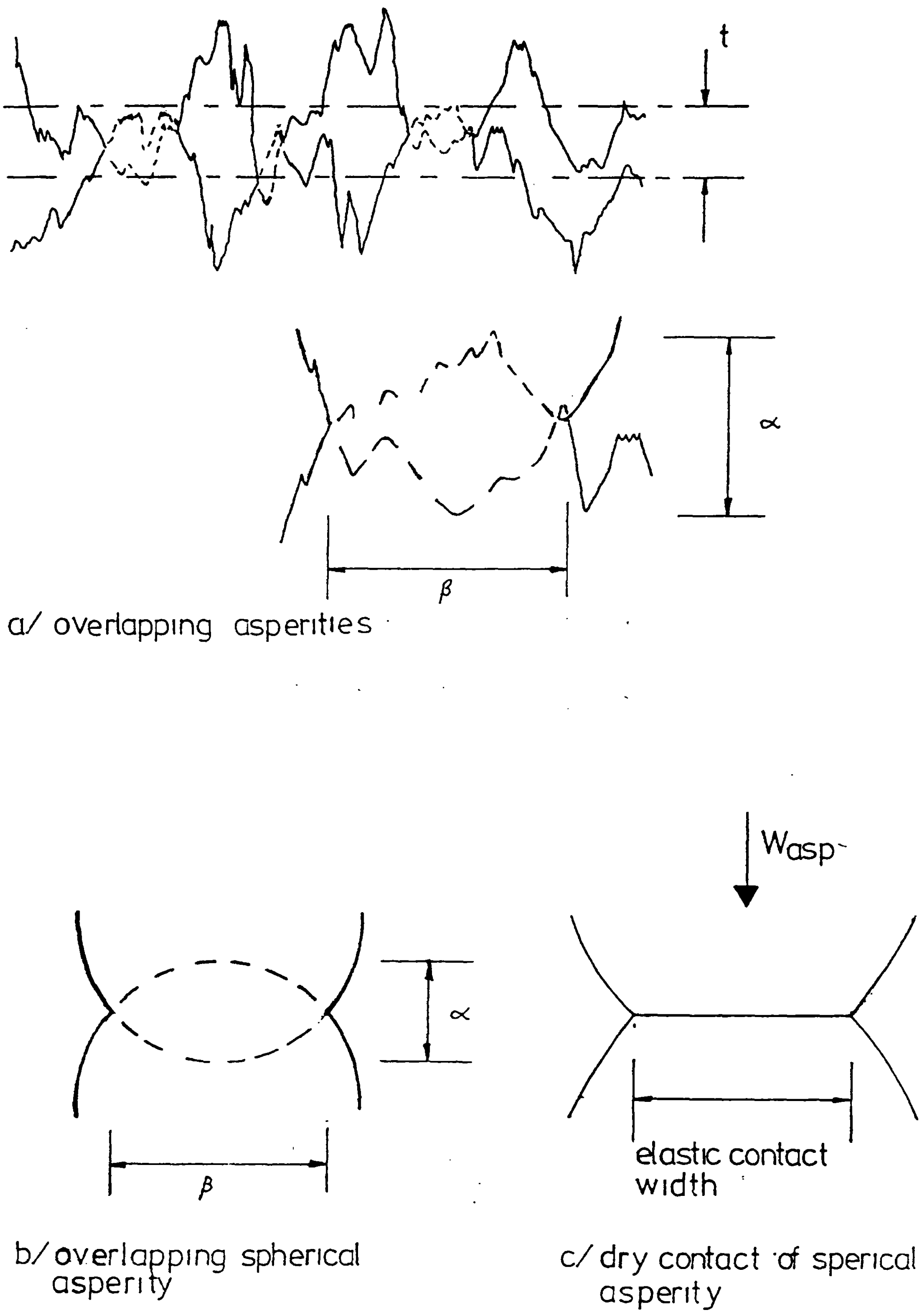

Figure 2.7 Pressures generated by apparent contact area of overlapping asperities.

When a load is applied between two rough bodies it is transmitted through the contact area. The body deforms and produces elastic pressure in the body. The force-compliance relationship (Section 2.3.2b), gives the compliance necessary to produce the same pressure distribution from the deformation of the surface asperities. As the assumed form of the macro pressure distribution across the contact area varies with x, then the compliance of the surfaces to transmit this pressure distribution must also vary with x. By matching the force/compliance relationship to the assumed macro pressure distribution the variation of the compliance with x, i.e. the deformed film shape, was found. This expression contained the unknowns p_o, p_2 and c. These were found from the known applied load and by matching the deflections caused by the pressure distribution to the undeformed body shape. The resulting deformed shape was not parallel in the contact zone but retained a slight curvature.

2.3.3. Solution of Reynolds Equation

The three parts of the analysis were then combined to solve Reynolds equation. The deflected film shape $(t(x))$ and minimum gap (t_m), (Section 2.3.2c), were used with the expressions relating the average film thickness to the compliance, (Section 2.3.2a) to furnish the required expressions for $E(H)$, $E(H^3)$ and $E(H_m)$. These were used in Reynolds equation which was solved to find q. The condition $q_{max} = 1/\alpha$ was applied at the position of the minimum film thickness and the body temperature at which this condition was just achieved was found. A higher body temperature than this would result in $q_{max} < 1/\alpha$. As the surfaces are unable to move closer together to increase the hydrodynamic pressure generated in the inlet, the hydrodynamic system would fail and the high viscosity fluid interposed between the asperities would be lost which could lead to scuffing failure.

There were several possible sources of error in the analysis. The major inaccuracy was thought to be in the surface data analysis. In calculating the expectation film thickness values, E(H) etc., the surfaces were allowed to overlap without interference. This ignores the effect of elastic deformation of the asperities. The force/compliance contact simulation was for $t = 0.5$ to 2 . The expression fitted to the results was extrapolated to $t = -4$, which was also a cause for concern.

2.3.4. Comparison to Experimental Values

The discs analysed were from a two disc scuffing test. Typically in these tests, the surface speeds and oil supply temperature are set at the beginning of the tests and the load is applied in steps at set time intervals until the discs fail. Each increase in load increases the frictional traction which raises the disc temperature. The predicted temperature for failure of the discs in question was 150°C , compared to the measured temperature of 180°C at scuffing failure.

This test was one from a series of scuffing tests by Bell and Dyson (1972). Several of the other tests from the series and some from a series by Bell, Dyson and Hadley (1975), had the same initial surface roughness. It was assumed that the discs underwent similar surface modification during the tests as the original pair of discs and so would have similar surface height distributions at failure. The analysis of the discs from the original test was therefore used to predict the temperatures at failure of a number of these other tests. Although several criticisms of the analysis had been made there was nevertheless an encouraging correlation between the temperatures which suggested that scuffing failure could be linked to the breakdown of the hydrodynamic lubrication. The theory obviously needed testing over a wider range of conditions.

Further programs to test the hypothesis were carried out by Rossides (1980) at Cardiff University and by Story (1984) at Leicester University.

2.4. The Rossides, Story, & Bell & Dyson Test Results

2.4.1. Rossides tests

Rossides improved the surface data acquisition procedure to provide direct on-line recording of the necessary surface roughness parameters. He also produced a more accurate extrapolation of the force-compliance relationship. It was argued that at large degrees on interpenetration, an increase in load would mainly enlarge existing areas of contact, rather than creating new contacts. The force compliance relationship would then be expected to follow that of a single asperity contact, i.e. mean apparent pressure $\alpha(\text{compliance})^{-3/2}$.

He did a series of tests at a fixed slide/roll ratio for a range of rolling and sliding speeds and surface roughness combinations - 10 tests with a straight mineral oil and one with an additive oil. For these tests the predicted failure temperatures were found using his improved version of Dyson's criterion. He also reworked the result of the original Bell & Dyson test for which the load-compliance relationship had been found. These temperatures and the corresponding measured failure temperatures are compared in Fig.2.8.

2.4.2. Story Tests

Story at Leicester performed two series of tests. In the first, the effects of surface finish direction, axial or circumferential with the same nominal roughness value, sliding speed at constant rolling speed and oil viscosity, were investigated. Axial surface finish, low sliding speed and higher viscosity increased scuffing resistance. The second set of tests was designed to more closely investigate the effect of different roughness combinations and oil supply temperature. The scuffing resistance decreased with the higher oil supply temperature (50°C), and with rougher surfaces.

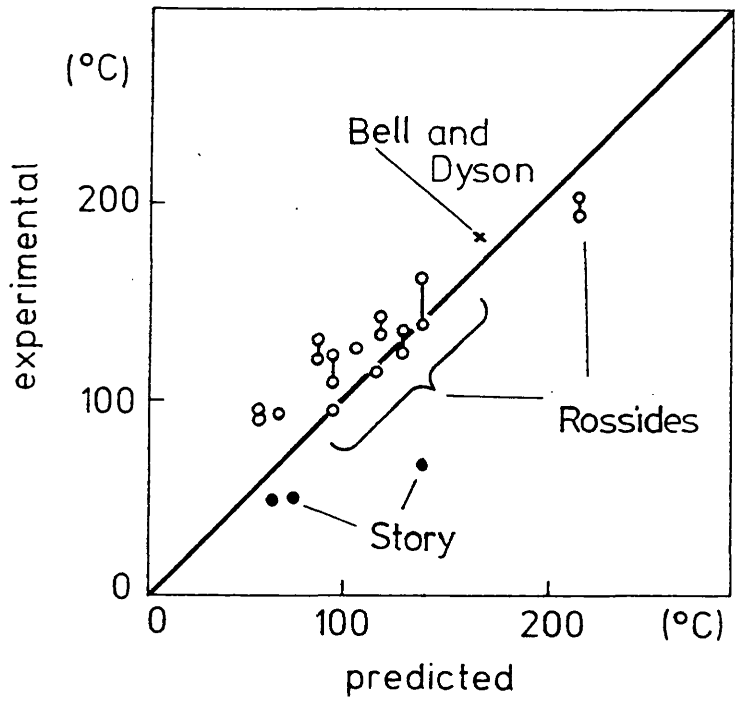

Figure 2.8 Comparison of predicted and experimental bulk temperatures for scuffing failure.

Rossides analysed three of Story's tests to predict the critical bulk temperature at failure. These are also shown in Fig.2.8. Whereas the Rossides tests with the straight mineral oil had all failed at temperatures greater than or just below the predicted value, the three Story tests which were analysed failed at temperatures lower than those predicted.

2.4.3. Comparison of Tests Types

The three sets of tests covered similar ranges of surface speeds and surface finishes but the Rossides tests and the Bell & Dyson tests reached higher loads and disc bulk temperatures before failing, Fig.2.9. The Rossides tests and Bell & Dyson tests started at an oil supply temperature of $78 \pm 3°C$, except for one of the Rossides tests which had an oil supply temperature of 45°C, compared to 30°C or 50°C in the Story tests. The higher temperature Dyson and Rossides tests therefore started at more severe hydrodynamic conditions in terms of λ, the roughness to film thickness ratio. Although this ratio has been shown to be no clear indicator of failure, the Story tests did start operating with more favourable conditions and so could reasonably be expected to run to higher loads. In fact, in terms of this ratio, the Rossides tests ran with considerable interaction before failure, whereas the Story tests failed at relatively low values of λ.

Several other differences occurred between the test types. The post-run surfaces in the Rossides tests were well run-in. The Story's discs from the tests at a lower slide/roll ratio had similar running in to the Rossides tests, but those at the same slide/roll ratio as the Rossides tests showed little surface modification. Post-run surface profiles of a Rossides and Story test are shown in Fig.2.10.

There was also a difference in the temperature/time response of the Story and Rossides tests. Following an increase in load, the temperature changes in the Rossides tests were smaller and the temperatures reached

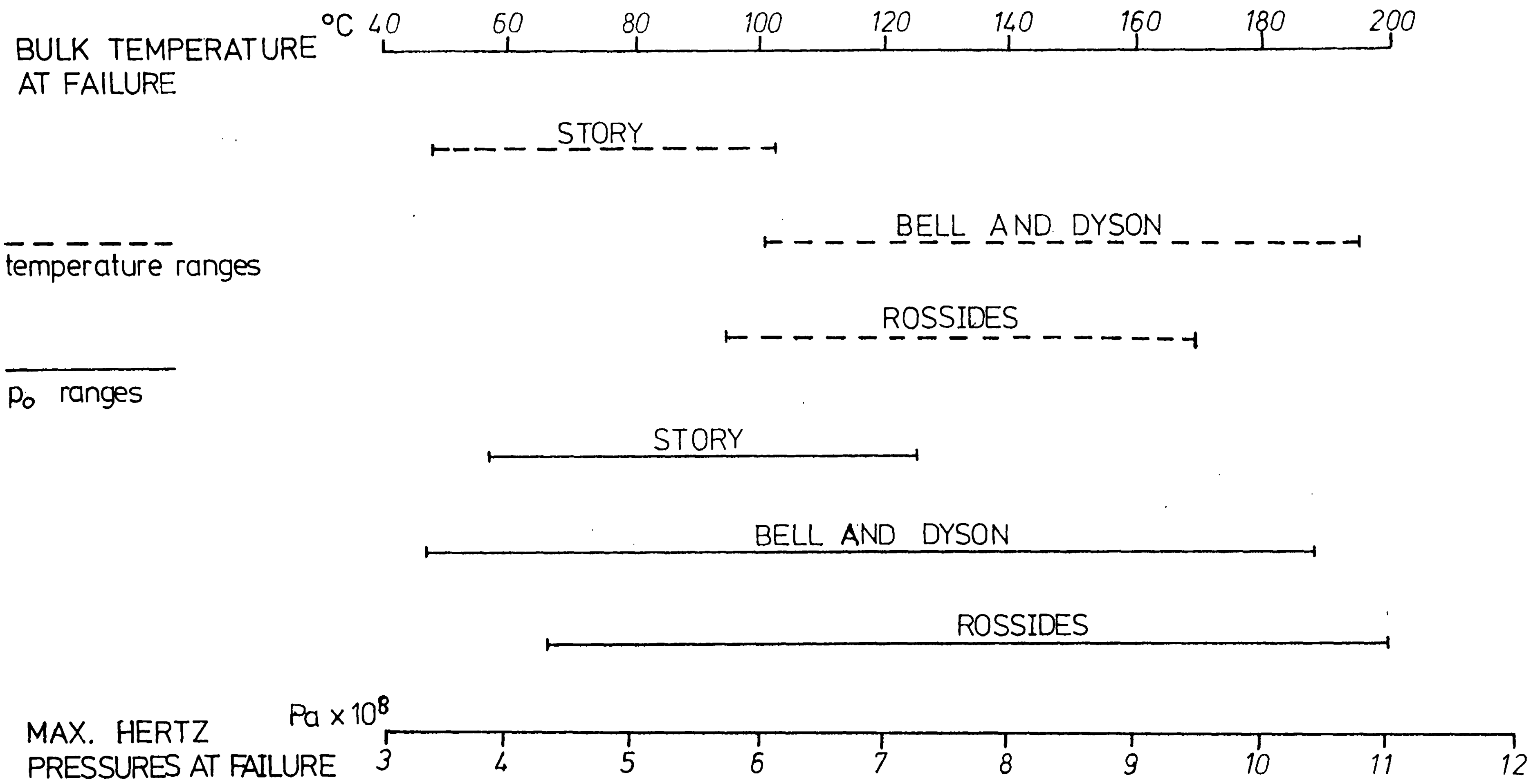

Figure 2.9 Ranges of failure load and bulk temperature for the Story, Rossides and Bell and Dyson test series.

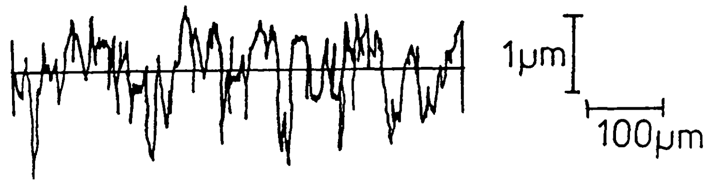

pre-run

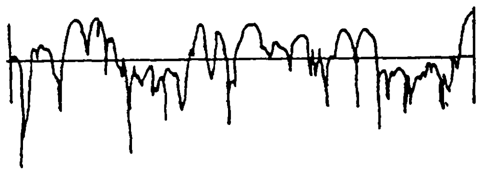

post-run

ROSSIDES TYPE TEST — $u_S = 4{\cdot}14$ m/s
(after Bishop)

pre-run

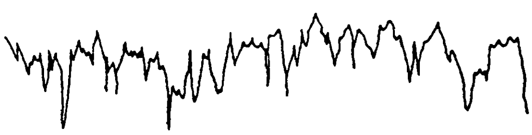

post-run (not relocated)

STORY TEST — $u_S = 4{\cdot}23$ m/s
(scales not given)

Figure 2.10 Post-run surfaces from a Story and a Rossides test.

equilibrium faster than those in the Story tests. The temperature in some of the Story tests did not reach equilibrium by the end of the five minute increment period.

Two types of failure pattern were therefore emerging. The first, as in the Cardiff and Shell tests, where there were failures at higher loads and temperatures, failing in accordance with the Dyson criteria, running with considerable surface interaction prior to failure and in which the unscuffed portions of the post-run surface showed considerable running-in. The Rossides tests had more rapid changes in temperature. On the other hand, in the Story type tests, which started with apparently better lubricating conditions, failures were at lower loads and temperatures: the temperatures lower than those predicted by the Dyson postulate were slower to reach equilibrium than the Rossides tests, failed without much asperity interaction and showed less post-run surface modification.

For otherwise similar ranges of conditions, in terms of surface speeds and surface roughness, the only differences between the two groups of tests were in the initial and operating conditions and the test machine. The oil supply temperature for the Shell tests and for the Cardiff tests was $78 \pm 3\,°C$, except for the one at Cardiff which started at $45\,°C$, compared to $30\,°C$ or $50\,°C$ for the Leicester tests. The Shell and Cardiff groups used a loading sequence in which the first load was small and the size of the load stages increased during the test. The Leicester loading sequence had a higher initial load but equal load increments thereafter.

Differences in test machine design were thought to be responsible for the different thermal response during the tests. The Leicester two disc machine was a converted ex-pitting machine and was consequently quite sturdy with large bulk parts. The Cardiff test machine was similar to that used at Shell, and was a much trimmer design. The differences in the operating procedure, that is the initial temperatures and loading sequences and the thermal response of the test machine, were thought to be responsible for the differences in the test results. Why this might be so was not immediately apparent as it was the conditions prior to failure, not the intermediate stages of a test which were generally considered important.

2.5. Supporting Literature

The results of several other workers lent credence to the suggested causes for the test types. Fein (1967) attempted to resolve the discrepancy in the total contact temperature at failure found by different investigators who used the same test machine and lubricant. He investigated the effect of operating conditions by running a series of tests with a variety of run-in procedures followed by the same step-load sequence. It was reported that longer run-ins with thinner films prior to the main test sequence increased the load carrying capacity and failure temperature, and that "the load carrying capacity and critical temperature depend on the entire time-temperature-load-velocity history of the discs and can be varied by more than 550°F ". This supported the suggestion that the different initial and operating conditions of the two groups of workers could influence the failure conditions.

The role of the thermal response of the test machine had previously been demonstrated by Crook & Shotter (1957). They compared the results of a test run with the discs insulated from their shafts, and of a test run with the same conditions but without the insulation. For a single load there was a larger temperature rise in the insulated test, which failed before equilibrium was established. In the uninsulated test the temperature reached equilibrium at a lower temperature and the test did not fail. The accepted role of temperature at that time was that proposed by Blok (1939) of a total critical temperature in the contact zone which depended on the oil material combination being used. Crook and Shotter suggested that the temperature could be an important factor in scuffing from a hydrodynamic point of view, which had until that time not been appreciated. On the basis of their result they suggested the following mechanism of failure.

If, on applying a load, the conditions are such that asperities are brought into contact then the asperities may be reduced by wear or flow. At the same time heat is generated in the contact which raises the disc temperature. This reduces the film thickness which in turn brings more asperities into contact. Crook and Shotter argued that if the asperities easily ran in, the heat input would be reduced and if the machine was able to quickly remove the heat produced from the discs, then equilibrium would soon be established. On the other hand, if the asperities were not easily run in and the machine did not naturally cool the discs then the film thickness would be reduced further, bringing more asperities into contact causing a run-away situation until failure occurred.

A similar conclusion was reached by Christensen (1965) who found that the temperatures in the discs did not stabilise until twenty minutes after a load increase and stated that the ability of the surface to run in was a crucial factor in this.

The thermal response of the tests and the degree of running-in of the test types indicated that an uneasy balance between the ability of the surfaces to run in and the rate of change of temperature could be the cause of the different test types, the thermal response of the tests being dependent on the machine design.

Story (1984) suggested that the type of failure was determined by the ability of the surfaces to run in. She argued that if running in took place the surfaces would survive to more severe conditions than surfaces which were unable to run in. As there was support for the suggestion that the operating conditions and the machine thermal response could influence the failure conditions, both effects were therefore considered to warrant further investigation.

The ability of the surface to run in seemed to be of importance in determining the failure conditions. Bishop had shown that the majority of the surface modification occurred early in a test and Fein that running in was promoted by longer running with thinner films. As the initial conditions of the test types were different, in an attempt to find the reason for the more successful running-in in the one set of tests, interest switched from the prediction of scuffing failure conditions to the differences that the tests underwent in the earlier stages. Baglin questioned the effect of bringing the surfaces together in different ways in the early stages of a test. The result of this investigation is reported in the next section.

2.6. The Baglin Model and its Predictions

2.6.1. Conditions for onset of micro-ehl

Micro-ehl films are those formed between asperity tips and the opposing surface when the asperity is deformed with respect to the macro shape of the system. The existence of micro-ehl films had been suspected for some years. For example, Fein (1965) explained scuffing test results in terms of a squeeze film mechanism beneath the asperity tips. Cheng (1983) expressed the belief that the understanding of such films would lead to the better prediction of wear, pitting and scuffing. Baglin suspected a possible connection between these films and operating conditions. Subsequent theoretical analysis (Baglin (1986a and b)) found the conditions at which these films might be expected.

It is accepted that ehl theory for smooth surface is adequate to predict the separation between the mean levels of rough surfaces if they are well separated.

As the film thins due to increasing load and temperature then two effects of roughness become more pronounced. The roughness alters the pressure build-up in the inlet zone. For circumferentially ground surfaces, the inlet becomes a less efficient generator of pressure. To compensate, the film thickness is reduced so that sufficient pressure is generated in the inlet zone to maintain the parallel film shape.

The second effect occurs within the contact region. The roughness causes ripples in the otherwise nominally smooth pressure distribution. These are caused by the resistance to side leakage from the local film thickness variations. For circumferentially ground surfaces the ripples formed are normal to the main flow direction.

Baglin found the magnitude and the form of the ripples formed for a circumferentially cylinder loaded against a flat smooth surface, Fig.2.11. The ground surface was modelled as a simple sinusoid with wavelength $2L$, and amplitude d_o, superimposed on the surface of a cylinder. The main load bearing area was treated as a tilting pad rather than a parallel flat (Archard & Baglin (1986)). This enabled variations in the pressure within the conjunction to be explored. The appropriate form of Reynolds equation was first solved using an averaged approach to give the macro film thickness and the slope of the tilting pad region. The problem was then solved deterministically for a rigid sine wave form superimposed on the macro film shape to give the size and form of the pressure ripples formed along the centre line, that is at $x = -b$, $p = p_o$, Fig.2.12.

The magnitude of the pressure ripple ΔP in terms of two non-dimensional groups is shown in Fig.2.13. The size of the pressure ripple, $\Delta P = P_{max} - P_{min}$, increases with longer wavelengths and with the amplitude of the sine wave, with thinner films and with lower average pressures. The ripples were also shown to become more concentrated about the peak of the asperity as the magnitude increases.

With the excess pressures concentrated about the asperity peaks, it is likely, if the pressure ripple is large enough, that the asperities will be elastically deformed. Whether deformation of the asperity would occur for a given set of conditions was based on the following criterion.

The integration of the pressure ripple in the y direction gives the hydrodynamic load/unit length borne by the asperity. If the same load was borne by the asperity in dry contact then it would elastically deform and give a maximum pressure value P_{asp}, Fig.2.14. If the ripple form

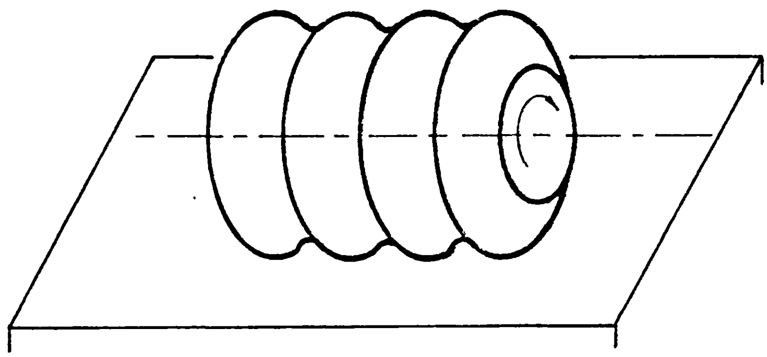

Figure 2.11 Configuration used in micro-ehl onset model -circumferentially ground cylinder loaded against a plane surface.

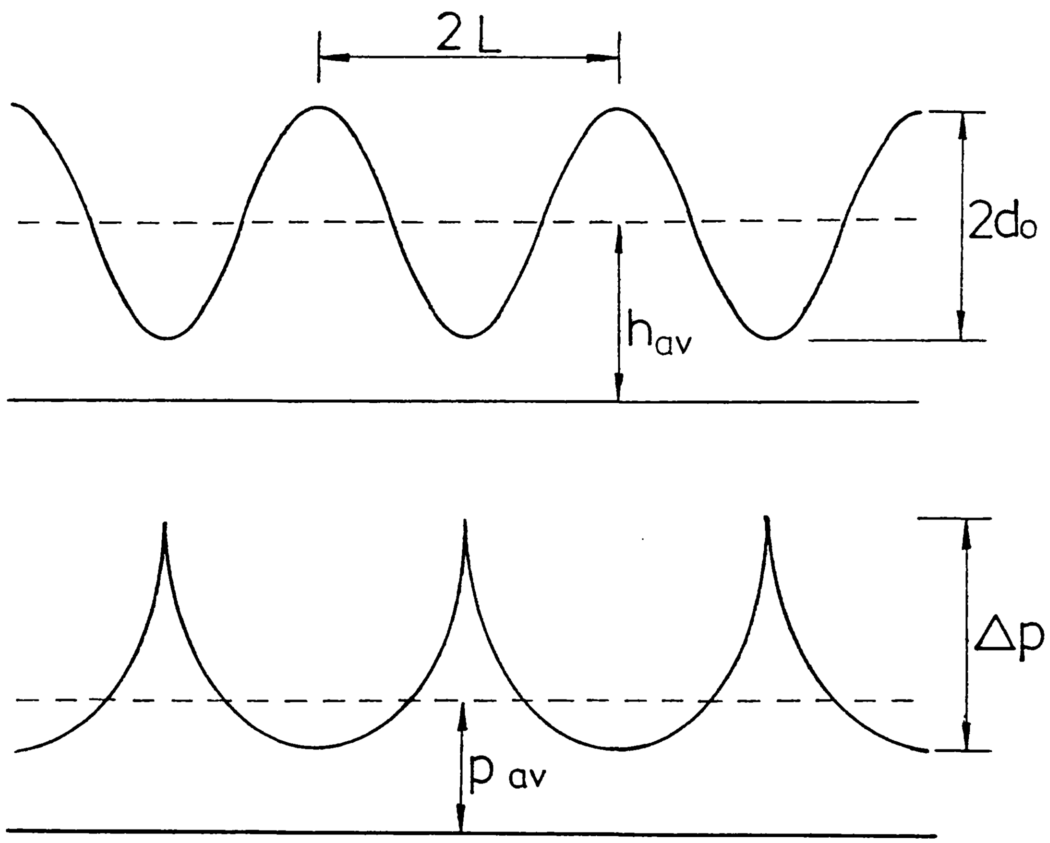

Figure 2.12 Asperity shape and pressure ripple form.

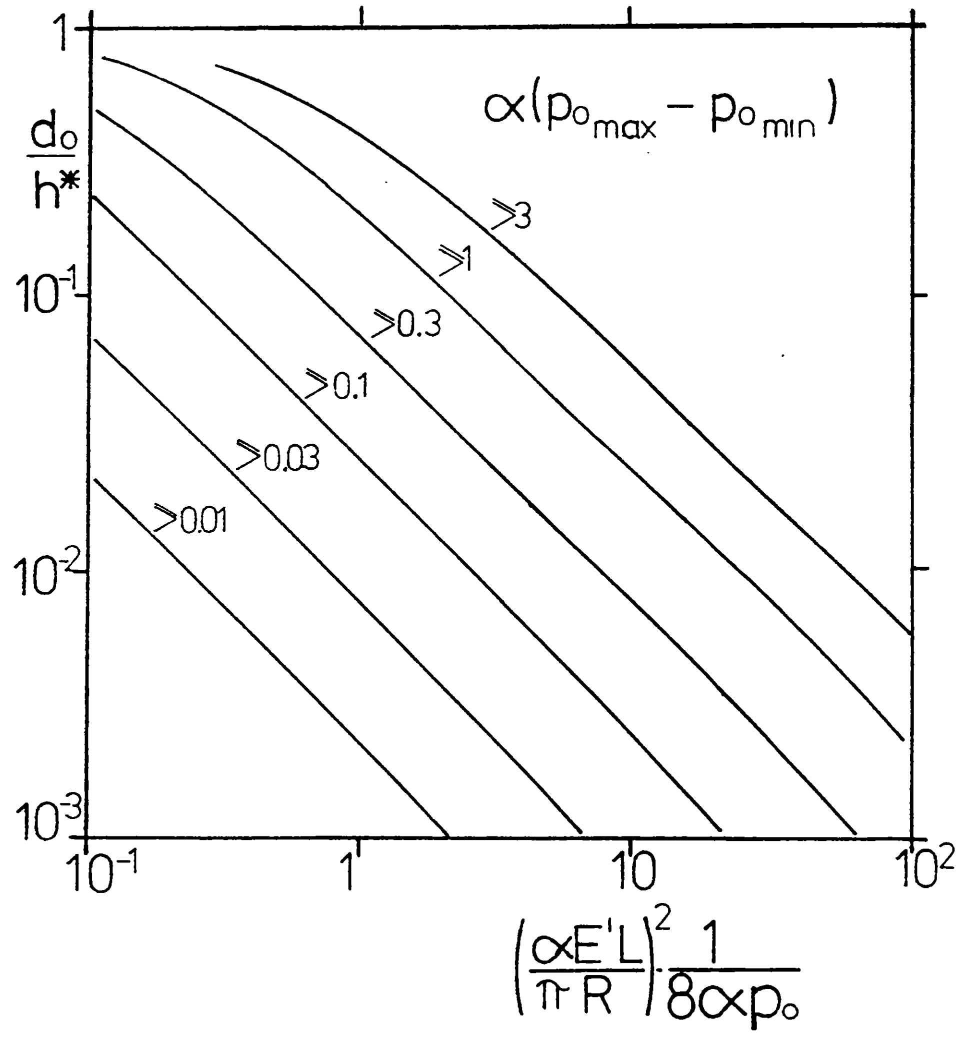

Figure 2.13 Pressure ripple magnitude

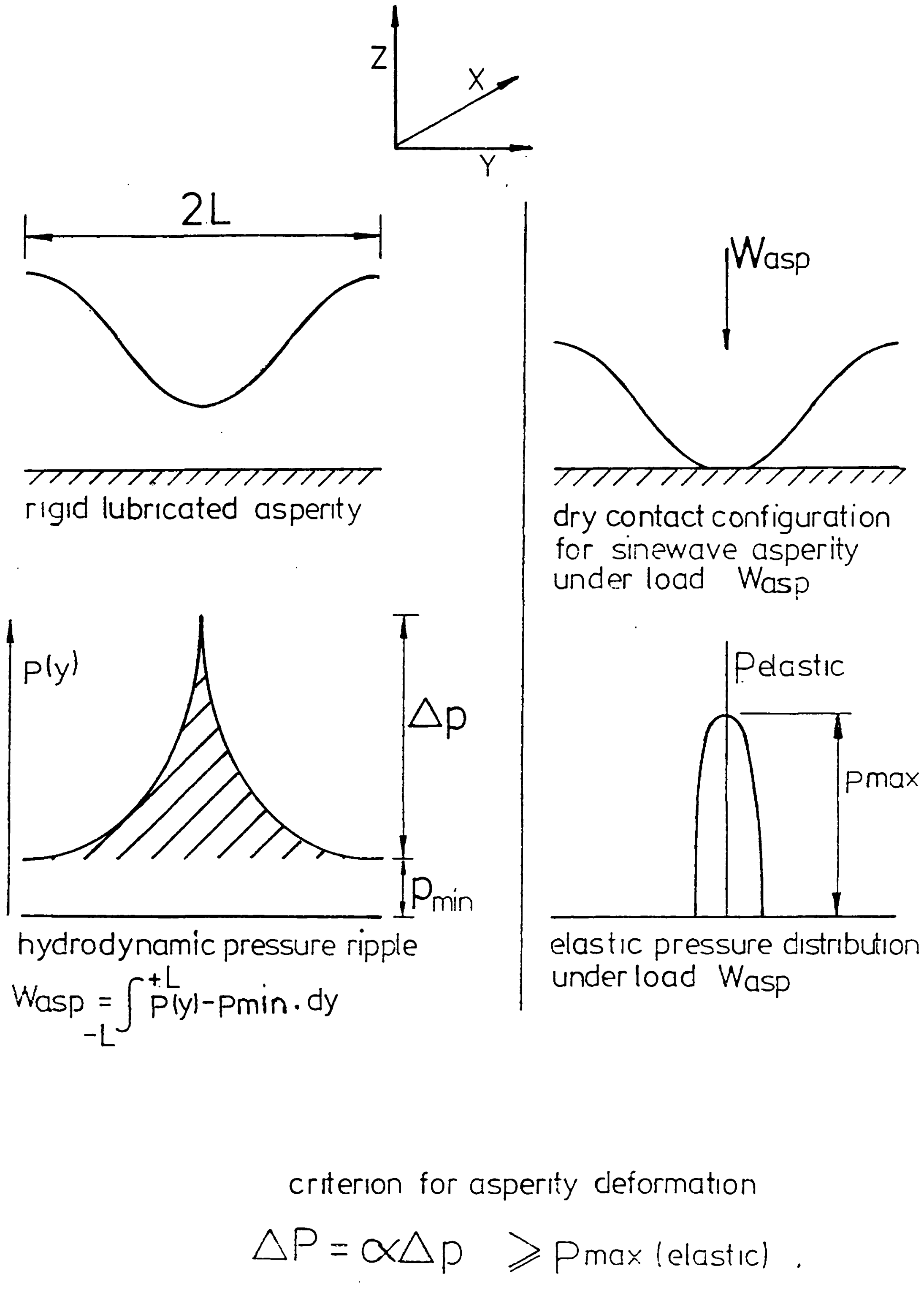

Figure 2.14 Criterion for asperity deformation due to generated pressure ripple.

is such that $\Delta P < P_{asp}$ then the pressure ripple is considered to be too spread out for significant deformation to occur. Conversely, if $\Delta P > P_{asp}$ then deformation or flattening of the asperity peak would result. The system would then be operating in micro-elastohydrodynamic lubrication, or micro-ehl.

By equating the two pressure maxima in this way the limit to rigid asperity behaviour for a given waveform was found. This limit, in terms of the operating conditions for a range of sinewave shapes is shown in Fig.2.15. The axis parameters are a non-dimensional load/wavelength parameter and a roughness to film thickness parameter. Micro-ehl will occur with conditions to the upper right of the line for a given sinewave shape.

As the film thins, if the asperities remained undeformed, the peaks would touch the opposing flat surface when $d_o/h^* = 1$. Fig.2.15 shows that, for all waveforms, on increasing load and temperature micro-ehl will occur before $d_o/h^* = 1$. The local deformation of the asperity tips would therefore delay contact between the asperity peaks and the opposing surface to a thinner film.

2.6.2. Relation to real surfaces

A real surface is made of roughness components of different wavelengths and amplitude, Fig.2.16a. The analysis showed that sine waves with the longer wavelengths produced larger and more concentrated pressure ripples and had smaller elastic pressure maxima, P_{asp} . Asperities with the longer wavelength are therefore the most likely to deform as shown in Fig.2.15. To model a real surface by an equivalent sinewave, the wavelength is taken as that of the mainscale roughness of the surface. For a real surface the longest wavelength components are those produced by the tool feedmark and can be found from the periodicity of the autocorrelation function of the surface, Fig.2.16b (Whitehouse & Phillips (1978)). The amplitude, d_o , is taken such that the sinewave and the rough surface have the same root mean squared value, σ , Fig.2.16c.

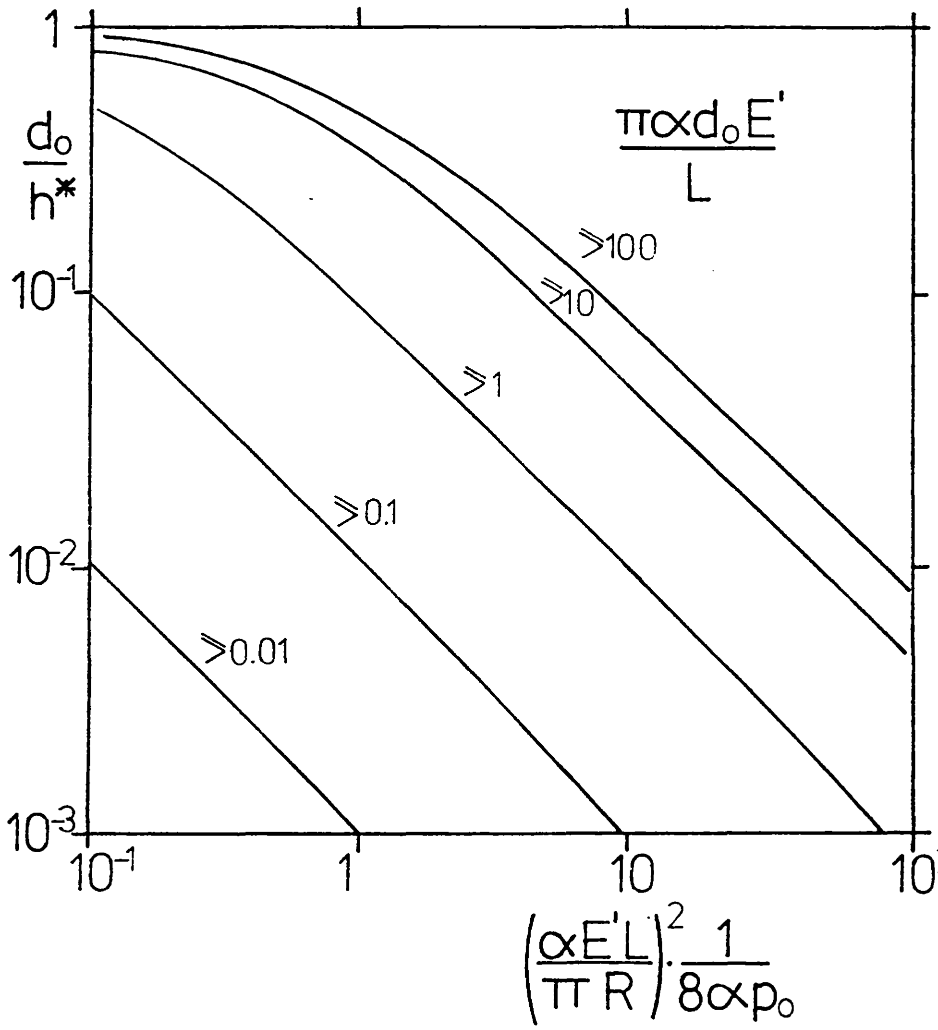

Figure 2.15 Conditions for the onset of micro-ehl for a range of asperity shapes.

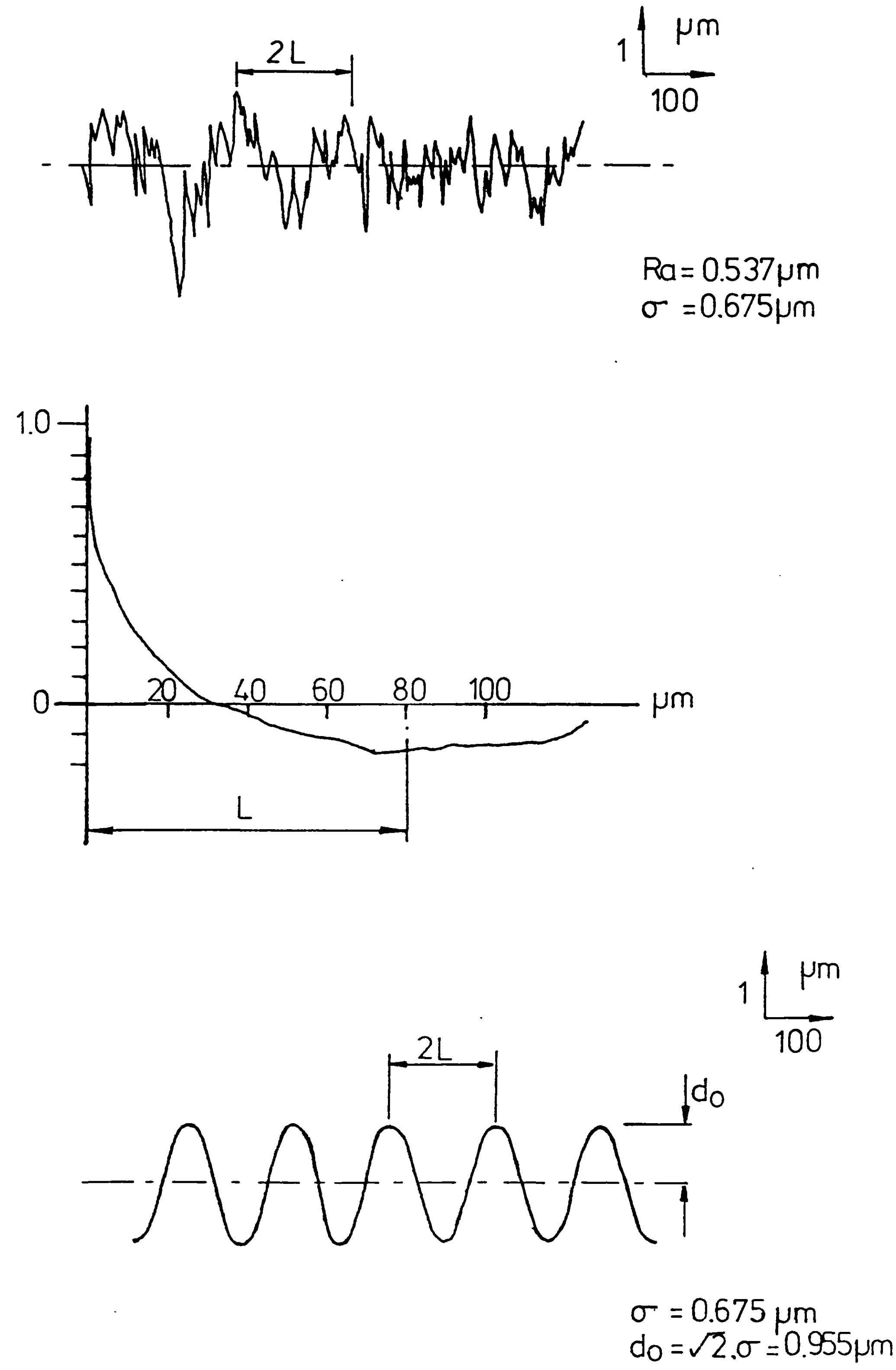

Figure 2.16 a/ Ground surface profile,
b/ autocorrelation function for ground surface and
c/ equivalent sin wave representing ground surface.

The maximum peak height depends on the roughness distribution and is, for a typical ground surface, greater than the equivalent amplitude, d_o. With real surfaces, whether contact occurs before the onset of micro-ehl depends on the operating conditions and the maximum peak heights. Fig.2.17a shows a typical ground surface with the average film thickness h^*, measured to the mean line of the surface, greater than the maximum peak height, in this case 3σ. As the surfaces approach, the behaviour depends on the size of the pressure ripple. If the conditions are such that the ripple remains small and asperity deformation does not occur, then contact between the secondary asperities and the opposing surface is expected when the maximum peak height equals the average film thickness, h^*, Fig.2.17b. Conversely, with more favourable conditions, the pressure ripple may be able to deform the mainscale roughness before the surfaces contact. The system will then be operating with micro-ehl and contact will be delayed to a thinner film, Fig.2.17c.

2.6.3. Relations to operating conditions in two disc tests

Fig.2.18 shows the section of Fig.2.15 which corresponds to the range of conditions found in a typical two disc scuffing test. For a typical ground surface the value of $\frac{\pi\alpha E' d_o}{L}$, which determines the position of the onset line ranges from 20 - 100. This range is shown in the graph by the shaded band. If the surface roughness distribution is assumed to be semi-gaussian, whichis appropriate for ground surfaces, then the maximum peak height will be $3 \times \sigma$, where σ is the root mean squared roughness value. The $h^* = 3\sigma$ line gives the amplitude to film thickness ratio at which contact will first occur between the peaks of the asperities of opposing surface.

The directions of increasing load and temperature are shown on the plot. Conditions to the right of the line, i.e. those at which micro-ehl is expected, are, for a given roughness amplitude and wavelength,

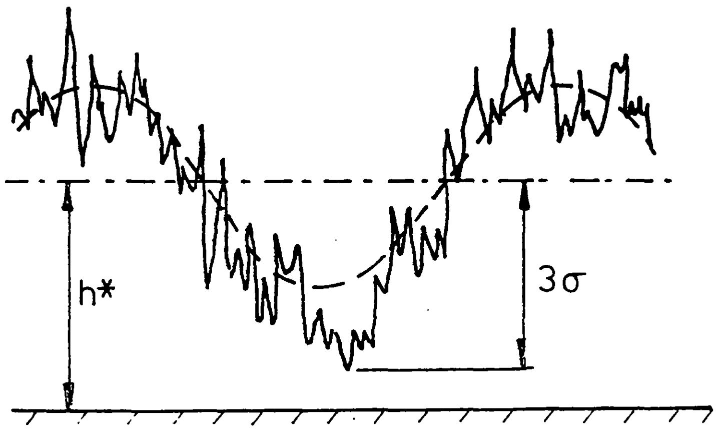

a) E.h.l with rough surfaces

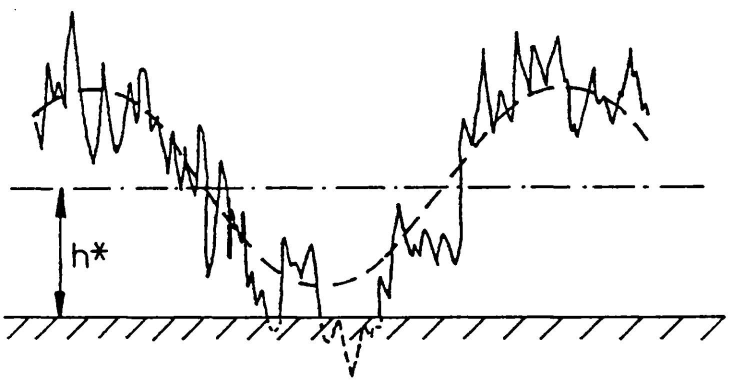

b) Mixed lubrication

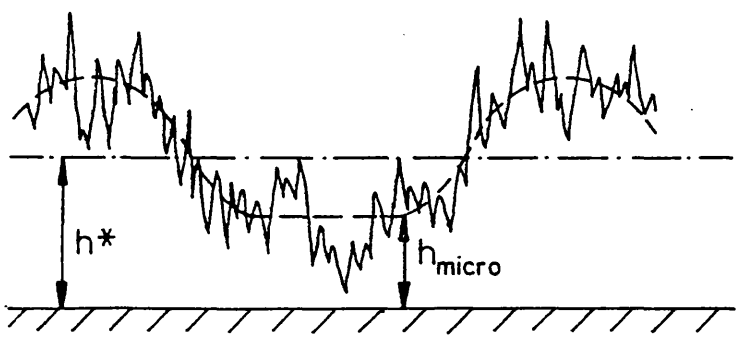

c) Micro-e.h.l.

Figure 2.17 Lubrication of real surfaces.

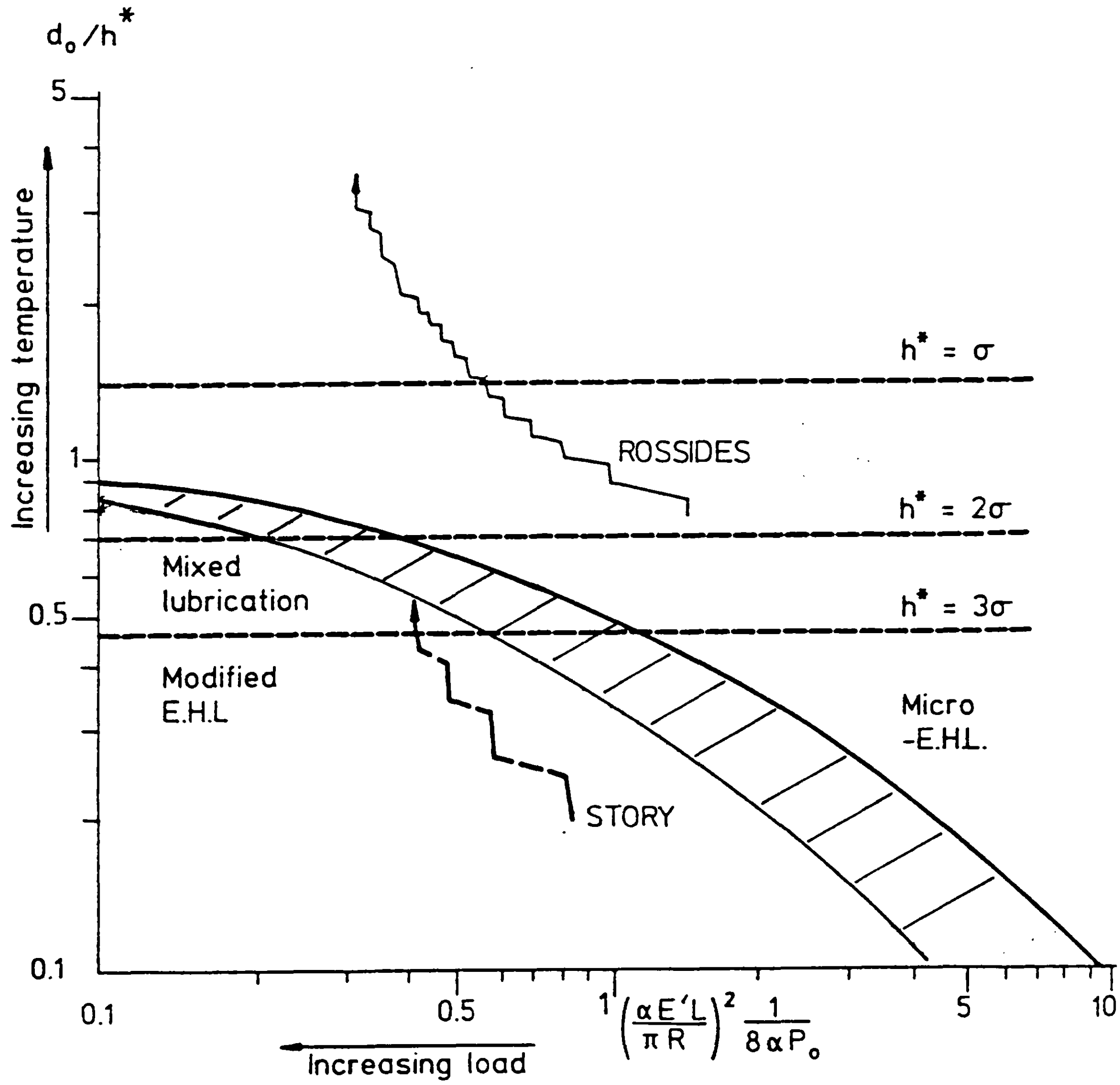

HV1 solvent, refined mineral oil, no additives	Temperature (°C)	40	100	150
	η_0 (cP)	87.3	9.51	3.44
	α (MPa)$^{-1}$	0.023	0.017	0.015

	$\bar{u}$ m/s	$u_1 - u_2$ m/s	Initial temperature °C	Final temperature °C	Pre-run *Ra* μm	Post-run *Ra* μm
(a) Story	4.49	2.99	30°	55°	0.29 0.28	0.29 0.26
(b) Rossides	3.86	3.86	65°	110°	0.38 0.38	0.26 0.17

Figure 2.18 Regimes of lubrication for conditions found in two disc scuffing tests.

achieved with lighter loads and thinner films - thinner films being a result of higher temperatures. It will be recalled that these were the differences between the initial conditions of the Rossides and the Story tests. The test histories of two of these tests are shown on the figure. Briefly the plotting convention is that the vertical lines show the change in conditions between the beginning and the end of an increment caused by the increasing temperature. The horizontal or sloping lines show the change between the end of one increment and the beginning of the next due to the increased load. There is no attempt to represent the variation of temperature with time within an increment.

The Story test begins in region 1. The incremental changes in load and the resultant temperature changes are such that the test crosses the $h^* = 3\sigma$ line before conditions at which micro-ehl is expected, are reached. The Rossides test starts and operates throughout with conditions which predict micro-ehl. Although the degree of deformation of the main-scale asperities in this region is not known, it is conceivable that the result of micro-ehl films in this test would be to delay surface contact until thinner average films and more severe conditions.

This analysis provided a possible explanation as to why the different operating conditions used by the two groups of workers could give rise to the different test types, the secondary differences in running-in being a consequence of operation in the different regimes.

Investigation into the possible relationship between the regimes of lubrication, as proposed by the Baglin model and the role of the machine thermal characteristics, forms the backbone of this thesis.

The tests reported in the next chapter were to test this role of operating conditions on regimes of lubrication. Investigations on the role of the test machine on the thermal response of the test were started by Story and is continued in Chapters 5, 6 and 7.

CHAPTER 3

TEST MACHINE DETAILS AND FIRST TEST SERIES

3.1 Introduction

The dynamics of gear teeth contacts varies during the meshing cycle. This makes it difficult to analyse the results of gear rig lubrication tests. Two discs and other similar machines, such as the four ball, simplify the problem by running at constant conditions and so are often used in preference to gear test rigs. By altering the disc speeds and radii, the conditions in two disc machines can be chosen to match those at a particular point in the meshing cycle of a gear set, for example, at the pitch line, (Fig.3.1). The absence of the rapid changes in conditions may limit the application of test results to real machinery. The scuffing tests of Story, Bell and Dyson and Rossides discussed in the previous chapter, were all two disc machine tests.

The first aim of the work reported in this thesis is to provide experimental verifications of the operating conditions predicted by Baglin's model for the onset of different regimes of ehl lubrication. The results of the test series designed to do this are reported in this chapter. For these tests a two disc machine which could cover the necessary range of initial and operating conditions had been designed and constructed at Leicester University Engineering Department workshops, (Williams, Finnis & Kelly (1988)). Section 3.2 describes this machine, the instrumentation developed, largely by Williams, to monitor the test conditions and the procedures adopted to prepare and run a test. Section 3.3 gives details of the test programme and the results. Section 3.4 discusses the results with particular reference to the different suggested regimes of lubrication.

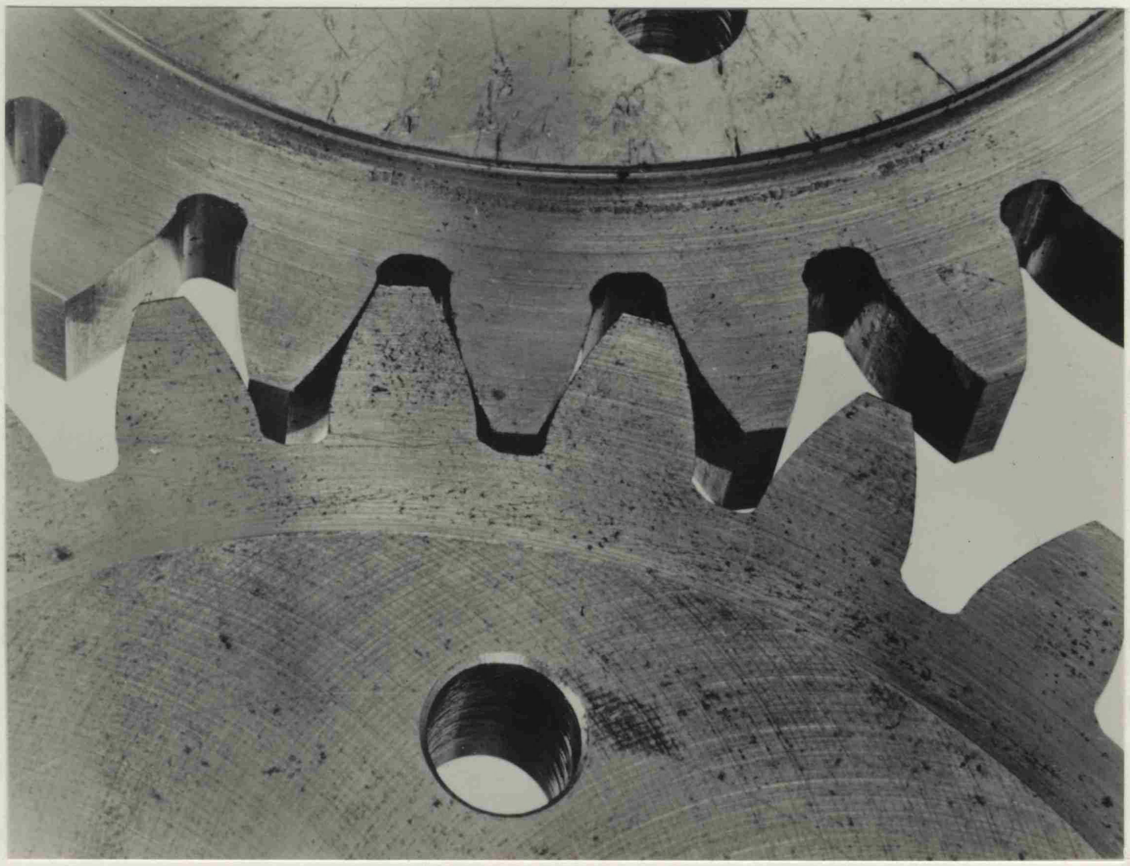

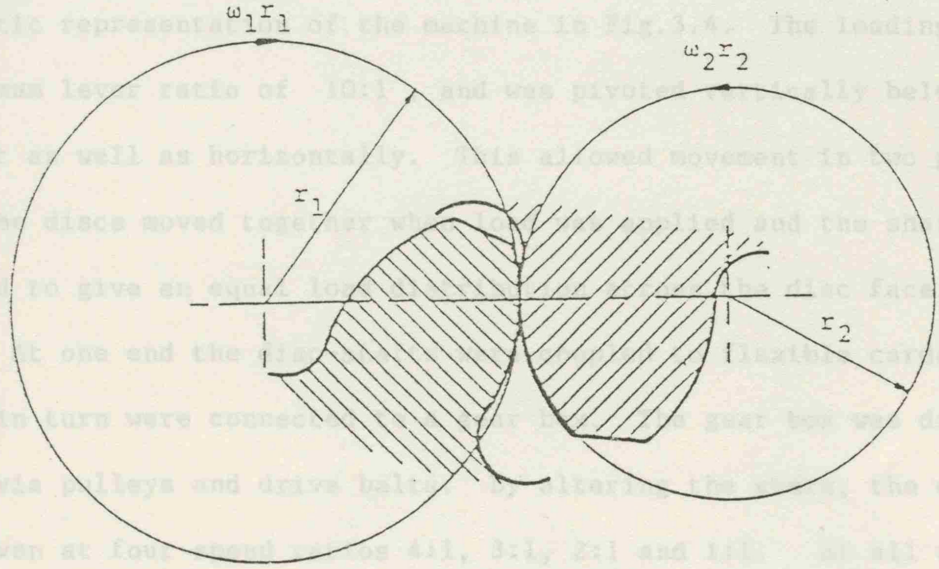

Figure 3.1 Simulation of gear teeth conditions with discs.

3.2 Test equipment and procedure

3.2.1. The two disc machine

The two disc machine is mounted on a 5 ft. x 3 ft. welding bed. It consists of a fixed frame, a movable loading arm/frame and a disc drive gearing system on top of the bed and a 1500 r.p.m. drive motor, an oil-bath and a pump below. Fig.3.2 shows a general view of the machine. The whole unit was enclosed in a test cell to minimise air pollution and noise. The air within the test cell was filtered by a filter-mist centrifugal unit. Each test was run and monitored from outside the unit.

Two 3 in. diameter discs were used for each test. Each disc was mounted on the tapered portion of a hollow shaft, on the ends of which are fitted removable tapered roller bearings which run in cantilevered bearing housings. The discs were located midway between the housings. Fig.3.3 shows the discs mounted in the machine. The cantilever arms of the housings for one shaft were gripped in the fixed part of the frame and those of the other shaft in the movable loading frame as shown in the schematic representation of the machine in Fig.3.4. The loading arm gave a maximum lever ratio of 10:1 , and was pivoted vertically below the contact as well as horizontally. This allowed movement in two planes so that the discs moved together when load was applied and the shafts self-aligned to give an equal load distribution across the disc face.

At one end the disc-shafts were coupled to flexible cardan shafts which in turn were connected to a gear box. The gear box was driven by the motor via pulleys and drive belts. By altering the gears, the discs could be driven at four speed ratios 4:1, 3:1, 2:1 and 1:1. At all the speed ratios, the slower disc was held in the movable frame and rotated at 750 r.p.m. in the direction shown in Fig.3.4.

The discs and the portion of the shafts between the bearing housings were enclosed in a perspex box. The oil was heated in a five litre bath and was pumped via a 10 μm filter, through the lid of the box

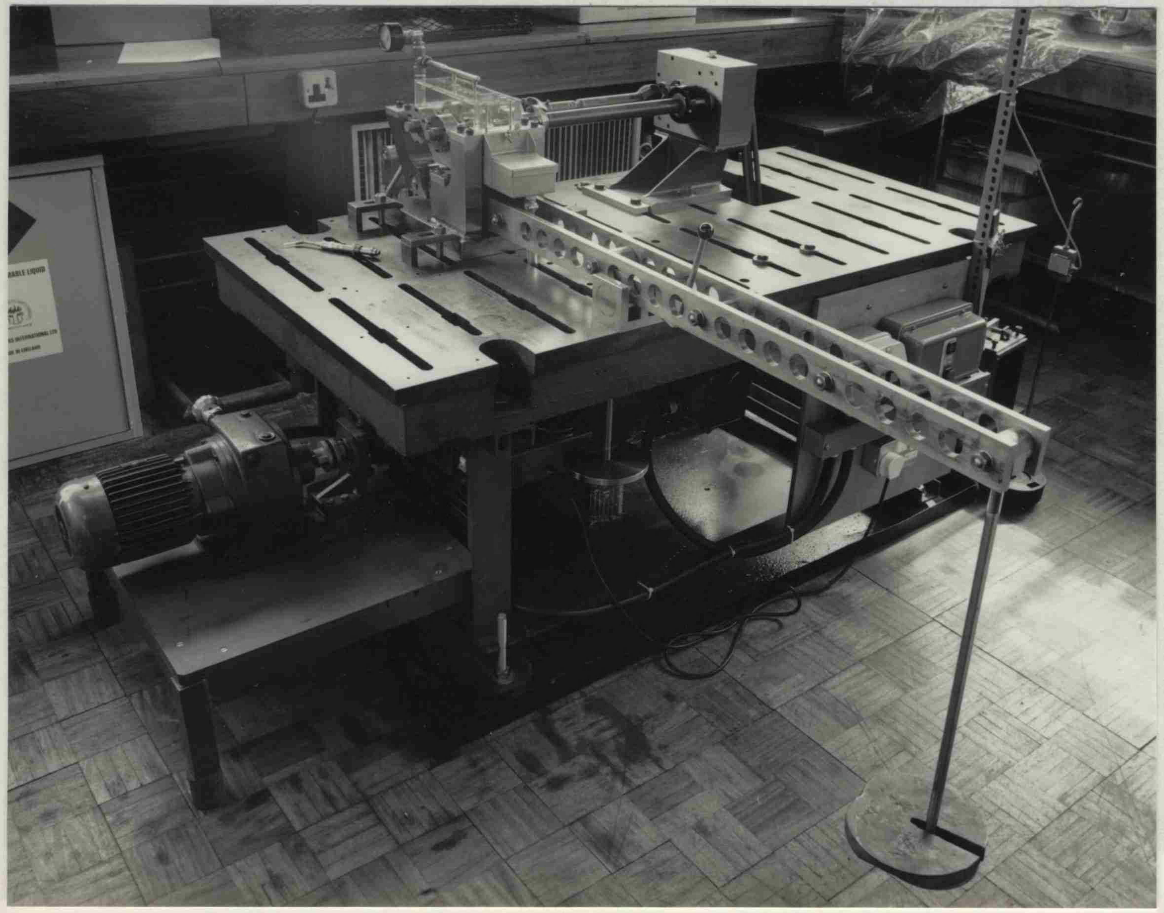

Figure 3.2 General view of test machine.

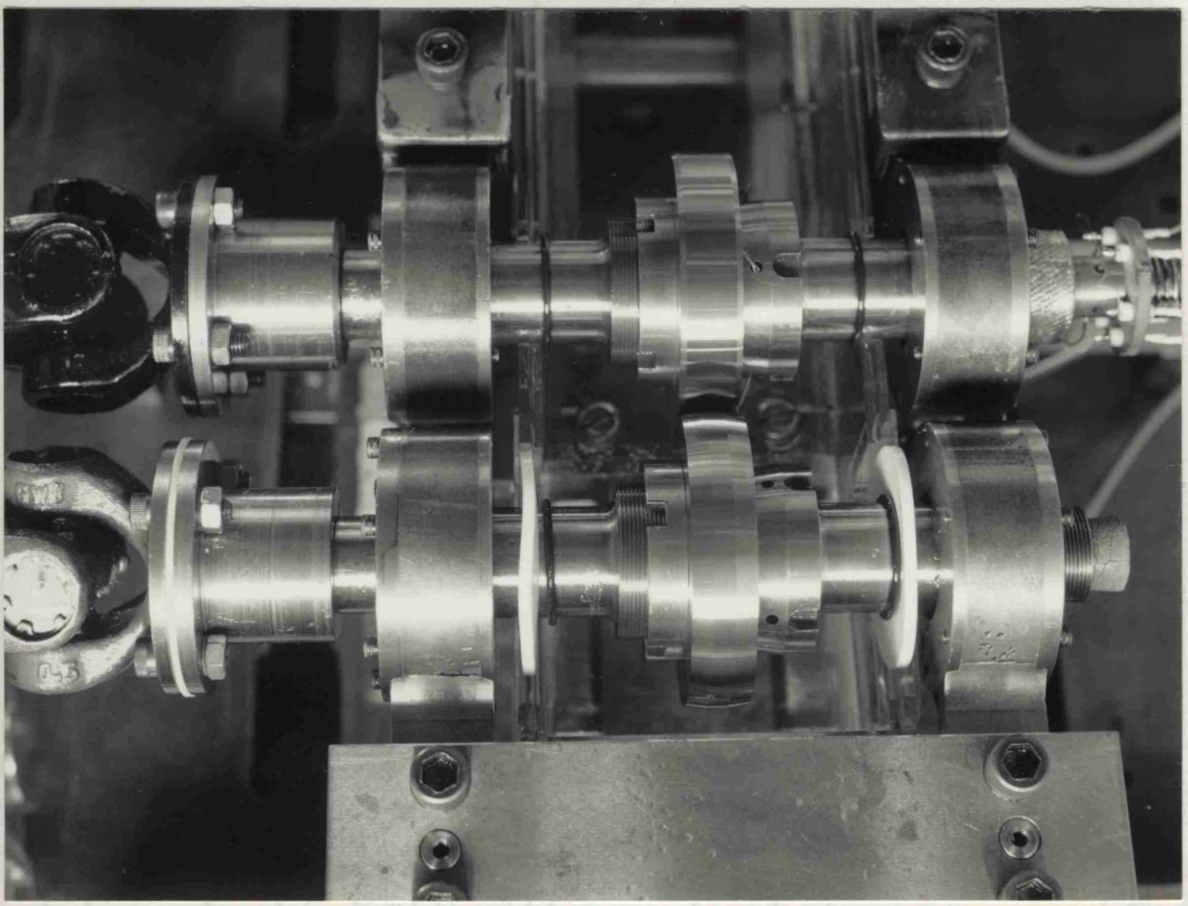

Figure 3.3 Discs mounted in machine.

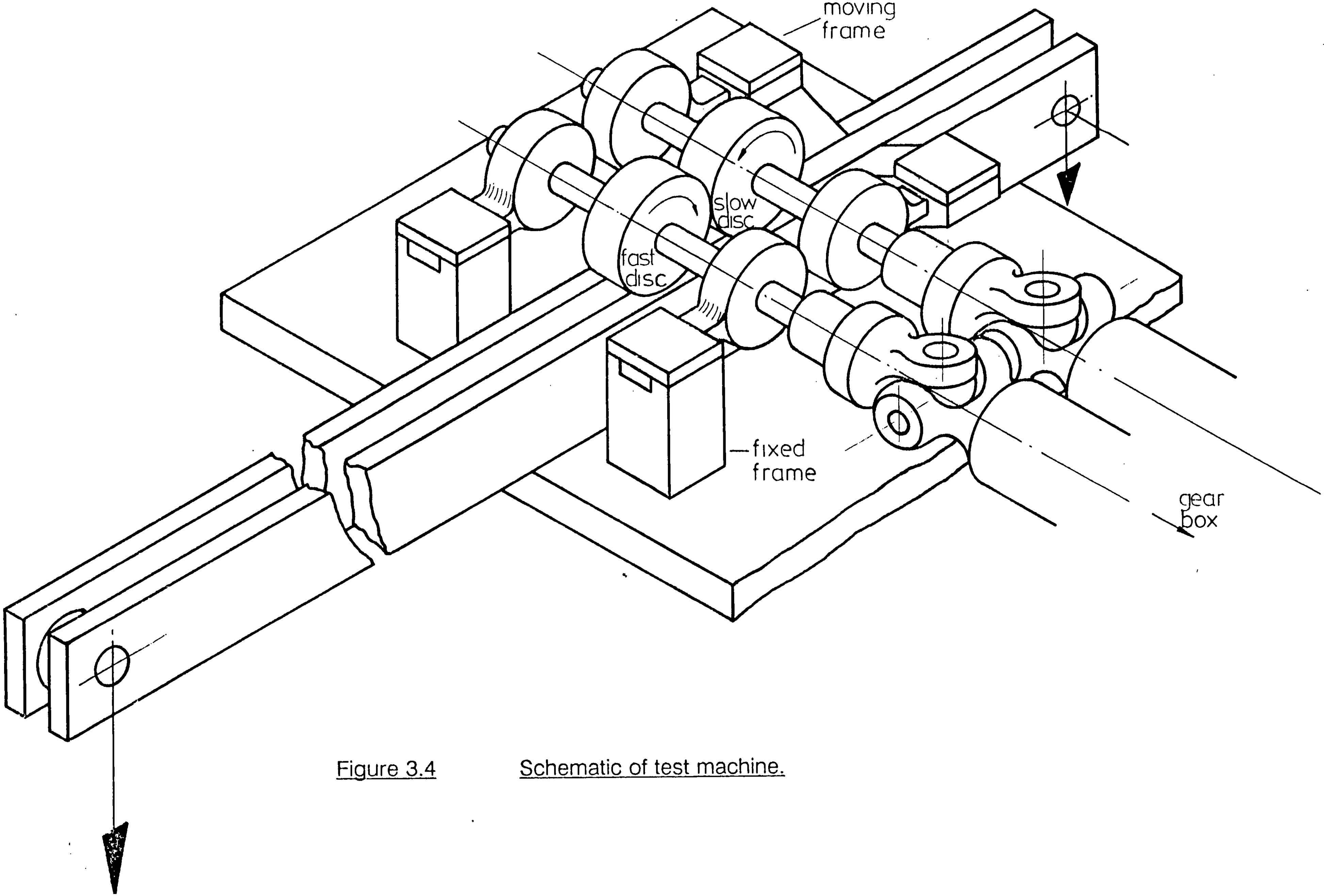

Figure 3.4 Schematic of test machine.

to outlets above each of the discs - the oil drained back from the box to the bath for recirculation.

3.2.2. The discs

The discs were 3 in. diameter and 0.625 in. wide, made of EN36 steel and case hardened to a depth of 1.5 mm with a surface hardness of 700 DPN. All the discs were circumferentially ground, the 'rough' discs to Ra of 0.34 $\pm$ 0.04 μm and the 'smooth' discs to Ra of 0.1 $\pm$ 0.03 μm. The rough discs were champhered to reduce edge loading effects, the resulting central land being 5 mm . A rough and a smooth disc were used for each test with the rough disc on the slower shaft in the moving part of the frame. Three thermocouple holes were drilled in the side face of the smooth disc at distances 2 mm , 4 mm and 8 mm below the surface, (Fig.3.5).

3.2.3. Monitoring and control system

A Research Machine Ltd. 380Z mini computer monitored the oil supply temperature, the bulk temperature of the faster disc and the frictional force, and controlled the loading system. In addition the level of the electrical resistance between the discs was monitored with a resistance breakdown counter and the surface roughness of the discs was measured before and after test using a Talysurf 4 profilometer. The instrumentation to control and monitor the test whilst running, was situated outside the test cell, as shown in Fig.3.6.

The extensive "user-friendly" software developed by Williams for the 380Z included facilities for the calibration and checking of transducers and the creation of loading sequence programs. On initiating the test program, the length of the load increments (minimum of 2 mins) and the loading sequence to be used, are chosen by the operator via the keyboard. Other details such as the disc identification, speeds and the gear ratio being used are also entered.

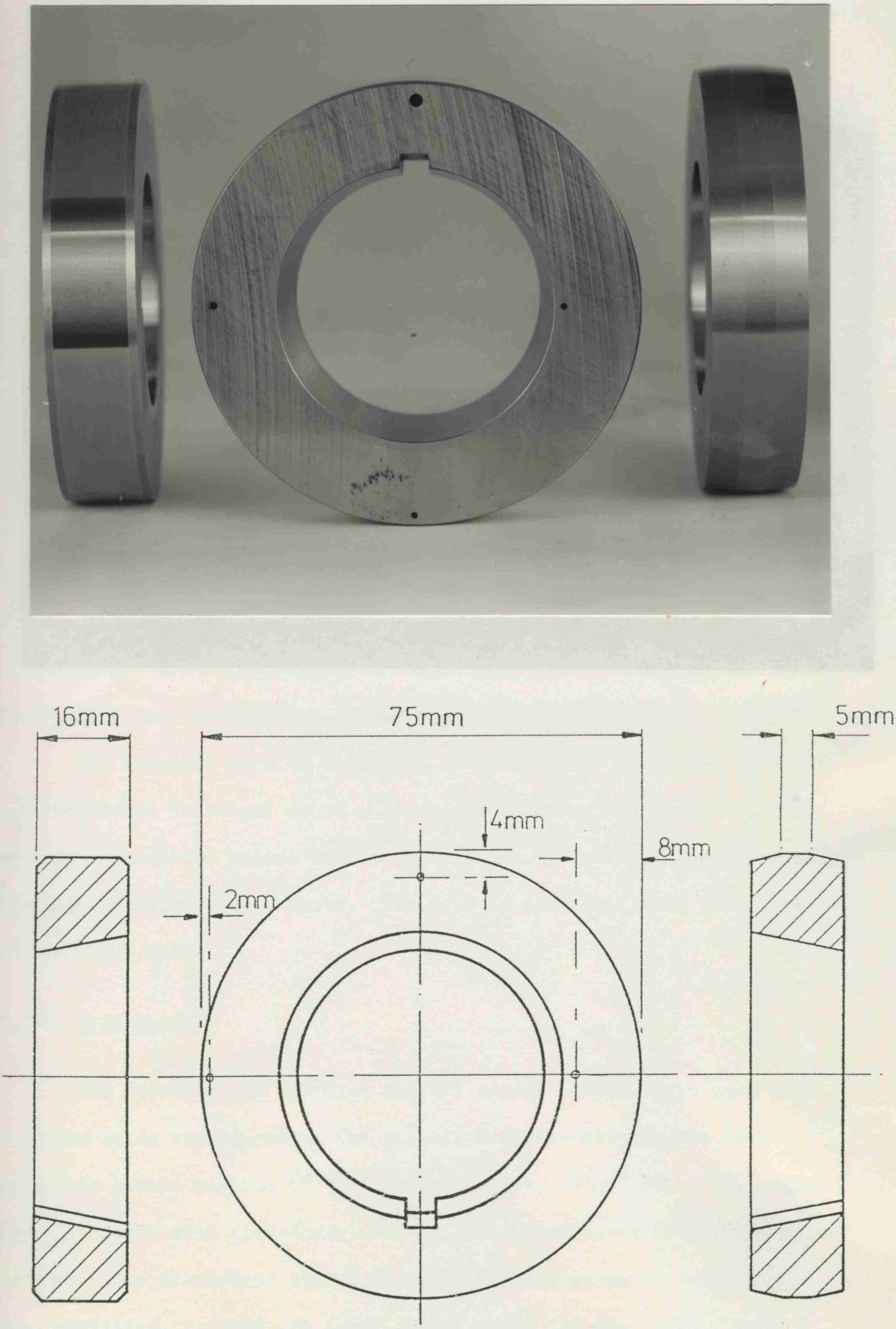

Figure 3.5 Test discs.

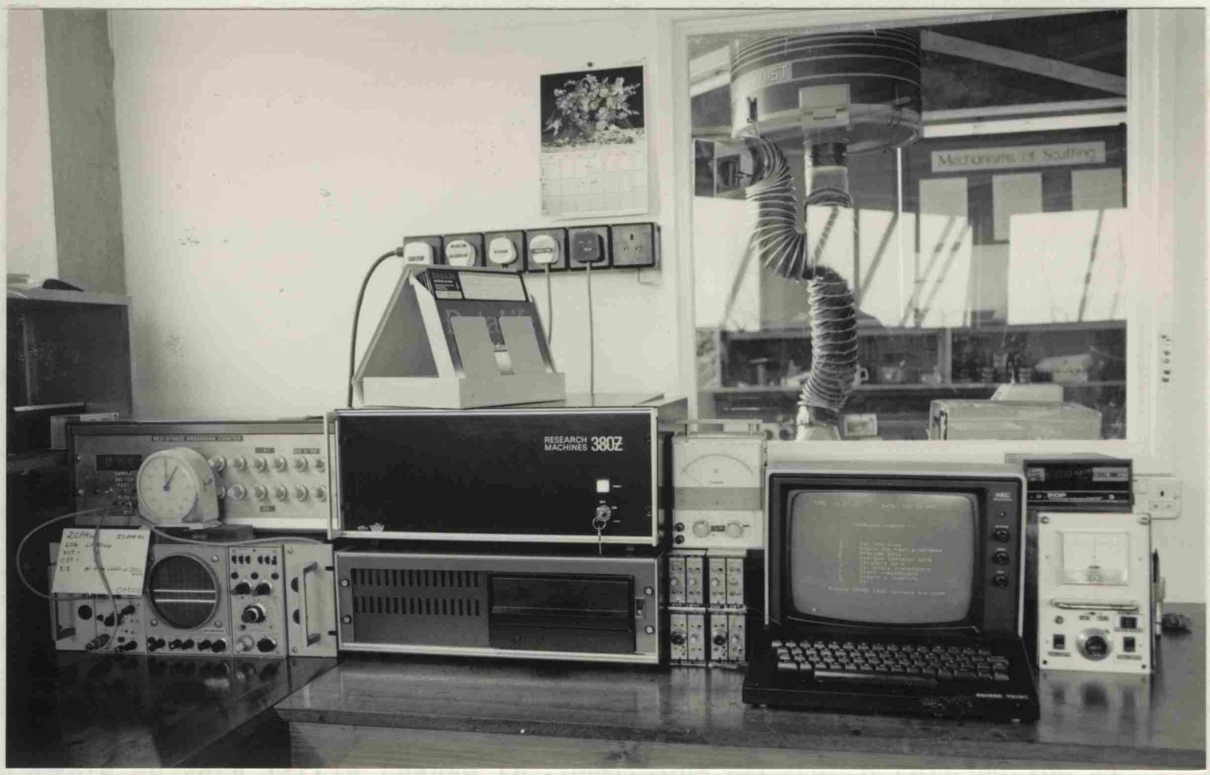

Figure 3.6 Instrumentation situated outside test cell.

During a test the system records the disc bulk temperature, the oil supply temperature and the frictional traction. Data for the disc bulk temperature and the frictional traction is collected every second for the first minute of an increment and at 20 equal intervals for the rest of the increment. This information is displayed for the present and previous test in graphical form on a v.d.u. screen. The oil supply temperature is recorded at the beginning of each increment. A 'Fastscan' process is available by which data is collected every 0.3 secs. for a six second period. This process is employed at the beginning of each increment and at the request of the operator via the keyboard at any time during an increment. During this six sescond period the data for the 4 mm and 8 mm thermocouples is not recorded. At the end of each increment all the recorded data is transferred to a 'floppy disc' for permanent storage. During this time no monitoring or recording of data takes place. This is allowable as very little change in conditions occurs in this period if equilibrium has already been established.

The recorded data is available in a hard copy tabulated form for any individual increment or in a condensed form for the whole test and includes calculated values of the coefficient of friction and the flash temperature at each data point. The data is also available in a variety of graphical forms.

3.2.4. Transducers

The friction and the disc and oil supply temperatures were all measured using transducers. The signals from the transducers were amplified before passing to the microprocessor, (Fig.3.7). The amplifier gain for each transducer was set during the calibration procedure such that the transducer signal for the expected range of operation, when amplified, matched the input signal range for the '380Z', 0-10 V . The input signal to the '380Z' was applied to an analogue to digital converter which divided the signal into 265 discrete units before it was

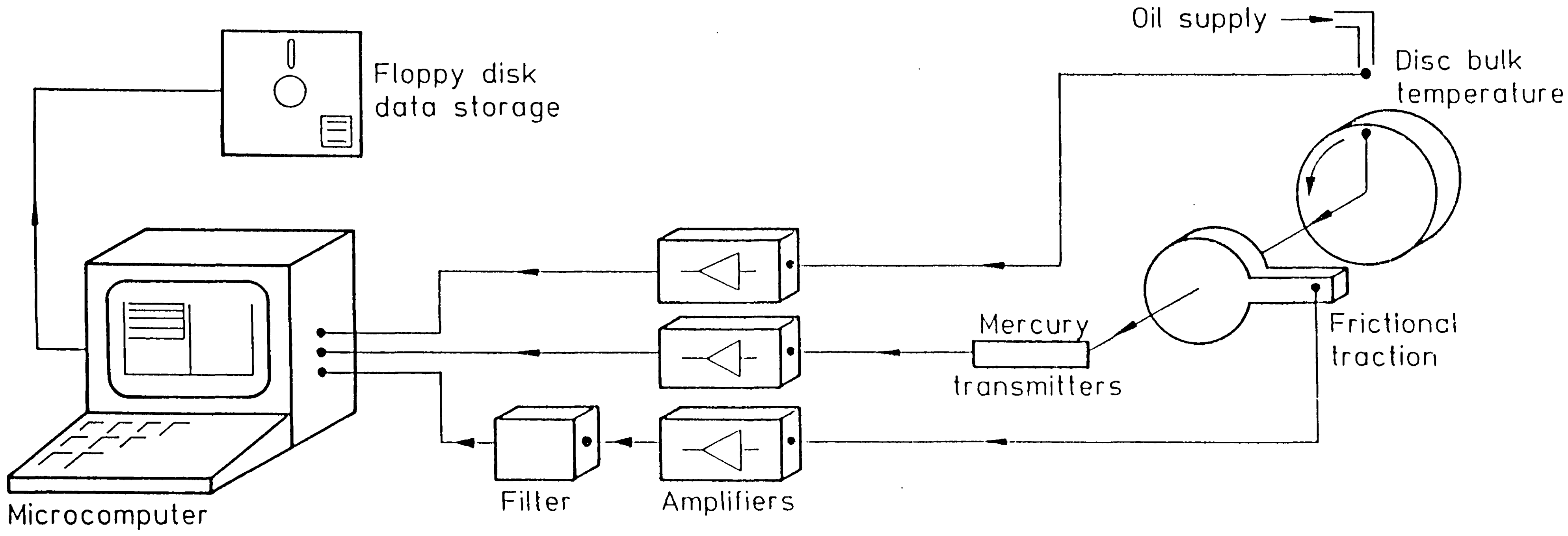

Figure 3.7 Schematic representation of monitoring system.

processed. Each data point is the average of four such readings.

The frictional traction was measured by strain gauges 'cemented' to the arms of the cantilevered bearing housings. Due to the dimensions of these arms, the strains produced at low loads were very small. Consequently, semi-conductor, temperature-compensated strain gauges had to be used to detect them. These had a gauge factor of approximately 130 compared to a typical value of 5 for normal foil gauges. Because of the sensitivity of the gauges, vibrations from the gear box and drive mechanism obscured the friction readings so, after amplification, an electronic filter was used to remove signals of frequency $>$ 1 Hz, i.e. those caused by machine vibrations. The 'cleaned up' signal then passed to the monitor for processing.

The strain-gauged cantilevers were mounted in the fixed side of the frame. Originally it was intended to use two gauged cantilevers for each test. Due to the frailty of the strain gauges and their position, they were very susceptible to damage during assembly or stripping down of the rig. This and the time taken for repair or replacement, resulted in only one gauged arm being used for most of the experiments.

The system was calibrated to measure a maximum frictional traction between the discs of 400 N. Digitisation of the signal, results in the lowest detectable value, i.e. 1 unit, being ~ 1.6 N, which is comparable to the frictional traction at the lowest test loads. This can result in errors of coefficient of friction in the initial test stage. For example, with each data point being the average of four readings, and with values of 1.5, 1.5, 1.5 + 1.6 N as the three lowest values would not be be detected - the average value would be given as 0.4 N. Problems in the friction measurement at low loads are discussed with reference to the test results in Section 3.3.4.

To calibrate the strain gauges, the cantilever arm was mounted in a separate block so that weights could be hung directly from the housing. The amplified output signal, in bits, was displayed on the screen. Before weights were applied the amplifier 'level' was adjusted to give zero output. Weights, equivalent to the maximum traction to be measured, were then applied and the amplifier gain adjusted until the measured signal approached 250 units The weights were then removed and reapplied in stages and the measured signal at each stage was plotted against the load No deviation from linearity was discernible. With the calibration figure, obtained from the gradient, entered into the program the frictional tractions could be calculated from the transducer signals.

The disc bulk temperature was measured in the fixed disc, by up to three, type K (NiCr/NiAl) thermocouples. These were discharge welded to the bottom of the holes in the side face of the smooth disc The thermocouple wires passed through holes in the shaft, down the hollow centre to the flexible connector at the undriven end of the shaft. This connector mated to and drove a mercury slipringless transmitter, the signal from which was amplified before passing to the monitor.

Two slipringless transmitted units were available for use. The transmitters had six channels, two being required for each thermocouple. Due to the failure of a number of these channels at different times, it was not always possible to use three thermocouples. In this case the 2 mm thermocouple was always used and the 4 mm or 8 mm thermocouples omitted As the rough disc was electrically insulated from the rest of the machine so that the resistance count rate monitor could function, only the temperature in the smooth disc could be measured.

The system was calibrated to measure bulk temperatures up to 250 C. The amplifier gain was set by a similar method to that used for the strain gauges A d.c. millivolt source generator was used to simulate the thermocouple output and the signal was applied through the flexible connector and the mercury slipringless transmitter unit to the amplifier

The oil supply temperature was measured by a Type K thermocouple in the outlet above one of the discs. The oil supply temperature was measured at this point rather than in the oil bath, as a temperature difference of a few degrees could occur between the two positions. This system amplifier was calibrated, again with the d.c. millivolt source generator to measure oil supply temperatures up to 120 C.

3.2.5. Loading System

Originally it was intended that the load would be applied by hand, using dead weights on the hangers on the loading arm. These hangers were positioned to give a 10:1 or 6:1 lever ratio. During an explorative series of tests it was found that a complicated sequence of applied weights was needed to obtain the required loading sequence between the discs. By applying these weights manually, shock loading and errors or delays in applying the correct load were likely to occur.

An automatic loading system was installed to overcome this problem, (Fig.3.8). The system was controlled by the microcomputer and a closed loop system. Load was applied by a stepper motor and ball-jack, through a load cell to the 10:1 loading point, (Fig.3.9). The demand load signal from the microcomputer (0-10 V) was compared to the load cell output signal (0-10 V) by a servo amplifier. The servo amplifier then activated the jack to minimise any difference in the signals. The system constantly corrected itself, i.e. it was self-damping, the demand and response load equalising to within 1%. There was also a quick response to a large rise in the demand signal. For example, a 2 kgf load increase at the beginning of an increment was applied within 0.6 secs of the change in the demand signal and stabilised within 1.5 secs. The system was calibrated to give a maximum load of 40 kgf at the 10:1 loading point. (Loads quoted in kilogram-force are equivalent to that weight at the 10:1 hanger ratio.)

With pre-programmed loading sequences the control system ensured accuracy and repeatability of the applied loads. There was a possible drawback of edge loading due to the loss of the self-aligning mechanism between the discs. This was minimised by careful positioning of the jack and by a flexible chain which linked the load cell to the loading arm. In

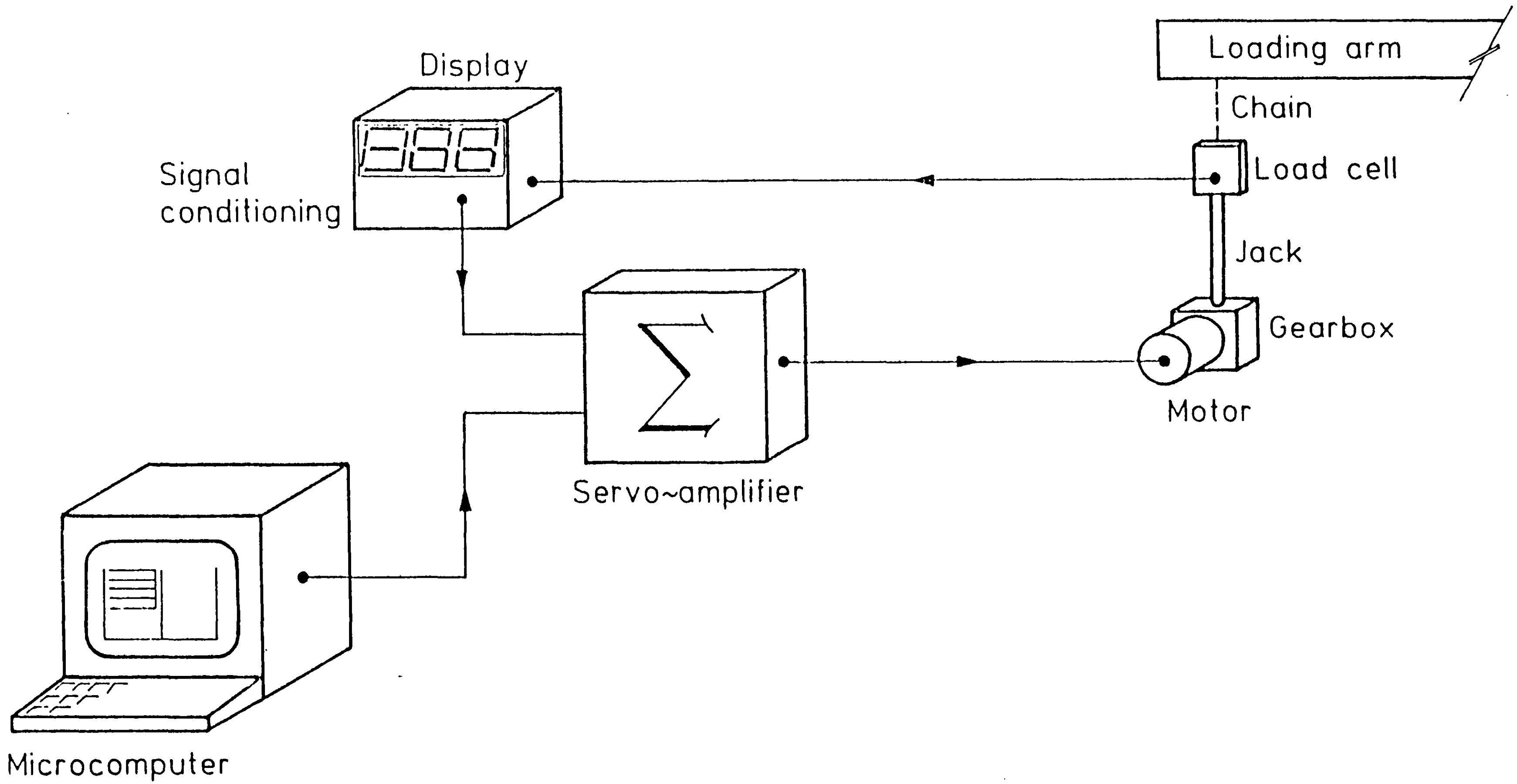

Figure 3.9 Schematic representation of closed loop loading system.

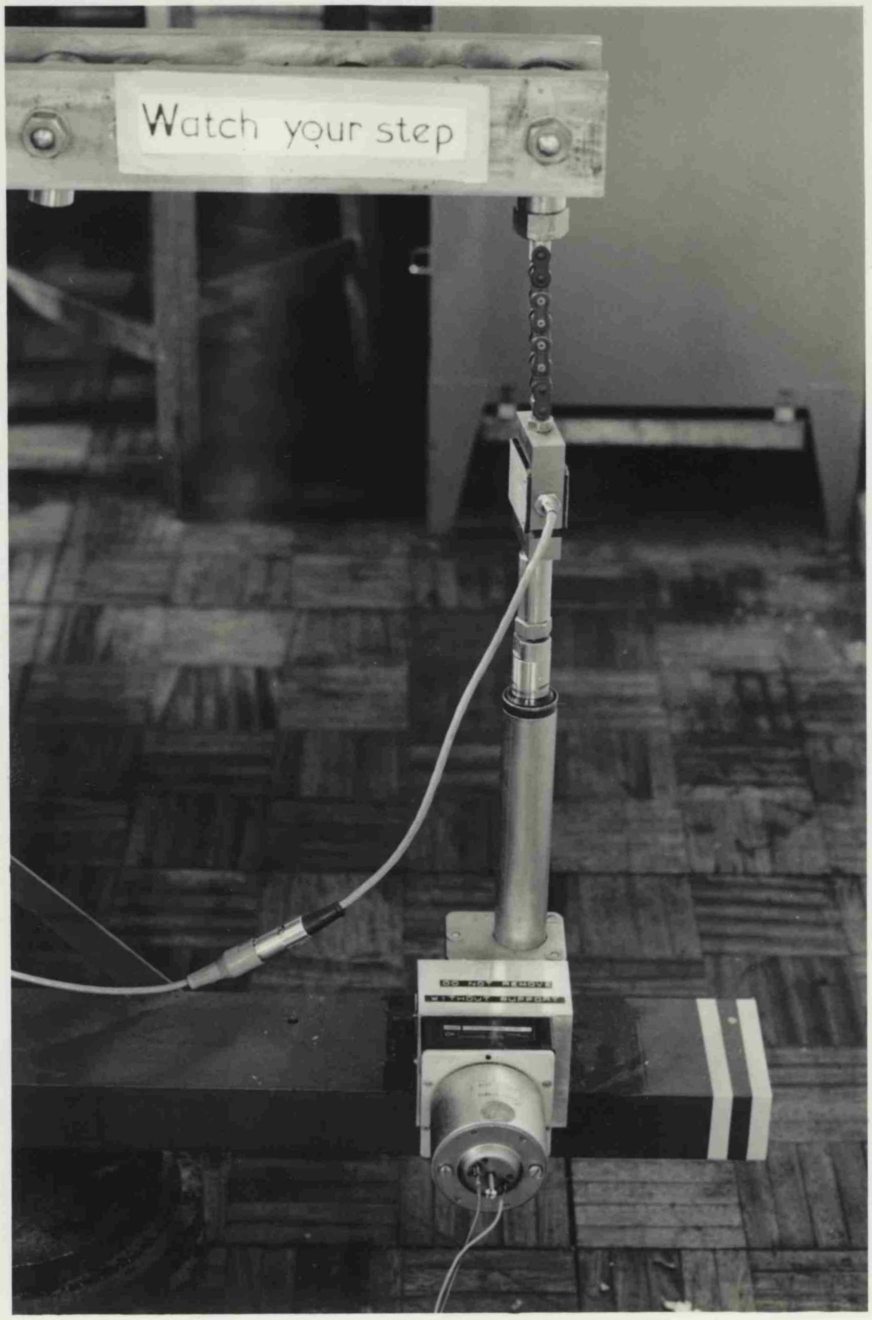

Figure 3.9 Loading system.

subsequent tests, scuffing was initiated on both sides of the track so no major misalignment problem was suspected.

3.2.6. Count rate

The resistivity of oil is high (10^6 kΩm - 10^{10} kΩm) compared to that of steel (10^{-6} Ωm). This difference makes it possible to use drops in the resistance between the discs to indicate whether there is a complete oil film (high resistance) or metal to metal contact (low resistance) through the oil film. A resistance count rate monitor was available which could detect this change in resistance. The discs had to be electrically insulated from one another. The free disc shaft and loading arm were insulated from the rest of the machine by tufnol inserts at the main pivot bearing and at the coupling between the disc shaft and the drive shaft. The connections from the discs to the monitor were made via the bearing housings.

A simplified version of the monitor circuit is shown in Fig.3 10. A constant voltage is applied to a dummy and active circuit. The discs are connected in parallel to R2 in the active circuit. The resistances are chosen so that R1 = 20 R2 which, with the discs out of contact, maintains a voltage of 100 mV across R2. This voltage is small enough to prevent discharge between the discs. Following work by Christensen (1965) and earlier work with the same monitor at Leicester by Haltoff (1970). R2 is set at 100Ω. This is the 'breakdown' resistance of the oil film. A cathode ray oscilloscope displays the voltage between the discs, Vc. The comparator takes the difference in voltage across R2 of the two circuits, i.e. Vd-Va. With the discs out of contact the voltage across R2 for each circuit is the same and Vd-Va = 0. When the resistance between the disc falls to or below 100Ω, then Va $\leq$ 50 mV and Vd-Va $\geq$ 50 mV which the comparator registers as a contact.

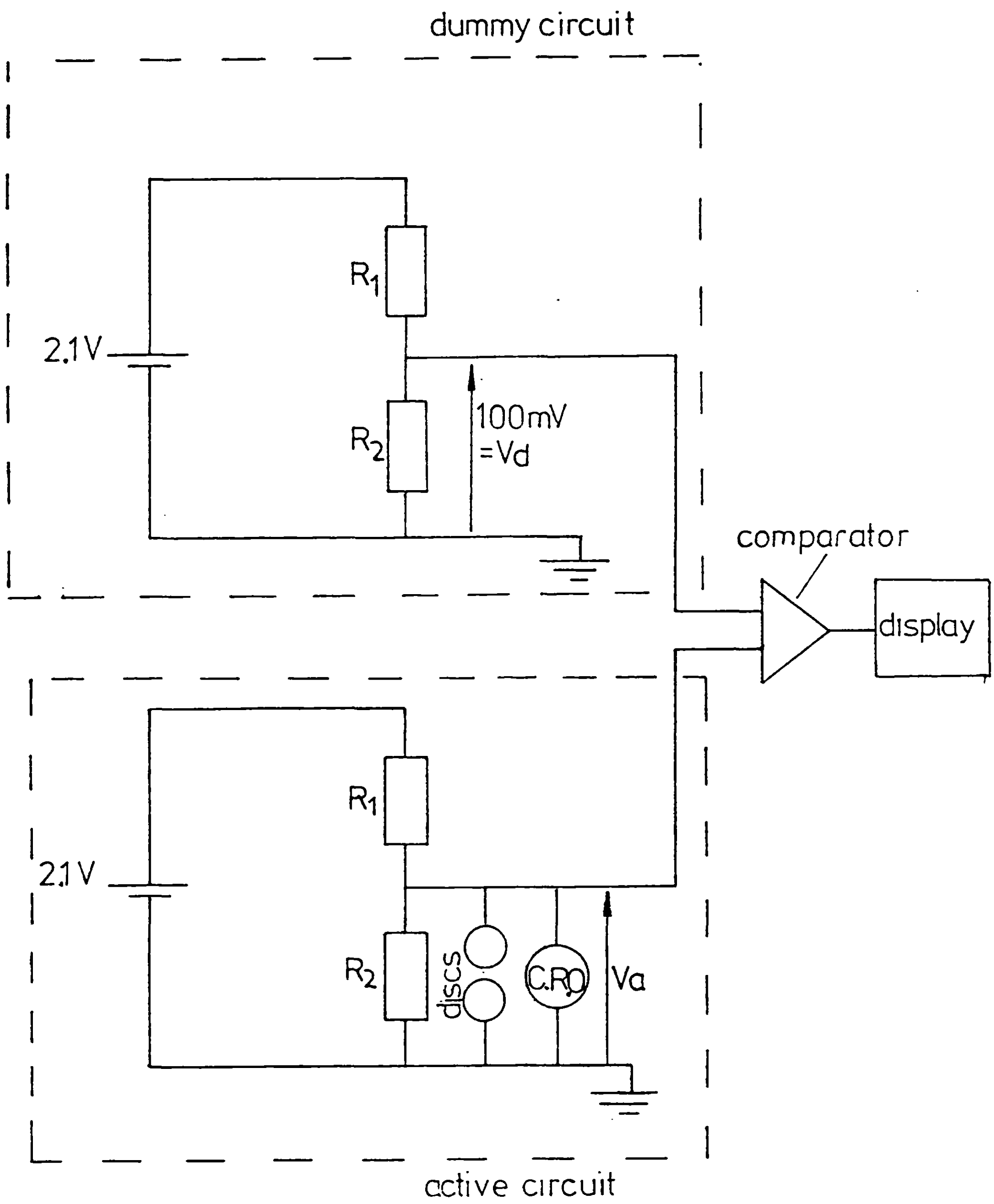

Figure 3.10 Circuit diagram of resistance countrate monitor.

The monitor counts over a one second period the number of times that the resistance between the discs falls to or below 100 Ω. The count is not the number of individual contacts over this period as the monitor cannot recognise overlapping events. A count is made approximately every other second and the information is displayed on a digital readout. No direct method of recording the data was available so the c.r.o. screen and the digital readout were video recorded during testing for future analysis. A typical selection of displays as shown on the c.r.o. screen are given in Fig.3.11.

3.2.7. Surface roughness measurement

Any surface modification that occurred during a test was shown by comparing pre- and post-test surface profiles and roughness measurements. These were made with a Talysurf 4 profilometer. It was originally thought that readings would need to be taken at different stages of a test. In order that these measurements could be taken 'in situ' without dismantling the machine, the gearbox and column were mounted on a small plate which sat on the machine bed, between guide rails which positioned the stylus over the discs. The profiles were taken across the track at right angles to the circumferential ground surface.

A relocation method was devised so that the same tracks on the surface, pre- and post-testing, could be compared. Before the discs were mounted on the machine, four equidistant indentations (~200 μm across) were made around the disc edge with a diamond hardness testing machine. A graticuled microscope was mounted on the Talysurf arm such that, with the arm lowered, the microscope focused on the disc edge, (Fig.3.12). The discs were rotated until the graticule lined up with the centre of the diamond shaped indentation. The stylus was located axially on the track edge at the beginning of each traverse. The repositioning of the stylus in the circumferential direction was $\pm$ 10 μm. A pair of relocated traces are shown in Fig.3.13. Due to the slight circumferential misalignment

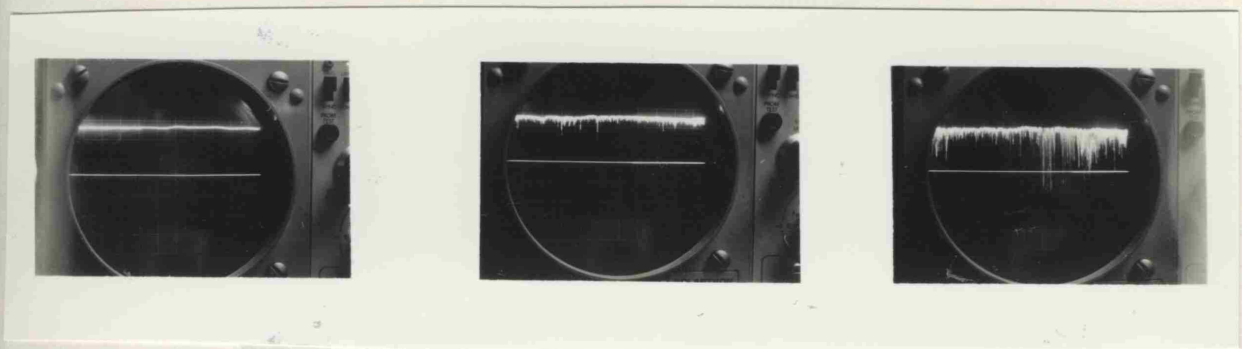

a/ zero contact

b/drop in resistance

c/ first registered contact

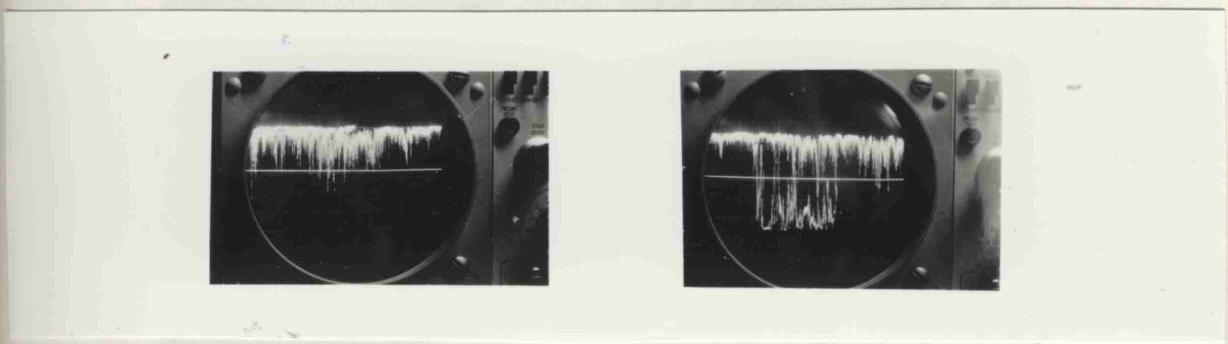

d/ increasing contact

e/scuffing

Figure 3.11 Displays from resistance countrate monitor.

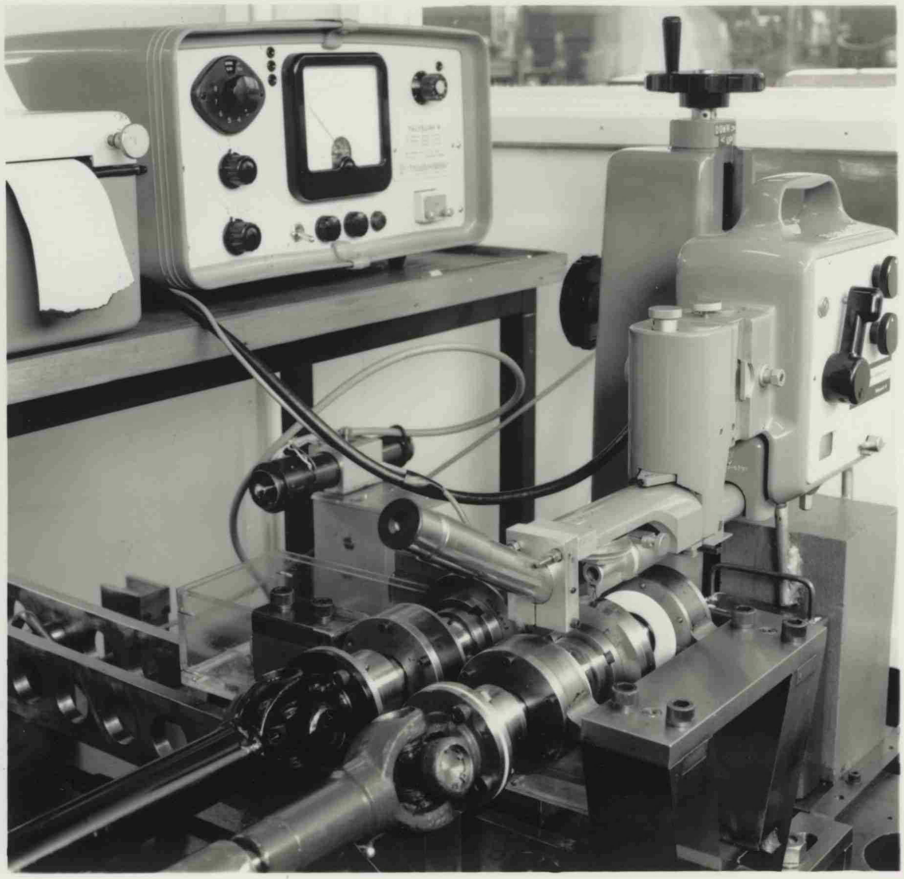

Figure 3.12 Talysurf in position on test machine.

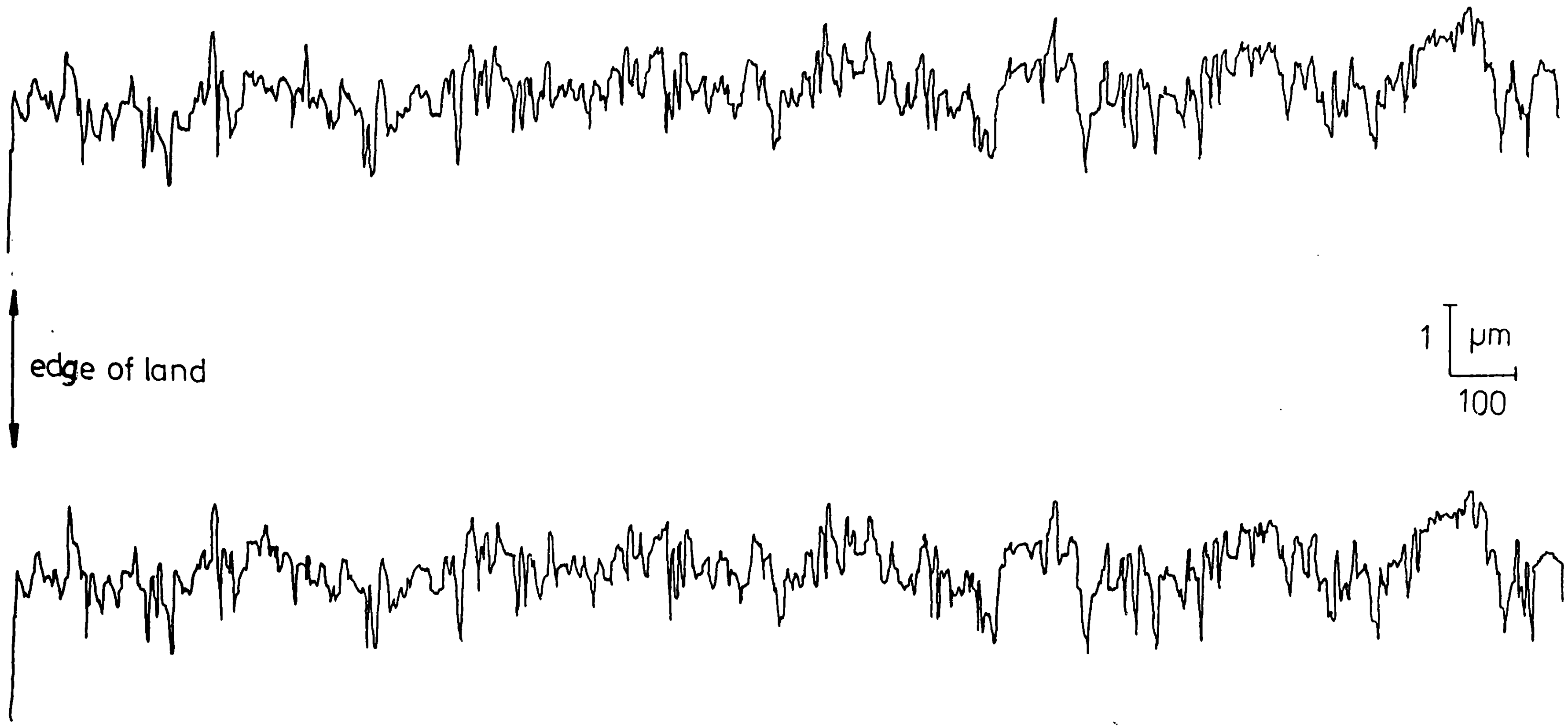

Figure 3.13 Relocated surface profiles.

there are some minor differences between the traces but the main features can be identified and the Ra values for the two traces are the same.

Three readings were taken. pre- and post-test, at each of the four positions around the disc surface and averaged to give the Ra value for the disc.

3.2.8. Test preparation and running procedure

After a series of trial tests, the following procedure was adopted for all subsequent tests. The diamond indentations were made on the selected pair of discs which were then cleaned for two minutes in acetone in an ultrasonic bath. The thermocouples were discharged welded to the bottom of the holes in the smooth disc. After a visual inspection of the surface to check for defects, the discs were mounted on the shafts and the bearings and cantilevered housings greased and assembled on the shafts' ends. The cantilevers were then slotted into the frame and located with plugs before the restraining plates and bolts were fitted. The drive shafts were coupled to the disc shafts and the electrical insulation between the discs checked with an avo-meter. The discs were once again wiped with acetone before measuring the surface roughness. The top of the perspex box was then fitted and all the instrumentation connections, including the soldering of the thermocouples to the connector, made. The machine was then ready to run a test.

The oil bath was set to a temperature which would result in the required initial disc bulk temperature and the machine was run with the discs 0.25 mm apart, with the oil circulating for approximately two hours until all the oil supply and the disc bulk temperatures had been stabilised. During this time the instrumentation was checked. The temperature was read directly from the thermocouples using an electric Comark thermometer and the 'level' of the amplifiers was altered accordingly. The strain gauge amplifier level was also adjusted to give zero friction with the machine running so that any subsequent value could be attributed to the traction between the discs and not to any other source, such as bearing friction.

On starting the test program test details were selected by the operator. During the test, the load was applied automatically at the beginning of each increment according to the chosen loading sequence. A sharp rise in the friction or temperature levels displayed on the monitor or a change in the audible pitch of the machine indicated that the discs had scuffed. As soon as a scuff was detected by the operator, the load was removed by manual override of the system through the servo-amplifier. When the test program was stopped the remaining unstored information from the failure increment was transferred to the floppy disc.

After the post-test Talysurf measurements had been taken the machine was stripped down and the shafts bearings and bearing housings were cleaned with paraffin ready for the next test. The used discs were stored, covered with a thin layer of the test oil, in a heated cabinet.

3.3. Test programme and results

3.3.1. Aims

It has been suggested that the initial and sequence of operating conditions determines the type of lubricaton, ehl, mixed or micro-ehl, in line contacts. The test programme reported in this chapter was designed to investigate this and had two main aims.

The first aim was to produce on one machine, by matching the different operating and initial conditions used by Story and by Rossides, tests with different failure conditions and degrees of running-in. This would eliminate the suggestion that the different test results of these workers were solely a result of the thermal response of the test machines used.

The second aim of the test series was to cover a wider range of initial and operating conditions in order to investigate the possible regimes of lubrication suggested by the micro-ehl onset model. It was thought that the Story and Rossides tests, due to their initial conditions and incremental changes, operated in different regimes.

The test program was therefore designed to incorporate the conditions used by Story and Rossides and to start and operate in different regimes of operation, ehl, mixed and micro-ehl.

3.3.2. Test programme details

Twelve tests were run, all using OM100, a straight mineral oil with the physical properties given in Table 3.1. The twelve tests used combinations of two loading sequences, three initial temperatures and two gear ratios. The loading sequences used, matched as closely as possible, those used by Story and by Bell and Dyson. The Rossides loading sequence was similar to that of Bell and Dyson except that the initial load was slightly greater in the Rossides sequence. For simplicity the Story type loading sequence in which the load is increased in equal steps is referred to as the linear (LIN) sequence and the Dyson type loading sequence in which the load steps gradually, increase in size is referred to as the logarithmic (LOG) sequence. The loading sequences are given in Table 3.2. The weight in kgf at the 10:1 hanger, the load in N/m at the discs and the maximum Hertz pressure for dry contact between the discs are given for load stage.

The three initial disc bulk temperatures used were nominally 30°C, 50°C and 70°C. The low and high temperatures corresponded to the Story and Dyson tests respectively and 50°C was used as an intermediate value. A slow disc speed of 750 r.p.m. and gear ratios of 3:1 and 2:1 were used as these provided the closest match to the rolling and sliding speeds used by Story and Rossides. The design of the gear drive arrangement was such that a change in the sliding speed was accompanied by a change in the rolling speed. The discs speeds for the two ratios are given in Table 3.3

The tests were all run using the experimental procedure outlined in Section 3.2.8. Five minute increments were used in all the tests. A

TEMPERATURE °C	40	60	100
DYNAMIC VISCOSITY, (at 1 atmos.) Ns/m^2	0.074	0.028	0.007
PRESSURE COEFFICIENT OF VISCOSITY ($0<p<50 \times 10^6$ N/m^2) m^2/N	2.25×10^{-8}	2.0×10^{-8}	1.62×10^{-8}

Table 3.1 Oil Properties (OM100)

	Logarithmic Sequence			Linear Sequence		
Incr.	Load at 10:1 kg	Load at disc kN/m	p_o Pa $x10^6$	Load at 10:1 kg	Load at disc kN/m	p_o Pa $x10^6$
1	0.2	3.92	87	2.0	39.2	275
2	0.4	7.85	123	4.0	78.5	389
3	0.9	17.7	184	6.0	117.7	476
4	1.4	27.5	230	8.0	157.0	550
5	1.9	37.3	268	10.0	196.2	615
6	2.4	47.1	301	12.0	235.4	674
7	2.9	56.9	331	14.0	274.7	728
8	3.4	66.7	359	16.0	313.9	778
9	3.9	76.5	384	18.0	353.2	825
10	4.9	96.1	431	20.0	392.4	869
11	5.9	115.8	473	22.0	431.6	912
12	6.9	135.4	511	24.0	470.9	953
13	7.9	155.0	546	26.0	510.0	991
14	9.9	194.2	612	28.0	549.4	1029
15	11.9	233.5	671	30.0	588.6	1065
16	13.9	272.7	725	32.0	627.8	1100
17	16.9	331.6	799	34.0	667.1	1134
18	19.9	390.4	868	36.0	706.3	1167
19	22.9	449.3	931	38.0	745.6	1199
20	25.9	508.2	989	40.0	784.8	1230
21	31.9	625.9	1098	42.0	824.0	1260

Table 3.2 Details of loading sequences.

GEAR RATIO	3:1	2:1
FAST DISC rev/min SPEED U_1 m/sec	2250 9.0	1500 6.0
SLOW DISC rev/min SPEED U_2 m/sec	750 3.0	750 3.0
SLIDING SPEED m/s $U_1 - U_2$	6.0	3.0
ROLLING SPEED m/s $(U_1 + U_2)/2$	6.0	4.5

Table 3.3 Test speeds.

trial test series had shown that the disc temperatures reached equilibrium within this time. With the additional time for data transferal the incremnt length is approximately 6 mins.

The tests will be identified by the letters given in Table 3.4.

3.3.3. Failure observations

All the tests were run until failure. In five of the tests scuffing initiated on the drive shaft side of the discs, in four on the free side and in the remaining three on both sides of the dsics. This waylaid the fears of a possible imbalance in the loading system. Fig.3.14 shows three of the discs after failure.

The initial and failure values of the 3:1 and 2:1 ratio tests are given in Tables 3.5a and 3.5b respectively. Six of the tests failed within 20 secs. of a load increase and five within 1.5 mins., whilst test J failed 4 mins. from the beginning of the increment. In all the tests the load was removed immediately a scuff was detected leaving, in most cases, sufficient undamaged surface for post-run profiles to be measured.

A decrease in the sliding and hence rolling speed, enhanced the scuffing resistance, in terms of the failure load. Regardless of the initial temperature or loading sequence, all the 2:1 tests failed at higher loads and disc bulk temperatures, and ran to higher calculated nominal surface interaction, that is roughness to film thickness ratio, than any of the 3:1 tests. The 3:1 tests failed at loads in the range 4.9 kgf to 12 kgf with disc bulk temperatures of 55 C to 88 C and the 2:1 tests in the range 28 kgf to 36 kgf and with disc bulk temperatures between 121°C and 160°C.

In the 3:1 tests there was a tendency for the failure load to decrease and the disc bulk temperature at failure to increase with increasing initial bulk temperature. There was no such obvious trend in the 2:1

	GEAR RATIO = 3:1			GEAR RATIO = 2:1		
INITIAL DISC TEMP.	30'C	50'C	70'C	30'C	50'C	70'C
LOG LOADING	A	B	C	G	H	I
LIN LOADING	D	E	F	J	K	L

Table 3.4 Summary of test series conditions.

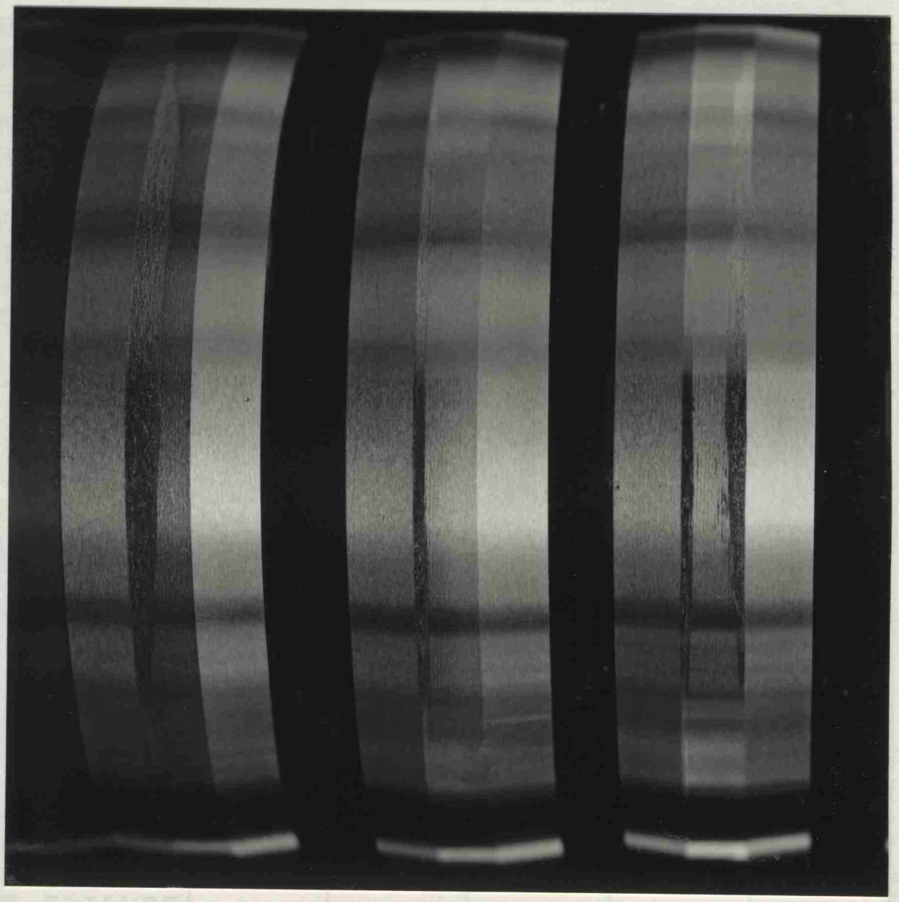

Figure 3.14 Scuffed discs.

TEST	A	B	C	D	E	F
LOADING SEQUENCE	LOG	LOG	LOG	LIN	LIN	LIN
OIL SUPPLY TEMPERATURE °C	29	53	77	25	52	72
INITIAL DISC TEMPERATURE °C	28	46	71	24	49	68
FAILURE INCREMENT	15	14	10	6	3	3
FAILURE LOAD - kgf (10:1)	11.9	9.9	4.9	12	6	6
p_0 AT FAILURE $N/m^2 \times 10^6$	671	612	431	674	476	476
DISC BULK (2mm) TEMPERATURE AT FAILURE °C	55	76	86	62	67	88
COEFFICIENT OF FRICTION AT FAILURE	.016	.045	.027	.022	.022	.027
FLASH TEMPERATURE AT FAILURE °C	25	62	22	34	21	28
TIME TO FAILURE IN LAST INCREMENT SECS	84	17	13	53	84	69

Table 3.5a Failure conditions - 3:1 tests.

TEST	G	H	I	J	K	L
LOADING SEQUENCE	LOG	LOG	LOG	LIN	LIN	LIN
OIL SUPPLY TEMPERATURE °C	31	53	78	*	53	75
INITIAL DISC BULK (2mm) TEMPERATURE °C	30	50	68	27	48	68
FAILURE INCREMENT	21	21	21	14	16	18
FAILURE LOAD - kgf (10:1)	31.9	31.9	31.9	28	32	36
p_o at FAILURE $N/m^2 \times 10^6$	1098	1098	1098	1029	1100	1167
DISC BULK (2mm) TEMPERATURE AT FAILURE °C	124	124	138	121	145	160
COEFFICIENT OF FRICTION AT FAILURE - μ	.071	.071	.066	.065	.070	.066
FLASH TEMPERATURE AT FAILURE °C	134	137	106	111	132	135
TIME TO FAILURE IN LAST INCREMENT -SECS	11	14	20	20	233	64

(* - faulty thermocouple)

Table 3.5b Failure conditions - 2:1 tests.

tests. There seemed to be little benefit in either of the loading sequences.

The pre- and post-run surface roughness values shown in Table 3.6 are the average of twelve values, three measurements at each of four positions around the disc surface. The pre-run values showed more scatter than was desired which does not facilitate comparison of the degree of running-in which occurred in the tests. ΔRa , the difference between the pre- and post-run Ra values of the rough discs is taken as a crude measure of the degree of running-in. In terms of these values three levels of running-in were arbitrarily defined, for ease of discussion, as 'low' (ΔRa = 0.0 - 0.03 μm) , 'moderate' (ΔRa = 0.045 - 0.075 μm) and 'marked' (ΔRa >> 0.075 μm) . These flexible categories arose as a result of the grouping of the results. The 3:1 tests produced either 'low' or 'moderate' running in and all the 2:1 tests produced 'moderate' running-in, except test L where the running-in was 'marked', being almost twice that of any other test. This test also had the highest failure load and the highest calculated degree of surface interaction.

3.3.4. Incremental variations in friction

In Fig.3.15 the coefficient of friction and the disc bulk temperature for the twelve tests are plotted against time. These graphs are as produced by the monitoring system. Whilst they show the variation of the friction coefficient and the bulk temperature within an increment, it is difficult to compare values of friction and temperature for the LOG and LIN load sequences at equivalent loads.

To ease comparison, in Fig.3.16 the coefficients of friction are replotted against the maximum Hertz pressure, p_o , for each increment which are given in Table 3.2. The conditions at the beginning and end of an increment are plotted at the appropriate p_o value and are joined by a vertical line. For continuity the conditions at the end of an increment are joined to the initial condition of the next with a horizontal or

TEST	A	B	C	D	E	F
PRE - RUN						
ROUGH DISC Ra- μm	0.303	0.328	0.379	0.360	0.327	0.355
SMOOTH DISC Ra- μm	0.094	0.099	0.104	0.107	0.100	0.093
do	0.561	0.606	0.695	0.665	0.604	0.650
POST - RUN						
ROUGH DISC Ra- μm	0.291	0.269	0.318	0.343	0.302	0.308
SMOOTH DISC Ra- μm	0.102	0.080	0.106	0.096	0.093	*
ΔRa ROUGH DISC	0.012	0.059	0.061	0.016	0.025	0.047

* Insufficient unscuffed surface for measurement

Table 3.6a Surface roughness values - 3:1 tests.

TEST	G	H	I	J	K	L
PRE - RUN						
ROUGH DISC Ra- μm	0.340	0.318	0.312	0.301	0.331	0.370
SMOOTH DISC Ra- μm	0.080	0.092	0.093	0.094	0.079	0.098
do	0.617	0.586	0.577	0.558	0.602	0.678
POST - RUN						
ROUGH DISC Ra- μm	0.271	0.267	0.244	0.233	0.257	0.233
SMOOTH DISC Ra- μm	0.081	0.097	0.099	0.100	0.093	0.081
ΔRa ROUGH DISC	0.068	0.051	0.068	0.068	0.074	0.136

Table 3.6b Surface roughness values - 2:1 tests.

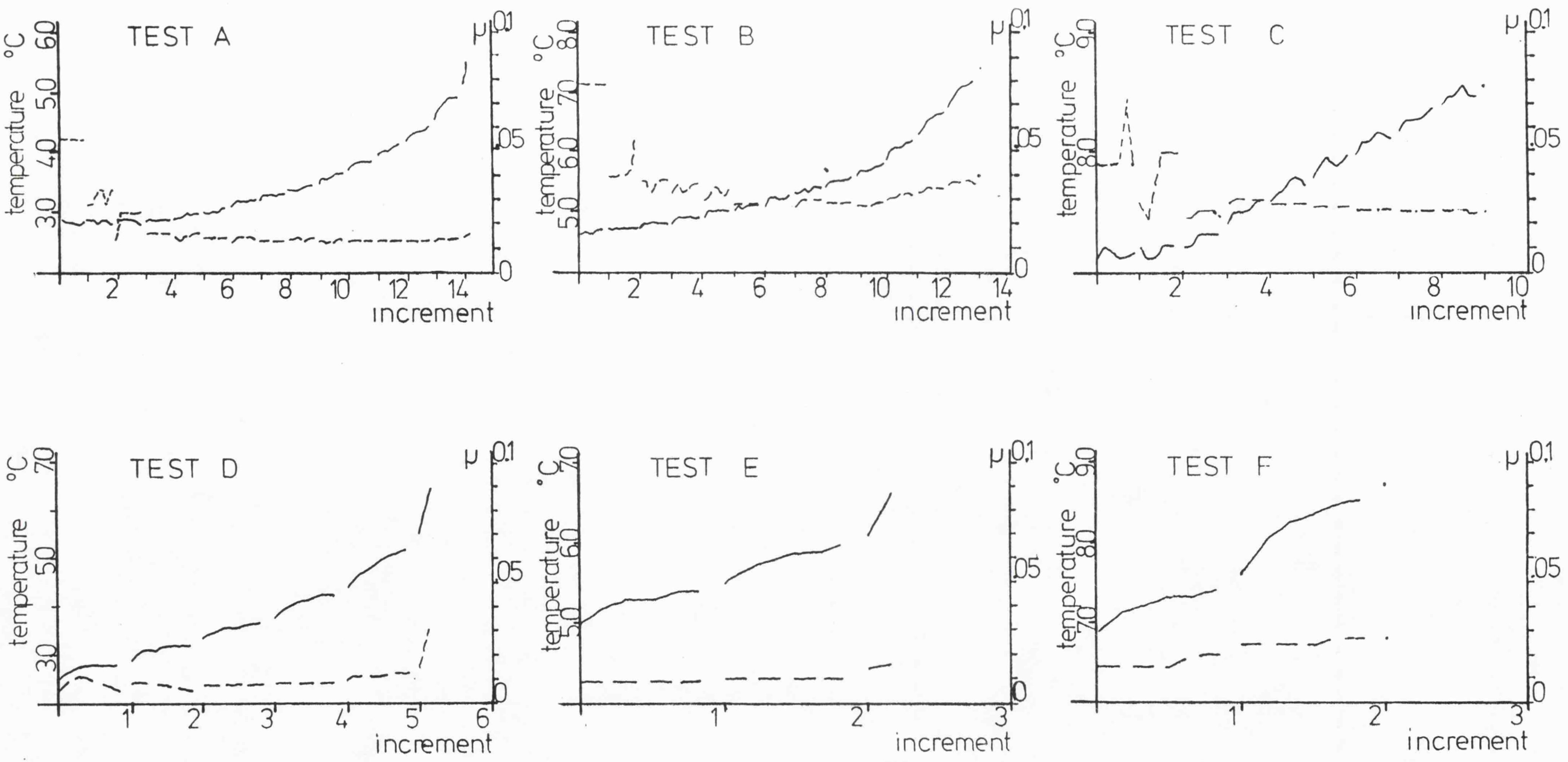

Figure 3.15a Variation in bulk temperature and friction coefficient - 3:1 tests.

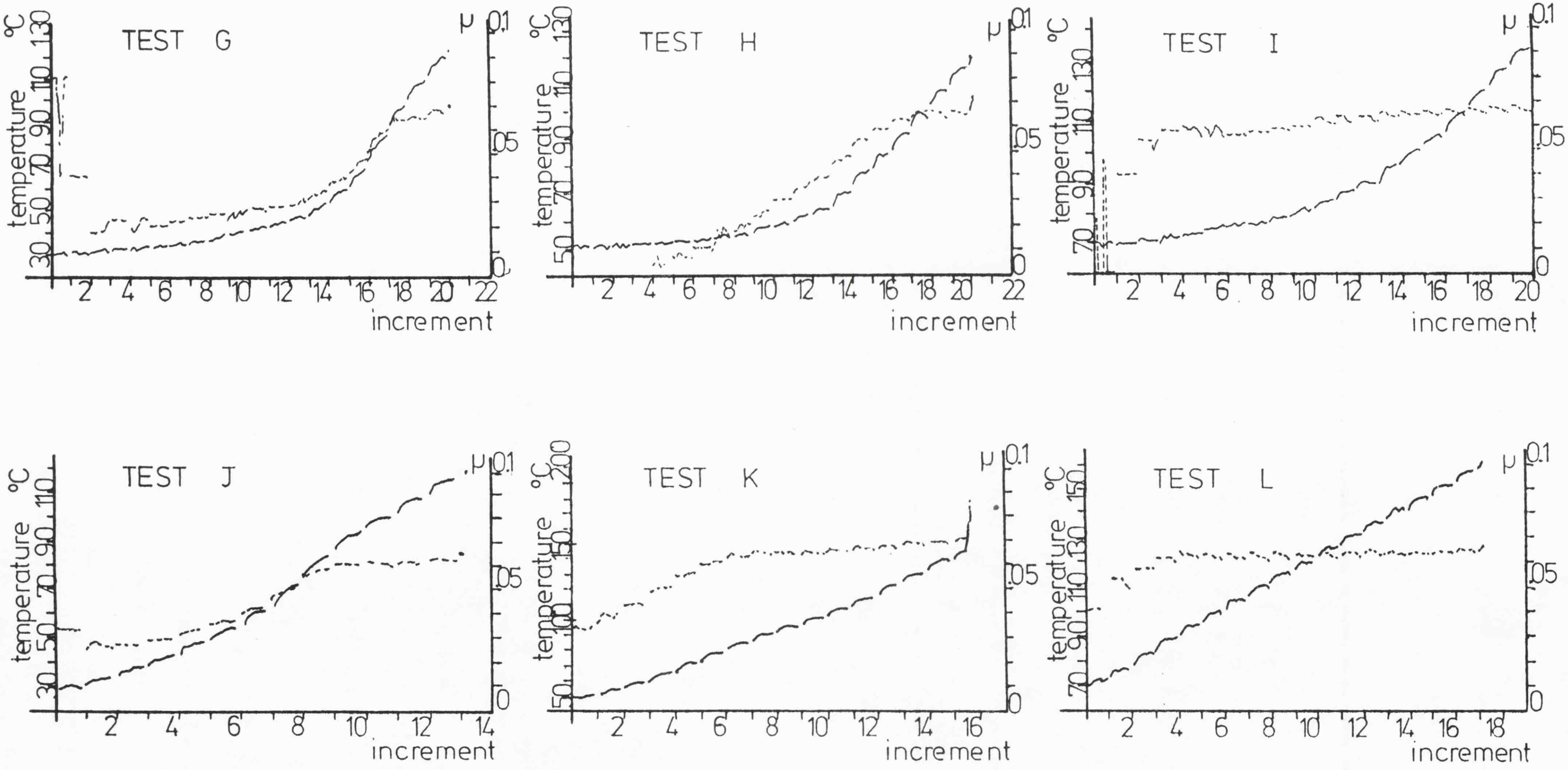

Figure 3.15b   Variation in bulk temperature and friction coefficient - 2:1 tests.

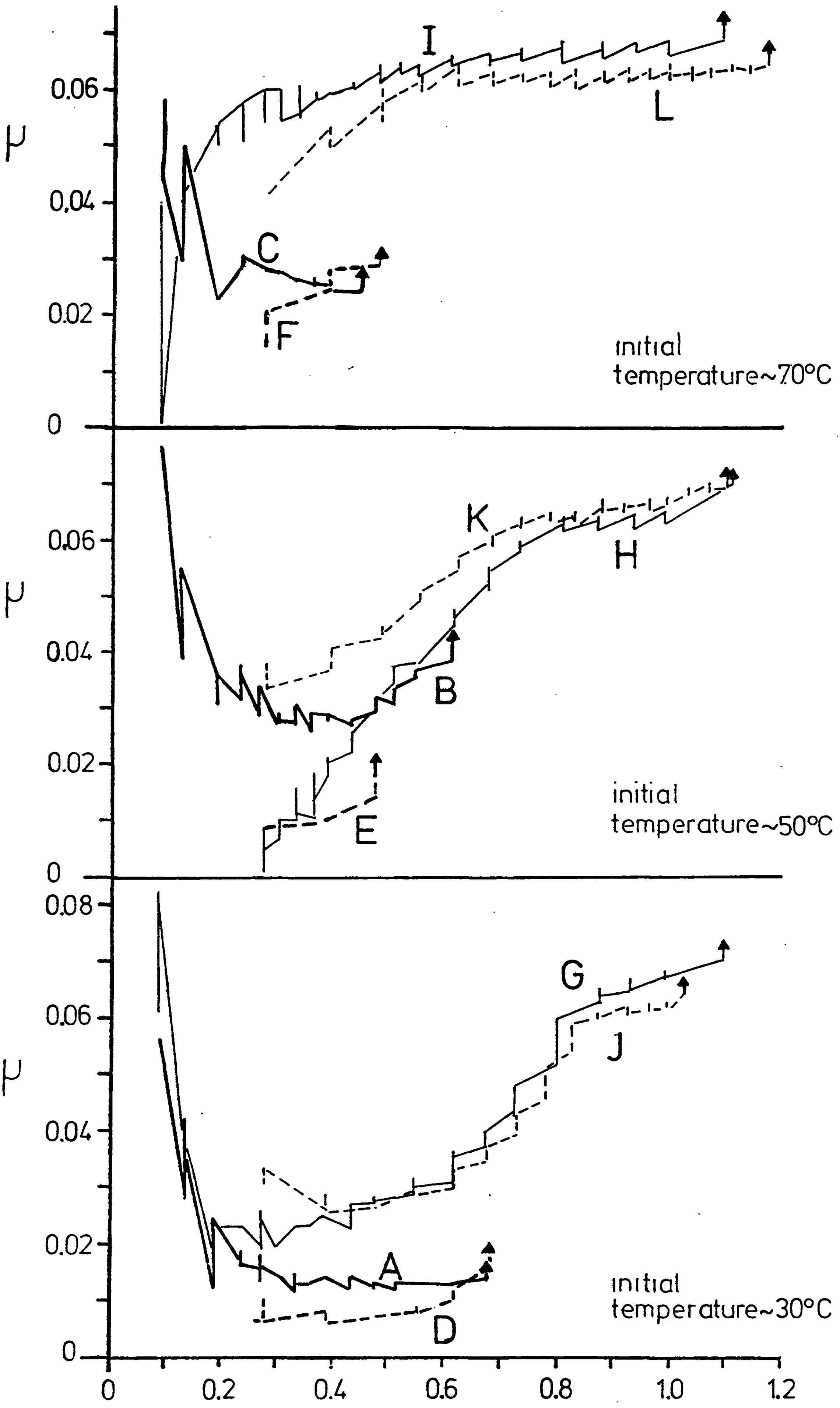

Figure 3.16 Coefficient of friction / load for the 3:1 and 2:1 tests.

sloping line. Where the friction coefficient has passed through a maximum or a minimum during the increment this is indicated by an extension of the vertical line. There is no attempt to represent the change of friction coefficient with time during an increment.

The coefficients of friction vary from 0.008 to 0.07 . The 3:1 tests generally have a lower coefficient of friction than the 2:1 tests.

There are several ways in which the friction varies with the pressure. In the 2:1 tests the friction coefficients may differ in the early stages but rise in all the tests to a similar value (μ = 0.06 - 0.07) at higher loads (> 0.8 GPa) .

In the LOG sequence tests, the initial load is low enough for the system, if the surfaces were smooth, to operate in the classical lubrication regime. Although the traction produced is low on an absolute scale, it is high relative to the load and this results in a high initial coefficient of friction as shown in the LOG tests A, B, H and C . Due to the higher initial load in the LIN sequence the system operates from the start with ehl and has a lower initial coefficient of friction. The different friction in the early stages for the LOG and LIN loading sequences is best seen by comparing the LOG test G to the LIN test J.

There are several anomalies in the friction results. For the LOG test H, there was no registered traction in the first increment. In test I the friction in the first increment oscillates between 0 and 0.8 N which causes the friction coefficient to vary between 0 and 0.041 . There are two possible reasons for zero registered friction, both due to the measuring system. Firstly, the frictional traction in the classical regime is low and in tests H and I it may have failed to reach the lowest detectable level (Fr = 0.4 N). Secondly, at the beginning of the tests the amplifier output level was wound down, while the machine was running, until the measured traction was zero. Unfortunately it was possible to 'wind down' the amplifiers level below zero which, if the friction is small, could also result in the friction being undetected in the first increment of these tests. The effect on the coefficient of friction of this small constant error in the frictional force would become negligible with increasing frictional force at higher loads. These problems make it difficult to compare the friction at low loads.

The second anomaly was the difference in the general levels of friction between the 3:1 and the 2:1 tests. At intermediate loads, comparing the equivalent tests at the same loads the coefficient of friction in all the 3:1 tests, except test B, is lower than in the 2:1 tests. For example, comparing tests E and K, both 50 C°LIN tests, the coefficient of friction in the 3:1 test, E , is around 0.01 whilst over the same load range in tests K it is 0.03 - 0.04.

The tests at the 3:1 ratio were the first tests in the series to be run. During this time many teething problems were encountered with the strain gauges. These included damage to the fine wires of the strain gauges due to inadequate protection and the detrimental effect of the hot oil on the bonding between the strain gauge encapsulation and the surface of the cantilever. Several different cantilever strain gauge sets were used until the problems were resolved. As a result, it may be questioned whether the difference in the levels of friction between the two test batches were real or a consequence of the problems with the instrumentation. Tests B and E were each repeated twice, both to resolve the differences in the friction levels and to check the repeatability of the test results.

The results of the repeats of tests B and E, i.e. tests B1, B2, E1 and E2 are compared with those of the original 3:1 tests, B and E in Table 3.7. The friction coefficients for the six tests are compared in Fig.3.17. The levels of friction in the repeat LOG tests are consistent with those of test B and those of the 2:1 tests. In the LIN repeat tests (E1 and E2) the friction coefficient is much higher than in the original test E and is more consistent with the general levels in the 2:1 tests. Although no concrete reasons for the differences could be found, they were

TEST	B	B_1	B_2	E	E_1	E_2
LOADING SEQUENCE	LOG	LOG	LOG	LIN	LIN	LIN
OIL SUPPLY TEMPERATURE °C	53	56	53	52	53	56
INITIAL DISC BULK (2mm) TEMPERATURE °C	46	54	49	49	50	54
FAILURE INCREMENT	14	10	10	3	2	2
FAILURE LOAD - kg (10:1)	9.9	4.9	4.9	6	4	4
Po at FAILURE N/m^2 $x10^6$	612	431	431	476	389	389
DISC BULK (2mm) TEMPERATURE AT FAILURE °C	76	68	65	67	61	68
COEFFICIENT OF FRICTION AT FAILURE	.045	.036	.044	.022	.057	.063
FLASH TEMPERATURE AT FAILURE °C	62	29	36	21	50	43
TIME TO FAILURE IN LAST INCREMENT -SECS	17	35	95	84	112	140

Table 3.7a Failure conditions - 50 °C, 3:1 tests.

TEST	B	B_1	B_2	E	E_1	E_2
PRE - RUN						
ROUGH DISC Ra- µm	0.328	0.316	0.363	0.327	0.370	0.387
SMOOTH DISC Ra- µm	0.099	0.093	0.097	0.100	0.092	0.089
do	0.606	0.583	0.665	0.605	0.675	0.703
POST - RUN						
ROUGH DISC Ra- µm	0.269	*	0.326	0.302	*	0.359
SMOOTH DISC Ra- µm	0.080	*	0.091	0.093	*	*
ΔRa ROUGH DISC	0.059	*	0.037	0.025	*	0.028

* insufficient unscuffed surface for measurement

Table 3.7b Surface roughness values - 3:1 50 °C tests.

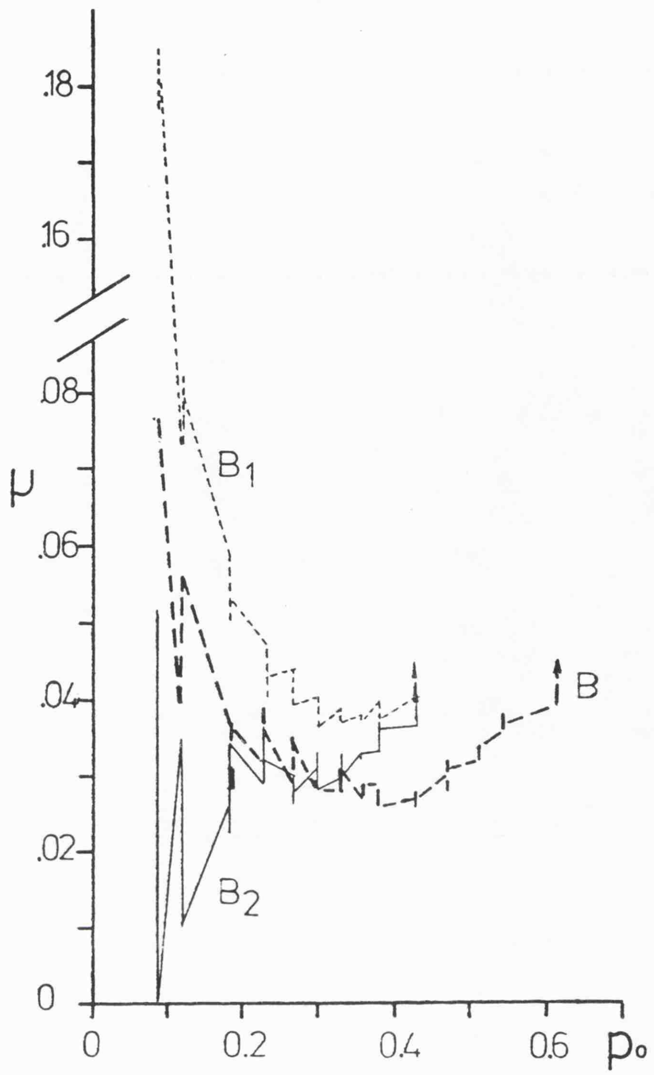

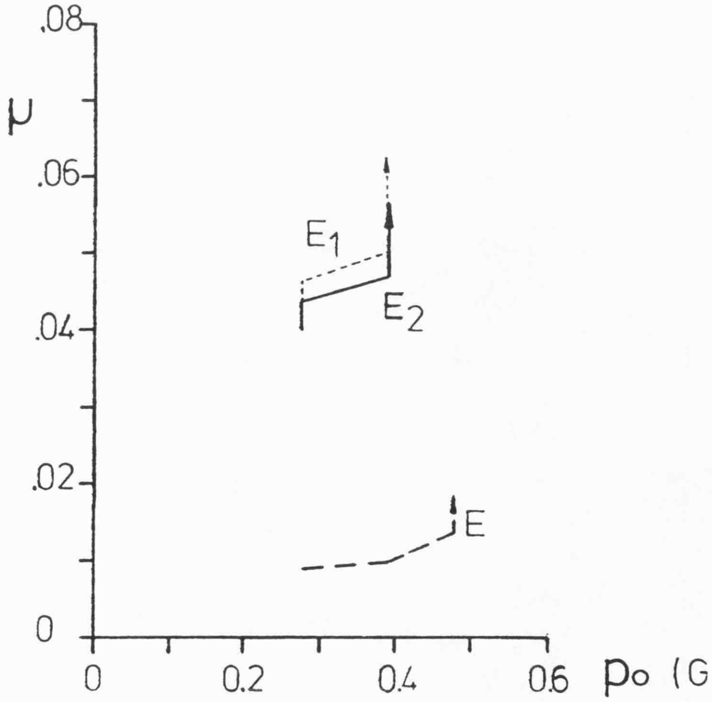

Figure 3.17 Coefficient of friction / load for the 3:1 , 50 C tests.

suspected to be connected to the measurement problems discussed. The levels of friction in the initial 3:1 tests are therefore treated with some caution.

3.3.5. Incremental changes in temperature

In Fig.3.18a the bulk temperatures of tests A-L replotted against p_o using the same convention as that used to plot the coefficient of friction results. The results for the repeat tests are given in Fig.3.18b

It is worth noting that the 3:1 tests with the lower coefficients of friction have comparable rises in temperature to the repeat tests at the 3:1 ratio, i.e. tests B1, B2, E1, E2 and to the early stages of the equivalent 2:1 tests. In Chapter 6 it is shown that the incremental temperature rises are linearly related to the coefficient of friction and to the load. The lower coefficients of friction in the initial 3:1 tests should be reflected in smaller temperature changes in these tests. That they do not is further evidence of an error in the measured levels of friction in the original 3:1 tests.

The change in bulk temperature with p_o follows similar paths for all the tests, although at the 2:1 ratio the average rise in temperature with pressure is greater in the tests at the lower oil supply temperature than in those at the higher temperature, particularly in the later stages of the tests. Due to the shorter duration of the 3:1 tests no similar comparison is possible.

3.3.6. Count rate data

The count rate is the number of times in a one second period that the resistance drops below the set value and returns to the base level. Fig.3.19 shows the count rate information for test J in which the count rate at ten second intervals is plotted. The increments are clearly defined by the changes in the count rate activity. Three patterns of behaviour can be identified. In the first pattern random low level counts

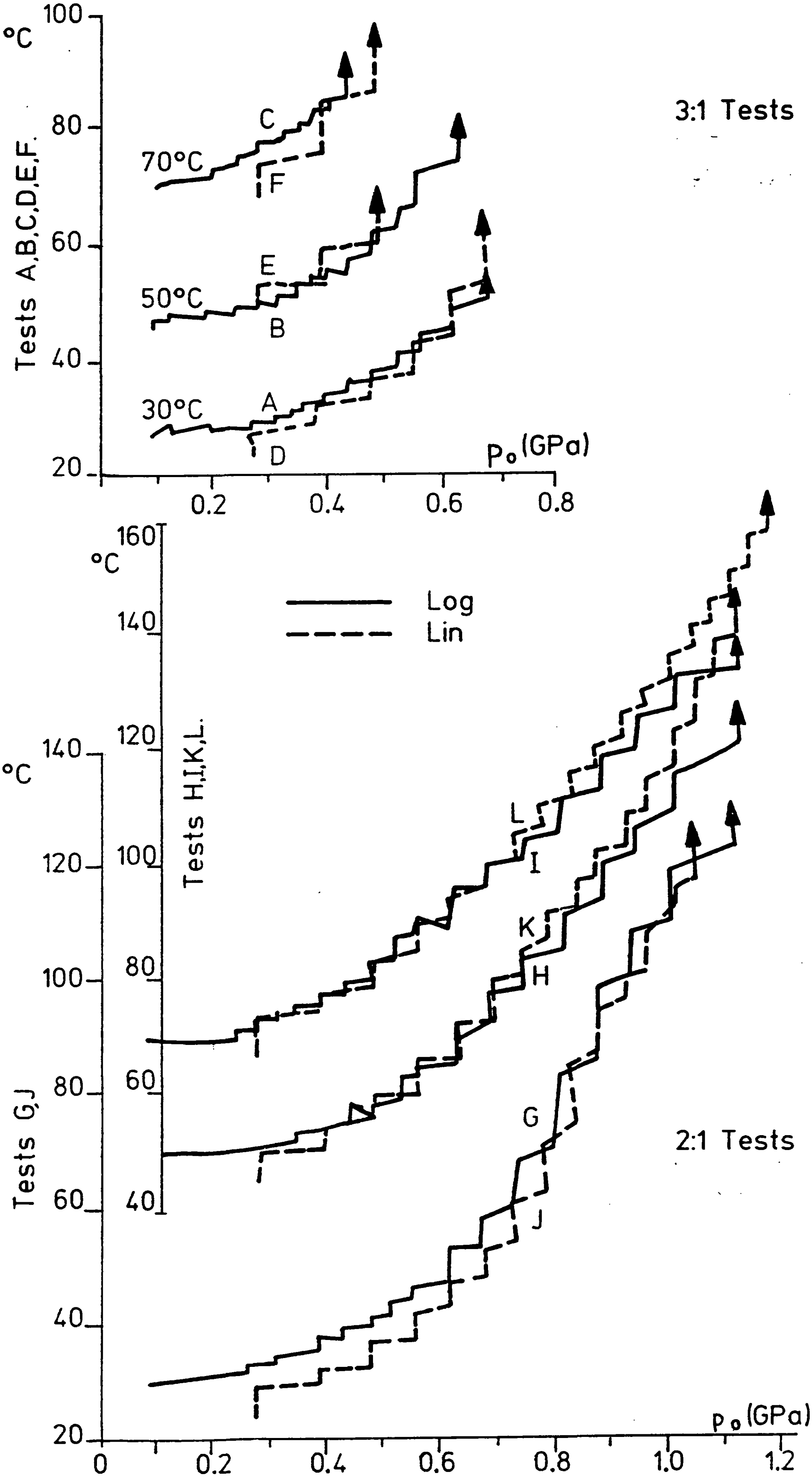

Figure 3.18a Bulk temperature / p , 3:1 and 2:1 tests.

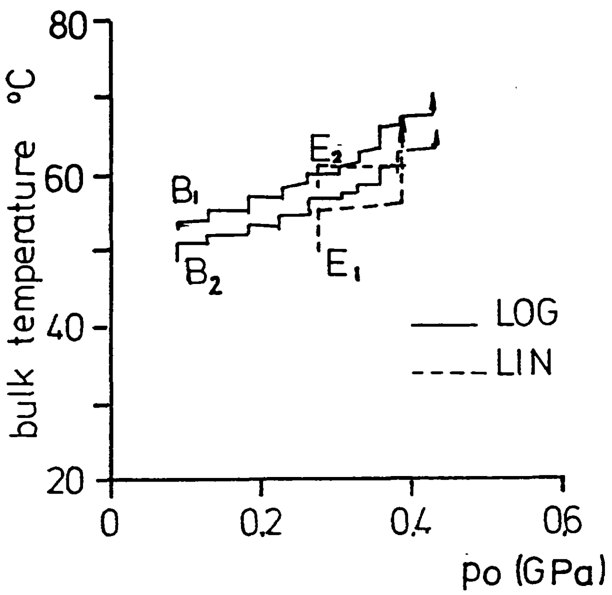

Figure 3.18b Bulk temperature / p_o for the 3:1, 50 C tests.

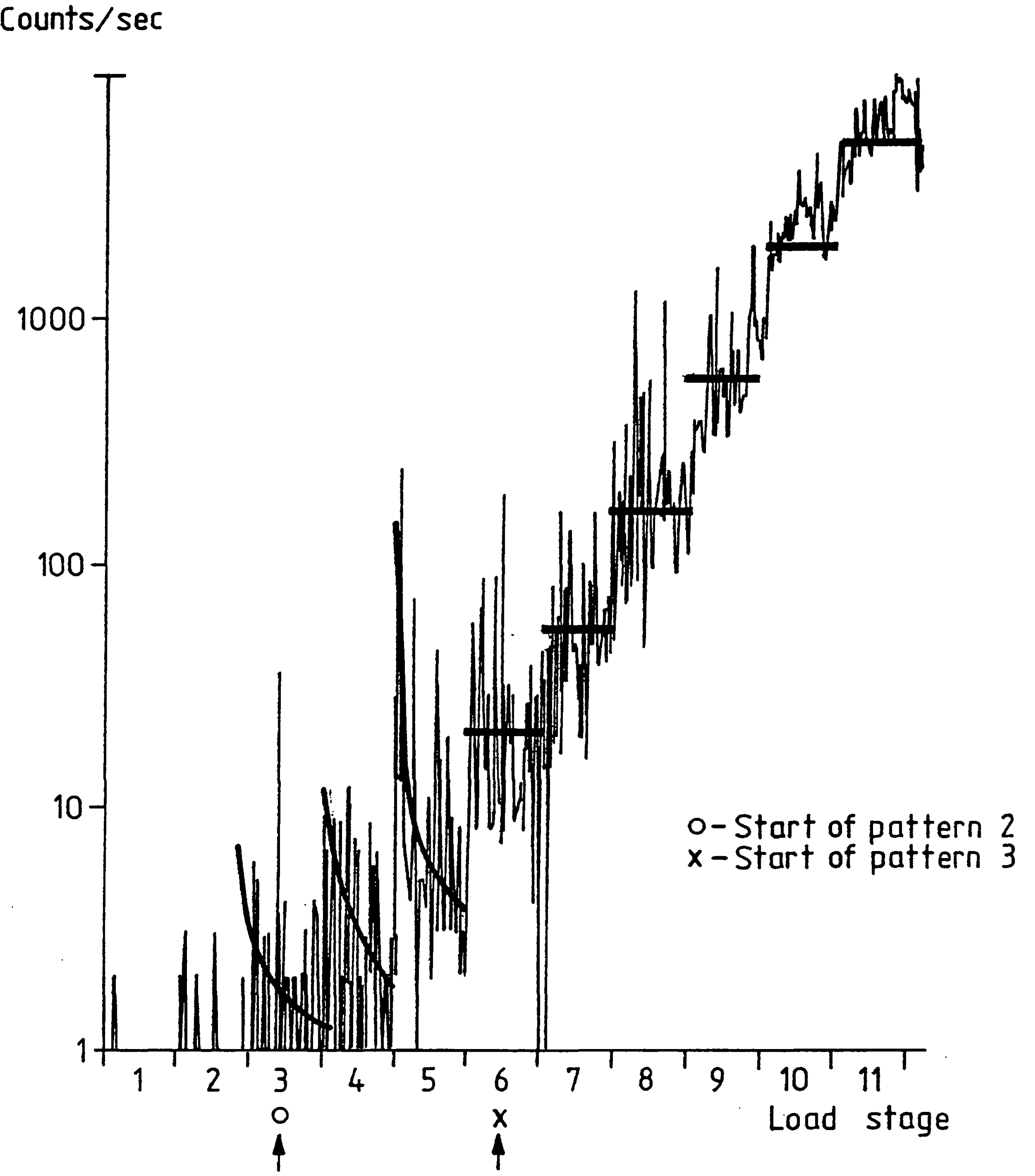

	3:1 Load stage (Pressure in MPa)						2:1 Load stage (Pressure MPa)					
Test	A	B	C	D	E	F	G	H	I	J	K	L
Pattern 2	10 (431)	3 (184)	3 (184)	4 (550)	—	—	—	4 (230)	4 (230)	3 (476)	2 (389)	2 (389)
Pattern 3	14 (612)	12 (511)	8 (359)		—	—	—	(546)	14 (612)	6 (674)	4 (550)	4 (550)

Figure 3.19 Plotted countrate data for tests J and the increments for the O and X contact levels.

were found to occur at film thicknesses as high as $h^* = 13\sigma$, i.e. greater than $h^* = 3\sigma$ at which contact would be expected. The second pattern is characterised by an increase in count rate activity following the application of the load with the activity decaying during the increment to the zero level. The third pattern again has a marked increase in the count rate following the increase in load but has sustained activity throughout the increment. The load increments at which each pattern first occurred are tabulated in Fig.3.19. In test D the third or sustained contact pattern did not occur. In tests E, F and G the count rate monitoring device malfunctioned and so count rate information is not available for these tests. The count rate data become more significant when the tests histories are related to the model of the onset of mixed and micro ehl - which is the subject of section 3.4. First the results will be examined in relation to two of the most commonly used scuffing failure criteria.

3.3.7. <u>Results in terms of two proposed failure criteria</u>.

Both the constant total contact temperature criterion and the frictional power intensity criterion of scuffing failure were discussed in Chapter 2. The values of the bulk, flash and total contact temperature for each test are given in Table 3.8. The flash temperatures are calculated using the measured coefficient of friction just prior to failure and the expression for the flash temperature in the contact due to Blok (1937).

In Table 3.9 the frictional power intensity in the contact is given for each test again at conditions just prior to failure. The total contact temperature at failure ranges from 80°C to 138°C in the 3:1 tests and 232°C to 295°C in the 2:1 tests, a difference of 215°C over the full range of conditions. The lower values in the 3:1 tests are for those with the lowest measured coefficients of friction. In test B and the repeat tests B1, B2, E1 and E2 the friction was similar to that in the 2:1 tests but the total contact temperatures at failure are still considerably less than the 2:1 tests, the range being 94°C for test B1 to 295°C in test

3:1 Tests

TEST	A	B	C	D	E	F
BULK TEMPERATURE °C	55	76	86	62	67	88
FLASH TEMPERATURE °C	25	62	22	34	21	28
TOTAL CONTACT TEMPERATURE °C	80	138	108	96	88	116

2:1 tests

TEST	G	H	I	J	K	L
BULK TEMPERATURE °C	124	124	138	121	145	160
FLASH TEMPERATURE °C	134	137	106	111	132	135
TOTAL CONTACT TEMPERATURE °C	258	261	244	232	277	295

3:1 repeat tests

TEST	B_1	B_2	E_1	E_2
BULK TEMPERATURE °C	68	65	61	68
FLASH TEMPERATURE °C	26	36	50	43
TOTAL CONTACT TEMPERATURE °C	94	101	111	111

Table 3.8 Total contact temperatures at failure.

3:1 tests

TEST	A	B	C	D	E	F
μ	0.016	0.045	0.027	0.022	0.022	0.027
P_{av} ($N/m^2 x10^6$)	527	480.7	338.5	529.4	373	373
FRICTIONAL POWER INTENSITY - $x10^6$ watts/m^2	50.6	129.8	54.8	69.8	49.2	60.4

2:1 tests

TEST	G	H	I	J	K	L
μ	0.071	0.071	0.066	0.065	0.07	0.066
P_{av} ($N/m^2 x10^6$)	862	862	862	808	863.9	916.5
FRICTIONAL POWER INTENSITY - $x10^6$ watts/m^2	183.6	183.6	170.7	157.6	181.4	181.5

3:1 repeat tests

TEST	B_1	B_2	E_1	E_2
μ	0.036	0.044	0.057	0.063
P_{av} ($N/m^2 x10^6$)	338.5	338.5	305.5	305.5
FRICTIONAL POWER INTENSITY - $x10^6$ watts/m^2	73.1	89.4	104.5	115.5

Table 3.9 Frictional power intensity at failure.

L, a difference of 220°C. These results show that the Blok total contact temperature criterion is not valid even though the range of conditions in terms of surface speeds and initial temperatures is relatively small.

The frictional power intensity is also calculated using the measured coefficient of friction. There is a similar difference between the two speed ratios for the frictional power intensity prior to failure as that for the total contact temperatures. The values for the 3:1 tests range from 49.2 W/mm^2 to 129.8 W/mm^2 with test B again having the highest value. The range for the 2:1 tests is smaller, 157.6 W/mm^2 to 183.6 W/mm^2, with an average value of 176.4 W/mm^2, which would seem to offer some support to this criterion. However, including the 3:1 test B and the repeat 3:1 tests with the 2:1 results increases the range from 73.1 W/mm^2 to 183.6 W/mm^2 whilst the average value at failure drops to 142.8 W/mm^2. Although the results were encouraging for the 2:1 tests a small change in the slide/roll ratio has a large effect on this parameter at failure.

3.4. Discussion of results wrt aims

The results will now be considered with respect to the two main aims of this test series. First, several points need to be made about applying the mixed/micro-ehl onset model to real surfaces, the plotting convention used and some of the assumptions made when representing a test history on the micro-ehl onset graph.

3.4.1. Use of model with real surfaces

The model described in section 2.5 was of a cylindrical body with circumferential roughness in the form of a sine wave, loaded against a flat plate. The conditions which would result in micro-ehl were given in terms of various operating parameters, including the wavelength, 2L , and the amplitude, d_o, of the surface roughness.

A real ground surface is composed of different superimposd scales of roughness. The behaviour of real surfaces can be compared with that predicted by the model if the combined roughness is represented by an 'equivalent' sine wave acting on a smooth surface, where the wavelength of the equivalent sine wave is the same as the longest component of the real surface roughness and it has an amplitude, d_o , such that the rough surfaces and the sine wave have the same root mean square roughness value.

The Talysurf gives surface roughness in terms of a centre line average height, Ra . If it is assumed that the distribution of the surface heights is semi-gaussian with a standard deviation, or root mean square (r.m.s.) surface height from the mean level of σ , then $\sigma = 1.25 \times Ra$ and the highest asperities are 3σ above the mean level of the surface. When two rough surfaces are used, the combined or effective roughness is given by $Ra' = \sqrt{Ra_1^2 + Ra_1^2}$ and hence the combined r.m.s. value by $\sigma' = 1.25\ Ra'$. The r.m.s. value of a sine wave $\sigma = d_o/\sqrt{2}$ where d_o is the wave amplitude. Therefore for two rough surfaces each with a semi-gaussian surface height distribution, the amplitude of the equivalent sine wave is given by $d_o = 1.77\ Ra'$.

Contact therefore will first be expected between the highest asperities of two such opposing surfaces when their average separation, h^* - measured between the mean levels of each surface thins to $3\sigma'$ or $3.75\ Ra'$. In terms of the amplitude of the equivalent sine wave, first contact is expected between the surfaces when $h^* = 3\sigma/\sqrt{2}$, i.e. when $d_o/h^* = 0.47$.

At $d_o/h^* > 0.47$, some of the load will be carried by the asperity contacts and the remainder by residual hydrodynamic action - the system is operating with mixed lubrication.

3.4.2. Calculation of film thickness values

The film thickness appears in the model in the d_o/h^* group. The film thickness h^* , is that at the centre of the contact and has been calculated from the Dowson and Higginson film thickness formula.

$$h^* = 1.25 \times h_{min} = 3.31 \times R'^{0.43} \times E'^{(-0.03)} \times (\bar{\eta u})^{0.7} \times \alpha^{0.54} \times W'^{(-0.13)}$$

The viscosity and pressure viscosity enhancement coefficient of the oil are determined by the bulk temperature of the bodies in the inlet region (Archard and Kirk (1961)). The temperature measured by the 2 mm thermocouple has been used for this purpose.

This formula assumes smooth surfaces and is not strictly applicable with rough surfaces which might affect film thickness behaviour. In the ehl region the predicted effect of roughness on film thickness is small when the film thickness is several times greater than the roughness, in which case the Dowson and Higginson film thickness equation is adequate to predict the film thickness between the mean levels of the surfaces. With thinning films and with circumferentially ground surfaces the roughness is predicted by Chow and Cheng (1976) to have an increasing detrimental effect on film thickness. For the present case it can be shown (Section 4.5) that when the surfaces are close but not touching, the expected reduction in average film thickness due to the roughness compared to the value for smooth surfaces, is around 6%.

At present there is no way of calculating film thickness in the mixed and micro-ehl regimes of ehl. The film thickness for all three regimes - e.h.l., mixed and micro-ehl, has therefore been determined using the Dowson and Higginson film thickness formula and is taken as the thickness between the mean levels of the undeformed surfaces. This is already accepted practice in the mixed lubrication regime. These values are therefore not absolute but serve as a useful indication of the severity of the test conditions.

3.4.3. Test histories and count rate data

The convention used to plot a test history on the micro-ehl plot is that a vertical line represents the change in conditions during an increment due to the change in temperature and a horizontal line, the change in conditions due to the increase in load from the end of one increment and the beginning of the next, and so on. There is no attempt to show the variation with time within an increment on the plots. The final conditions are taken as those just prior to scuffing.

The complete test histories on the micro-ehl onset plot are shown in Figs.3.20a and b for the 3:1 and 2:1 tests respectively. The dotted horizontal lines are at different values of the h^*/σ ratio for the undeformed surface roughness and the film thickness between the mean levels of the undeformed surfaces. The $h^* = 3\sigma$ line is the predicted level of first contact between undeformed surface and so forms the boundary to the ehl/mixed lubrication regions. The increments in which the decaying and the sustained count rate patterns are first observed are indicated by an 'O' and by an 'X' respectively on the test histories.

At both gear ratios, three tests start in the ehl region (region 1) and three in the micro-ehl regions (region 3).

At the 3:1 speed ratio tests C and D most closely reproduce the test conditions used by Bell and Dyson/Rossides and by Story respectively, and similarly tests I and J at the 2:1 speed ratio.

At the 3:1 ratio tests A, D and E start in the ehl region. The initial conditions are primarily determined by the effect of the disc bulk temperature on the film thickness, h^*, and by the load, p_o. For example, test D, a Story type test, starts with a high initial load but with a low initial temperature so that the surfaces are initially separated by a thick film. With increasing severity of conditions (load and temperature) these three test histories move towards the ehl/mixed lubrication boundary. Test A fails before crossing into the mixed lubrication regime. Tests D and E cross the boundary between the ehl and mixed lubrication regions in the ultimate and penultimate increments respectively and fail soon after, at $d_o/h^* \sim 0.62$.

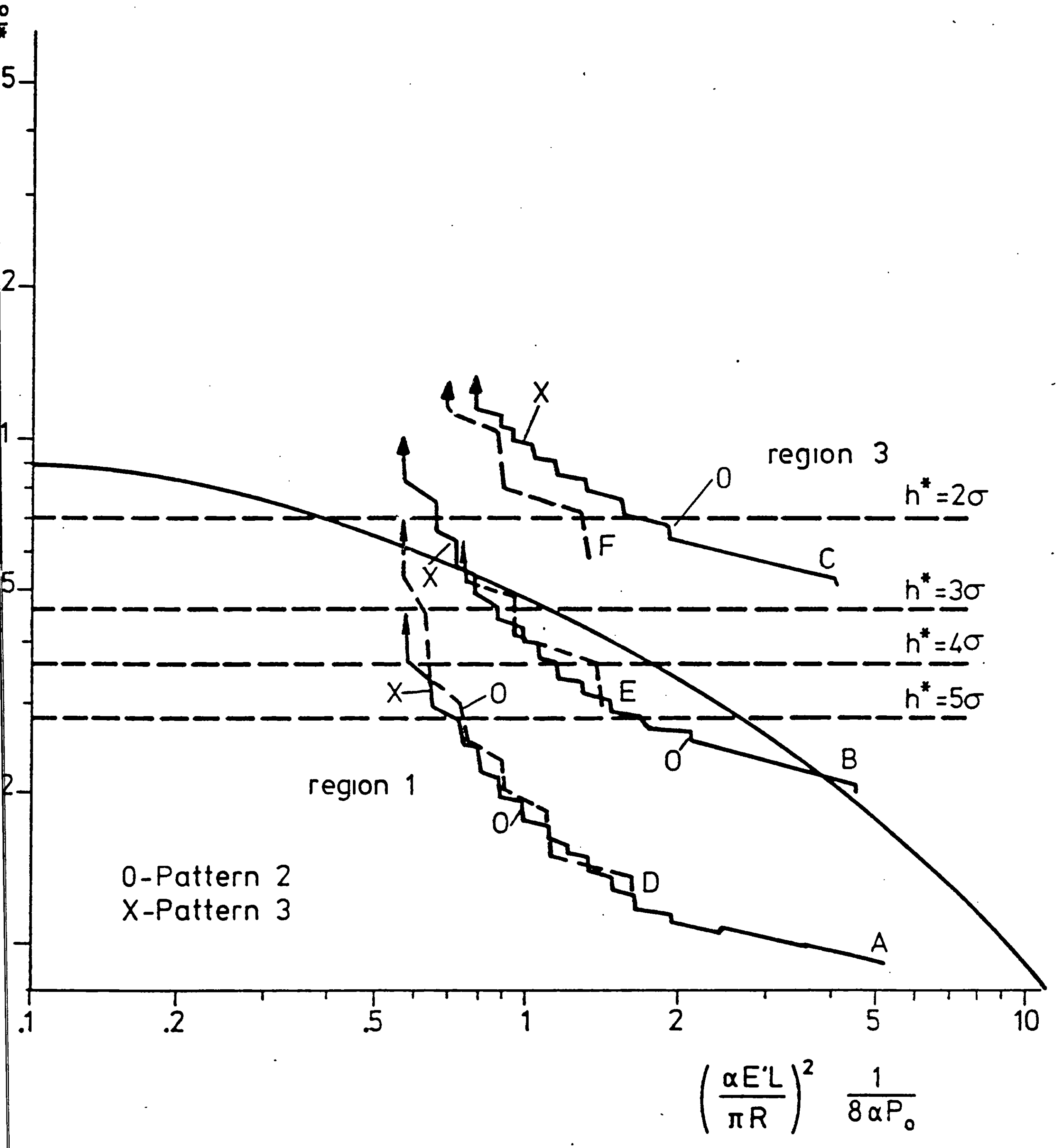

Figure 3.20a Test histories of the 3:1 tests on the micro-ehl onset plot.

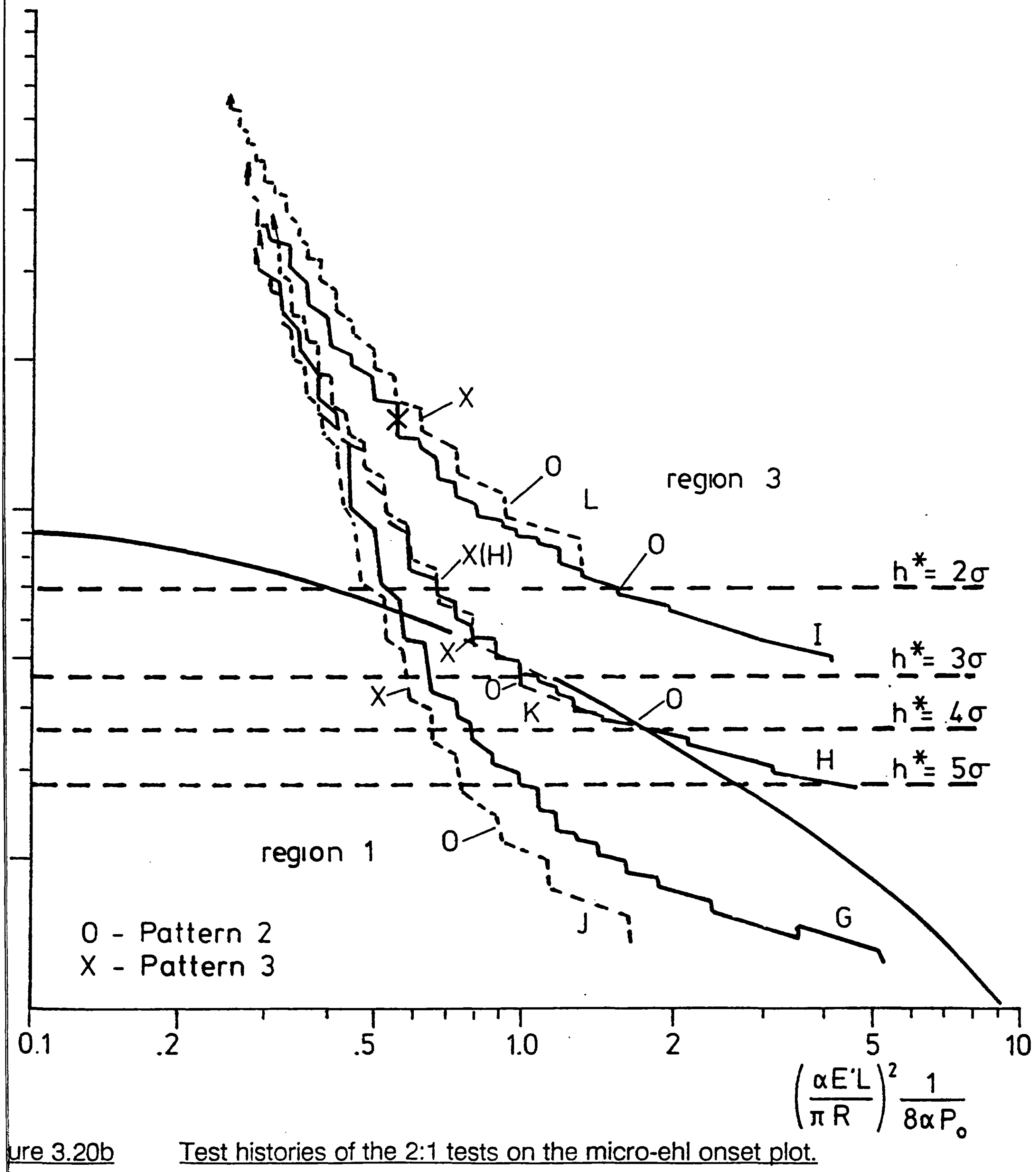

ure 3.20b Test histories of the 2:1 tests on the micro-ehl onset plot.

The 3:1 tests, B, C and F start with conditions thought to be conducive to micro-ehl. For example, test C, a Bell and Dyson type test, has a high initial temperature which results in a thin initial film although it has a low initial load. The d_o/h^* levels throughout tests C and F suggest considerably more interaction than in tests A, D and E. On increasing severity of conditions these tests run to yet thinner nominal films before failing at $d_o/h^* \sim 1.2$, and at greater disc bulk temperatures than tests A, D and E. Test B also starts in the micro/ehl region. The behaviour of this test, as plotted, crosses into the ehl region. It must be reiterated that the behaviour of the system once operating with micro-ehl is not yet known and the plotted behaviour as such is purely conjectural. That this test ran to greater d_o/h^* values than A, D and E again suggests considerable nominal surface interaction, although not as great as that in tests C and F.

Comparison of the pre- and post-run surface roughness values (Table 3.6) shows that 'moderate' running-in has taken place in those tests initiated in the micro-ehl region (B, C and F), whereas 'low' surface modification has taken place in those initiated in the ehl region. Pre- and post-run surface profiles of tests C and D are shown in Fig.3.21.

These differences for the 3:1 tests in failure temperatures, degree of surface interaction before failure, and levels of surface modification or running-in are similar to those noted between the test types of Story on the one hand, and of Bell and Dyson/Rossides on the other. The differences have been reproduced here on a single test machine by altering the sequence of operating conditions of the tests. This indicates that the differences between the original sets of tests were to some extent due to the test conditions and not solely to the test machines used. The fact that the differences between the Story type test, D, and the Bell and Dyson type test, C, were reflected in the other tests starting in the same regimes of lubrication strongly suggests that the differences must be attributed to operation in different regimes of elastohydrodynamic

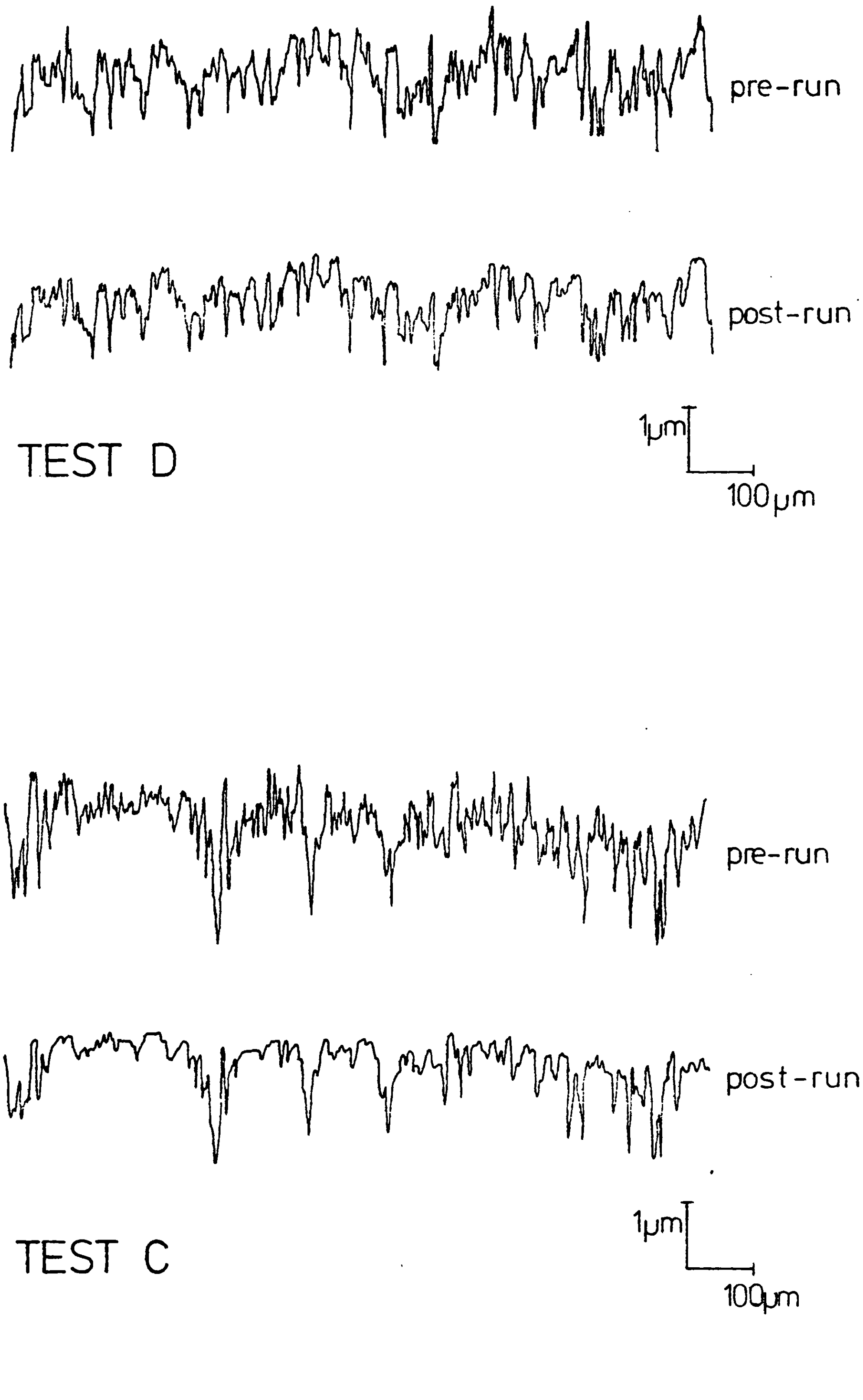

Figure 3.21 Pre and post run surface roughness profiles of tests C and D.

lubrication rather than simply to differences in either loading sequence or initial temperature.

Of the 2:1 tests (Fig.2.20b), G, J and K start in the ehl region. These tests follow similar paths to the equivalent 3:1 test before passing into the mixed regime at similar values of the load group. However, the 2:1 test survived the transition to mixed lubrication and gone on to operate with a very high degree of nominal surface interaction before scuffing.

The 2:1 test histories which start in the micro-ehl region H, I and L, also follow similar paths to the corresponding 3:1 tests but again extend to more severe conditions. The load group and nominal d_o/h^* levels at failure are similar for all the 2:1 tests. The extent of running-in for five of the six tests are also similar, being in the 'moderate' range. The sixth test, L, exhibited 'marked' surface modification.

Obvious differences in failure condition and running-in that can be associated with the different regimes of lubrication are not apparent in the 2:1 tests. Indirect evidence which points to the existence of the predicted regimes can be found in changes of count rate pattern at both speed ratios and in temperature and friction variations for the 2:1 tests.

Count rate data was not available for tests E, F and G. Of the remaining tests, in those starting at 30°C, A, J and D start operation with the surfaces well separated, the '0' pattern emerged at $d_o/h^* < 0.47$, the predicted level for first contact. Possible reasons for these low levels are discussed in Chapter 4. In test A, the sustained pattern, 'X' , also emerges before predicted first contact and the test fails in the next increment. Test D fails before the second pattern has formed. In test J, the sustained pattern occurs at the predicted $h^* = 3\sigma$ level and the test continues for many load increments thereafter.

In contrast, the four high temperature tests start operation with considerable nominal interaction of the surfaces. However contact does not occur immediately and sustained contact does not appear until $d_o/h^* \sim 1$

in test C and $d_o/h^* \sim 1.6$ in the 2:1 tests I and L .

The emergence of corresponding count rate patterns at very different levels of nominal d_o/h^* in the low and high temperature tests, supports the model concept of elastic deformation of the mainscale asperities by hydrodynamic pressue ripples in micro-ehl. In the high temperature tests this would delay the contact of the secondary asperities to thinner films, whereas in the low temperature tests where the asperities remain undeformed, contact would be expected at the d_o/h^* levels observed.

The results of the intermediate temperature, 50°C, tests are not so clear cut. Tests B and H started in the micro-ehl region and E and K in the ehl region. In test K contact is observed around the expected level. For test E for which there is no count rate information, a comparison with count rate data for test El, which had a similar test history, can be made. First contact was observed in test El at a slightly higher level, well into the second increment, in which the discs fall. In tests B and H which start in the micro-ehl region, contact should be delayed to nominal values of $d_o/h^* > 0.47$ but the 0 pattern emerges below the level predicted for the contact of undeformed surfaces, and at thicker nominal films than in the ehl tests El and K. However, the level at which sustained contact is observed in tests B and H is higher than in test K.

These results also highlight a difference between the tests of the two gear ratios. In the 3:1 tests, although the X contact is delayed to more severe conditions in the micro-ehl tests, all the tests fail within two increments of, or before, the X pattern is recorded. All the 2:1 tests run for many increments after sustained contact is recorded, regardless of when contact first occurs.

3.4.4. Test histories, count rate data and variations in friction and temperature.

The friction and temperature variations for the tests at the 2:1 speed ratio also exhibit different behaviour, according to which side of the predicted ehl/micro-ehl transition line they run. This is best seen by comparing tests J and L. Because of the shorter duration of the 3:1 tests such patterns are difficult to detect if they exist at all, and so a corresponding comparison has not been attempted.

In Fig.3.22a and b, the coefficients of friction and the bulk temperatures above the initial temperature at the end of each load stage are plotted against the applied load; the points at which the first O and X contact patterns emerge and at which $h^* = 3\sigma$ are indicated. These points are associated with a difference in form of the friction and temperature variations.

In test L the coefficient of friction is initially 0.04 and rises over the first three increments before levelling to 0.07 for the rest of the test. The first sustained contact pattern is also in the third increment at a calculated d_o/h^* value well above 0.47.

In test J the coefficient of friction is initially 0.035 and decreases to 0.025 in the next increment. The coefficient of friction begins to increase after the third increment. This is also the increment where d_o/h^* reaches 0.47 and where the first sustained contact pattern is observed. The increase in friction is therefore probably due in this case to asperity interaction. The friction coefficient continues to rise until the tenth increment where it levels to 0.06 - 0.07.

These changes are reflected in the temperature variations. The constant level of friction coefficient in test L is reflected in the almost linear change of temperature with load for most of this test. The size of the temperature rise per load stage in test J increases after the third increment. After the tenth increment there is an inflexion in the curve, and for the last few increments the response is almost linear; this was the point at which the coefficient of friction levelled.

Although expected friction levels for the mixed lubrication and micro-ehl regions are not known, the different patterns of friction coefficient and the temperature changes with load are consistent with the

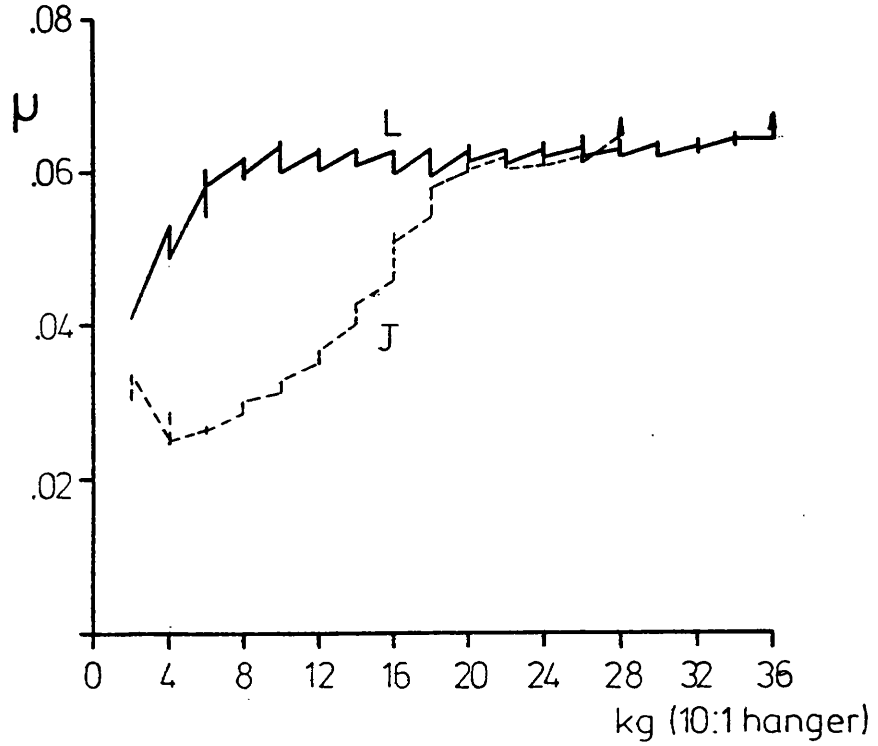

Figure 3.22a Coefficient of friction / load for tests J and L.

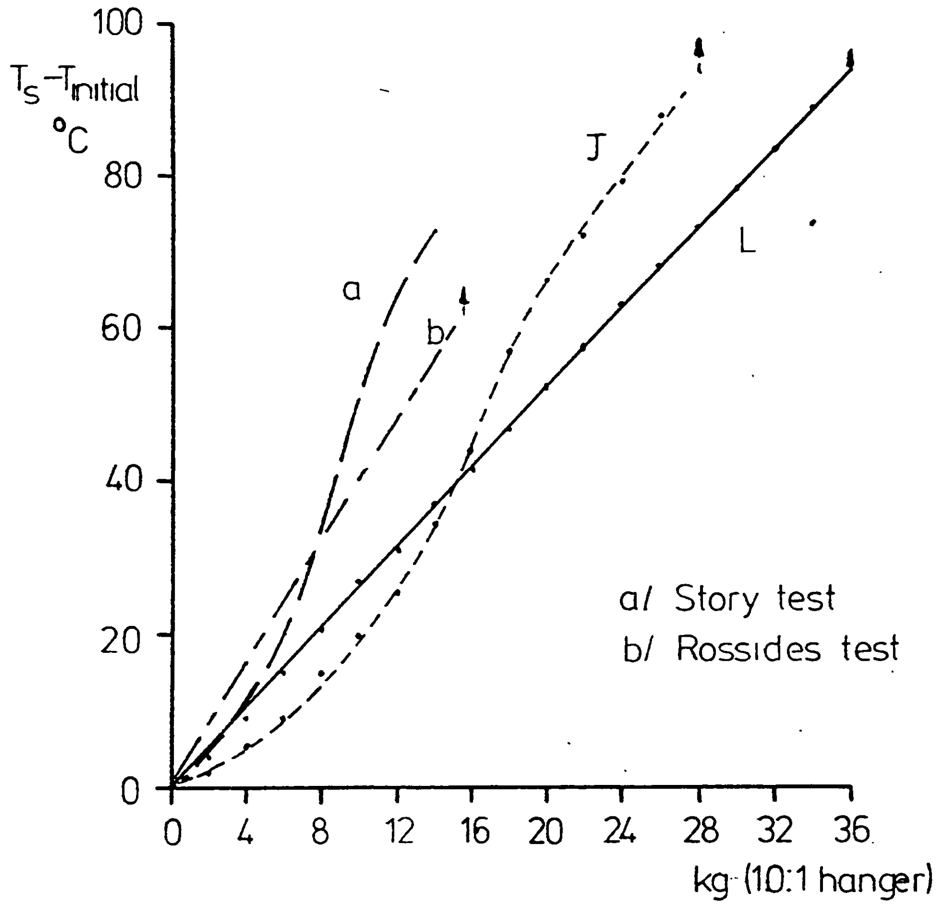

Figure 3.22b Steady state bulk temperature / load for tests J and I and a Rossides and a Story test.

contact results and clearly associate with the predicted changes in mode of lubrication.

Similarly $T - T_{initial}$/load responses are also shown for a test by Story and by Rossides in Fig.3.22b. It is noted that these results have again been reproduced here on one machine by altering the operating conditions and so are not a direct consequence of machine design.

It was observed that the tests of Rossides had a smaller increase in temperature with load and were quicker to equilibrium than the tests of Story. No noticeable difference was found in the time to equilibrium within an increment for the different test types produced here and so this aspect of the temperature variation is likely to be machine dependent.

3.5. Conclusions

The test series has broadly met both of its aims. Tests D and J most closely reproduce the operating conditions of the Story tests and C and I the Rossides tests. At the 3:1 speed ratio, there was a difference in the levels of nominal interaction reached before failure and in the degree or running-in between tests D and C. These were also noted between Story tests at the higher sliding speed and the Rossides tests. The Story type test at the lower sliding speed, test J, also ran to more severe conditions than the test D and had a higher degree of surface modification. A similar observation was made of the Story tests at the two sliding speeds. There was, however, no noticeable variation in the temperature/time response of the tests following an increase in load, of the two simulated test types as in the tests of the original workers, which indicates that this difference was probably due to the test machines used.

In terms of the proposed regimes of lubrication, at the 3:1 ratio the failure of the tests moving from ehl to mixed, soon after nominal contact, compared to the successful operation of those running-in the micro-ehl region to higher nominal levels is consistent with the concept of micro-ehl delaying the contact between the asperities. The 'moderate' running-in of the three tests starting in the micro-ehl region at the 3:1 ratio is further evidence for the two regimes.

At the 2:1 ratio, the nominal interacton at failure and degree of running-in was similar for all the tests, except test L which had 'marked' modification. Unlike the 3:1 tests the similarity of the results offers no support for the existence of different forms of lubrication. However, the nominal interaction at which contact was first indicated by the count rate monitor and the thermal and friction patterns indicate differences in test behaviour at this ratio.

The results suggest that at both slide/roll ratios, different regimes of lubrication are produced and that these are dependent on the operating conditions. Some of the differences in the original tests of Rossides and Story were reproduced by operating in the different regions. In either regime the lower slide/roll ratio favours further running once contact has occurred.

Contact was indicated at higher nominal interaction than expected in the high temperature tests at both speed ratios. In the tests, starting around 50°C, i.e. near the transition line, the contact behaviour is somewhat mixed. The test starting at the lower temperature moved from ehl to mixed and contact was indicated in these tests with thicker films than expected.

The next chapter examines some posible causes of the early contact in the low temperature tests. The remainder of the chapters deal with thermal effects.

CHAPTER 4

COMBINED EFFECTS OF SURFACE ROUGHNESS AND LUBRICANT STARVATION ON FILM THICKNESS IN AN EHL LINE CONTACT

4.1 Introduction

Inconsistencies were noted in the values of film thickness at first contact in some of the tests reported in Chapter 3. The film thickness values in these tests were calculated assuming ideal behaviour but the results implied that the films were thinner. In this chapter the extent to which surface roughness and an inadequate lubrication supply may alter film thickness is explored.

As outlined in Section 2.2, the lubrication of heavily loaded machine components such as gears or roller bearings is a complex process, the analysis of which requires that the equations defining the elastic deformations of the surfaces and the hydrodynamic pressures generated in the fluid film be solved simultaneously, to be compatible. The first solution for elastohydrodynamic lubrication was reported by Grubin (1949). He simplified the problem by assuming that the lubricated surfaces at high loads would adopt the shape produced by the same load in dry contact but that they would be separated by a thin lubricating film. By adopting this film shape the need for simultaneous solutions was removed.

More sophisticated solutions, such as that by Dowson and Higginson (1966), used an iterative procedure to solve simultaneously the two halves of the problem. These were made possible by computerised numerical integration procedures and covered a larger range of conditions than the Grubin analysis, which was limited to heavy loads. They also provided a more accurate representation of the pressure distribution and the film shape within the conjunction. Both types of solution give values of film thickness in good agreement with experiment, for example with measurements by Dyson, Naylor and Wilson (1965).

These solutions made several simplifications about the system. For example, that the surfaces were smooth, the system was isothermal and the inlet region was filled with lubricant. In practical systems these assumptions are not always justified. Later solutions in which these assumptions were individually relaxed, showed that each factor could significantly affect film thickness, pressure distribution and frictional traction compared to the ideal behaviour. For example, Cheng (1967) and Goksem and Hargreaves (1978) investigated the effect of shear heating in the inlet region; Castle and Dowson (1972) and Wolveridge, Baglin and Archard (1971) the effect of starvation, i.e. an inadequate supply of lubricant, whilst Christensen (1969-70), Berthe and Godet (1974) and Chow and Cheng (1976) examined the effect of surface roughness.

In many practical applications, two or more such factors may be operating in tandem. A high speed gear may be subject to both inlet shear heating and starvation, whilst the geometry of a cam and tappet may make it necessary to consider both surface roughness and starvation effects. Goksem and Hargreaves (1978) have provided a solution, by the numerical integration of Reynolds equation, which gives the combined effects of inlet shear heating and starvation on the rolling traction and the film thickness in elastohydrodynamic line contacts.

This chapter concentrates on the changes in the film thickness caused by two of these factors, circumferential surface roughness and starvation acting in combination in an ehl line contact. In Section 4.2 an analytical expression is established to show that effect of circumferential surface roughness on the film thickness in an ehl contact. In Section 4.3, the solution is extended to show the effect of roughness and starvation in combination on the film thickness.

Section 4.4. examines the possible synergistic effects of the two factors and discusses the conditions for which a simpler approach to the problem of combining the effect of the factors is valid.

In the final part of this chapter the possible reduction of the film thickness due to the surface roughness and starvation is examined for those tests reported in Chapter 3 in which contact was registered at thicker films than predicted.

4.2. Film thickness with circumferentially finished surfaces

4.2.1. Method of solution

All surfaces which are involved in lubrication systems are rough due to manufacturing processes. When the average film thickness is much greater than the combined roughness of the surfaces, the behaviour of the system can be predicted quite confidently from smooth surface theories. However, when the film thickness is of the same order of size as the surface irregularities, the roughness of the surface has been shown to have a serious effect on film thickness.

The averaged or stochastic approach to rough surface lubrication was first developed by Tzeng and Saibel (1967) for transverse roughness on a slider bearing. Christensen, (1969-70), incorporated the effects of roughness into Reynolds equation for both longitudinal and transverse roughness. He provided averaged forms of Reynolds equation for both circumferential and transverse roughness. The result was applied to a slider bearing in which the surfaces are considered rigid and the lubricant isoviscous, to show the effect of roughness on film thickness and load bearing capacity. Chow and Cheng (1976) produced an elastohydrodynamic solution by combining Christensen's stochastic treatment of surface roughness, with the Grubin assumption that the macro shape of the body surfaces would be that for dry contact. It uses the full Hertz expression for the film shape and the resulting forms of Reynolds' equation were solved numerically to give the reduced pressure, for a given set of operating conditions. The result was for a single value of non-dimensional film thickness and load.

A solution is presented in this section to show the effect of circumferential roughness on film thickness in elastohydrodynamic line contacts. It also combines the Grubin approach to elastohydrodynamic line contacts with the stochastic treatment of the surface roughness given by Christensen. An approximation to the Hertz film shape, which was developed by Crook (1957), is used. This allows direct integration of the Reynolds equation without recourse to numerical methods.

4.2.2. Form and solution of Reynolds equation

4.2.2.1. Stochastic assumptions and approach to Reynolds equation

For rough surfaces and an isothermal incompressible lubricant, the appropriate form of Reynolds equation is

$$\frac{\partial}{\partial x}\left[\frac{H^3}{12\eta}\frac{\partial p}{\partial x}\right] + \frac{\partial}{\partial y}\left[\frac{H^3}{12\eta}\cdot\frac{\partial p}{\partial y}\right] = -\bar{u}\frac{\partial H}{\partial x} + \frac{\partial H}{\partial t} \qquad (4.1)$$

where H is the local film thickness at any point (x,y). The surfaces being considered are circumferentially ground and random at right angles to the direction of flow, (Fig.4.1).

$$H = h_a(x) + \delta(y)$$

where $h_a(x)$ = average film thickness and $\delta(y)$ = random roughness element = $h_1 + h_2$ where h_1 and h_2 are the local deviation of each surface from the mean level. $\delta(y)$ has a zero mean when averaged over a representative length of the surface. If it is assumed that the roughness forms parallel ridges and valleys superimposed upon a general curvature of the surface in the x direction, then H at any point (x,y) is constant with time so that $\partial H/\partial t = 0$ in eqn.(4.1).

Christensen (1969), to obtain an averaged solution to Reynolds equation, took expectation values of the terms. Taking expectation values of eqn.(4.1) gives

$$\frac{\partial}{\partial x} E\left[\frac{H^3}{12\eta}\cdot\frac{\partial p}{\partial x}\right] + \frac{\partial}{\partial y} E\left[\frac{H^3}{12\eta}\cdot\frac{\partial p}{\partial y}\right] = -\bar{u}\frac{\partial E(H)}{\partial x} \qquad (4.2)$$

where E( ), the expectation operator, is defined as

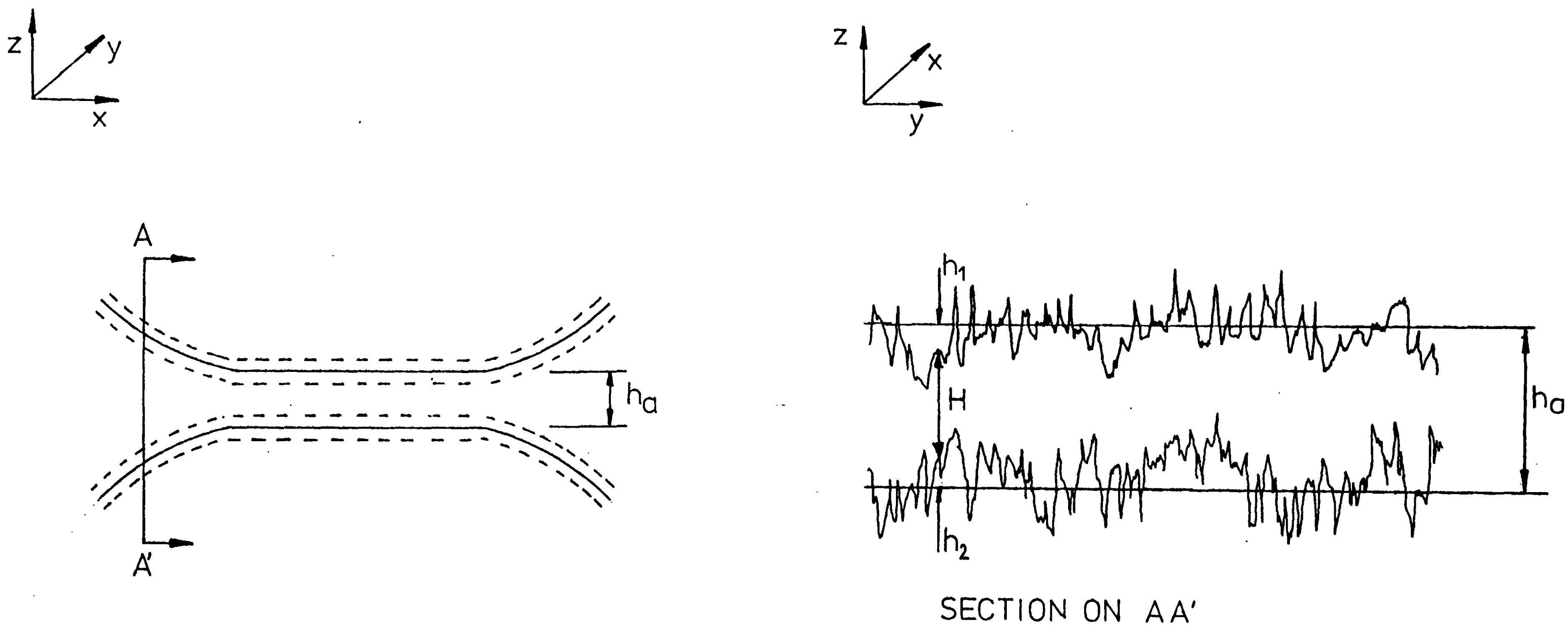

Figure 4.1 A contact with circumferentially ground surfaces with elastohydrodynamic lubrication.

$$E(X) = \int_{-\infty}^{\infty} X.f(X).dX$$

where $f(X)$ is the probability density function of the stochastic variable part of X .

Both the pressure variation in the y direction and the side leakage (flow in the y direction) can be treated in a similar fashion as the film thickness.

Let
$$\frac{1}{\eta}\frac{\partial p}{\partial x} = \frac{1}{\eta}\frac{\partial p_a}{\partial x} + \varepsilon_p$$

where p_a is the averaged pressure gradient and ε_p are the local variations with y of the pressure gradient.

Similarly, let
$$\frac{H^3}{\eta}\frac{\partial p}{\partial y} = Q_{av} + \varepsilon_q$$

where Q_{av} is the average side leakage and ε_q the local variation in the side leakage.

If both ε_p and ε_q are small and have zero mean over the representative length, then their effect can be taken as negligible. Furthermore, if the bearing is infinitely long in the y direction then the net side leakage, $Q_{av} = 0$.

Using these assumptions, eqn.(4.2) reduces to

$$\frac{d}{dx}\left[\frac{dp_a}{dx} \cdot \frac{E(H^3)}{12\eta}\right] = -\bar{u}\,\frac{dE(H)}{dx} \qquad (4.3)$$

If the probability density function of the variable part of H^n, is $f(\delta)$ then

$$E(H^n) = \int_{-\infty}^{\infty} H^n.F(\delta).d\delta$$

which, on replacing H by $(h_a+\delta)$ and expanding, gives

$$E(H^n)=(h_a^n \int_{-\infty}^{\infty} f(\delta)d\delta)+(n\,h_a^{n-1}\int_{-\infty}^{\infty}\delta f(\delta).d\delta) + \left(\frac{n(n-1)}{2}\right).h_a^{n-2}\int_{\infty}^{\infty}\delta^2 f(\delta).d\delta + .. \qquad (4.4)$$

Using the identities (Christensen, 1969)

$$\int_{-\infty}^{\infty} f(\delta)d\delta = 1 ,$$

$$\int_{-\infty}^{\infty} \delta f(\delta)d\delta = 0 \quad \text{as } \delta \text{ has zero mean by definition}$$

$$\int_{-\infty}^{\infty} \delta^r.f(\delta)d\delta = 0 , \quad \text{if } r \text{ is an odd integer and if the surface is symmetric, and}$$

$$\int_{-\infty}^{\infty} \delta^2 f(\delta)d\delta = \sigma^2 \quad \text{, the variance}$$

eqn.(4.4) reduces to

$$E(H) = h_a \qquad \text{for } n = 1$$

and to

$$E(H^3) = h_a^3 + 3\, h_a\sigma^2 \qquad \text{when } n = 3 .$$

Using these identities in eqn.(4.3) gives

$$\frac{d}{dx}\left[\frac{dp_a}{dx}\;\frac{(h_a^3 + 3\sigma^2 h_a)}{12\eta}\right] = -\,\bar{u}\,\frac{dh_a}{dx}$$

On integrating this becomes

$$\frac{dp_a}{dx} = -\,12\eta\,\bar{u}\left(\frac{h_a - h_a^*}{h_a^3 + 3\sigma^2 h_a}\right)$$

or, in terms of the reduced pressure q_a

$$\frac{dq_a}{dx} = -\,12\,\eta_o\bar{u}\left(\frac{h_a - h_a^*}{h_a^3 + 3\sigma^2 h_a}\right) \qquad (4.5)$$

where h_a^* is the average film thickness in the parallel region of the contact.

This form of Reynolds equation for rough surfaces is equivalent to that for smooth surfaces given by eqn.(2.5)

$$\frac{dq}{dx} = -\,12\,\eta_o\bar{u}\left(\frac{h - h^*}{h^3}\right) \qquad (4.6)$$

4.2.2.2. Crook approximation to film shape

For elastohydrodynamic line contacts, the Crook approximation to the Hertz film shape in the converging entry zone is

$$h_a = h_a^* \left[1 + \frac{4\sqrt{2}}{3} \cdot \frac{b^{1/2} \cdot x^{3/2}}{2\,R' h_a^*} \right] \qquad \text{where} \quad \frac{1}{R'} = \frac{1}{R_1} + \frac{1}{R_2}$$

Defining

$$\tau = \left(\frac{4\sqrt{2}}{3}\right)^{2/3} \cdot \frac{b^{1/3} x}{(2\,R' h_a^*)^{2/3}}$$

gives

$$\partial x = \left(\frac{3}{4\sqrt{2}}\right)^{2/3} \cdot \frac{(2\,R' h_a^*)^{2/3}}{b^{1/3}} \cdot d\tau$$

and the Crook approximation to the film shape becomes

$$h_a = h_a^* \,(1 + \tau^{3/2})$$

Substituting these expressions for h_a and dx in eqn.(4.5) gives

$$\frac{dq_a}{d\tau} = \frac{-12\eta_o \bar{u} (R')^{2/3}}{b^{1/3} . (h_a^*)^{4/3}} \cdot \frac{3}{2}^{2/3} \cdot \left[\frac{\tau^{3/2}}{(1+\tau^{3/2})^3 + 3\left(\frac{\sigma}{h_a^*}\right)(1+\tau^{3/2})} \right] \qquad (4.7)$$

$\frac{dq_a}{d\tau}$ is the reduced pressure gradient in the converging entry region at a non-dimensional distance, τ , from the inlet edge of the contact region, for a surface roughness/film thickness ratio σ/h_a^* .

4.2.2.3. Boundary conditions and integration of Reynolds Equation

In a fully flooded contact the inlet zone is assumed to be filled with lubricant and so the pressure begins to build up at a large distance from the edge of the parallel region. The boundary conditions to the Reynolds equation are therefore taken as

$$\tau_i = \infty , \; q_a = 0$$
$$\tau = 0 , \; q_a = \bar{q}_a$$

where $\bar{q}_a$ is the average reduced pressure at the edge of the parallel region.

Integration of eqn.(4.7) between these limits gives

$$\bar{q}_a = - \frac{12\eta_o \bar{u} (R')^{2/3}}{b^{1/3} . (h_a^*)^{4/3}} \cdot \frac{3}{2}^{2/3} \cdot I_a \qquad (4.8)$$

where

$$I_a = \int_{\tau=0}^{\tau_i=\infty} \left[\frac{\tau^{3/2}}{(1+\tau^{3/2})^3 + 3\left(\frac{\sigma}{h_a^*}\right)^2 (1+\tau^{3/2})} \right] d\tau$$

This is integrated in Appendix A1 to give

$$I_a = \frac{4\sqrt{3}\pi}{27} \left(\frac{h_a^*}{\sigma}\right) \left[\left(1 + 3 \frac{\sigma}{h_a^*}\right)^{2} \right)^{1/3} . \cos\left(\frac{2}{3}\right)\tan^{-1}\left(\frac{\sqrt{3}\sigma}{h_a^*}\right) \Big) - 1 \right] \tag{4.9}$$

which, substituted in eqn.(4.8), gives

$$\bar{q}_a = - \frac{12\eta_o \bar{u}(R')^{2/3}}{b^{1/3}.(h_a^*)^{4/3}} . \frac{3^{2/3}}{2} . \frac{4\sqrt{3}\pi}{27} \left(\frac{h_a^*}{\sigma}\right) \left[\left(1 + 3\left(\frac{\sigma}{h_a^*}\right)^2\right)^{1/3} . \cos \frac{2}{3} \tan^{-1}\left(\frac{\sqrt{3}\sigma}{h_a^*}\right) - 1 \right] \tag{4.10}$$

the reduced inlet pressure generated at x=0 with rough surfaces, in terms of the operating variables, and the non-dimensional roughness parameter σ/h_a^*. The equivalent expression for the reduced inlet pressure generated with smooth surfaces can be found by integrating eqn.(4.6) with the same film shape and boundary conditions to give

$$\bar{q} = \frac{12\eta_o \bar{u}(R')^{2/3}}{b^{1/3} (h_a^*)^{4/3}} . \frac{3^{2/3}}{2} . \frac{4\pi}{27\sqrt{3}} \tag{4.11}$$

where $I = \int_0^\infty \frac{\tau^{3/2}}{(1+\tau^{3/2})^3} d\tau = \frac{4\pi}{27\sqrt{3}}$.

Both expressions are for a flooded contact.

4.2.3. Accuracy of the Crook approximation

The Crook approximation for the film shape in the inlet region arises from the first term of the series expansion of the full Hertz expression. Although the simplification allows Reynolds equation to be integrated analytically, it could limit the range of application of the solution to more heavily loaded conditions. $B = \frac{b}{\sqrt{2Rh^*}}$, can be considered as the ratio of the deformation of the surface to the film thickness at the pressure maximum. Increasing values of B indicate increasing severity of hydrodynamic conditions. For smooth surfaces Wolveridge, Baglin and

Archard (1970/71) show that the results using the Crook approximation were accurate to within 5% of those using the full Hertz expression for $B^2 > 4$ (Baglin, 1975).

To assess the validity of the Crook approximation used here with rough surfaces, the solution can be compared to that of Chow and Cheng (1976), who used the full Hertz expression and numerically integrated the resulting form of Reynolds equation. Their results were expressed, for a range of a non-dimensional roughness parameter, as a ratio of the reduced pressure at the edge of the parallel region generated with rough surfaces to the equivalent pressure obtained with smooth surfaces.

Eqns.(4.10) and (4.11) can be combined to give the same ratio, which for constant operating conditions including the average film thickness, reduces to

$$\frac{\bar{q}_a}{\bar{q}} = \frac{I_a}{I} \tag{4.12}$$

This ratio and the equivalent ratio of Chow and Cheng are plotted in Fig.4.2. The ratio formed here is for any operating conditions but the accuracy of the Crook approximation decreases at less severe conditions. The ratio of Chow and Cheng was for the operating condition of non-dimensional load, $W' = w/E'R = 3 \times 10^{-5}$ and a non-dimensional film thickness $Ho = h_a/R = 10^{-5}$. These conditions correspond to $B^2 = 3.27$, which is only just outside the limit given above for the Crook approximation. As can be seen from the graph, excellent agreement exists between the two solutions.

4.2.4. Film thickness formula

In elastohydrodynamic lubrication the pressures throughout the conjunction must simultaneously satisfy both the elastic deformation and Reynolds' equation. It was shown in Section 2.2.3 that for smooth surfaces, for the elastic pressure distributions to be matched by the hydrodynamic pressures over most of the contact region which results in a parallel film. then $\bar{q}$ must equal $1/\alpha$. This requirement for elastohydrodynamic

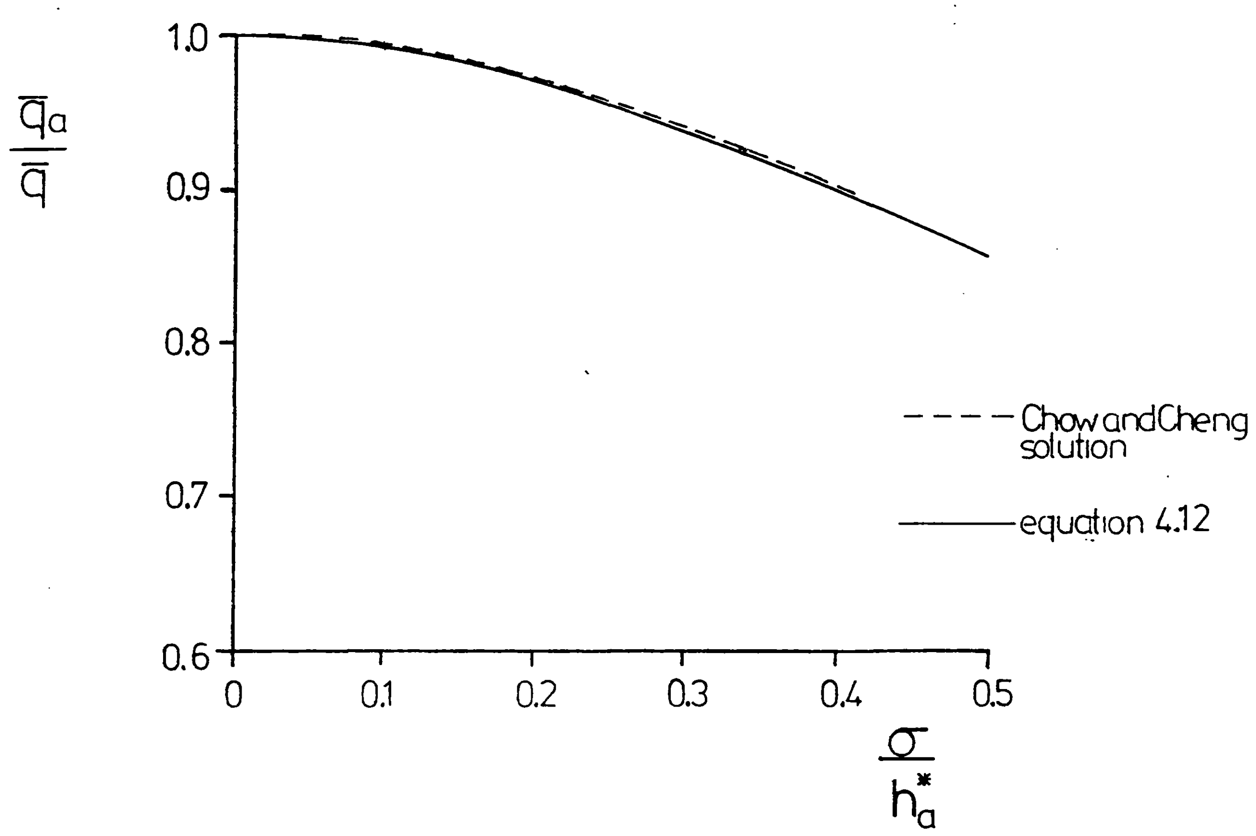

Figure 4.2 Variation of reduced inlet pressure ratio with σ/h_a^*

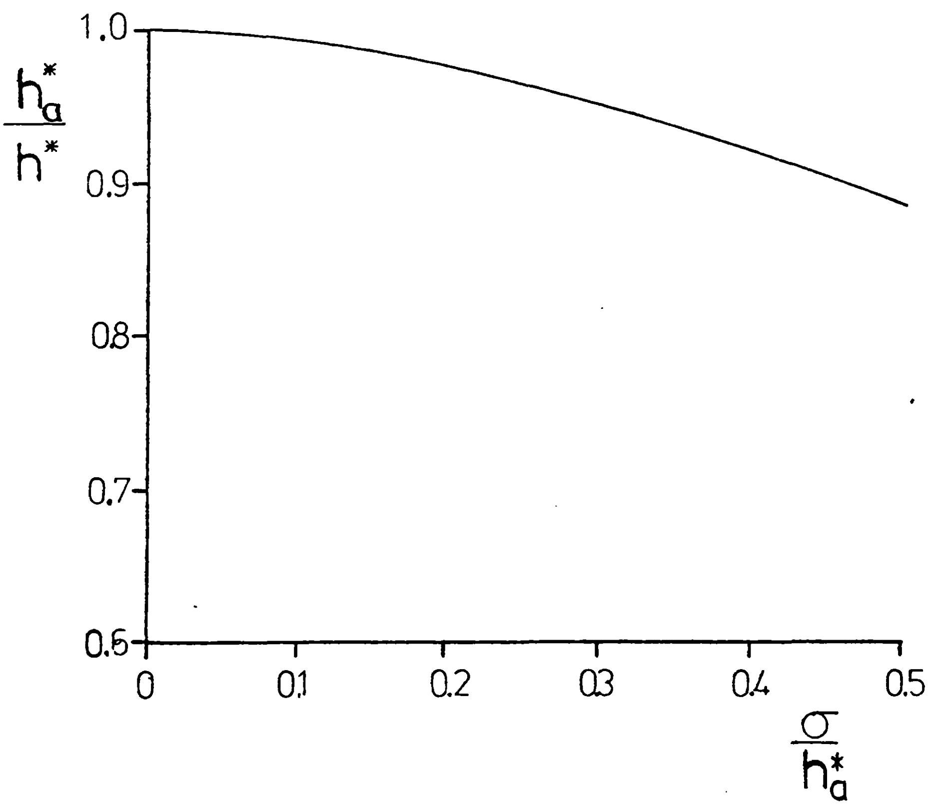

Figure 4.3 Variation of film thickness ratio with σ/h_a^*

lubrication is not changed by the inclusion of surface roughness. Fig.4.2 shows that increasing surface roughness at a constant average film thickness, causes $\bar{q}_a$ to drop below $1/\alpha$. p would then reduce substantially and the assumption of near parallel surfaces would become invalid. Instead it seems likely that as lubrication conditions become more hostile the domination of elastic effects will increase and the film thickness move increasingly towards parallelism. The conclusion is then that $\bar{q}_a$ must remain close to $1/\alpha$ for any degree of roughness to maintain a parallel film and this condition is achieved by a change in the film thickness.

Rearrangement of eqns.(4.10) and (4.11) using the condition

$$\bar{q}_a = \bar{q} = 1/\alpha$$

gives for rough surfaces

$$h_a^* = \left\{\frac{12\eta_0\bar{u}(R')^{2/3}}{b^{1/3}} \cdot \frac{3}{2}^{2/3} \cdot \alpha \cdot I_a\right\}^{3/4} \tag{4.13}$$

and for smooth surfaces

$$h^* = \left\{\frac{12\eta_0\bar{u}(R')^{2/3}}{b^{1/3}} \cdot \frac{3}{2}^{2/3} \cdot \alpha \cdot I\right\}^{3/4} \tag{4.14}$$

For otherwise constant operating conditions, eqns.(4.13) and (4.14) can be combined to give

$$\frac{h_a^*}{h^*} = \left[\frac{I_a}{I}\right]^{3/4} \tag{4.15}$$

which is the ratio of the average film thickness formed with rough surfaces to the film thickness formed with smooth surfaces as a function of the non-dimensional roughness parameter σ/h_a^* . This ratio is plotted against σ/h_a^* in Fig.4.3.

As the ratio is a function of the unknown film thickness h_a^* it cannot be used directly to find the film thickness for conjunctions with a known surface roughness. It is more convenient if the ratio is expressed as a function of the smooth surface film thickness h^* , which can be calculated for a given set of conditions by the Dowson and Higginson film thickness formula.

Using the simple iteration procedure, outlined in Fig.4.4, the film thickness ratio was converted to a function of the parameter σ/h^*.

The 'corrected' ratio is plotted in Fig.4.5, from which the reduction ratio for any roughness can be found directly using the equivalent smooth surface film thickness.

4.3. Effect of roughness and starvation in combination

4.3.1. Introduction

In the solution of Reynolds equation in the previous section, it was assumed that the inlet region of the contact was completely filled with lubricant, in which case the pressure begins to build up in the inlet region at a large distance from the contact area. This is the fully flooded condition for which the upper limit in the integration of Reynolds equation is $p=0$ at $x=\infty$.

When the inlet region is partially filled with lubricant, the pressure generation begins closer to the edge of the parallel contact area, (Fig.4.6). This is the starved condition. The change in pressure distribution may, in turn, alter the film thickness and load carrying capacity of the system. Solutions presented to show the effect of starvation have been mainly numerical. For example, for the classical regime, Boness (1966) and Dowson and Whitaker (1965), for a rigid cylinder loaded against a plane surface, computed the reduction in load carrying capacity. Results were presented for a range of the non-dimensional inlet parameter and for a chosen value of R/h_o.

For elastohydrodynamic line contacts Orcutt and Cheng (1966) produced a solution to give the film thickness for a single operating condition for a range of inlet positions. Castle & Dowson (1972), also by numerical procedure, provided a set of solutions for the film thickness, pressure distribution and rolling traction for a range of operating conditions and inlet positions.

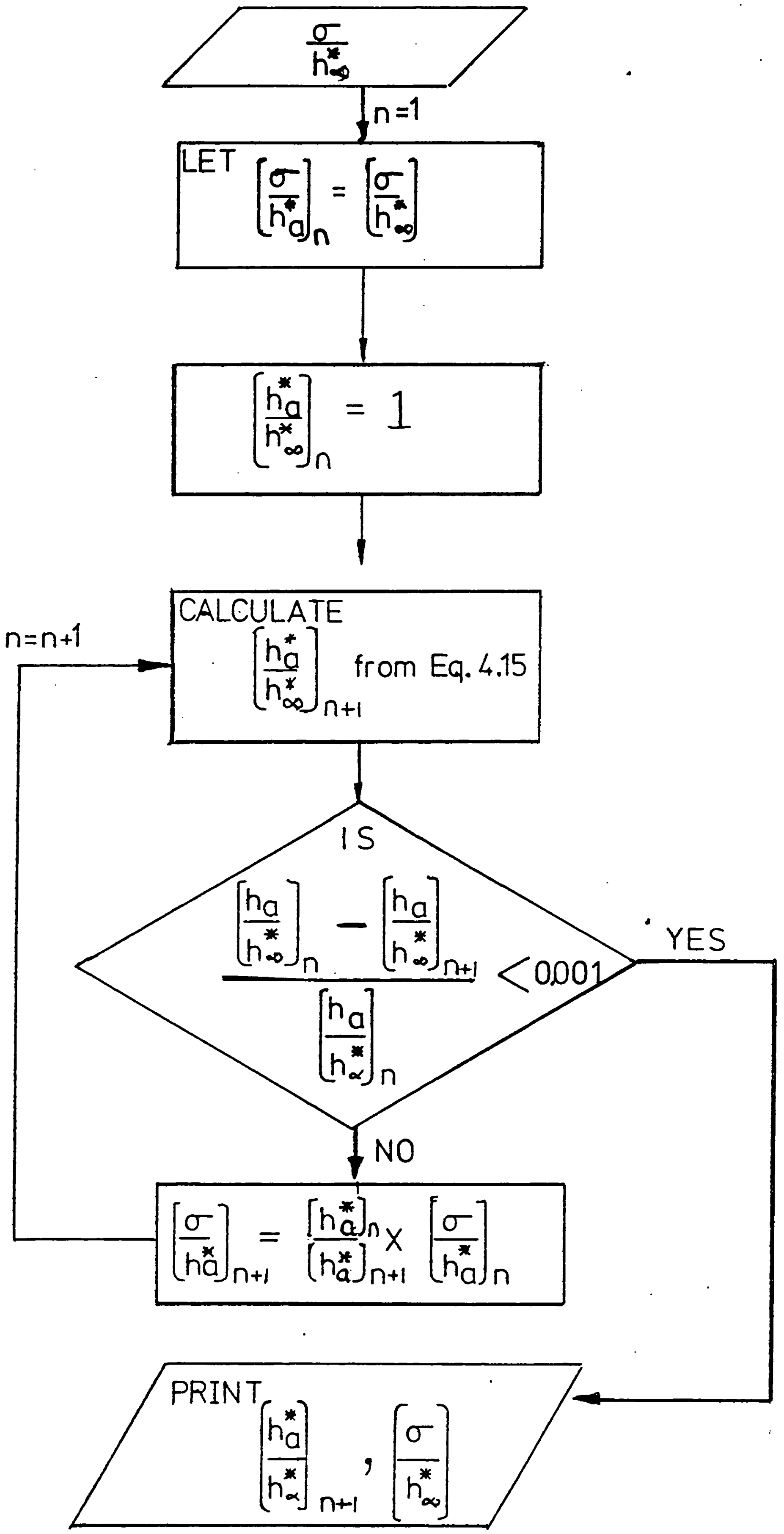

Figure 4.4 Scheme to convert $\left[\frac{h^*_a}{h^*_\infty}\right]$ from a function of $\left[\frac{\sigma}{h^*_a}\right]$ to a function of $\left[\frac{\sigma}{h^*_\infty}\right]$

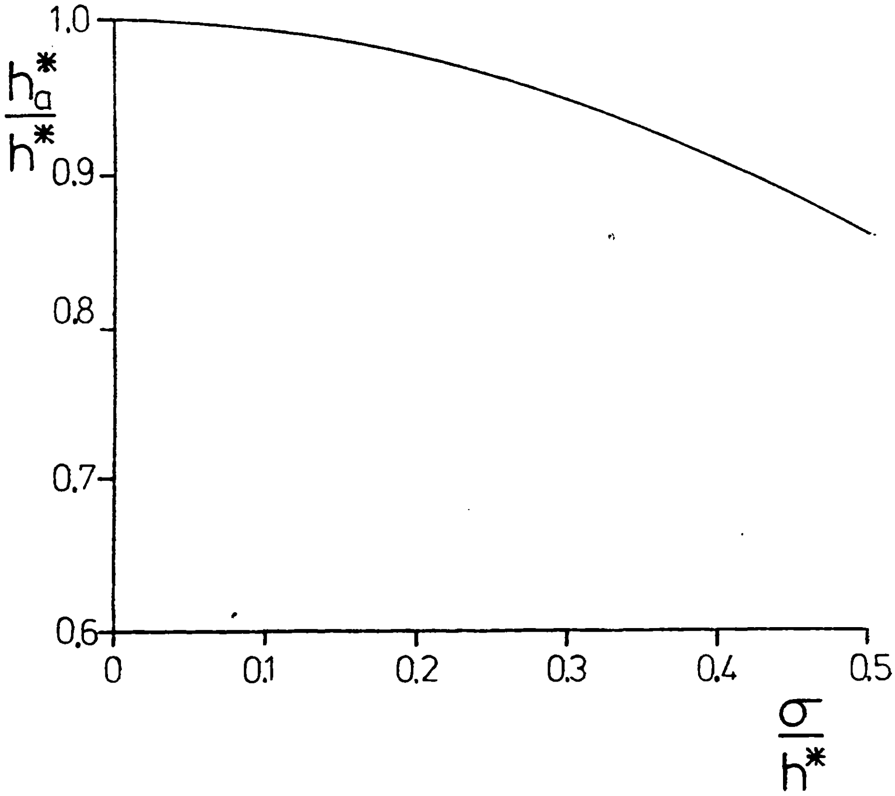

Figure 4.5 Variation of film thickness ratio with σ/h^*

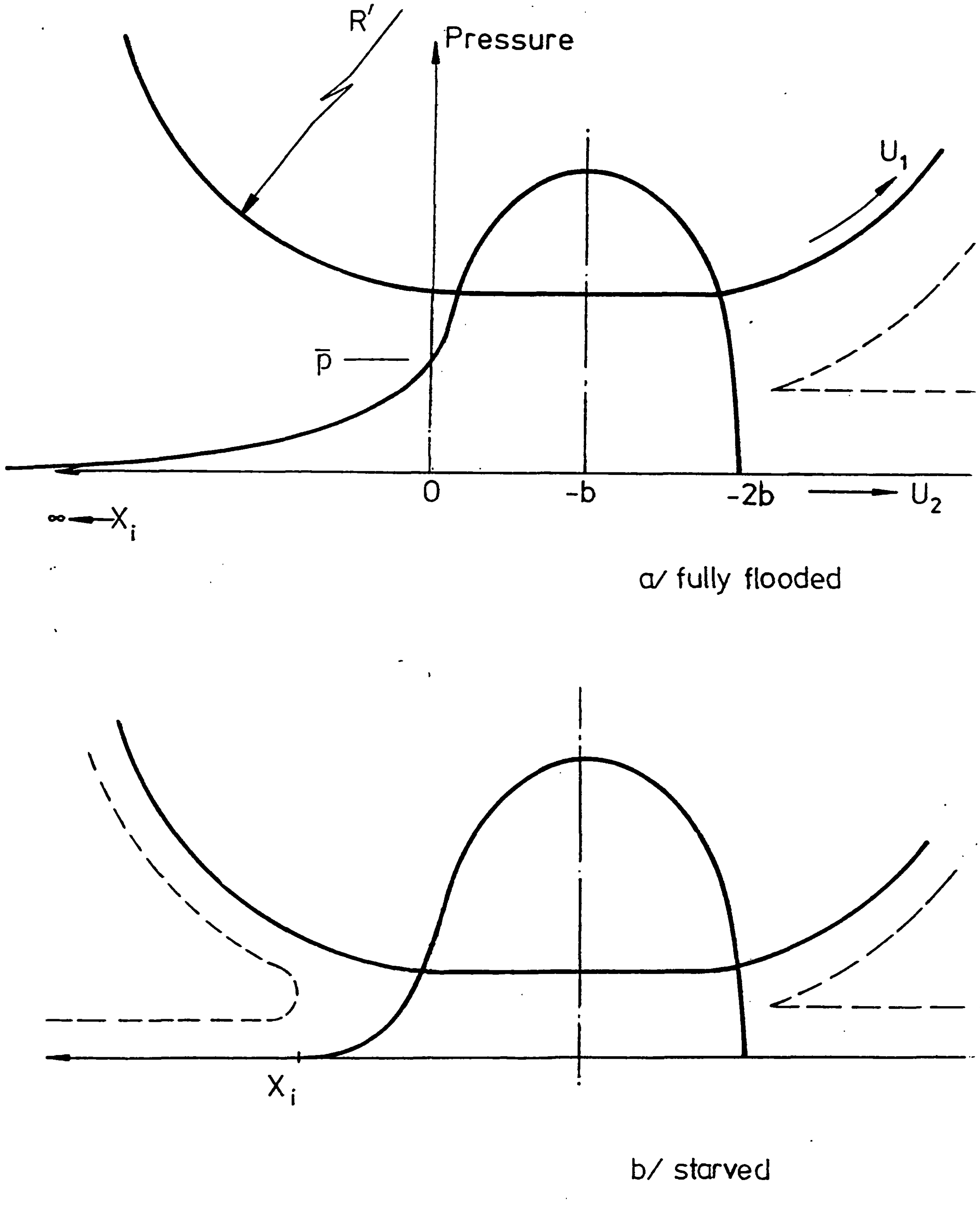

Figure 4.6 The effect of inlet boundary position on film thickness and pressure distribution.

Wolveridge, Baglin & Archard (1971) presented a semi-analytical solution to both the classical and the ehl problem. They compared the starved to the equivalent fully flooded film thickness and plotted this against a non-dimensional starvation parameter, which included the inlet boundary position. The effects of starvation could be expressed, for any operating condition, as a single function of the inlet boundary parameter. The specific results from Castle and Dowson's numerical procedure were, when normalised in the appropriate manner, in excellent agreement with those from this generalised semi-analytical solution.

An approach to the starvation problem similar to that of Wolveridge, Baglin & Archard can be combined with the form of Reynolds equation for rough surfaces from Section 4.2, to find the film thickness in a starved conjunction with rough surfaces.

4.3.2. Solution of Reynolds equation for rough surfaces and a starved inlet

For a starved contact the limits of integration are

$$\tau = \tau_i \ , \ q_{a\tau} = 0$$
$$\tau = 0 \ , \ q_{a\tau} = \bar{q}_{a\tau}$$

where τ_i is the non-dimensional inlet distance parameter.

Reynolds equation for rough surfaces, eqn.(4.7), integrated between these boundary conditions, gives

$$\bar{q}_{a\tau} = \frac{12\eta_o \bar{u}(R')^{2/3}}{b^{1/3}\,(h^*_{a\tau})^{4/3}} \cdot \frac{3}{2}^{2/3} \cdot I_{a\tau} \tag{4.16}$$

where

$$I_{a\tau} = \int_{\tau=0}^{\tau=\tau_i} \left[\frac{\tau^{3/2}}{(1+\tau^{3/2})^3 + 3\left(\frac{\sigma}{h^*_{a\tau}}\right)^2 (1+\tau^{3/2})} \right] d\tau$$

This is integrated in Appendix A1. The resulting expression for $I_{a\tau}$ is a function of τ_i and $\sigma/h^*_{a\tau}$ but due to its length is not repeated here.

The equivalent expression to eqn.(4.16) for a fully flooded conjunction with smooth surfaces was given by eqn.(4.11).

The condition for effective ehl used to find the film thickness for fully flooded rough and smooth surfaces in Section 4.2 can be extended to starved contact with rough surfaces, i.e.

$$\bar{q}_{a\tau} = \bar{q}_a = \bar{q} = 1/\alpha \ .$$

Using this condition and assuming constant operating conditions, eqns.(4.16) and (4.11) can be combined to give

$$\frac{h^*_{a\tau}}{h^*} = \left\{\frac{I_{a\tau}}{I}\right\} \qquad \text{where} \quad I_{a\tau} = f\left(\frac{\sigma}{h^*_{a\tau}} \ , \ \tau_i\right) \tag{4.17}$$

$h^*_{a\tau}/h^*$ is the ratio of the film thickness with rough surfaces and a starved inlet to that with smooth surfaces and a fully flooded inlet, i.e. ideal behaviour. In Fig.4.7, this ratio is plotted against τ_i, the inlet position parameter, for a range of values of the roughness parameter, $\sigma/h^*_{a\tau}$.

A relaxation of either of these factors reverts the solution to the appropriate single factor solution (Appendix A1). As the starvation parameters tend towards infinity, the ratio reverts to that for the fully flooded rough contacts given in Section 4.2. These are the asymptotic values shown in Fig.4.7. As the roughness parameter tends to zero the ratio tends to that for a starved contact with smooth surfaces given by Wolveridge et al., which is also plotted in Fig.4.7.

In eqn.(4.17) both the roughness parameter and the inlet parameter are functions of the unknown film thickness $h^*_{a\tau}$, which, as with the ratio given by eqn.(4.15), limits the application of the solution.

The same problem was faced by Wolveridge et al in their study of starvation effects on film thickness with smooth rollers. They were able to redefine their inlet parameter by physical reasoning to a second parameter, ψ_i, which was a function of the fully flooded film thickness. Due to the more complex nature of the expression for $I_{a\tau}$, compared to the equivalent

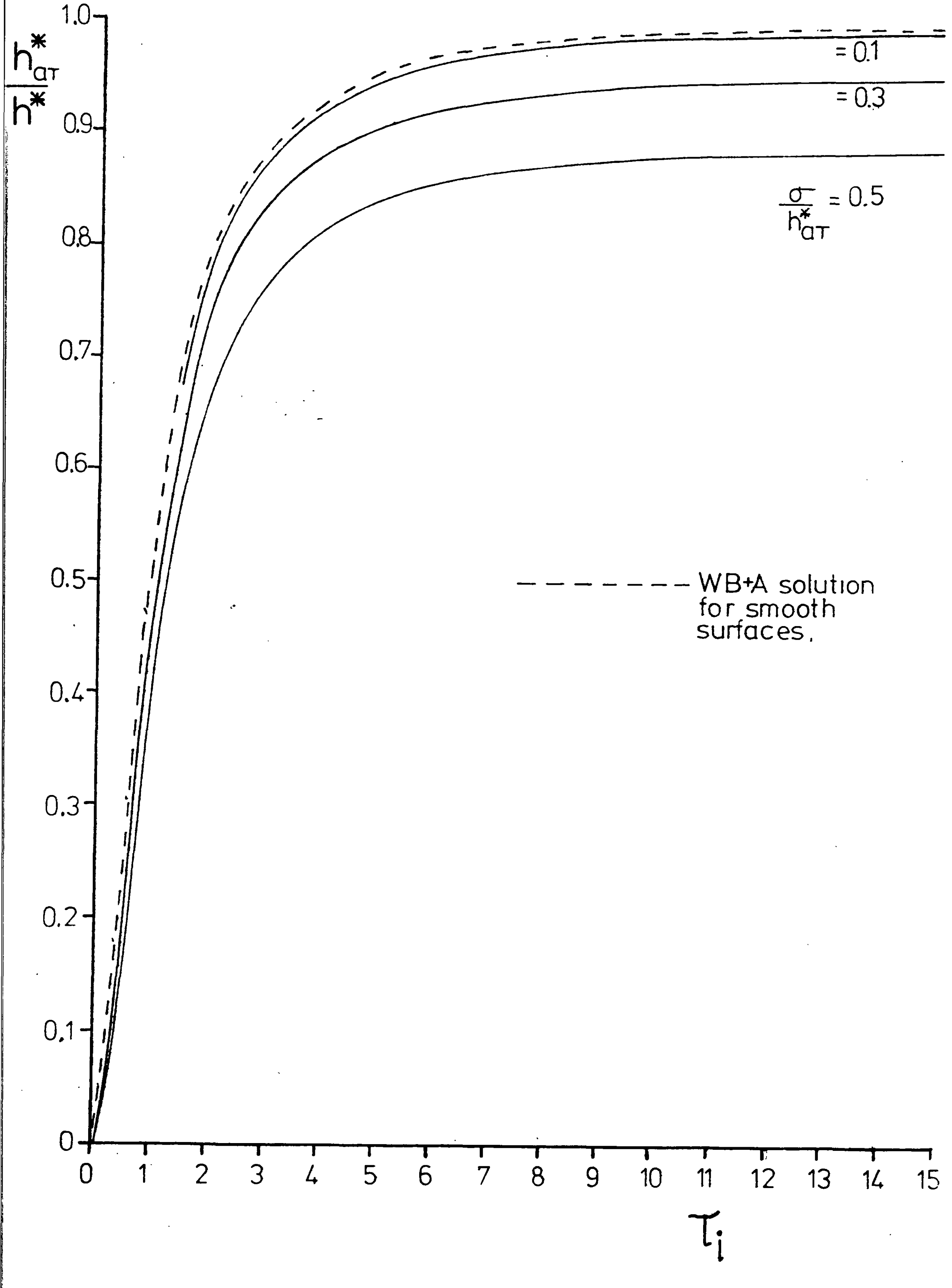

Figure 4.7 Variation of $\frac{h^*_{a\tau}}{h^*}$ with inlet position parameter τ_i, for a range of $\sigma/h^*_{a\tau}$

expression for smooth surfaces by Wolveridge et al, the same approach is not possible here. Instead the iterative scheme introduced in Section 4.2.4 has been extended to convert both the roughness and the inlet position parameters. This iterative scheme is outlined in Fig.4.8. The film thickness ratio becomes a function of the roughness parameter, σ/h^* and $\bar{\Psi}_i$ where $\bar{\Psi}_i = \left(\frac{4\sqrt{2}}{3}\right)^{2/3} \cdot \frac{b^{1/3} x_i}{(2R'h^*)^{2/3}} = \left(\frac{4\sqrt{2}}{3}\right)^{2/3} \cdot \Psi_i$ where Ψ_i is the inlet position parameter used by Wolveridge et al. The film thickness ratio $h^*_{a\tau}/h^*$ is replotted in Fig.4.9 in terms of these parameters.

If the operating conditions are known, the ideal film thickness h^* can be calculated from the Dowson and Higginson equation. This can then be used with the inlet boundary position and surface roughness to give $\bar{\Psi}_i$ and σ/h^*. The film thickness ratio of the reduced to the ideal film thickness can then be found directly from Fig.4.9.

As the ratio of the roughness to the film thickness increases, a limit occurs at which overlapping and contact between the higher asperities and the opposite surface will be expected. The system would then be operating in mixed lubrication. This solution has been derived for no contact conditions. The results have been presented for $\sigma/h^* \to 0$ to values of σ/h^* which would result in a small overlap of the opposing asperities for a typical ground surface. If the resulting values of corrected film thickness are such that they predict a large degree of surface interaction then these values will be nominal, i.e. the values which result if the surfaces could overlap without interference. Use of the solution at higher values of σ/h^* should therefore be cautious.

4.4. Synergistic effects

The combined effect of surface roughness and lubricant starvation on the film thickness in an elastohydrodynamic line contact has been found. In this section the synergistic effect on film thickness of these two factors is examined. The effect of roughness alone on film thickness was found in Section 4.2. A film thickness ratio was formed as a function

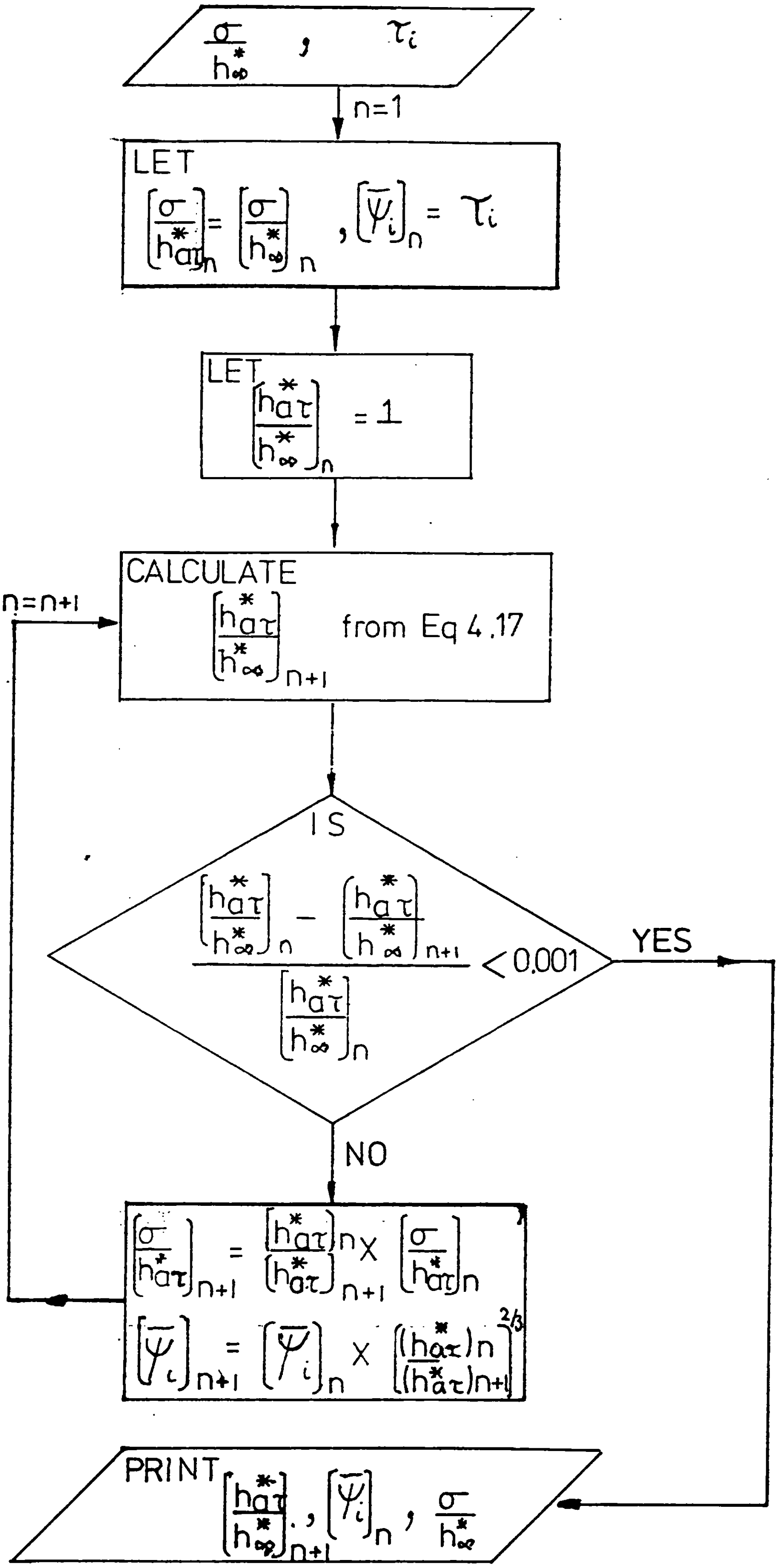

Figure 4.8 Iterative scheme to convert $\left[\frac{h^*_{a\tau}}{h^*_\infty}\right]$ from a function of $h^*_{a\tau}$ to a function of h^*_∞

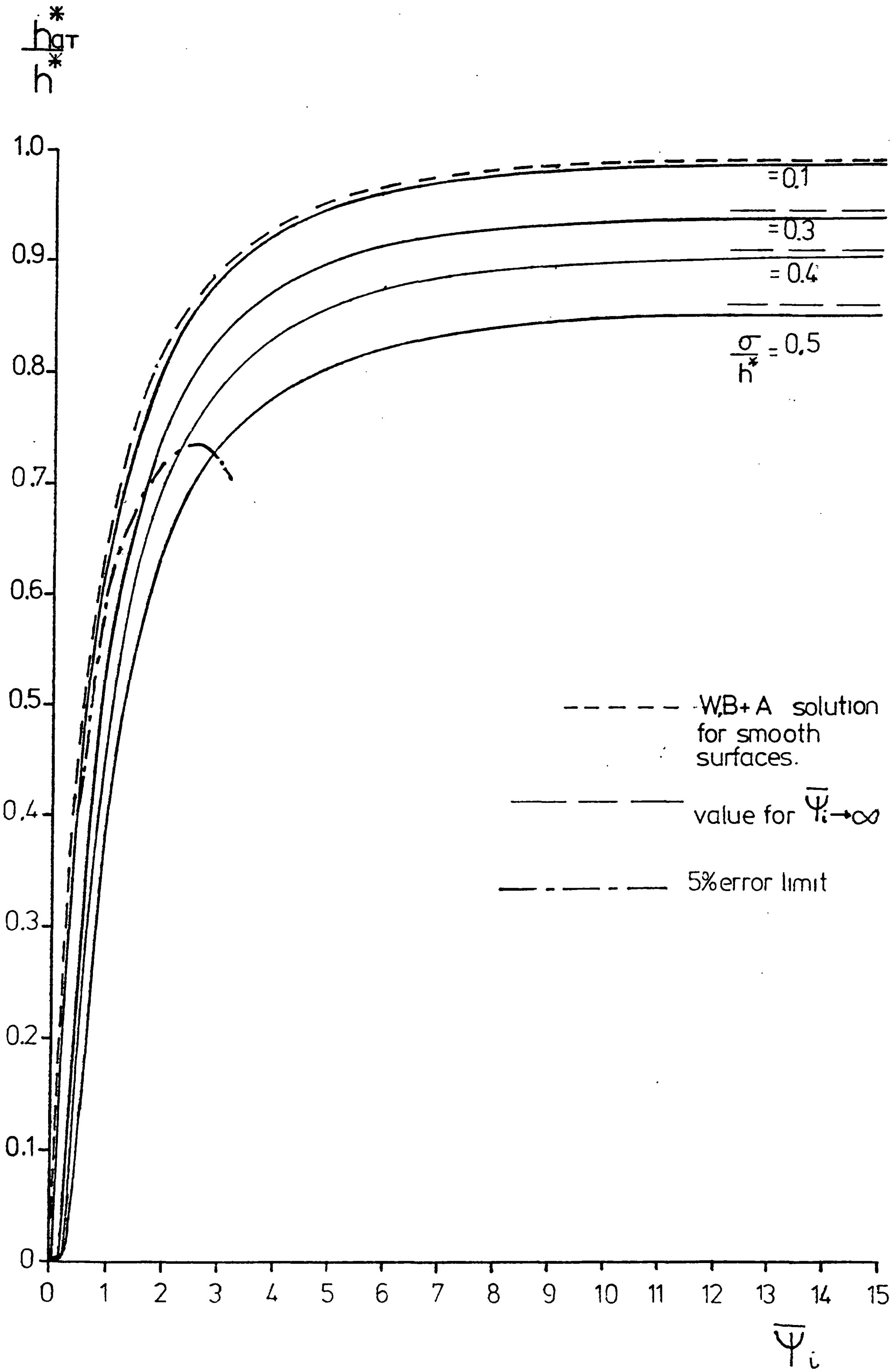

Figure 4.9 Variation of film thickness ratio $\frac{h^*_{aT}}{h^*}$ with inlet position $\overline{\Psi}_i$ for a range of σ/h^*

of the roughness parameter σ/h^* . A film thickness ratio to show the effect of starvation with smooth rollers was given by Wolveridge et al. Simply multiplying the two ratios for the single factor solutions together gives a new ratio - $(h^*_{a\tau} / h^*)_{sep}$ - the effect on film thickness of both factors acting separately in the same system.

This new ratio is plotted in Fig.4.10. The two ratios, that for combined effects and that for the two factors acting separately are similar at higher values of $\bar{\Psi}_i$. With increasing starvation, i.e. $\bar{\Psi}_i$ decreasing, the reduction ratio for the two factors combined decreases more rapidly than the ratio obtained from considering the two factors acting separately. The limit for the two ratios agreeing to within 5% is shown.

Several factors were mentioned at the outset of this chapter, i.e. surface roughness, starvation, and inlet shear heating, which could affect film thickness. The more factors that are included makes the solution of Reynolds equation more difficult. This chapter has discussed the interaction between roughness and starvation. The solution for the combined effects of inlet shear heating and starvation has been provided by Goskem & Hargreaves (1978). To this author's knowledge there is no solution available for the missing two factor solution, that for inlet shear heating and surface roughness. This solution should be possible and would be of a similar complexity to that presented here. In theory, a three factor solution, which would include roughness, starvation and inlet shear heating effects should be possible, but the analytical solution would be very tedious and a large number of charts would be needed to cover the combinations of conditions met in practice. It has been shown how simple multiplication of two single factor solutions serves as a reasonable approximation to the full solution if the effect of each factor is not too severe. For example, for the solution of combined roughness and starvation effects, the ratio from the two single factor solutions was within 5%, of the full solution for values of $\frac{h^*_{a\tau}}{h^*}$ of $1 \rightarrow 0.4$ for $\sigma/h^* = 0.1$, and of $1 \rightarrow 0.7$

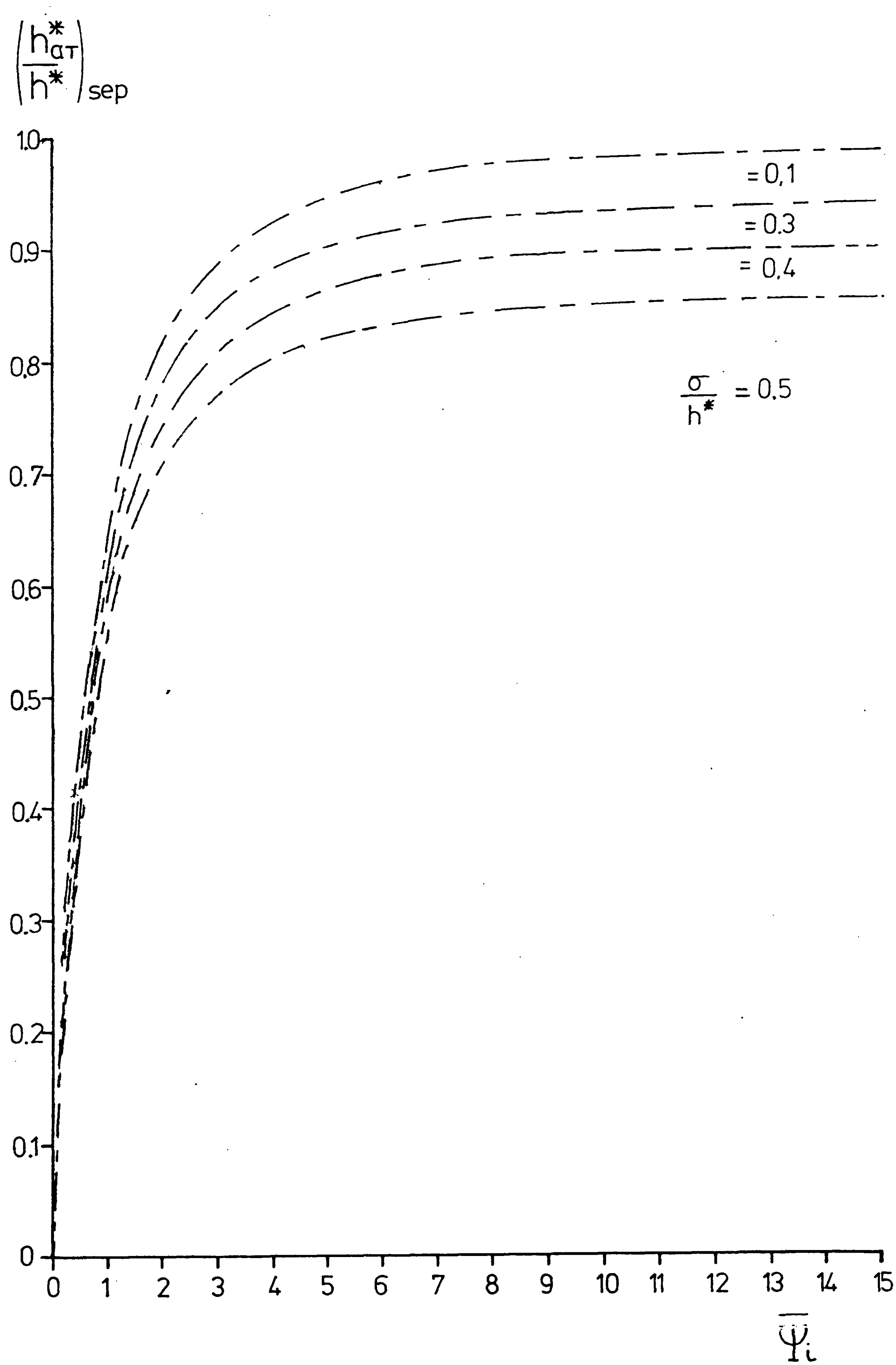

Figure 4.10 Variation of film thickness ratio $\left[\frac{h^*_{a\tau}}{h^*_{\infty}}\right]_{sep}$ from combination of separate solutions.

for a σ/h^* ratio of 0.5. It is expected that a three factor solution formed by an extension of this process using existing single factor solutions would give a reasonable approximation to the full solution again, providing the effect of each factor was not too severe.

4.5. Correction factors applied to test film thickness values

For those tests reported in Chapter 3 which progressed from ehl to mixed lubrication, i.e. with undeformed asperities, first contact was expected between the opposing surface asperities when $h^* = 3\sigma'$. Surface roughness and film thickness values at which the O and X contact patterns were first observed are given for three of these tests, tests A, D and J, in Table 4.1. The ratio of σ/h^* at contact in these tests was less than expected and there are several possible causes for this:

a) Analytical solutions of elastohydrodynamic lubrication give the thickness of films, h^*, which are assumed parallel in the contact region. In practice the film is not exactly parallel. A narrowing exists at the rear of the conjunction. The film thickness in this region h_{min} is of the order, $h_{min} \sim 0.8\, h^*$. Contact between the surfaces would be expected to occur first in this region, i.e. at $h_{min} = 3\sigma'$ or $h^* = 3.75\sigma'$. Comparison with the values of σ'/h^* for first contact in Table 4.1 shows that although this correction improves the correlation between the experimental and expected values, there is still a discrepancy between the values.

b) The properties of the oil in the inlet region are determined by the quasi stationary surface temperature of the discs, (Archard & Kirk (1961)). The film thickness values for the tests reported in Chapter 3 were calculated using the viscosity of the fluid at the temperature measured by a thermocouple embedded 2 mm below the discs surface. It is shown in Section 6.7 that in tests A, D and J, at the conditions at first contact, the temperatures 2 mm below

TEST	A	D	J
Ra rough disc µm	0.303	0.36	0.301
Ra smooth disc µm	0.095	0.107	0.094
Ra′ µm	0.317	0.376	0.315
σ' =1.25 Ra′	0.397	0.469	0.394
CONTACT LEVELS	O X	O	O X
σ/h^* at contact levels	0.124 0.209	0.178	0.151 0.298
h^* at contact levels µm	3.21 (~8σ) 1.9 (~4.8σ)	2.63 (~5.6σ)	2.6 (~6.6σ) 1.32 (~3.4σ)
Expected h^* at first contact (=3σ) µm	1.19	1.41	1.18

Table 4.1 Surface roughness and /h values at first (O) and sustained (X) contact levels for tests A, D and J.

the surface were 1°C below those at the surface. This small error in the temperature is not sufficient to account for the discrepancies between the measured and predicted values of σ/h^* .

c) With two rough surfaces, the combined roughness value Ra', is found from the individual roughness values using the relationship $Ra' = \sqrt{Ra_1^2 + Ra_2^2}$. For a semi-gaussian distribution of surface heights the combined standard deviation of the surface is given by $\sigma' = 1.25 \times Ra'$. Halling & Nuri (1985) has shown that this distribution has a cut off of 3σ , i.e. the maximum peak to valley height of the surface is 6σ . As the maximum peak heights of the disc surfaces could not be obtained with the surface roughness measurement equipment available, these relationships were used to give values of σ and maximum peak height from the measured Ra values of the discs.

To show whether these assumptions gave reasonable values of peak heights for the disc surfaces, the peak to valley heights were measured from the surface profile traces from a number of the discs. The error between the measured and assumed peak heights was small (< 3%). The assumptions used therefore seem valid for the present case and would not be the source of error in the σ/h^* values at contact. (See Table 4.2)

d) The film thickness values were calculated from the Dowson & Higginson film thickness formula. This is strictly only applicable when surfaces are smooth, the inlet filled with lubricant and when there is no inlet shear heating. The possible reduction of film thickness due to the circumferential surface roughness and to roughness and starvation combined for tests A, D and J can be found from the results of Sections 4.2 and 4.3.

The roughness parameters σ/h^* at the contact levels given in Table 4.1 can be used with Fig.4.5 to give the film thickness ratio

TEST	TEST A	TEST D	TEST J
Ra (rough disc) μm	0.303	0.36	0.301
σ (=1.25xRa) μm	0.378	0.45	0.376
MAX PEAK HEIGHT (=3σ) μm	1.136	1.35	1.129
MAX PEAK-VALLEY HEIGHT μm (measured from traces)	2.2045	2.75	2.27
MAX PEAK HEIGHT μm (from centre line)	1.1023	1.375	1.135
MAX PEAK HEIGHT* μm (in terms of σ)	3.24σ	3.05σ	3.02σ

* (where σ = 1.25 measured Ra value)

Table 4.2 Comparison of peak heights from
i/assumed relationship - peak heights =3σ and
ii/ measurement from surface roughness profiles.

h_a^*/h^*. This ratio, the corrected value of film thickness h_a^* and σ/h_a^* are given in Table 4.3 for the three tests. The change in the film thickness due to the roughness effects alone is small and does not make up the discrepancy between the predicted and experimental values of film thickness at first contact.

The degree of starvation which may exist in a system is less easily found. Starvation is usually associated with an inadequate supply of lubricant in the inlet zone. In the two disc machine the volume of lubricant being supplied to the discs was thought to be sufficient to prevent this problem. However, other workers have investigated the problem of inlet position. It has been shown that an adequate lubricant supply does not always guarantee fully flooded behaviour.

The position of the meniscus (Fig.4.6) was explained by Lauder (1965) as that where zero reverse flow occurs. In this position the Couette type flow, which is caused by the difference in the surface speeds, is equal to but in the opposite direction to the Poiseille flow - the backflow caused by the pressure gradient generated in the converging inlet wedge. At the time this boundary condition was not generally accepted but was regarded as a particular feature of Lauder's apparatus.

However, Saman (1974) observed that following an initial charge of lubricant, a meniscus was formed in the inlet region with excess lubricant being stored in bands around the edge of the discs. Following a change of operating conditions the lubricant migrated either to or from the side bands until a new meniscus position was established. The inlet position may therefore not be determined solely by the lubricant supply.

The observations made by Saman, prompted Dowson, Saman and Toyoda (1979) to reappraise the boundary condition originally proposed by

TEST	A	D	J
σ' μm	0.397	0.469	0.394
CONTACT LEVELS	O X	O X	O X
σ'/h^* at contact levels	0.124 0.209	0.178	0.151 0.298
h_a^*/h^* (from Fig 4.5)	0.99 0.976	0.983	0.988 0.948
σ'/h_a	0.125 0.214	0.181	0.153 0.314
h_a^*	$\sim 8\sigma$ $\sim 4.7\sigma$	$\sim 5.5\sigma$	$\sim 6.5\sigma$ $\sim 3.2\sigma$
$\overline{\Psi}_i$	1.05	1.05	1.163
$h_{a\tau}^*/h^*$	0.63 0.62	0.625	0.66 0.61
$h_{a\tau}^*$	$\sim 5\sigma$ $\sim 3\sigma$	$\sim 3.5\sigma$	$\sim 4.3\sigma$ $\sim 2\sigma$

Table 4.3 Corrected film thickness values due to i/ roughness and ii/ roughness and starvation effects.

Lauder. Using the zero reverse flow condition they showed that the non-dimensional inlet position was a function of the surface speeds. Whether this boundary condition is appropriate for the present machine is not known but will be used here to demonstrate the possible effects of starvation on the experimental values of film thickness using the two disc machine.

The method to find the inlet position from the work of Dowson, Saman and Toyoda is given in Appendix A2. The resulting non-dimensional inlet boundary parameters, $\overline{\Psi}_i$, are given in Table 4.3. Using these values of $\overline{\Psi}_i$ and the roughness parameters σ/h^*, the film thickness ratios $h^*_{a\tau}/h^*$ can be found from Fig.4.9. These ratios and the corrected values of film thickness at the first and sustained contact levels are given in Table 4.2.

The experimental values when corrected for the combined effect of starvation and surface roughness are more in line with the predicted values. For example, in test D the original value of film thickness at first contact was $h^* = 2.64$ µm or $h^* = 5.6\sigma$, compared to a corrected value of $h^* = 1.41$ µm or $h^* = 3.56\sigma$, when starvation and roughness effects are taken into account.

If it is assumed that the contact will first occur in the region of the restriction in the film thickness at the rear of the contact, i.e. when $h_{min} = 3\sigma$ for which $h^* = 3.75\sigma$, the values of film thickness at contact is improved further.

It must be restated that these values assume the zero reverse flow condition for the inlet position. Whether this is applicable in the present case is not known. From the non-dimensional form of the inlet position, found using the zero reverse flow inlet boundary condition, the inlet distance from the edge of the parallel zone can be found. For the present examples these are of the order of 0.5 mm. From observations of the system this would seem to be an exaggeration of the extent of the starvation. The starvation effects,therefore, may not be as marked as those calculated.

Both theoretical work, to determine the physical condition which determines the inlet position and experimental work to verify this, is needed before the results of any analysis to show the effect of starvation can be applied with any confidence.

4.6. Conclusions

This chapter has examined the effect of circumferential surface roughness (Section 4.2) and of circumferential surface roughness and lubricant starvation in combination (Section 4.3) on the film thickness in an ehl conjunction. The results have been expressed as a ratio of the film thickness reduced by these factors, to that for ideal behaviour at the same conditions. The single factor solutions for surface roughness was given in Section 4.2 and that for starvation was provided by Wolveridge et al (1971). It has been shown that the simpler approach to find the combined effects of multiplying these single factor solutions, gives reduction ratios $h^*_{a\tau}/h^*$, to within 5% of those obtained from the full solution for values of $h^*_{a\tau}/h^*$, from 1 to ~ 0.4 for $\sigma/h^* = 0.1$ and raising from 1 to 0.7 for $\sigma/h^* = 0.5$.

The surfaces of the discs used for the experiments reported in this chapter were rough and by observation the inlet region could not be considered to be filled with lubricant. There was a possibility therefore that the film thickness in these tests would be effected by both these factors. Correction of the film thickness values using the results of Section 4.3 and an assumed position of the inlet boundary, improved the correlation between the predicted and experimental values of σ/h^* at first contact. Assuming that contact would first occur around a restriction in the film at the rear of the contact, improved the correlation further.

Section 4.4 shows how the theory of this chapter can be used to modify film thickness values to account for the effects of roughness and starvation. To do this both the roughness and inlet position parameters must be known. The roughness parameter can be found by measurements of the surface roughness and using the Dowson & Higginson film thickness formula as shown in Section 4.4. The physical parameters which determine the inlet distance, x_i , are not yet established and this remains a major problem in applying any work dealing with starvation effects.

Notation

Chapters 5, 6 and 7

N.B. Several symbols have different meanings to those for the previous chapters.

a'	-	pole of inverse Laplace transform	
A	-	contact area	
c	-	specific heat capacity of disc	J/Kg °C
C_p	-	specific heat capacity of fluid	J/Kg °C
C_m	-	represents steady state disc bulk temperature series	
d_{mn}	-	represents decay exponent in series of bulk temperature transient terms	
D_{mn}	-	represents disc bulk temperature in transient series	
F	-	Laplace transform of T'	
F_1, F_2, F_3	-	parts of F	
$g(R,\theta,t).v(\ell)$	-	represents heat soruce Fourier series	
h_a	-	axial heat transfer coefficient	$J/m^2 s$ °C
h_r	-	radial heat transfer coefficient	$J/m^2 s$ °C
Ha	-	axial Biot number $= \frac{h_a L}{k}$	
Hr	-	radial Biot number $= \frac{h_r R}{k}$	
I_o, I_p	-	Modified Bessel function	
J_o, J_p	-	Bessel function	
k	-	thermal conductivity of discs	J/ms °C
K_p	-	Bessel function	
K	-	decay exponent $(1/\tau_c)$	
ℓ	-	distance in axial direction	m
$2L$,	-	disc length	m
Pr	-	Prandtl number $= C_p \eta/\kappa$	
$\dot{q}$	-	rate of heat flow through an element	J/s
Q	-	total rate of heat generation in a contact	J/s
r	-	distance in radial direction	m
R	-	disc radius	m

s	-	Laplace operator	
S_m	-	$i\sqrt{s+\lambda_m^2}$	
t	-	time	sec
t_c	-	time constant	sec
T	-	temperature (bulk and flash)	°C
T_{amb}	-	ambient temperature	°C
T'	-	$T - T_{amb}$	°C
T^*	-	bulk temperature above ambient	°C
T^*_s	-	steady state bulk temperature above ambient	°C
ΔT^*_s	-	change in T^*_s between increments	°C
T_f	-	surface flash temperature	°C
$\hat{T}_f$	-	average T_f over contact area	°C
$V(\ell)$	-	function for variation of heat soruce strength with ℓ	
V'	-	proportion of track to disc length with champhered disc	
y	=	r/R - non-dimensional radial distance	
y_1	-	non-dimensional radius of central insulation	
Y_p	-	Bessel function	
z	=	ℓ/L - non-dimensional distance in L direction	
$\beta, \beta_{TOT}, \beta_c$	,	heat source strength for one disc, in the contact between two discs, for a champhered disc	- J/m^2s
γ	-	arbitrary constant	
$\Gamma = \frac{L}{R}\gamma$		(where $\Gamma \tan \Gamma = Ha$)	
θ	-	radial position	- rad
$2\theta^*$	-	angular width of heat soruce	- rad
κ	-	$k/\rho c$ - thermal diffusivity of disc	- m /s
κ'	-	thermal diffusivity of lubricant	
ν	=	$\kappa/\beta R$ - non-dimensional group	
ρ	-	density	- Kg/m
τ	=	$t\,\kappa/R^2$ - non-dimensional time	
τ_c	-	non-dimensional time constant	

Λ - term in decay exponent (where $Hr = \dfrac{\Lambda_n \, J_1(\Lambda_n)}{J_o(\Lambda_n)}$)

ω - disc angular velocity - rad/sec

Ω - $\dfrac{\omega R^2}{\kappa}$ non-dimensional disc angular velocity

CHAPTER 5

PREDICTION OF TEMPERATURE IN FINITE ROTATING DISCS

5.1 Introduction

5.1.1. The role of temperature

The second line of investigation reported in this thesis is concerned with predicting the thermal response of the test machine and its effect on test behaviour and failure conditions and is the subject of the next three chapters. The reason for this study were outlined in Chapter 2. In brief, when comparing the result of Story and Rossides, in addition to the more obvious differences in failure load, temperature and running-in behaviour, different thermal responses were also observed. The thermal response was suggested by Crook and Shotter (1957) to have an influence on scuffing failure conditions. They proposed that whether a system survived a change in conditions would depend on the ability of the surfaces to run-in compared to the rate of change of film thickness. The rate of change of film thickness following an increase in load is related to the rate of change of the bulk temperature.

In the tests reported in Chapter 3 some of the differences between the test types were reproduced by altering the operating conditions but the temperature/time response to a change in load conditions was similar for both test types. This indicates, as suggested by Story, Archard & Baglin (1980) that the temperature/time response was a property of the test machine.

To explore the role of rate of change of bulk temperature in scuffing failure, we wish to predict the changes in the bulk temperature and its distribution in the discs of a two disc scuffing machine. In this chapter an analytical model is developed to do this. Chapter 6 shows how the result of the analysis is applied to the two disc machine configuration and Chapter 7 reports tests which attempt to alter test failure conditions by changing the thermal response of the machine.

In the first section of this chapter the way in which the temperature in such a system builds up is described and various components of the temperature and their use in several scuffing criteria are defined. Some previous solutions to the problem of temperature prediction are also reviewed in this section. The present model is described and developed in sections 5.2 and the stages of the solution are detailed in section 5.3. In section 5.4 the resulting terms which represent the bulk temperature variation are examined in some detail.

5.1.2. Temperatures in a two disc system

Before application of a load in a two disc test, the temperature of the rotating bodies will be approximately uniform and determined by the 'oil' temperature and ambient conditions. On the application of a load, heat is generated in the resulting contact region, by shearing of the fluid film if conditions are purely hydrodynamic and by shearing of the junctions between opposing asperities if the system is in mixed lubrication.

The contact region is a heavily loaded small area, fixed in space, through which each element on the surface passes as the bodies rotate. As a point on the surface of either body passes through the contact area, its temperature increases. The magnitude of this increase is termed the 'surface flash' temperature. As the point moves out of the contact, the flash temperature decays, due to conduction into the body and convection from the surface. The heat conducted into the body produces a sub-surface flash temperature, the magnitude of which decreases rapidly with depth below the surface. The net effect of heat being continuously generated around the surface and conducted into the bodies is to raise the underlying temperature throughout the whole body, not just in those areas which experience a significant flash temperature. This underlying temperature is termed the "bulk temperature" and was defined by Blok (1937) as 'the temperature representative of the fairly uniform level of those parts of the temperature fields in the rubbing bodies that do not lie too close to the conjunction zone'. Experimentaly, this is the temperature measured by embedded thermocouples.

The "transient bulk temperature" describes the variation of the bulk temperature with time following the application of a load. In most practical systems, losses occur from the rubbing bodies to the environment and to other parts of the machine. These losses limit the rise in bulk temperature above ambient. The bulk temperature stabilises to its "steady state" value when the net losses equal the heat transferred to the body from the heat source. At steady state there may be a spatial variation in the bulk temperature and the regions near the surface will still experience the periodic flash temperature.

The "quasi stationary surface temperature" is the level to which the surface temperature tends as the flash decays on each rotation. This is not necessarily the same as the bulk temperature which is the underlying temperature well removed from the influence of the flash.

Different components of the temperature are important from a lubrication point of view and have been used in various scuffing failure criteria. These have been reviewed in Chapters 1 and 2, but some of the main uses are recapped here. The film thickness in elastohydrodynamic lubrication is dependent on the viscosity of the lubricant in the inlet region of the contact which was shown by Archard & Kirk (1961) to be determined by the bulk temperature of the bodies rather than the oil supply temperature.

The 'total contact temperature' in the Blok (1937) scuffing failure criteria temperature was defined as the flash surface temperature generated in the contact region superimposed on the underlying bulk temperature.

Ku and Li (1977) thought it more appropriate, due to the variation of the bulk temperature with depth, to define the total contact temperature as the surface flash temperature superimposed on the quasi-stationary surface temperature.

The role of temperature in the Dyson criteria for failure of lubrication with rough surfaces was that of the bulk temperature on the hydrodynamics of the system. Crook and Shotter argued that it was the rate of change of bulk temperature and the corresponding change in film thickness that was of importance in determining failure conditions.

5.1.3. Previous models

Various solutions have been published which cover particular aspects of temperatures produced in rotating cylinders. Some of these solutions are outlined below. In all cases the model is of a single cylinder with the heat being generated by an independent heat source, rather than in the contact between two rotating bodies. Of the solutions reviewed here only that by Story (1984) was extended to account for two contacting bodies.

The starting point in the solution presented by Jaeger (1944), was an infinitely long two-layered cylinder with an instantaneous line source at some position in the cylinder. This was gradually adapted in a number of stages by superposition of solutions. The final result predicted the bulk and flash temperatures in an infinitely long cylinder with a band source of heat rotating about its surface. There was no allowance for heat loss from the surface and consequently the bulk temperature did not reach steady state.

Des Ruisseaux and Zerkle (1970) produced the transient and steady state solution for infinitely long cylinders with heat loss from the surface. Their method was similar to Jaeger's, i.e. superposition of simpler solutions, but included an additional boundary condition which represented the heat loss from the surface.

Ling (1973), by taking Fourier Transforms of the governing differential equation and the boundary conditions, produced a more direct solution. The boundary conditions could be applied directly and the inverse transform gave the required solution for the temperature. No attempt was made to evaluate the expression. This onerous task was performed by Gecim & Winer (1984) who used the same approach and evaluated the result for a range of the non-dimensional groups involved. Various modifications by Gecim & Winer to the solution, all for steady state conditions, have shown the effects of applying multiple heat sources, of hollow cylinders and of cylinders having finite length (Gecim & Winer (1986a)), and of a surface layer of a different material (Gecim & Winer (1986b)).

Story (1984) presented a solution for a cylinder having an infinite length with convective surface heat loss. It included the transient condition, as in the solution of Des Ruisseaux and Zerkle, but used a simpler approach. The cylinder was held stationary and the heat source rotated around the cylinder surface. The heat source and its rotation was modelled by a Fourier series. The need for moving coordinate systems or superposition of solutions was therefore excluded. The resultant solution predicted the variation of the bulk and flash temperature with time and position in the cylinder, initially at ambient temperature, following the application of the heat source.

The result matched that by Des Ruisseaux and Zerkle, although the simpler approach adopted by Story allowed modifications to be made to the initial solution. These showed the effects of introducing a shaft held at a constant temperature into the cylinder, of applying a number of heat sources and varying the strength of the heat source with time.

In a relatively thin disc, the convective heat loss from the side faces of the disc is expected to have a significant effect on the temperature. The solution presented in this chapter is to predict the temperature in a finite length cylinder due to a heat source at the surface, with heat loss from the peripheral surface and from the end faces. The solution gives both the steady state and transient solutions to the bulk and flash components of the temperature. The approach to the problem is similar to that of Story (1984) for infinite length discs. The details of the solution in that reference were somewhat scant and have not been published so the present solution which includes the additional dimension for heat loss and temperature variation has, for completeness, been spelt out in more detail.

5.2. Statement of the problem

5.2.1. The governing equation

The friction in an elastohydrodynamic contact produces heat, most of which is transferred into the contacting bodies, (Wolveridge & Archard (1972)). In a two disc machine the contact area position is fixed relative to the machine. The configuration for each disc in the pair is therefore a cylinder rotating through a stationary peripheral heat source that extends over the full length of the cylinder. Following Story, this can be modelled as a stationary cylinder with a heat source rotating at the appropriate speed around its surface as shown in Fig.5.1.

If the cylinder is free in space so that there is no heat loss to other parts of the machine, all the heat from the rotating heat source conducted into the cylinder will either be stored in the cylinder, raising its temperature, or lost from the surface of the side faces by convection, (see Fig.5.2a).

The heat transfer within the cylinder can be considered, by taking a small element of size Δr, $r\Delta\theta$, $\Delta \ell$, at position r,θ,ℓ shown in Fig.5.2b. If heat is conducted through the element in the three directions then the energy balance for the element is

$$\dot{q}_r + \dot{q}_\theta + \dot{q}_\ell = q_{stored} = c.\rho.r\Delta\theta.\Delta\ell.\frac{\partial T}{\partial t} \qquad (5.1)$$

For a material of thermal conductivity k, the net rate of heat flow, $\dot{q}_r$, through the element in the radial direction is

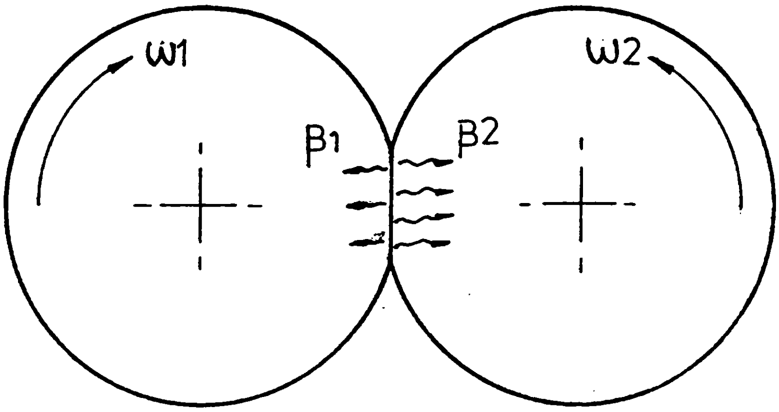

a/ heat input between two discs

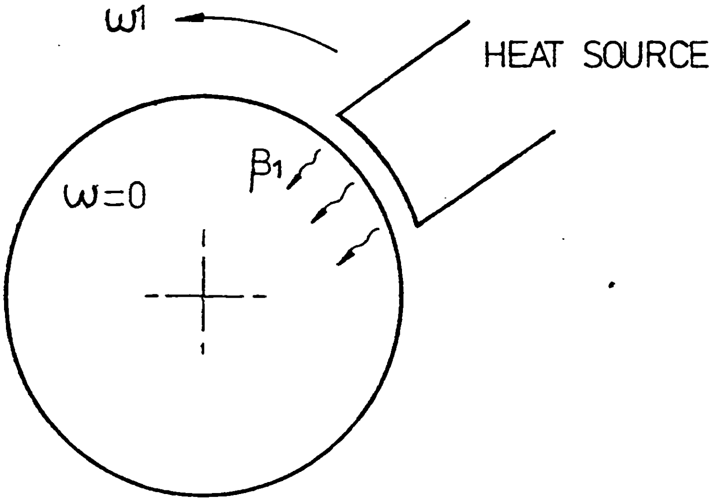

b/ equivalent for single disc

Figure 5.1 Single cylinder configuration to model heat input between two discs.

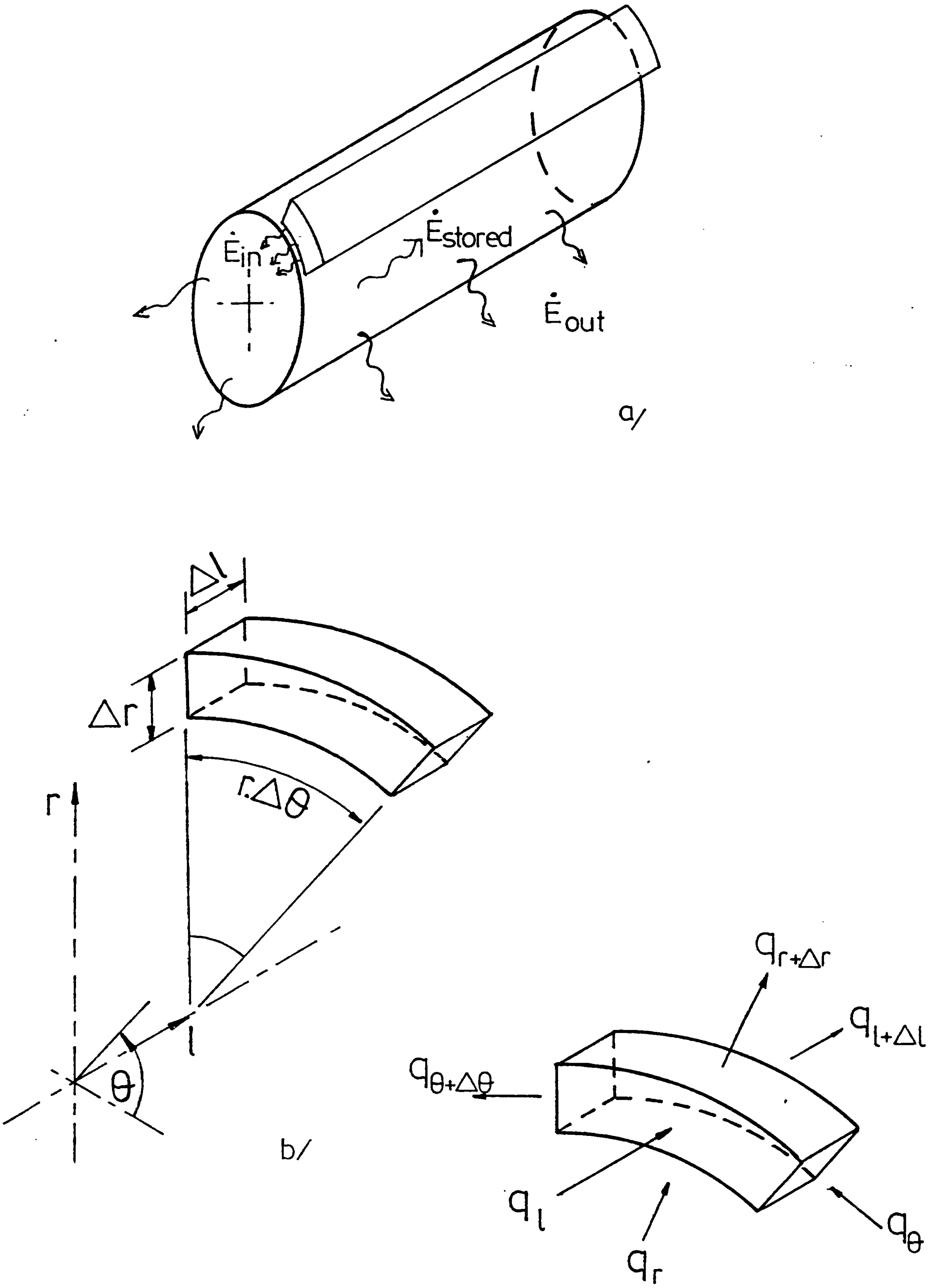

Figure 5.2 Heat transfer and energy balance for a cylinder and element from a cylinder.

$$\dot{q}_r = \dot{q}\Big|_{r+\Delta r} - \dot{q}\Big|_r = k\left[r + \Delta r \,.\, \frac{\partial T}{\partial r}\Big|_{r+\Delta r} - r\,\frac{\partial T}{\partial r}\Big|_r\right) \Delta\theta.\Delta\ell$$

With similar expressions for the heat flow in the angular and the axial directions the energy balance for the element (Eqn.(5.1)) becomes

$$\left[(r+\Delta r).\frac{\partial T}{\partial r}\Big|_{r+\Delta r} - r\,\frac{\partial T}{\partial r}\Big|_r\right]\Delta\theta\ \Delta\ell + \left(\frac{1}{r}\,\frac{\partial T}{\partial \theta}\Big|_{\theta+\Delta\theta} - \frac{1}{r}\,\frac{\partial T}{\partial r}\Big|_\theta\right)\Delta r.\Delta\ell$$

$$+ \left(\frac{\partial T}{\partial \ell}\Big|_{\ell+\Delta\ell} - \frac{\partial T}{\partial \ell}\Big|_\ell\right).r.\Delta\theta.\Delta r = \kappa^{-1}.\Delta r.\Delta\ell.r\Delta\theta.\frac{\partial T}{\partial t}$$

where $\kappa = k/\rho c$ is the thermal diffusivity of the material.

When divided throughout by $\Delta r, r\Delta\theta, \Delta\ell$, as $\Delta r\ , r\Delta\theta, \Delta\ell \to 0$ this expression becomes

$$\frac{1}{r}\,\frac{\partial}{\partial r}\left(r\,\frac{\partial T}{\partial r}\right) + \frac{1}{r^2}\,\frac{\partial^2 T}{\partial \theta^2} + \frac{\partial^2 T}{\partial \ell^2} = \kappa^{-1}\,\frac{\partial T}{\partial t} \qquad (5.2)$$

This is the general form of the equation which governs the heat flow within the cylinder. Solution of this partial second order differential equation using the appropriate set of system boundary conditions will give expressions for the temperatures in the cylinder.

5.2.2. Boundary conditions

The co-ordinate system and the dimensions of the cylinder are shown in Fig.5.3. The following assumptions and simplifications have been made to find the initial and boundary conditions for the problem and to model the heat source.

The cylinder is homogeneous, of radius R and length $2L$. The temperature is a function of r, θ, ℓ and time, t.

At the centre of the cylinder, $r=0$, the temperature is always finite.

The temperature at angular position θ is equal to the temperature at $2\pi+\theta$, i.e. the solution is singular.

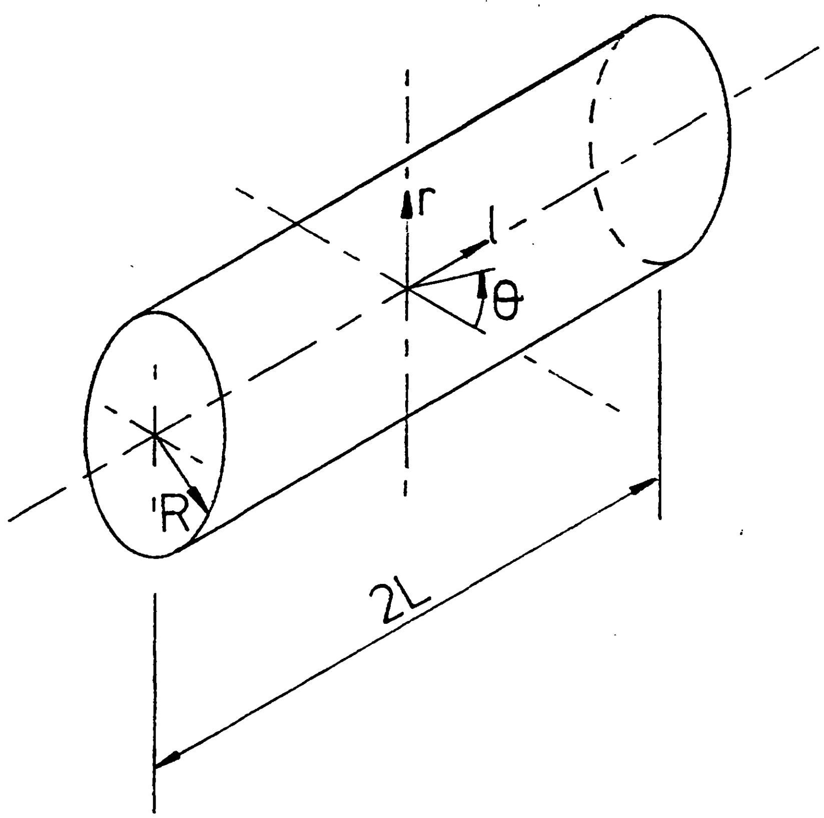

Figure 5.3 Co-ordinate system for a finite length cylinder.

The solution is symmetric in the axial direction so there is no axial temperature gradient at $\ell=0$.

There is convective heat loss from the entire peripheral surface and from the end faces of the cylinder.

These conditions can be expressed:

Initial condition $\quad T(r,\theta,\ell,0) = T_{amb}$

Boundary conditions

(i) $T(0,\theta,\ell,t) < \infty$

(ii) $T(r,\theta,\ell,t) = T(r,\theta+2\pi,\ell,t)$

(iii) $\frac{\partial T}{\partial \ell}(r,\theta,0,t) = 0$

(iv) $k\,\frac{\partial T}{\partial \ell}(r,\theta,\pm L,t) = -h_a.[T(r,\theta,\pm L,t) - T_{amb}]$

(v) $k\,\frac{\partial T}{\partial r}(R,\theta,\ell,t) = -h_r.[T(R,\theta,\ell,t) - T_{amb}] + g(R,\theta,t).v(\ell)$

where $g(R,\theta,t).v(\ell)$ is a Fourier series representing the heat source and h_a and h_r are the convective heat transfer coefficients from the end faces and peripheral surface respectively.

The heat source has strength β, angular width $2\theta^*$, extends over the full length of the cylinder and rotates with angular velocity ω rads/sec around the periphery of the cylinder. The variation with time of the heat input at a point on the surface R,θ,ℓ can be modelled as a square wave impulse of amplitude β, and duration $2\theta^*/\omega$ shown in Fig.5.4. The Fourier series which represents this wave form is

$$g(R,\theta,t).v(\ell) = \beta\left[\frac{\theta^*}{\pi} + \frac{2}{\pi}\sum_{q=1}^{\alpha} \frac{\sin q\theta^*.\cos q(\theta-\omega t)}{q}\right].v(\ell) \qquad (5.3)$$

where $v(\ell)$ represents the variation of the source strength along the length. For the initial analysis this will be taken as uniform, i.e. $v(\ell)=1$. Axial variation of the heat source is considered in Chapter 6.

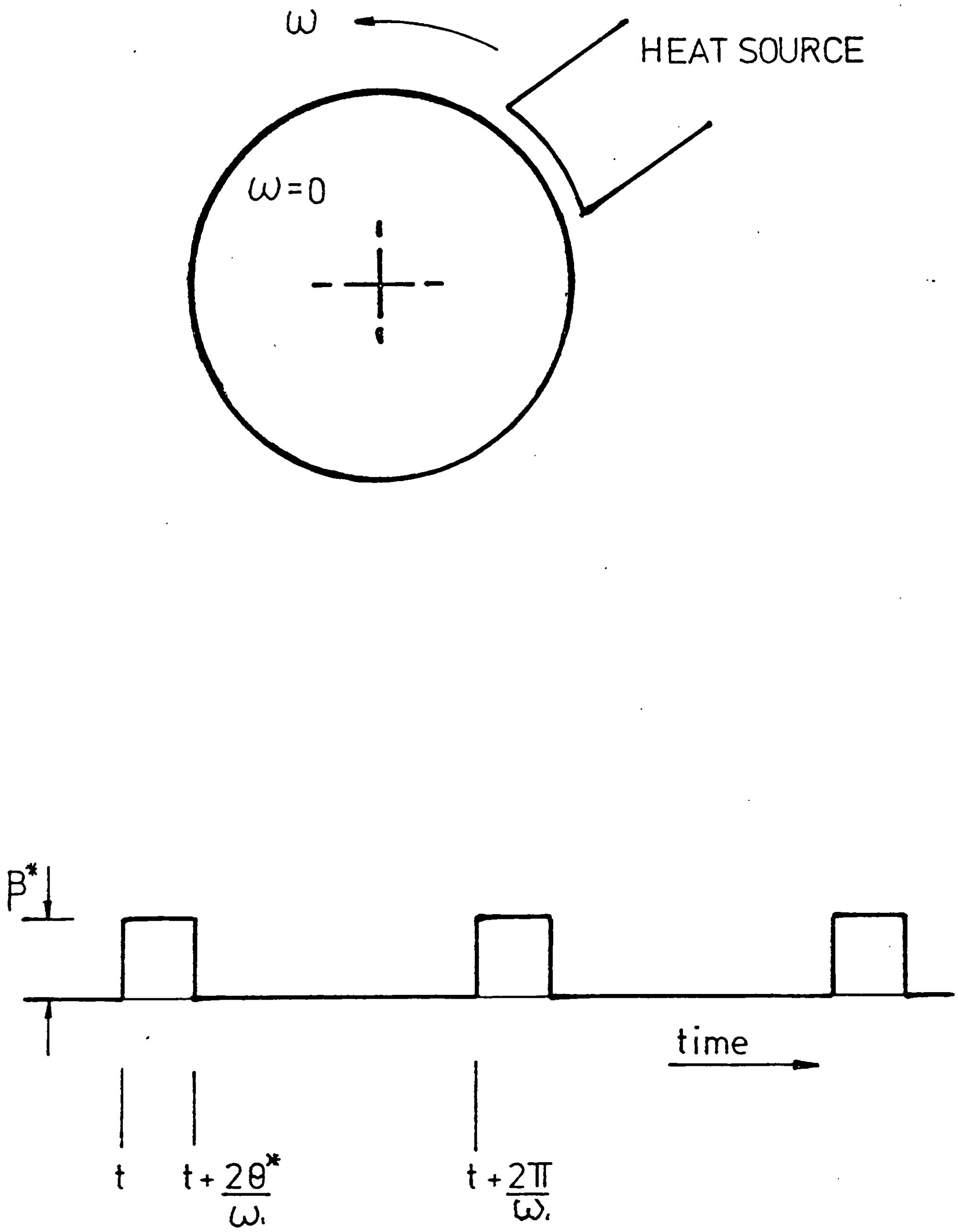

Figure 5.4 Variation of heat source strength with time on the disc surface.

5.2.3. Non-dimensional form

In the governing heat flow equation if T is replaced by $T' = T - T_{amb}$, then the temperature being considered is at all times the rise above the ambient. The remaining terms can be non-dimensional using the following differential equation (5.2) and boundary conditions can be simplified by introducing the following non-dimensional groups

$y = r/R$, $z = \ell/L$, $\tau = t\kappa/R^2$, $\Omega = \omega R^2/\kappa$, $\nu = \kappa/R\beta$, $Hr = h_r R/k$, $Ha = h_a L/k$

Equation 5.2, the governing heat flow equation, becomes

$$\frac{1}{y} \cdot \frac{\partial}{\partial y}\left(y \frac{\partial T'}{\partial y}\right) + \frac{1}{y^2} \quad \frac{\partial^2 T'}{\partial \theta^2} + \frac{R^2}{L^2} \quad \frac{\partial^2 T'}{\partial z^2} = \frac{\partial T'}{\partial \tau} \tag{5.4}$$

and the initial and boundary conditions become

(i) $T'(y,\theta,z,0) = 0$

(ii) $T'(0,\theta,z,\tau) < \infty$

(iii) $T'(y,\theta,z,\tau) = T(y,\theta+2\pi,z,\tau)$

(iv) $\frac{\partial T'}{\partial z}(y,\theta,0,\tau) = 0$

(v) $\frac{\partial T'}{\partial z}(y,\theta,\underline{+}1,\tau) = Ha\ T'(t,\theta,\underline{+}1,\tau)$ and

(vi) $\frac{\partial T'}{\partial y}(1,\theta,z,\tau) = -\ Hr\ T'(1,\theta,z,\tau) + g'(1,\theta,\tau)$.

$g'(1,\theta,\tau)$ is the non-dimensional form of the heat source Fourier series where

$$g'(1,\theta,\tau) = \frac{1}{\nu}\left[\frac{\theta^*}{\pi} + \frac{2}{\pi} \sum_{q=1}^{\alpha} \frac{\sin\theta^* \cos q(\theta-\Omega\tau)}{q}\right] \tag{5.5}$$

(The problem has not been completely non-dimensionalised as it still maintains the dimensions of T i.e. °C .)

This statement of the problem differs from that of Story for infinite length cylinders in the third and fourth boundary conditions and by the extra term in z in the governing heat flow equation.

5.3. Solution

5.3.1. Method of solution

Equation (5.4) is a homogeneous partial differential equation for T'. The solution to this equation must also satisfy the initial and boundary conditions, all of which are homogeneous except for the fifth boundary condition because of the generation term $g'(1,\theta,\tau)$. A direct separation of variables method cannot be used because of this inhomogeneity. The steps of the method used are outlined below.

1) Laplace transforms of the non-dimensional form of the partial differential equation (eqn.(5.4)), and the boundary conditions are taken. Applying the initial condition to the transformed equation removes the time dependence.

2) The transformed differential equation and the first four boundary conditions are separated into individual partial differential equations and functions of the variables y, θ and z.

3) The separated forms of boundary conditions i-iv are applied to the individual differential equations where appropriate, to obtain three partial solutions to the problem. These solutions still contain unknowns.

4) The three partial solutions are combined and the unknowns are found, using the fifth boundary condition and the properties of orthogonality.

5) The inverse Laplace transform of the resulting expression reintroduces the time dependence and gives the solution.

5.3.2. Solution stages

5.3.2a. Laplace transforms

The Laplace transform of a function $f'(t)$ with respect to t, $\mathcal{L}f'(t)$, is defined as

$$\mathcal{L}_t f'(t) = \int_0^\infty f'(t)e^{-st}\,dt$$

where s is the Laplace operator.

Similarly the Laplace transform, F, of the function $T(y,\theta,z,\tau)$ with respect to τ is

$$\mathcal{L}_\tau T'(y,\theta,z,\tau) = \int_0^\infty T'(y,\theta,z,\tau)e^{-s\tau}d\tau = F(y,\theta,z,s)$$

Expanding the first term of eqn.(5.4), taking Laplace transforms and applying the initial condition $T'(y,\theta,z,0) = 0$, gives

$$\frac{\partial^2 F}{\partial y^2} + \frac{1}{y}\frac{\partial F}{\partial y} + \frac{1}{y^2}\frac{\partial^2 F}{\partial \theta^2} + \frac{R^2}{L^2}\frac{\partial^2 F}{\partial z^2} = sF \tag{5.6}$$

The Laplace transforms of the boundary conditions are

$$F(0,\theta,z,s) < \infty$$

$$F(y,\theta,z,s) = F(y,\theta+2\pi,z,s)$$

$$\frac{\partial F}{\partial z}(y,\theta,0,s) = 0$$

$$\frac{\partial F}{\partial z}(y,\theta,\pm 1,s) = -\,Ha\,F(y,\theta,\pm 1,s)$$

$$\frac{\partial F}{\partial y}(1,\theta,z,s) = -\,Hr\,F(1,\theta,z,s) + G'(1,\theta,s) \tag{5.7}$$

where $G'(1,\theta,s) = \mathcal{L}_\tau g'(1,\theta,\tau) = \frac{1}{\nu}\left[\frac{\theta^*}{s\pi} + \frac{2}{\pi}\sum_{q=1}^{\infty}\frac{\sin q\theta^*}{q}\left(\frac{s\cos q\theta + q\Omega\sin q\theta}{s^2+q^2\Omega^2}\right)\right]$

5.3.2b Separation of the variables

Let $F(y,\theta,z,s) = U(u,\theta,s).Z(z)$. On re-arranging Eqn.(5.6) becomes

$$\frac{1}{U}\left(\frac{\partial^2 U}{\partial y^2} + \frac{1}{y}\frac{\partial U}{\partial y} + \frac{1}{y^2}\frac{\partial^2 U}{\partial \theta^2}\right) - s = -\frac{1}{Z}\cdot\frac{R^2}{L^2}\cdot\frac{\partial^2 Z}{\partial z^2}$$

Equating both sides of this expression to an arbitrary value $-\gamma^2$ gives

$$\frac{d^2Z}{dz^2} + \frac{L^2}{R^2}\gamma^2 Z = 0 \qquad (5.8a)$$

and

$$\frac{1}{U}\left(\frac{\partial^2 U}{\partial y^2} + \frac{1}{y}\frac{\partial U}{\partial y} + \frac{1}{y^2}\frac{\partial^2 U}{\partial \theta}\right) - (s+\gamma^2) = 0$$

Similarly, letting $U(y,\theta,s) = Y(y,s).\Theta(\theta)$, the separation process can be repeated on the second of these equations to give

$$\frac{d^2\Theta}{d\theta^2} + p^2\Theta = 0 \qquad (5.8b)$$

and

$$y^2\frac{d^2Y}{dy^2} + y\frac{dY}{dy} - (p^2 + y^2(s+\gamma^2))Y = 0 \qquad (5.8c)$$

where p^2 is another arbitrary constant.

The original differential equation has been separated into three differential equations, eqns.(5.8 a, b and c), in z, θ and y respectively.

The first four boundary conditions when separated give

$$Y(0).\Theta(\theta).Z(z) < \infty$$

$$\Theta(\theta) = \Theta(\theta+2\pi)$$

$$\frac{dZ}{dz}(0) = 0$$

$$\frac{dZ}{dz}(\pm 1) = -\, Ha\, Z(\pm 1)$$

The fifth boundary condition cannot be separated in this fashion and so remains

$$\frac{dF}{dy}(1,\theta,z,s) = -\, Hr\, F(1,\theta,z,s) + G'(1,\theta,s) \qquad (5.7)\text{bis}$$

5.3.2c. Applying the boundary conditions.

The separated forms of boundary conditions (i-iv) can be applied to the general solutions of eqns.(5.8a, b and c) where appropriate.

The general solution to eqn.(5.8a) is

$$Z = a \cos \frac{L}{R} \gamma z + b \sin \frac{L}{R} \gamma z$$

Applying the third boundary condition, gives $b = 0$, so

$$Z = a \cos \frac{L}{R} \gamma z$$

and applying the fourth boundary condition gives

$$\frac{L}{R} \gamma \tan \frac{L}{R} \gamma = Ha$$

This is an eigen condition for the problem, the roots of which are solutions to the equation for Z. This function is plotted in Fig.5.5 and shows that it has multiple roots, γ_m. There are therefore an infinite number of solutions to Z of the form

$$Z = a_m \cos \Gamma_m z \qquad m=1,2,3 \ldots$$

where $\Gamma_m = \frac{L}{R}\gamma_m$ and $\Gamma_m \tan \Gamma_m = Ha$.

Any combination of these solutions will also satisfy the problem so Z can be written as a summation of the solutions, i.e.

$$Z = \sum_{m=1}^{\infty} a_m \cos \Gamma_m z \qquad (5.9a)$$

The general solution to eqn.(5.8b) is

$$\Theta = c \cos p\theta + d \sin p\theta$$

This will only satisfy the second boundary condition if $p = 0$ or an integer value. Θ therefore, also has many solutions and can be expressed as a summation of these.

$$\Theta = \sum_{p=o}^{\infty} c_p \cos p\theta + d_p \sin p\theta \qquad (5.9b)$$

where $p=0,1,2,3,\ldots$.

Equations (5.9a and b) satisfy the first boundary condition providing a_m, c_p and d_p are $< \infty$.

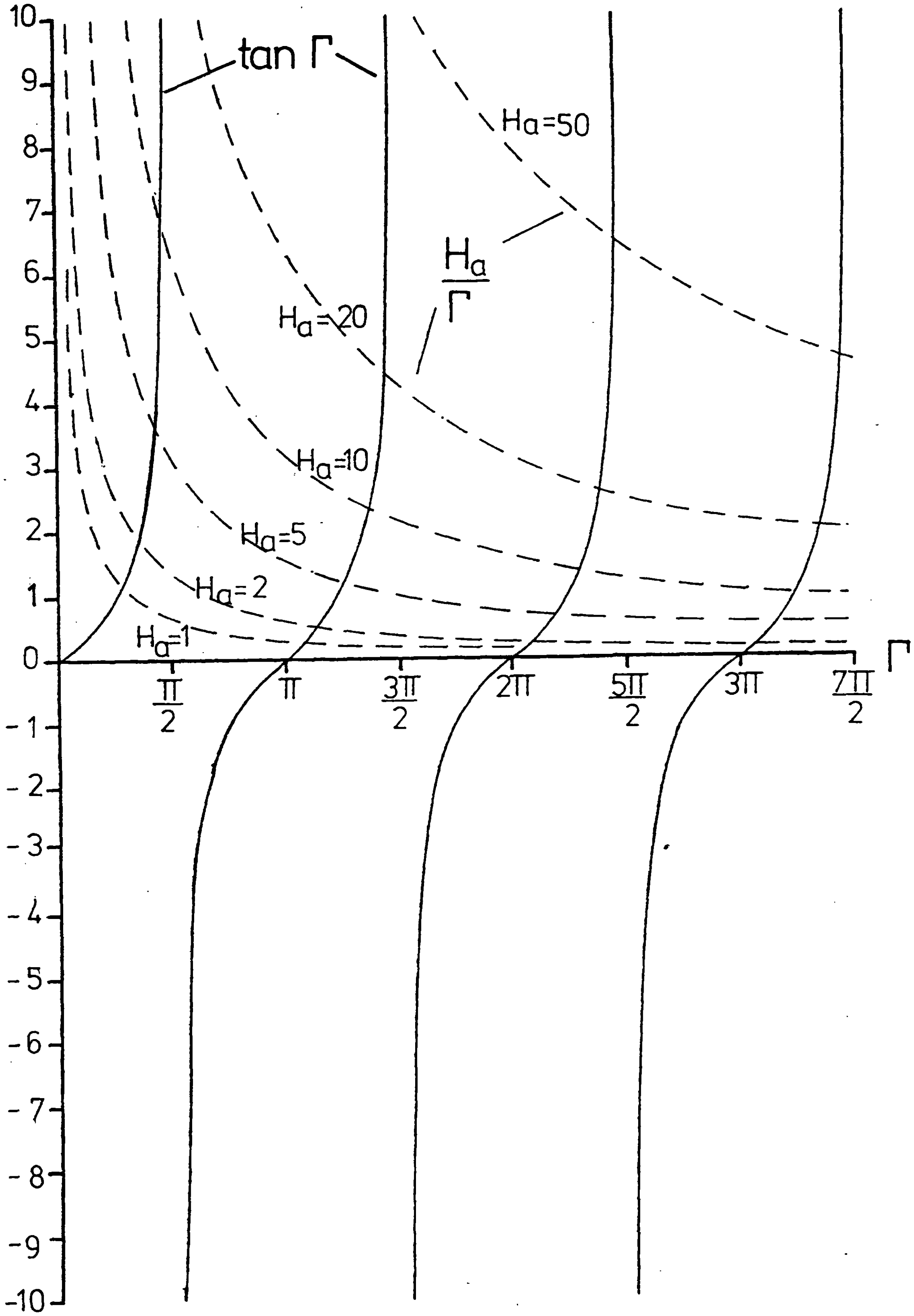

Figure 5.5 Variation of tanΓ and Ha/Γ with Γ.

The general solution to eqn.(5.8c) is

$$Y = e\, J_p\,(iy\sqrt{s+\gamma_m^2}) + f\, Y_p\,(iy\sqrt{s+\gamma_m^2}$$

where p equals zero or an integer value. J_p is a Bessel function of the first kind of order p and Y_p is a Bessel function of the second kind of order p.

At $y=0$, $J_p(0)=1$ and $Y_p(0)=\infty$ and so the solution will only satisfy the first boundary condition, that the temperature must be finite at the centre of the cylinder, if $f=0$. J_p and γ_m are both series solutions, which makes the full solution for Y

$$Y = \sum_{m=1}^{\infty} \sum_{p=o}^{\infty} e_{mp}\, J_p\,(iy\sqrt{s+\gamma_m^2}) \qquad (5.9c)$$

The full expression for F, where $F = Y(y).\Theta(\theta).Z(z)$ is found by combining eqns.(5.9a, b and c) to give

$$F = \sum_{m=1}^{\infty}\sum_{p=o}^{\infty} (A_{mp} \cos p\theta + B_{mp} \sin p\theta).\cos \Gamma_m z.J\,(iy\sqrt{s+\gamma_m^2}) \qquad (5.10)$$

where A_{mp} and B_{mp} are series' of constants which replace $a_m.c_p.e_{mp}$ and $a_m.d_d.e_{mp}$ respectively.

5.3.2d. Applying the fifth boundary condition

As the fifth boundary condition cannot be separated into individual functions for y, θ and z, it can only be applied to the full expression for F. This will assign values to the series of constants A_{mp} and B_{mp}.

Substituting for F and dF/dy at $y=1$ from Eqn.(5.10) in the fifth boundary condition eqn.(5.7) gives

$$\sum_{m=1}^{\infty} \sum_{p=o}^{\infty} (A_{mp}\cos p\theta+B_{mp} \sin p\theta).\cos \Gamma_m z.[(Hr+p)J_p(i\sqrt{s+\gamma_m^2})-(i\sqrt{s+\gamma_m^2}).J_{p+1}(i\sqrt{s+\gamma_m^2})]$$

$$= G'(1,\theta,s) \qquad (5.10b)$$

This equation can be solved to find the series of constants A_{mp} and B_{mp} in turn, by use of orthogonal funcitons.

A_{mp} and B_{mp} are both a double series of constants. An orthogonal function is first used on A_{mp} and B_{mp} to isolate one value from the m series, i.e. m=M to give A_{Mp} and B_{Mp}. The appropriate orthogonal functions are then used to evaluate A_{MO}, A_{MP} and B_{MP} in turn. The constants for p=0 are found separately from the rest of the p series. Details of these steps are given in Appendix A3. The resultant expressions for A_{mO}, A_{mp} and B_{mp} are

$$A_{mo} = \frac{\theta^*}{s\nu\pi} \cdot \frac{4 \sin \Gamma_m}{2\Gamma_m + \sin 2\Gamma_m} \cdot \frac{1}{Hr.J_o(S_m) - S_m J_1(S_m)}$$

$$A_{mp} = \frac{2}{\nu\pi} \cdot \frac{s \sin p\theta^*}{p(s^2+\Omega^2 p^2)} \cdot \frac{4 \sin \Gamma_m}{2\Gamma_m + \sin 2\Gamma_m} \cdot \frac{1}{(Hr+p)J_p(S_m) - S_m J_{p+1}(S_m)}$$

and $$B_{mp} = \frac{p\Omega}{S} \cdot A_{mp} \quad \text{where} \quad S_m = i\sqrt{s+\gamma_m^2}$$

When substituted into eqn.(5.10) F , the transformed temperature in the cylinder, becomes

$$F = \frac{1}{\nu} \sum_{m=1}^{\alpha} \left\{ \frac{4 \sin \Gamma_m}{2\Gamma_m + \sin 2\Gamma_m} \cdot \cos \Gamma_m z \cdot \left(\frac{\theta^*}{s\pi} \cdot \frac{J_o(yS_m)}{Hr.J_o(S_m) - S_m J_1 S_m} \right.\right.$$

$$\left.\left. + \sum_{p=1}^{\alpha} \frac{2}{\pi} \cdot \frac{\sin p\theta^*}{p(s^2+p^2\Omega^2)} \cdot (s \cos p\theta + p\Omega \sin p\theta) \frac{J_p(yS_m)}{(Hr+p)J_p(S_m) - S_m J_{p+1}(S_m)} \right) \right\} \tag{5.11}$$

where $\Gamma_m \tan \Gamma_m = Ha$, $\Gamma_m = L\,\gamma_m/R$ and $S_m = (i\sqrt{s+\gamma_m})$.

This equation consists of three main parts, say F1 , F2 and F3 which arose from A_{mo} , A_{mp} and B_{mp} respectively.

5.3.2e. Inverse Laplace transform

Taking the inverse Laplace transform of F gives the general expression for the temperature T' . As each part of F , i.e. F1, F2 and F3 , cannot be split into simpler functions for which standard inverse transforms are tabulated, the complex inversion formula must be used to invert F1, F2 and F3 in turn. The inversion of F1 gives the bulk temperature terms, T* , in the final solution and is detailed here. The inverse of F2 and F3 gives the flash temperature terms and is given in Appendix A4.

The inverse is found using the method discussed by Speigel (1956) the workable form of which reduces to, for F1 ,

$$\text{Inverse } F1(s) = \Sigma \text{ residues } (F1(s).e^{s\tau}) \text{ at the poles of } F1(s) .$$

A pole is a value of the Laplace operator, s , at which the denominator of the function $F1(s) = 0$. The residue of $F1(s).e^{s\tau}$ at a pole $s=a'$ is

$$\underset{s=a'}{\text{Residue}} = \underset{s\to a'}{\text{Limit}} \ (s-a').F(s)e^{s\tau}$$

Only those parts of F1 which are functions of s need be considered. The inverse of

$$\frac{1}{s} \cdot \frac{J_o\,(y.i\sqrt{s+\gamma_m^2})}{HrJ_o(i\sqrt{s+\gamma_m^2})-(i\sqrt{s+\gamma_m^2})J_1(i\sqrt{s+\gamma_m^2})}$$

is therefore required. The poles of this function are 1) s=0 and 2) s=a' such that $i\sqrt{\gamma_m^2 +a'} = \Lambda$ and $Hr = \dfrac{\Lambda J_1(\Lambda)}{J_o(\Lambda)}$

1) For the first pole

$$\underset{s=0}{\text{Residue}} = \underset{s\to 0}{\text{Limit}} \ \frac{(s-0)}{s} \ \frac{J_o\,(y.i\sqrt{s+\gamma_m^2})}{HrJ_o(i\sqrt{s+\gamma_m^2})-(i\sqrt{s+\gamma_m^2})\ J_1(i\sqrt{s+\gamma_m^2})}$$

In the limit as $s \to 0$;

$$i\sqrt{\gamma_m^2+s} \to i\gamma_m \;,\; e^{s\tau} \to 1 \;\text{ and }\; \frac{(s-0)}{s} \to 1 \;,\; \text{where the limit of } \frac{(s-0)}{s}$$

as $s \to 0$ is indeterminate and is found using L'hopitals rule. These limits make

$$\underset{s\,=\,0}{\text{Residue}} = \frac{J_o(i\gamma_m y)}{HrJ_o(i\gamma_m)-(i\gamma_m)J_1(i\gamma_m)}$$

2) For the second pole

$$\underset{s\,=\,0}{\text{Residue}} = \underset{s\to a}{\text{Limit}} \frac{(s-a')}{s} \quad \frac{J_o(y\ i\sqrt{s+\gamma_m^2})}{HrJ_o(i\sqrt{s+\gamma_m^2})-(i\sqrt{s+\gamma_m^2})\ J_1(i\sqrt{s+\gamma_m^2})}$$

In the limit as $s \to a'$;

$$i\sqrt{\gamma_m^2+s} \to \sqrt{\gamma_m^2+a'} = \Lambda \;,\; s \to -(\gamma_m^2+\Lambda^2),\; e^{s\tau} - e^{-(\gamma_m^2+\Lambda^2)\tau}$$

and using L'hopitals rule and standard Bessel function relationships

$$\underset{s\to a'}{\text{Limit}} \frac{(s-a')}{HrJ_o(i\sqrt{s+\gamma_m^2})-i\sqrt{s+\gamma_m^2}\ J_1(i\sqrt{s+\gamma_m^2})} \to -\frac{2\Lambda^2}{Hr^2+\Lambda^2}$$

The identity $Hr = \dfrac{\Lambda J_1(\Lambda)}{J_o(\Lambda)}$ has multiple roots for any value of Hr independent of $\gamma_m(Ha)$. These multiple roots, say Λ_n, introduce another series summation into the inverse of $\tilde{F1}$. The limits make

$$\underset{s\,=\,a'}{\text{Residue}} = -\sum_{n=1}^{\infty} \frac{1}{\Lambda_n^2+\gamma_m^2} \cdot \frac{2\Lambda_n^2}{\Lambda_n^2+Hr} \cdot \frac{J_o(\Lambda_n y)}{J_o(\Lambda_n)} \cdot e^{-(\gamma_m^2+\Lambda_n^2)\tau}$$

Summing the two residues and returning the terms which were not functions of s and therefore unaltered by the inverse process, gives the full expression for the inverse of F1 as

$$T^* = \frac{\theta^*}{\nu\pi} \sum_{m=1}^{\infty} \left[\frac{4 \sin \Gamma_m}{2\Gamma_m+\sin 2\Gamma_m} \cdot \cos \Gamma_m z \left\{ \frac{I_o(\gamma_m y)}{HrI_o(\gamma_m)+\gamma_m I(\gamma_m)} - \sum_{n=1}^{\infty} \frac{2\Lambda_n^2}{(\Lambda_n^2+\gamma_m^2)(\Lambda_n^2+Hr)} \cdot \frac{J_o(\Lambda_n y)}{J_o(\Lambda_n)} \cdot e^{-(\Lambda_n^2+\gamma_m^2)\tau} \right\} \right] \tag{5.12}$$

where $\Gamma_m = \frac{L\gamma_m}{R}$ and Γ_m is the mth root of $Ha = \Gamma_m \tan \Gamma_m$ and where Λ_n is the nth root of $Hr = \frac{\Lambda_n J_1(\Lambda_n)}{J_o(\Lambda)}$. In the first residue, that for $s = 0$, in order to remove the complex 'i' , the J_o and J_1 functions have been converted to the equivalent I_o and I_1 forms. I_o and I_1 are modified Bessel functions of the first kind of the orders 0 and 1 respectively.

T^* is independent of the angular position and speed of rotation of the heat source and describes the bulk temperature variation. It is the bulk temperature variation which is of major interest in the recent line of investigation. The inverse transforms of the second and third parts of F are detailed in Appendix A4 and give the variation of the flash components of the temperature which is not required in the present analysis. The full expression for the non-dimensional temperature T' is found by summing the inverse transforms of F1, F2 and F3 . The resulting solution would give both the periodic and steady state parts of the bulk and flash temperatures in a cylinder with a band heat source rotating around the surface with convective heat loss from the surface and end faces. The expression has dimensions of temperature but due to the non-dimensional groups included within the expression is applicable to any set of conditions. In the next section the bulk temperature terms given by equation (5.12) are examined in some detail. The flash temperature terms are discussed briefly in Appendix A4 but are not considered further here.

5.4. Bulk Temperature Solution

5.4.1. Form of solution

The bulk temperature in a finite cylinder (eqn.(5.12)) is directly proportional to the heat soruce strength, $\theta^*/\nu\pi$, is a function of Ha, Hr and L/R , varies with axial and radial position in the cylinder but is independent of angular position within the cylinder and the speed of rotation, Ω , of the heat source. The form of the bulk temperature expression can be simplified to

$$T^* = \frac{\theta^*}{\nu\pi}\left[\sum_{m=1}^{\infty}\left(C_m - \sum_{n=1}^{\infty} D_{mn} \quad e^{-d_{mn}\tau}\right)\right] \quad - \text{Eq 5.13}$$

where both parts are series solutions, and where

$$C_m = \frac{4\sin\Gamma_m}{2\Gamma_m+\sin 2\Gamma_m} \cdot \cos\Gamma_m z \cdot \frac{I_o(\gamma_m y)}{HrI_o(\gamma_m y)+\gamma_m I_1(\gamma_m)}$$

$$D_{mn} = \frac{4\sin\Gamma_m}{2\Gamma_m+\sin 2\Gamma_m} \cdot \cos\Gamma_m z \cdot \frac{2\Lambda_n^2}{(\Lambda_n^2+\gamma_m^2)(\Lambda_n^2+Hr^2)} \quad \frac{J_o(\Lambda_n y)}{J_o(\Lambda_n)}$$

and $\quad d_{mn} = (\Lambda_n^2+\gamma_m^2)$.

The initial condition to the problem stated that before the application of the heat source the bulk temperature in the cylinder was uniform and equal to the ambient, i.e. at $\tau=0$, $e^o=1$, and the expression reduces to

$$T^* = \frac{\theta^*}{\nu\pi}\left(\Sigma C_m - D_{mn}\right)$$

Proof of this identity is given in Appendix A5.

With increasing τ, each term in the second series decays. This causes the bulk temperature to rise in an exponential fashion to its steady state value, i.e. as $\tau \to \infty$, $e^{-\infty} \to 0$ and

$$T^* \to \frac{\theta^*}{\nu\pi} \cdot \Sigma C_m$$

Thus in eqn.(5.13) the first series ΣC_m represents the steady state bulk temperature and the second series, the bulk transient, gives the variation of the cylinder temperature with time from the initial to the steady state temperature.

The equivalent terms for the bulk temperature in an infinitely long cylinder were given by Story as

$$T^* = \frac{\theta^*}{\nu\pi} \left\{ \frac{1}{Hr} - \sum_{n=1}^{\infty} \frac{2J_o(\Lambda_n y)}{(\Lambda_n^2+Hr^2).J_o(\Lambda_n)} \cdot e^{-\Lambda_n^2 \cdot \tau} \right\}$$

where Λ_n are the roots of $\dfrac{\Lambda_n J_1(\Lambda_n)}{J_o \Lambda_n} = Hr$.

In Story's solution there is no axial heat flow or axial temperature variation. In this solution for a finite length cylinder, if the heat loss from the ends by convection is greatly reduced, say as by a layer of insulating material, then the axial variation in the heat flow and temperature will also be reduced, and the solution will tend to that for infinite length cylinders by Story. This can be confirmed by taking the limit of eqn.(5.11) as $h_a \to 0$, which is detailed in Appendix 6.

Axial and radial Biot numbers, Ha and Hr , were formed when the governing equations and boundary conditions were normalised. Biot numbers are a non-dimensional comparison of the heat transfer at the surface of a body to the conduction within the body. Both the steady state and transient terms are functions of the Biot numbers either directly or via the identities $Ha=\Gamma_m.\tan\Gamma_m$ and $Hr = \Lambda_n J_1(\Lambda_n)/J_o(\Lambda_n)$. Thermal circuit analogy can be used to give an insight into the effect of Biot numbers on body temperature.

The radial Biot number, $Hr=h_r.R/k$ can be rewritten as

$$Hr = \frac{R}{kA_c} \Big/ \frac{1}{h_r A_c}$$

where A_c is the 'conduction' area.

The numerator gives the thermal resistance, of an element of length R and area A_c , to radial heat transfer in the cylinder by conduction. The denominator is the resistance to heat loss from an area A_c of the surface of the cylinder by convection.

Similarly Ha can be rewritten as

$$Ha = \frac{h_a L}{k} = \frac{L}{kA_c} \Big/ \frac{1}{h_a A_c}$$

If the Biot number is small, then the internal resistance to heat transfer by conduction is small compared to the convection resistance at the surface. Therefore the temperature can generally be expected to be higher and its distribution more uniform in a body with a low Biot number, than in a body with a high Biot number for a given heat input.

The variation of the temperature with L/R and axial and radial Biot numbers applicable to a wide range of materials and environments will now be examined. The temperature and its variation for the conditions in a two disc machine are examined in more detail in Chapter 6.

5.4.2. Steady state results

The steady state temperature T_s^* is given by

$$T_s^* = \frac{\theta^*}{\nu\pi}\left[\sum_{m=1}^{\infty}\frac{4\sin\Gamma_m}{2\Gamma_m+\sin 2\Gamma_m}\cdot\cos\Gamma_m z\cdot\frac{I_o(\gamma_m y)}{HrI_o(\gamma_m)+\gamma_m I_1(\gamma_m)}\right]$$

The variation of the normalised steady state bulk temperature with the L/R ratio at $y=0$, $z=0$, in a finite length cylinder is shown in Fig.5.6a-d. Each figure is for a different value of Hr in the range 0.02 to 100 and the curves in each figure are for Ha values in the range 0.002 to 100. The temperatures are normalised with respect to the temperatures in an infinite length cylinder with the same radial Biot number, Hr , but with no axial heat loss, i.e. with respect to the temperature from the Story solution, T_s^* (infinite). The variation of the steady state temperature with Hr in an infinite cylinder for the Story solution is shown in Fig. 5.6e. The $\frac{4\sin\Gamma_m}{2\Gamma_m+\sin 2\Gamma_m}$ term is common to the steady state and transient terms. It is positive when $m=1$ and oscillates in sign for successive values of m . As the magnitude of A_m also decreases for successive terms in the m series, the series representing the steady state bulk temperature converges. To plot Fig.5.6 the series ΣC_m was evaluated until two successive values agreed to within 1% .

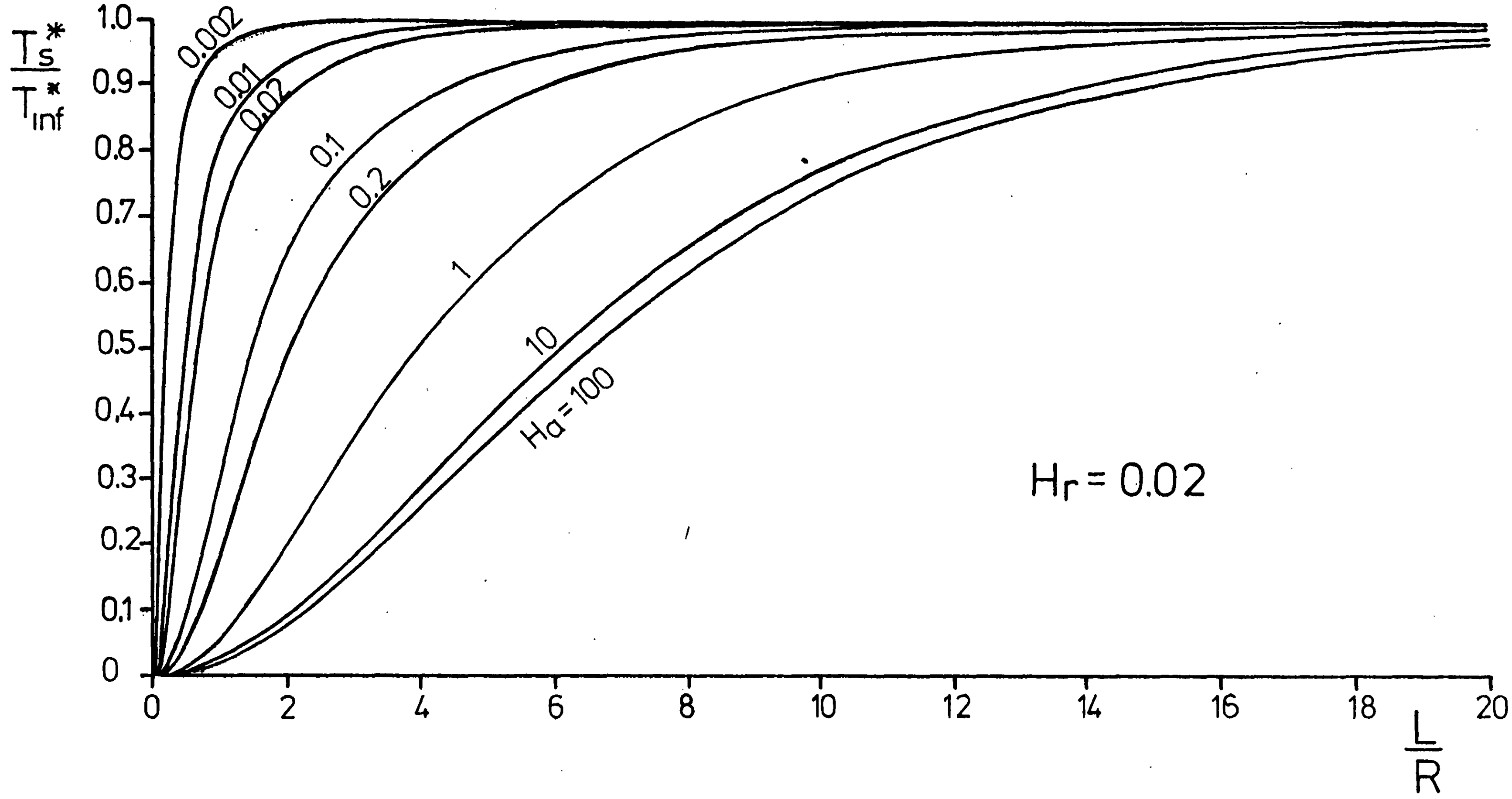

Figure 5.6a Variation of steady state temperature with L/R ratio at y = 0 in a finite length cylinder.

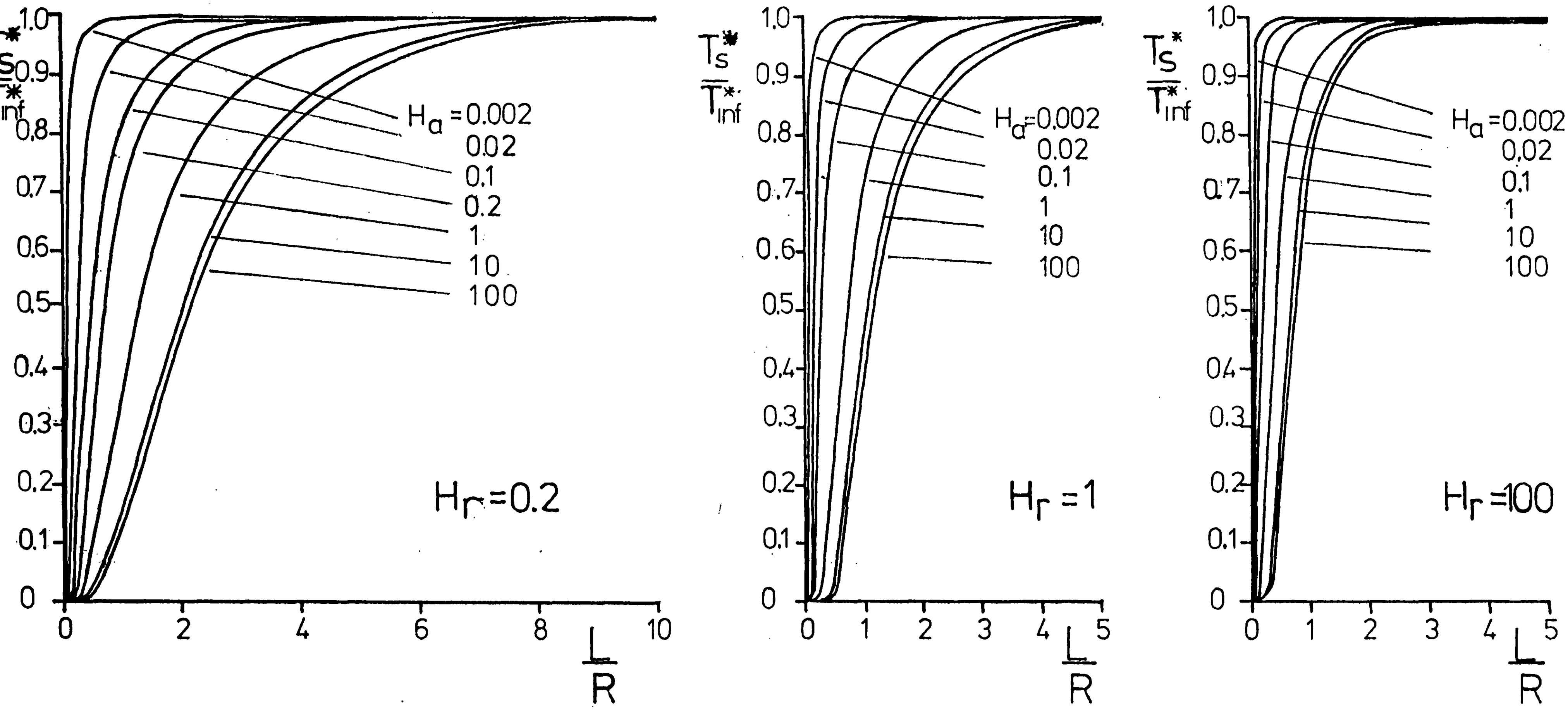

Figure 5.6 b,c+d Variation of steady state temperature with L/R ratio at y = 0 in a finite length cylinder.

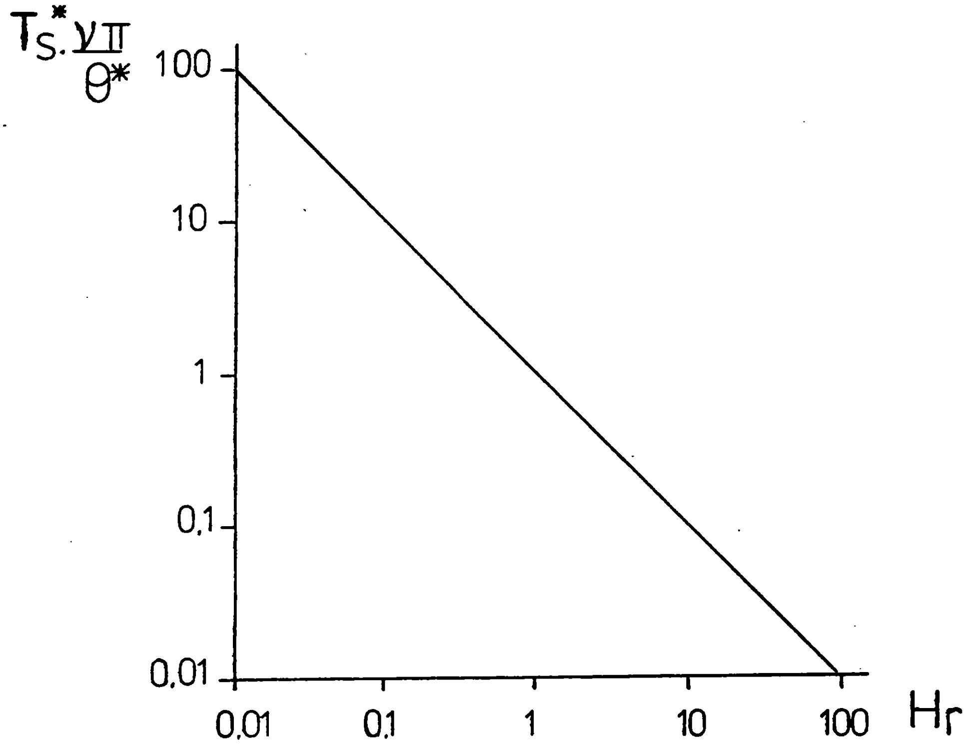

Figure 5.6e Variation of steady state temperature with Hr in an infinitly long cylinder.

Fig.5.6e, in combination with Figs.5.6a-d, show that increasing Hr or Ha at constant L/R reduces the temperature in finite length cylinders. The effect of the axial loss on the temperature becomes more pronounced at lower L/R , i.e. with short cylinders, and at low Hr . As L/R increases the effect of the axial heat loss on the temperature becomes negligible, i.e. T_s^*/T_s^* (infinite) $\rightarrow 1$. The L/R ratio at which the effect of the axial losses on the temperature at y=0, z=0 , becomes negligible increases with higher Ha and lower Hr .

5.4.3. Transient values

The bulk temperature transient is given by

$$\sum_{m=1}^{\infty} \sum_{n=1}^{\infty} D_{mn} \cdot e^{-d_{mn}\tau} = \sum_{m=1}^{\infty} \frac{4 \sin \Gamma_m}{2\Gamma_m + \sin 2\Gamma_m} \cdot \cos \Gamma_m z \left[\sum_{n=1}^{\infty} \frac{2 \Lambda_n^2}{Hr^2 + \Lambda_n^2} \cdot \frac{1}{\Lambda_n^2 + \gamma_m^2} \cdot \frac{J_o(\Lambda_n y)}{J_o \Lambda_n} \cdot e^{-(\Lambda_n^2 + \gamma_m^2)\tau} \right]$$

Both D_{mn} and d_{mn} are functions Ha, Hr and L/R . The magnitude of each term in the double series is D_{mn} and the exponential rate of decay is determined by d_{mn} .

Table 5.1 gives for the first few terms over each series for a combination of Hr, Ha and L/R values. At L/R=0.1, Ha=100 the series does not converge for the terms given. The Din series (Section 5.4.1) showed that $\sum_m \sum_n D_{mn} = \Sigma C_m$ at all conditions. Sufficient terms to prove this have not been evaluated, as lower values of Ha prevail in a two disc machine.

At all other conditions as in the steady state solution, successive terms in the series alternate in sign and decrease in size, i.e. the series converge and the series can be truncated without undue error when successive values become similar. The number of terms that have to be summed depends on the size of both the d_{mn} and D_{mn} terms. For example, referring to Table 5.1 when Ha and Hr are low and L/R=0.1 , d11 >> d12, d21 ... and D11 >> D12, D21 ... , and so at these conditions the double transient series can be replaced with reasonable accuracy by $D11.e^{-d11.\tau}$.

L/R		Ha=0.002	Hr=0.02		Ha=0.002	Hr=100		Ha=100	Hr=0.02		Ha=100	Hr=100	
		Γ_1	Γ_2	Γ_3	Γ_1	Γ_2	Γ_3	Γ_1	Γ_2	Γ_3	Γ_1	Γ_2	Γ_3
0.1	Λ_1	8.344	-5×10^{-7}	5×10^{-10}	0.0154	-1.5×10^{-6}	2.3×10^{-7}	0.0105	-3.9×10^{-4}	8.32×10^{-5}	4.66×10^{-4}	-1.76×10^{-5}	3.8×10^{-6}
	Λ_2	-0.333	negligible		-0.0105	negligible		-0.0247	9.6×10^{-4}	-2.1×10^{-4}	-1.48×10^{-3}	6.1×10^{-5}	-1.3×10^{-5}
	Λ_3	0.135			0.0085			0.0291	-1.3×10^{-3}	2.7×10^{-4}	2.51×10^{-3}	-1.18×10^{-4}	2.6×10^{-5}
1	Λ_1	47.83	-5×10^{-5}	8×10^{-9}	0.016	-1.5×10^{-6}	2×10^{-7}	1.035	-0.039	0.0168	0.0143	-0.0014	3.5×10^{-4}
	Λ_2	-0.34	negligible		-0.0106	negligible		-0.184	0.058	-0.0169	-0.0125	2.6×10^{-3}	-8.9×10^{-4}
	Λ_3	0.135			0.0085			0.0821	-0.04	0.0154	0.0105	-2.7×10^{-3}	1.2×10^{-3}
10	Λ_1	50.21	-3.7×10^{-3}	4.6×10^{-4}	0.016	-4.1×10^{-6}	1.4×10^{-6}	39.77	-3.29	0.787	0.202	-0.0065	0.0036
	Λ_2	-0.34	negligible		-0.0106	negligible		-0.429	0.141	-0.0824	-0.0134	0.0044	-0.0024
	Λ_3	0.135			0.0085			0.172	-0.057	0.034	0.0108	-0.0039	0.0021

Table 5.1a Transient terms Dmn for a range of Biot numbers and L/R ratios.

L/R		Ha=0.002 Hr=0.02			Ha=0.002 Hr=100			Ha=100 Hr=0.02			Ha=100 Hr=100		
		Γ_1	Γ_2	Γ_3	Γ_1	Γ_2	Γ_3	Γ_1	Γ_2	Γ_3	Γ_1	Γ_2	Γ_3
0.1	Λ_1	0.239	987	3948	5.868	993	3953	242	2177	6047	247	2182	6052
	Λ_2	14.9	negligible		30	negligible		256	2191	6061	271	2207	6077
	Λ_3	49.4			73.6			291	2226	6096	315	2225	6120
1	Λ_1	0.0418	9.9	39	5.67	15.54	45.1	2.46	21.8	60.5	8.09	27.4	66.1
	Λ_2	14.7	negligible		29.8	39.7	69.3	17.1	36.5	75.2	32.3	51.6	90.3
	Λ_3	49.2			73.4	83.2	113	51.7	71	110	75.8	95.2	134
10	Λ_1	0.0398	0.138	0.434	5.67	5.76	6.06	0.064	0.257	0.644	5.69	5.88	6.27
	Λ_2	14.7	negligible		29.8	29.9	30.2	14.7	14.9	15.3	29.9	30.1	30.5
	Λ_3	49.2			73.4	73.5	73.8	49.3	49.5	49.8	73.4	73.6	74.0

Table 7.1b Transient decay term, dmn, for a range of Biot numbers and L/R.

D11 , as for the steady state term C1 , is larger at low Ha, Hr and at larger L/R values. d11 , or the rate of decay, increases with increasing Biot number. On increasing L/R the d11 values tend to the equivalent values from the solution of Story. Therefore, with greater convection effect, the system reaches its equilibrium value more quickly and this value is low.

5.4.4. Length effects and variation of temperature with position

Before studying the variation of temperature within the cylinder, an ambiguity in the effect of Ha must be discussed. The plot of steady state temperature y=0, z=0 for Hr=0.2 from Section 5.4.2 is reproduced in Fig.5.7. Take the conditions represented by point 1 , i.e.

$$L/R = 2 \quad Ha = 0.2 \ , \ T_s^*/T_s^* \text{ (infinite)} = 0.41$$

The expected effect on temperature, of higher Biot numbers, - to reduce the steady state temperature due to the greater convective heat loss, has already been demonstrated. Changing h_a and consequently Ha at constant L/R , can be represented by a vertical line on the plot. It was shown that in the limit as $h_a \rightarrow 0$, Ha $\rightarrow 0$, the finite solution for the temperature tends to that of the infinite solution of Story.

However, if L increases whilst h_a , h_r , k and R are held constant then both the L/R ratio and Ha increase and the operating point moves along the path AB as shown, so the temperature increases. This is apparently the opposite effect of the Biot number on temperature as the previous case but the anomaly can be explained by physical reasoning. As the length increases, the heat source also increases so that the heat input and radial heat loss per unit volume remains constant. The axial heat loss from the cylinder ends is determined by the area of the end faces and h_a , both of which remain constant so the heat loss from the end faces per unit volume of material decreases. The net effect is a rise in

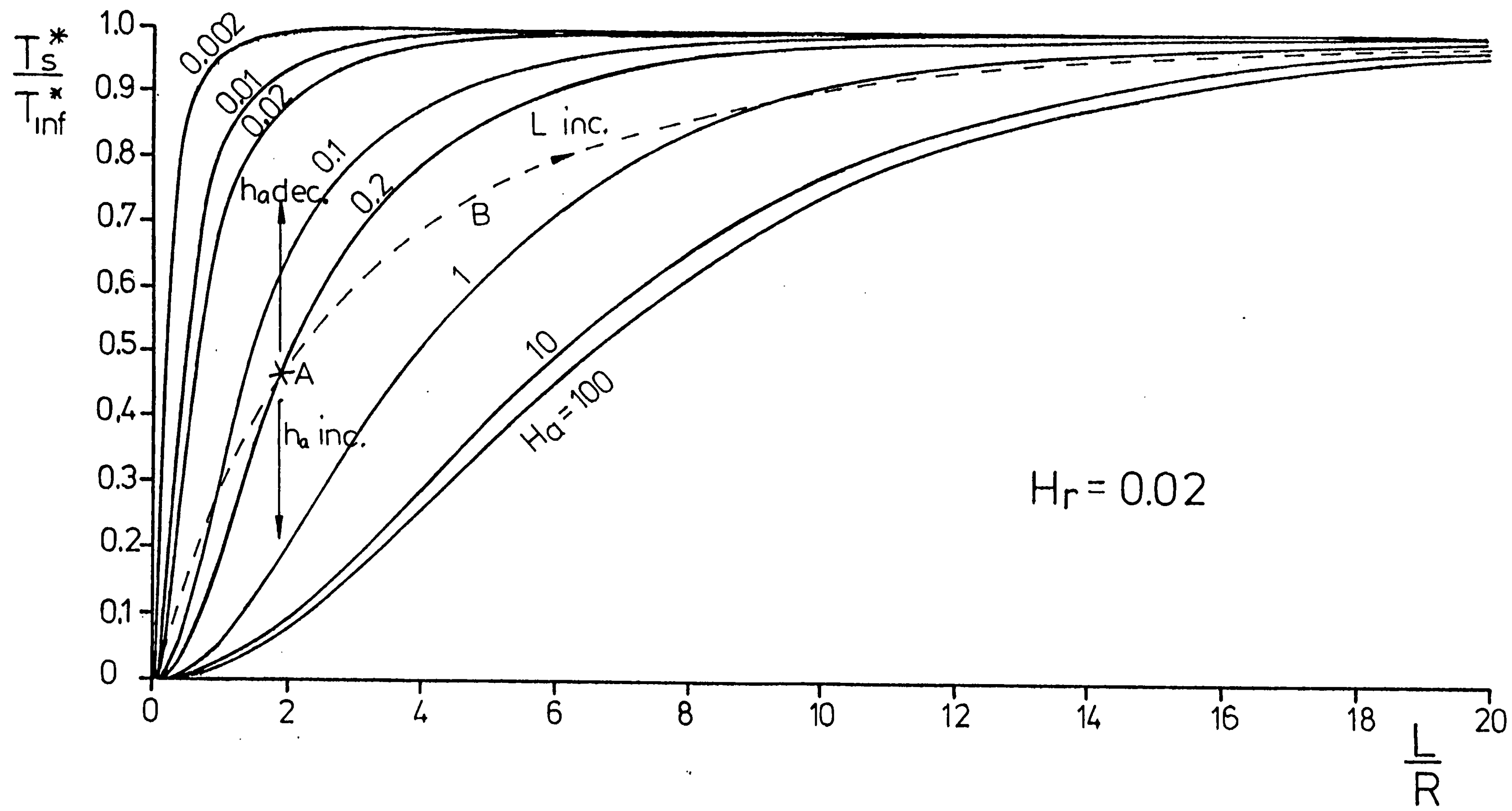

Figure 5.7 Effect on temperature of varying Ha by a/ L/R and b/ ha.

temperature. To increase h_a and hence Ha at a constant L/R increases the heat loss per unit volume of material, whilst the heat input per unit volume remains constant which results in a drop in the centre temperature.

The effect on temperature of the axial Biot number is therefore different according to whether it is changed via h_a or L as the variation with L also alters the L/R ratio.

Variation of temperature with position

Both the steady state and transient terms vary with y and z , i.e. radially and axially.

The axial variation in the temperature of each term in the series' for both the steady state and transient bulk temperatures is given by the factor

$$\cos\,(\Gamma_m.z) = \cos\left(\frac{L\,\gamma_m.z}{R}\right)$$

where $\Gamma_m.\tan\Gamma_m = Ha$.

At z=0 , the temperature is a maximum and it is symmetric about z=0 . The first five roots of the eigen condition, $\Gamma_m \tan \Gamma_m = Ha$, are given in Table 5.2. When Ha is small the first terms in the series $\sum_{m=1}^{\infty} C_m$ and $\sum_{m=1}^{\infty}\sum_{n=1}^{\infty} D_{mn}$ dominate and so the series can be reduced to C1 and $D11.e^{-d11.\tau}$.

As $Ha \to 0$, $\Gamma_1 \to 0$, and $\cos\,\Gamma_1 z \to 1$, for $-1 < z < +1$.

Therefore, for short cylinders, $L \to 0$, or cylinders with negligible end losses, $h_a \to 0$, there is little axial variation in the temperature. As Ha increases, as a result in the increase of h_a or L , Γ_1 also increases and the temperature variation becomes more pronounced. In the limit as Ha tends to large values, $\Gamma_1 \to \pi/2$, the distribution of temperature becomes a half cosine with the temperature maximum in the

Ha	Γ_1	Γ_2	Γ_3	Γ_4	Γ_5
0.000	0.0000	3.1416	6.2832	9.4248	12.5664
0.002	0.0447	3.1422	6.2835	9.4250	12.5665
0.004	0.0632	3.1429	6.2838	9.4252	12.5667
0.006	0.0774	3.1435	6.2841	9.4254	12.5668
0.008	0.0893	3.1441	6.2845	9.4256	12.5670
0.010	0.0998	3.1448	6.2848	9.4258	12.5672
0.020	0.1410	3.1479	6.2864	9.4269	12.5680
0.040	0.1987	3.1543	6.2895	9.4290	12.5696
0.060	0.2425	3.1606	6.2927	9.4311	12.5711
0.080	0.2791	3.1668	6.2959	9.4333	12.5727
0.100	0.3111	3.1731	6.2991	9.4354	12.5743
0.200	0.4328	3.2039	6.3148	9.4459	12.5823
0.300	0.5218	3.2341	6.3305	9.4565	12.5902
0.400	0.5932	3.2636	6.3461	9.4670	12.5981
0.500	0.6533	3.2923	6.3616	9.4775	12.6060
0.600	0.7051	3.3204	6.3770	9.4979	12.6139
0.700	0.7506	3.3477	6.3923	9.4983	12.6218
0.800	0.7910	3.3744	6.4074	9.5087	12.6296
0.900	0.8274	3.4003	6.4224	9.5190	12.6375
1.000	0.8603	3.4256	6.4373	9.5293	12.6453
1.500	0.9882	3.5422	6.5097	9.5801	12.6841
2.000	1.0769	3.6436	6.5783	9.6296	12.7223
3.000	1.1925	3.8088	6.7040	9.7240	12.7966
4.000	1.2646	3.9352	6.8140	9.8119	12.8678
5.000	1.3138	4.0336	6.9996	9.8928	12.9352
6.000	1.3496	4.1116	6.9924	9.9667	12.9988
7.000	1.3766.	4.1746	7.0640	10.0339	13.0584
8.000	1.3978	4.2264	7.1263	10.0949	13.1141
9.000	1.4149	4.2694	7.1806	10.1502	13.1660
10.000	1.4289	4.3058	7.2281	10.2003	13.2142
15.000	1.4729	4.4255	7.3959	10.3898	13.4078
20.000	1.4961	4.4915	7.4954	10.5117	13.5420
30.000	1.5202	4.5615	7.6057	10.6543	13.7085
40,000	1.5325	4.5979	7.6647	10.7334	13.8048
50.000	1.5400	4.6202	7.7012	10.7832	13.8666
100.000	1.5552	4.6658	7.7764	10.8871	13.9981

Table 5.2 Roots of eigen condition $\Gamma_m \tan \Gamma_m = Ha$, (m = 1-5).

centre and tending to the ambient at $z=\pm1$. Larger axial Biot numbers are associated with higher internal resistance to the flow of heat by conduction and larger temperature gradients.

As the axial Biot number increases more terms in the series have to be evaluated. In the limit $Ha \to \infty$, Γ_m $((m-1)\pi + \pi/2)$, the variation with length of each term in the series will be over a number of cycles of a cosine but will still $\to 0$ at $z=\pm1$.

In summary, as L increases, the steady state bulk temperature at the centre $y=0$, $z=0$ of the cylinder increases to the equivalent temperature in an infinitely long cylinder with no end losses, but the axial temperature distribution becomes more severe. As h_a decreases the centre bulk temperature again tends to the 'infinite' solution but the distribution becomes more uniform.

Radial variation

The radial variation of the temperature is given by $I_o(\gamma_m . y)$ that is a function of Ha for the steady state terms and by $J_o(\Lambda_n . y)$, a function of Hr for the transient.

The steady state radial variation has the form shown in Fig.5.8a. The temperature is a minimum value at $y=0$, where $I_o(0)=1$, and a maximum at the surface, $y=1$, and is determined by γ_m . γ_m becomes larger with increasing Ha and decreasing L/R . That is the radial variation becomes greater with a high axial heat transfer coefficient, h_a , or with short cylinders. As $h_a \to 0$, the radial variation $\to 0$, as in the infinite solution.

The form of $J_o(\Lambda_n y)/y$, the radial variation of the transient, is shown in Fig.5.8b, and the roots of the condition $Hr = \Lambda J_1(\Lambda_n)/J_o(\Lambda_n)$ in Table 5.3.

At $y=0$, the centre of the cylinder $J_o(0)=1$, the maximum value. The minimum is at the surface and is determined for the first term in the transient series D11 by Λ_1 . The first root Λ_1, increases as Hr

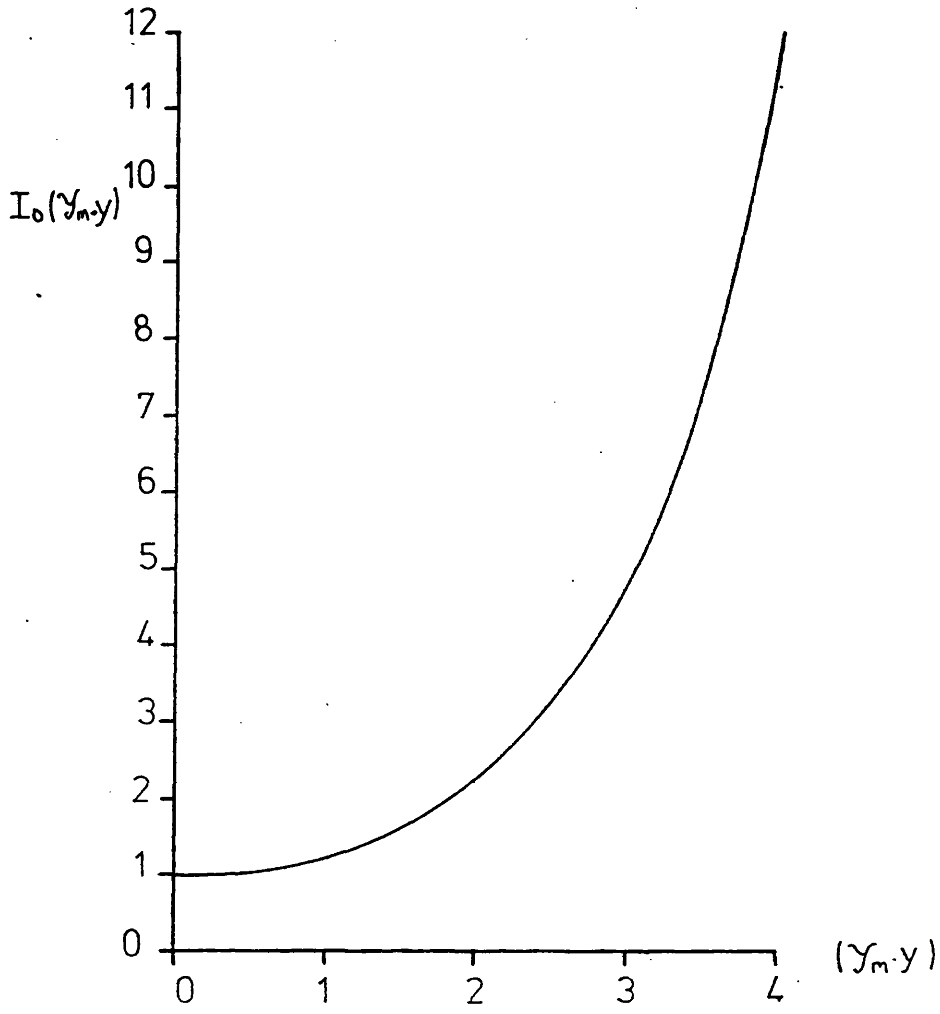

Figure 5.8a Radial variation of steady state bulk temperature at z = 0.

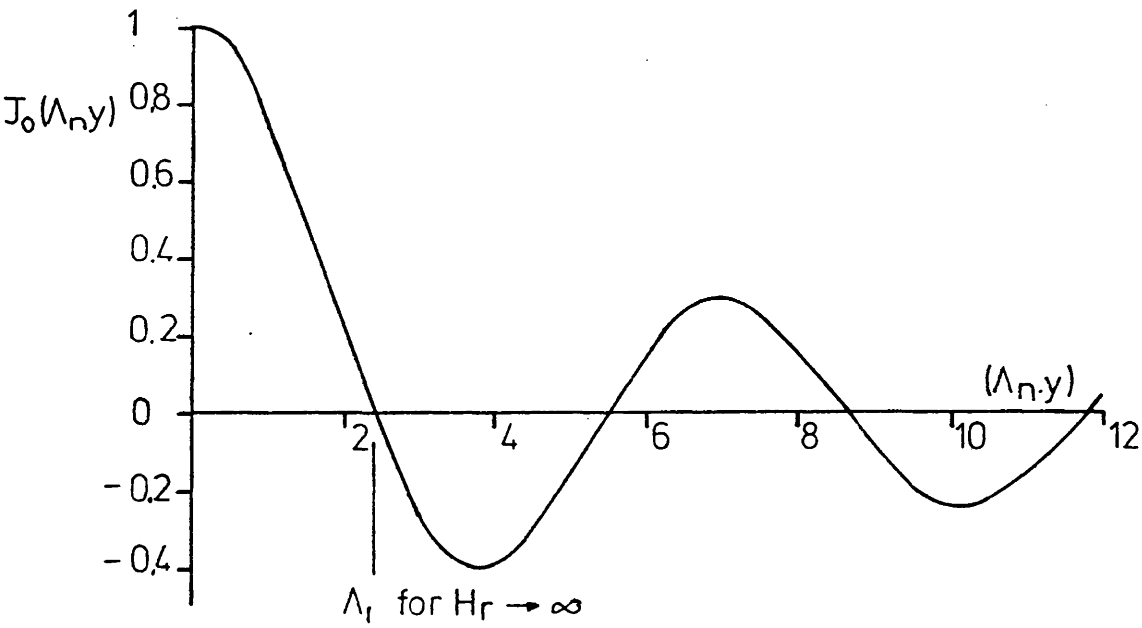

Figure 5.8b Radial variation of transient bulk temperature term.

Hr	Λ_1	Λ_2	Λ_3	Λ_4	Λ_5
0.00	0.0000	3.8317	7.0156	10.1735	13.3237
0.02	0.1995	3.8369	7.0184	10.1754	13.3252
0.04	0.2814	3.8421	7.0213	10.1774	13.3267
0.06	0.3438	3.8473	7.0241	10.1794	13.3282
0.08	0.3960	3.8525	7.0270	10.1813	13.3297
0.10	0.4417	3.8577	7.0298	10.1833	13.3312
0.20	0.6170	3.8835	7.0440	10.1931	13.3387
0.30	0.7465	3.9091	7.0582	10.2029	13.3462
0.40	0.8516	3.9344	7.0723	10.2127	13.3537
0.50	0.9408	3.9594	7.0864	10.2225	13.3611
0.60	1.0184	3.9841	7.1004	10.2322	13.3686
0.70	1.0873	4.0085	7.1143	10.2419	13.3761
0.80	1.1490	4.0325	7.1282	10.2516	13.3835
0.90	1.2048	4.0562	7.1421	10.2613	13.3910
1.00	1.2558	4.0795	7.1558	10.2710	13.3984
2.00	1.5994	4.2910	7.2884	10.3658	13.4719
3.00	1.7887	4.4634	7.4103	10.4566	13.5434
4.00	1.9081	4.6018	7.5201	10.5423	13.6125
5.00	1.9898	4.7131	7.6177	10.6223	13.6786
6.00	2.0490	4.8033	7.7039	10.6964	13.7414
7.00	2.0937	4.8772	7.7797	10.7646	13.8008
8.00	2.1286	4.9384	7.8464	10.8271	13.8566
9.00	2.1566	4.9897	7.9051	10.8842	13.9090
10.00	2.1795	5.0332	7.9569	10.9363	13.9580
15.00	2.2509	5.1773	8.1422	11.1367	14.1576
20.00	2.2880	5.2568	8.2534	11.2677	14.2983
30.00	2.3261	5.3410	8.3771	11.4221	14.4748
40.00	2.3455	5.3846	8.4432	11.5081	14.5774
50.00	2.3572	5.4112	8.4840	11.5621	14.6433
100.00	2.3809	5.4652	8.5678	11.6747	14.7834

Table 5.3 Roots of eigen condition $Hr = \dfrac{\Lambda_n J_1(\Lambda_n)}{J_0(\Lambda_n)}$, (n = 1-5).

increases so $J_o(\Lambda_1.y)$ decreases, that is the radial variation of the transient term becomes more pronounced.

Before the results of this chapter can be applied to predict temperatures for the specific case of the two disc machine, the size and strength of the common heat source, the effect of champhered discs reducing the contact area and the heat transfer coefficients and other parameters must be determined. This is the subject of the next chapter.

CHAPTER 6

PREDICTION OF BULK TEMPERATURE IN A TWO-DISC MACHINE SCUFFING TEST

6.1 Introduction

Chapter 5 has developed a general statement (eqn (5.12)) for the rise in bulk temperature at any location in a single finite cylinder resulting from a band heat source rotating around the surface for time t. In developing this model it was assumed that the heat source had angular extent $2\theta^*$ that it acted over the full length of the cylinder and had a uniform source strength β. It was also assumed that all the heat from the source was conducted into the discs.

Some modifications to this general statement for bulk temperature are needed if it is to be used to predict the temperature changes in the discs of a two disc machine. These adaptations are made in this chapter.

The discs in the two disc machine have the configuration shown in Fig.6.1a. In general parlance, the L dimension of the disc, due to the low aspect ratio, L/R, would be called the width. For continuity with the definitions for cylinders in the previous chapter it will be referred to here as the length of the discs. The 'length' of the heat source is also the dimension in the axial direction.

When two rotating discs are loaded together heat is generated in the resulting parallel contact region by shearing of the lubricant film. The contact region between the discs acts therefore as a heat source of, as yet, unknown strength to both the discs. The common heat source is stationary relative to the machine whilst both the discs rotate through it. The heat generated divides so that a proportion of it goes into each of the discs. In comparison, the model of Chapter 5 was for a single stationary cylinder with a heat source of known strength, rotating around the surface.

To find the heat source strength appropriate to each of the discs in the contacting pair, expressions are required for the total heat generated in the contact and the way in which it divides between the two discs. These points are discussed in Section 6.2.

In the model the heat source extended over the full length of the cylinder. In two discs machines the edges of one or both of the discs are often chamfered to reduce edge loading effects. This results in the contact region and hence the heat source, extending over only a portion of the disc length although the heat generated is conducted throughout the disc. In Section 6.3 the effect of a chamfered disc on the bulk temperature rise is examined.

The analysis assumed as an initial condition that the temperature of the cylinder is uniform and equal to the ambient and that the heat source strength is constant with time. These assumptions are reasonable for the first increment of a two disc test. For the second and successive increments, the change in load at the beginning of each increment causes a step change in the heat source strength applied to discs where the bulk temperature is already above the ambient. In Section 6.4 the theory of Chapter 5 is extended to cover the conditions of more than one increment.

In Sections 6.5 and 6.6 suitable heat transfer coefficients for a disc rotating in the two disc machine environment are determined.

The amendments to the general statement and the results of Sections 6.2-6.6 are combined in Section 6.7 to predict the bulk temperature changes in some of the tests reported in Chapter 3. The values are compared to those measured in the tests.

The thermal response of the Rossides and Story test, were thought to be a consequence of the machine. In Section 6.8 the results of this and the previous chapter are used to examine the extent to which the difference could have been expected.

6.2. Heat source strength

In an elastohydrodynamic contact heat is generated by shearing of the viscous fluid film in the parallel region. The film thickness is typically two to three orders of magnitude less than the Hertzian contact width, 2b, Fig.6.1 . Since the fluid film is bounded by material of much higher conductivity than the oil the heat conduction can be considered to only be in the cross film direction, i.e. into the discs. Archard (1972) has shown that as the time it takes for heat to conduct from the centre line of the contact to the disc surface, $\frac{h^2}{\pi^2 \kappa_1}$ is small compared to the time for an element of fluid to pass through the contact $2b/u$, then it can be assumed that all the heat generated in the fluid is conducted into one or other of the discs rather than being carried out of the contact in the oil.

The rate of total heat generation due to viscous shearing of the fluid film is

$$Q = \mu W U_s$$

where μ is the coefficient of friction, W is the total load between the discs, and U_s , the sliding speed.

The intensity of the common heat source between the discs, if the heat is generated at the same rate over a plane between the discs, is

$$\beta_{tot} = \frac{\mu W U_s}{4bL} \tag{6.1}$$

where $4bL$ is the contact area.

The surfaces of both discs pass through this common heat source and the heat generated divides between the two discs. Flash temperature theory can be used to determine what proportion of the heat passes into each of the discs.

When a heat source is applied to the surface of a body or when a point on the surface of a body moves through a heat source the temperature at the surface rises above the bulk temperature. This is termed the

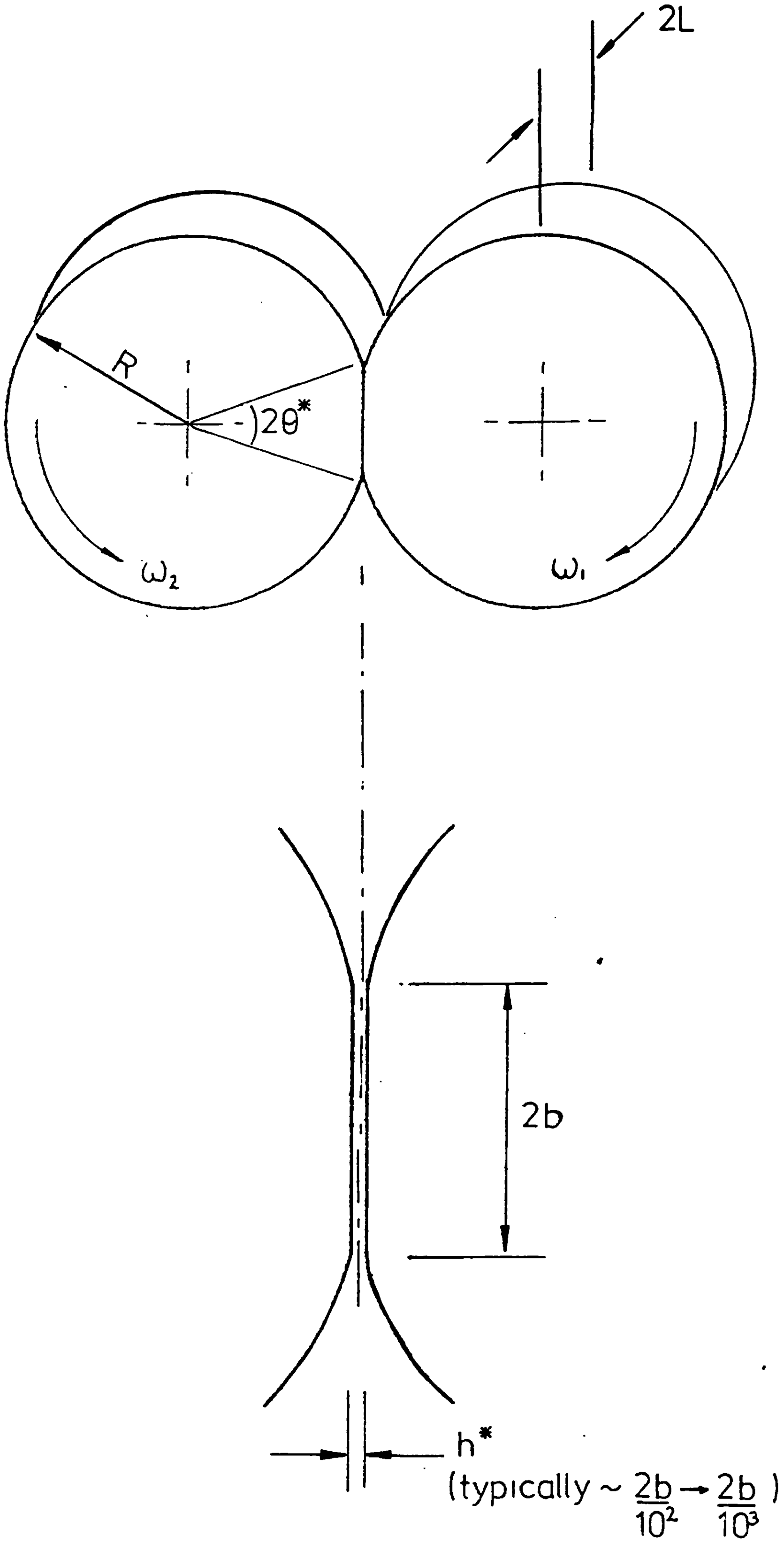

Figure 6.1 Configuration of a/ the discs and b/ the contact in a two disc machine.

surface flash temperature, say T_f. If the heat source has strength β then

$$T_f \propto \beta \cdot f(\text{variables})$$

where f(variables) denotes a function of several variables such as time and the material of the body. The appropriate function is determined by the relative speed of the heat source and the surface.

The assumption made by Archard (1959) to determine the division of the heat and the flash temperatures for two surfaces sharing a common heat source is used here. The assumption is that:

> the total heat produced in the contact divides between the two bodies such that at any instant the average temperature over the contact area of each surface is the same.

If the total heat produced in the contact area between the discs, β_{tot}, divides so that β_1 goes into body 1 and β_2 into body 2, then in the contact region the flash temperature rise on surface 1 is

$$T_f|_1 \propto \beta_1 \cdot f_1(\text{variables})$$

and on surface 2 is

$$T_f|_2 \propto \beta_2 \cdot f_2(\text{variables})$$

The total temperature is the flash superimposed on the bulk. The assumption that the heat divides so that the average temperature over the contact region is the same on each surface gives for the division of the heat between surface 1 and surface 2,

$$T^*|_1 + \hat{T}_f|_1 = T^*|_2 + \hat{T}_{f\ 2} \qquad (6.2)$$

where ^ denotes the average value over the contact area.

If the underlying bulk temperatures of the two contacting bodies are the same this reduces to

$$\hat{T}_f|_1 = \hat{T}_f|_2 \qquad (6.3)$$

The function of the variables which determines the flash temperature rise depends on the size of the non-dimensional group, $ub/2\kappa$, where u is the relative speed of the heat source to the surface. This parameter is a comparison of the time it takes for a point on the surface to pass through the contact compared to the time it takes an element of heat to conduct an equivalent depth into the discs. When $ub/2\kappa < 0.1$ the heat source is 'slow', and near steady state heat flow conditions prevail near the contact. When $ub/2\kappa > 5$, the heat source is 'fast', for which case sideways heat flow can be neglected and only linear conduction into the body occurs. For both the surfaces moving through the contact in the two disc machine, $ub/2\kappa > 5$, i.e. both surfaces are fast moving with respect to the heat source.

For a fast moving heat source the function of the variables for surface flash temperature was given by Carslaw and Jaeger (1947) as

$$f(\text{variables}) = \frac{2t^{1/2}}{(\pi\rho c\kappa)^{1/2}}$$

where t is the time that the point has been exposed to the heat source, and κ, ρ and c are the usual material properties. Therefore the flash temperature on the disc 1 is

$$T_f\big|_1 = \beta_1 \cdot \frac{2t^{1/2}}{(\pi\rho_1\kappa_1 c_1)^{1/2}}$$

and the average flash surface temperature over the contact area is

$$\hat{T}_f\big|_1 = \beta_1 \cdot \frac{2}{(\pi\rho_1\kappa_1 c_1)^{1/2}} \cdot \frac{\int_0^{t_1} t^{1/2}\,dt}{t_1}$$

where t_1 is the time for any point on surface 1 to go through the contact.

On evaluating the integral this becomes

$$\hat{T}_f\big|_1 = \frac{4}{3}\,\frac{\beta_1 t_1^{1/2}}{(\pi\rho_1 c_1\kappa_1)^{1/2}}$$

t_1 can be related to the contact width 2b and the surface speed u_1 to give

$$\hat{T}_f\big|_1 = \frac{4}{3}\,\frac{\beta_1(2b)^{1/2}}{(\pi\rho\ c\ \kappa\ )^{1/2}}\,\frac{1}{u_1^{1/2}} \qquad (6.4a)$$

Similarly for disc 2

$$\hat{T}_f\big|_2 = \frac{4}{3}\ \frac{\beta_2\ (2b)^{1/2}}{(\pi\rho_2 c_2 K_2)^{1/2}} \cdot \frac{1}{u_2^{1/2}} \tag{6.4b}$$

As the heat divides so that $\hat{T}_f\big|_1 = \hat{T}_f\big|_2$, eqns.(6.4a) and (6.4b) can be equated to give,

$$\frac{\beta_1}{(\pi\rho_1 c_1 K_1)^{1/2}}\ \frac{1}{u_1^{1/2}} = \frac{\beta_2}{(\pi\rho_2 c_2 K_2)^{1/2}}\ \frac{1}{u_2^{1/2}}$$

which, for bodies of the same material, reduces to

$$\frac{\beta_1}{u_1^{1/2}} = \frac{\beta_2}{u_2^{1/2}}$$

As it was initially assumed that all the heat goes into one or other of the discs, i.e. $\beta_{tot} = \beta_1 + \beta_2$ then, it can be shown that

$$\beta_1 = \beta_{tot} \cdot \frac{u_1^{1/2}}{u_1^{1/2} + u_2^{1/2}} \tag{6.5a}$$

and similarly

$$\beta_2 = \beta_{tot} \cdot \frac{u_2^{1/2}}{u_1^{1/2} + u_2^{1/2}} \tag{6.5b}$$

Therefore the common heat source strength, $\beta_{tot} = \mu W U_s/4bL$, is a function of the sliding speed. If the discs are of the same material and at the same bulk temperature the division between the discs is a function of the individual surface speeds. The heat source strength in the expression for the bulk temperature was

$$\frac{\theta^*}{\nu\pi} = \frac{\theta^* R\beta}{\pi K}$$

where $2\theta^*$ is the angle subtended by the heat source at the centre of the disc. When two discs are loaded together the high local pressures flatten the surface of the discs in the contact area. As the size of the flattened area is small compared to the dimensions of the discs, $b \sim R\theta^*$.

Using the expressions for β_{tot} (eqn.(6.1)) and its division, (eqns.(6.5a and b)), the term $\theta^*/\nu\pi$ becomes, for disc 1,

$$\frac{\theta_1^*}{\nu\pi} = \frac{1}{\pi K_1} \cdot \frac{\mu W U_s}{4L} \cdot \frac{u_1^{1/2}}{u_1^{1/2} + u_2^{1/2}} \tag{6.6}$$

and a similar expression gives the heat source strength for disc 2.

The heat source group for a disc in a contacting pair can therefore be calculated from the surface speeds, load, friction and disc dimensions, without prior knowledge of the contact area.

If the discs are originally at different temperatures then expressions for the division of heat can be similarly obtained by substituting expressions for the average flash temperature rise (eqn.(6.4a)) into eqn.(6.2) to give, again for bodies of the same material,

$$\beta_1 = \beta \cdot \frac{u_1^{1/2}}{u_1^{1/2} + u_2^{1/2}} + (T^*|_2 - T^*|_1) \cdot \frac{(\pi\rho c\kappa)^{1/2}}{(2b)^{1/2}} \cdot \frac{u_1^{1/2} \cdot u_2^{1/2}}{u_1^{1/2} + u_2^{1/2}} \qquad (6.7)$$

In addition to the surface speeds, the division of heat also depends on the difference in the disc bulk temperatures, the disc material and the size of the contact area. It requires computation at each increment in a scuffing test. A difference in the disc bulk temperatures reduces the proportion of heat which goes into the hotter disc.

6.3. The effect of disc chamfer

In Chapter 5 the heat source and its rotation was represented by the Fourier series

$$g(R,\theta,t).v(\ell) = \beta\left[\frac{\theta^*}{\pi} + \frac{2}{\pi}\sum_{q=1}^{\alpha}\frac{\sin q\theta^*.\cos q(\theta-\omega t)}{q}\right]. \quad v(\ell) \qquad (5.3)\text{bis}$$

For plain discs as the heat source is uniform along the length of the cylinder, the function $v(\ell)$, which represents the axial variation of the heat source, is taken as $v(\ell) = 1$.

With a chamfered disc the contact length is reduced, Fig.6.2a, but the heat generated in the contact area is still conducted into the whole discs. To allow for the variation of the heat source along the length of the discs, the function $v(\ell)$ can be replaced by a second Fourier series over 1 representing the function shown in Fig.6.2b.

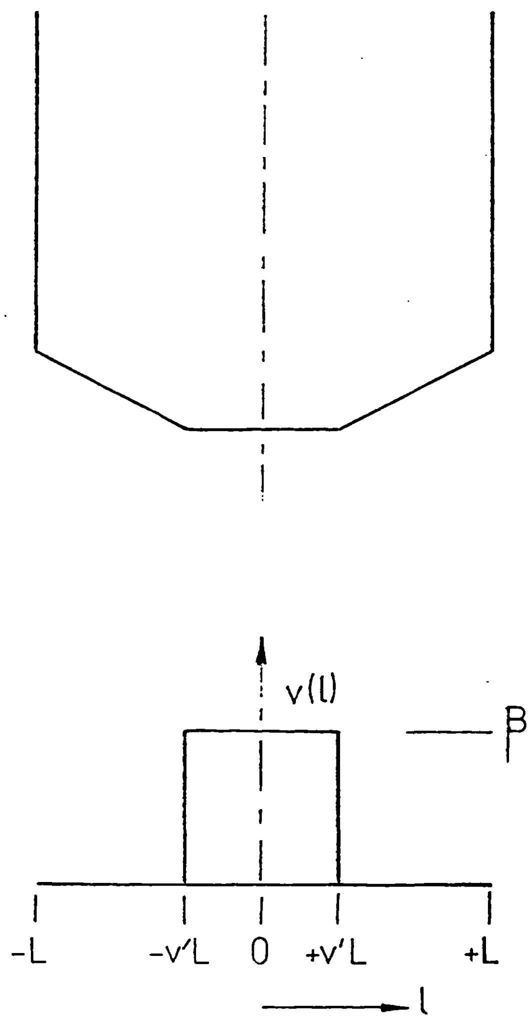

Figure 6.2 Variation of heat source strength with l for a champhered disc.

Since $v(\ell)$ is 'even' for the interval $-L$ to $+L$, i.e. $v(\ell) = v(-\ell)$, the appropriate form of the Fourier series is

$$v(\ell) = \frac{1}{2} a_o + \sum_{j=1}^{\alpha} a_j \cos j \frac{\pi\ell}{L}$$

where

$$a_o = \frac{2}{L} \int_o^L v(\ell) d\ell \quad \text{and} \quad a_j = \frac{2}{L} \int_o^L v(\ell).\cos j \frac{\pi\ell}{L} . d\ell$$

Evaluation of a_o and a_j gives

$$v(\ell) = v' + \sum_{j=1}^{\alpha} \frac{2}{j\pi} . \sin(j\pi v')\cos\left(\frac{j\pi\ell}{L}\right)$$

where v' = the proportion of the cylinder length over which the heat source extends or $2v'L$ = heat source length.

The full expression representing the heat source for a chamfered disc becomes,

$$g(R,\theta,t).v(\ell) = \beta\left[\frac{\theta^*}{\pi} + \frac{2}{\pi}\sum_{q=1}^{\alpha}\frac{\sin q\theta^* \cos q(\theta-\omega t)}{q}\right]\left[v' + \sum_{j=1}^{\alpha}\frac{2}{j\pi}\sin(j\pi v_i')\cos\left(j\frac{\pi\ell}{L}\right)\right]$$

This expression for $g(R,\theta,t).v(\ell)$, makes the fifth boundary condition when normalised and Laplace transformed

$$\frac{\partial F}{\partial z}(1,\theta,z,s) + HrF(1,\theta,z,s) = G'(1,\theta,s).v(z)$$

$$= \frac{1}{\nu}\left[\frac{\theta^*}{s\pi} + \frac{2}{\pi}\sum_{q=1}^{\alpha}\frac{\sin q\theta^*(s\cos q\theta + q\Omega\sin q\theta)}{q(s^2+q^2\Omega^2)}\right].\left[v' + \sum\frac{2}{j\pi}\sin j\pi v'.\cos j\pi 2\right] \qquad (6.8)$$

The solution given in the previous chapter for the temperature in finite cylinders is unaltered by this modification until the fifth boundary condition is applied to the expression for F, the transformed temperature, to find the series' of constants A_{mp} and B_{mp}, (Section 5.3.2d). Substituting for F and dF/dy at $y=1$ from eqn.(5.10) into the fifth boundary condition, eqn.(6.8) gives

$$\sum_{m=1}^{\alpha}\sum_{p=o}^{\alpha}(A_{mp}\cos p\theta + B_{mp}\sin p\theta)\cos\Gamma_m Z.((Hr+p)J_p(S_m) - S_m J_{p+1}(S_m))$$

$$= G'(1,\theta,s)\left[v' + \sum_{j=1}^{\alpha}\frac{2}{j\pi} . \sin j\pi v'.\cos j\pi 2\right]$$

Multiplying both sides by the orthogonal function $\int_0^1 \cos \Gamma_m z.dz$ gives on integrating and rearranging

$$\sum_{p=o}^{\alpha} (A_{Mp}\cos p\theta + p_{Mp}\sin p\theta)(Hr+p)J_p(S_M) - S_M J_{p+1}(S_M)$$
$$= \sum_{m=1}^{\alpha} \frac{4v'\sin\Gamma_m}{2\Gamma_m+\sin 2\Gamma_m} - \sum_{j=1}^{\alpha} \frac{4\sin\Gamma_m}{2\Gamma_m+\sin 2\Gamma_m} \cdot + \Gamma_m\left[\frac{2}{j\pi} \cdot \frac{\sin(v'\pi j)2\cos j\pi}{j^2\pi^2+\Gamma_m^2}\right] \quad (6.9)$$

The equivalent term to the right hand side of this expression for plain discs was $\frac{4\sin\Gamma_m}{2\Gamma_m+\sin 2\Gamma_m}$. This new term is v' x the original plus an extra series summed over j . The remaining steps of the solution, inverse transforms etc., remain unchanged by this modification to the heat source Fourier series. The temperature in a disc with the heat source acting only over the central portion of its track, $2v'L$, is therefore given by eqn. (5.11) but with the $\sum_{m=1}^{\alpha} \frac{4\sin\Gamma_m}{2\Gamma_m+\sin 2\Gamma_m}$ term replaced by the series given on the right hand side of eqn.(6.9). The exponential rate of decay, d_{mn} , of each term in the transient series is not altered by this modification.

It must be noted, that as the heat source length has been reduced, the heat source strength for a chamfered disc β_c , becomes

$$\beta_c = \frac{\mu W u_s}{4v'bL}$$

where W is the total load, and the heat source group therefore becomes for disc 1

$$\left(\frac{\theta^*}{v\pi}\right)_c = \frac{U_1^{1/2}}{U_1^{1/2}+U_2^{1/2}} \cdot \frac{\mu W U_s}{4K v' L} \quad (6.10)$$

The first term in the j series is the largest and the successive terms alternate in sign so that the series converges. The number of terms in the j series that have to be evaluated increases with Ha . For large Ha, due to its complex nature, the series has not been evaluated. When Ha is small, the sum of the j series terms is small compared to $\frac{4v'\sin\Gamma_m}{2\Gamma_m+\sin 2\Gamma_m}$, and so the additional series over j can be neglected. For the same value of $\theta^*/v\pi$, i.e. for the same heat source strength, β , and size $2\theta^*$, the temperature in a chamfered disc is reduced to v' times that for a plain disc. This is the case for the heat transfer coefficients for the two disc machine found later in this chapter and the error in the disc temperature if the j series is neglected is $<2\%$.

6.4. Extension of solution to predict temperatures in the second and successive increments using Duhamels theorem

The bulk temperature is a function of $(\theta^*/v\pi)$, the non-dimensional heat source group, which is itself a function of the load W , and the coefficient of friction μ , and several other variables. The procedure for the tests reported in Chapter 3 was, as in many two discs scuffing tests, to increase the load at set intervals of time. This change in load and any resulting change in coefficient of friction, μ , results in a change in the heat source strength. Except for the beginning of the first increment this occurs when the discs bulk temperature is greater than the ambient. The analysis assumes a constant heat source strength applied to a disc initially at uniform temperature equal to the ambient and is as such only applicable to the first increment of a test. In this section the solution is extended to cover more than one increment.

'Duhamels theorem' can be used to find the response of a system to a time varying boundary condition providing that the response of the system to a unit step in the boundary condition at time $t = 0$, is known. The response of the system must be linear and have at the most only one inhomogeneity, which can be either in the boundary conditions or in the differential equation of the problem.

Consider the boundary condition which varies with time as shown in Fig.6.3a. It consists of continuously varying portions which can be split up into small steps ΔBC_i occurring at intervals Δt and a number of finite jumps, ΔBC_j occurring at time t_j . Duhamels theorem states that due to the linearity of the system, the response of the system at time t' is

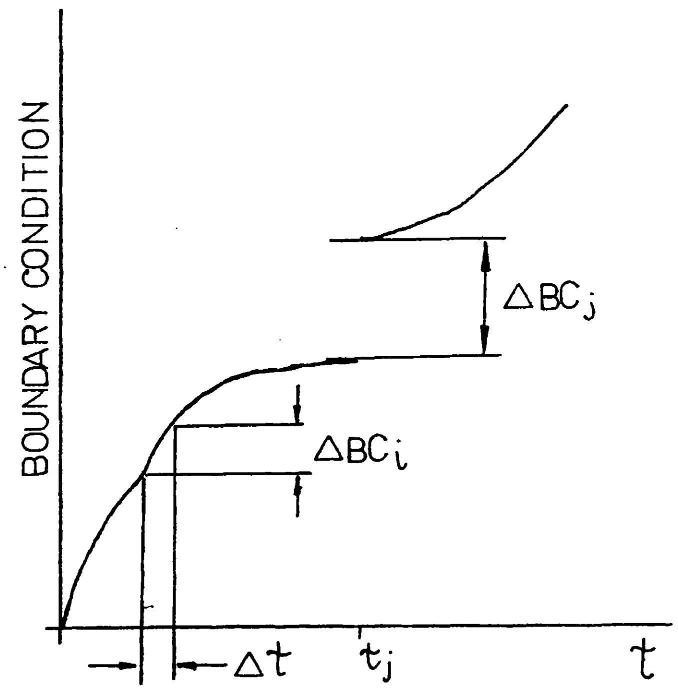

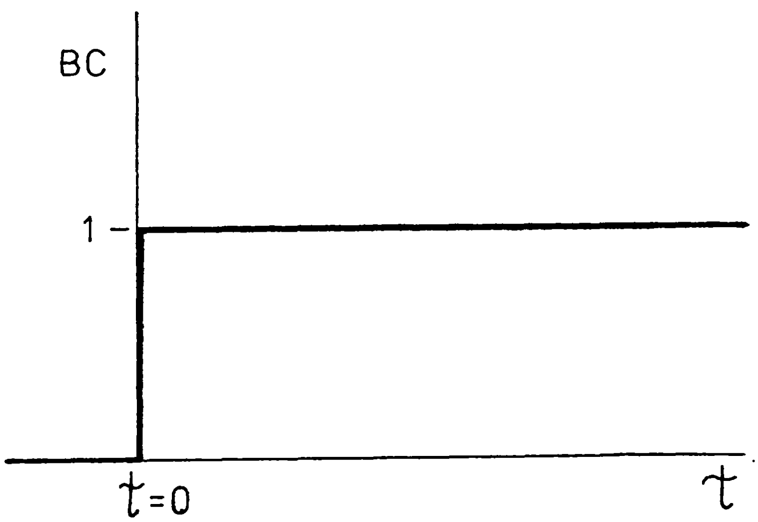

Figure 6.3 Variation of a boundary condition with time and unit step change of the boundary condition at $\tau = 0$.

simply the sum of the response to each small step and all the finite jumps in the boundary condition up to that time.

If the response at time t, to a unit step change in the boundary condition at $t = 0$, (Fig.6.3b) is, $S(x,y,t)$ then Duhamels theorem gives the response at time t' to the varying boundary condition, BC, as

$$S(x,y,t') = \int_{t=o}^{t'} S(x,y,t'-t) \cdot \frac{dBC(t)}{dt} \cdot dt + \sum_{j=1}^{j} S(x,y,t'-t\ ).\Delta BC_j \quad (6.11)$$

The first term on the left-hand side is the net effect of the gradually varying part of the boundary condition and the second term that due to the finite jumps.

In a scuffing test the size of heat source group $\theta^*/v\pi$, changes for each increment due to the change in the load and any resulting change in friction. The heat source strength group arose from the fifth boundary condition to the problem,(eqn.(5.3)). Duhamels theorem (eqn.(6.11)) can be used to find the response of the system when the fifth boundary condition varies with time, i.e. for more than one increment, providing the response to the system of a unit step in the heat source group at time $t = 0$ is known. This is given by eqn.(5.12) with $\theta^*/v\pi = 1$. In the shortened notation of Section 5.4 the bulk temperature at time τ, for $\theta^*/v\pi = 1$ is

$$T^* = \sum_{m=1}^{\infty} (C_m - \sum_{n=1}^{\infty} D_{mn} \cdot e^{-d_{mn}\tau}) \quad (6.12)$$

During a scuffing test μ and W change but the surface speeds are set for for the whole test. For the purposes of the modification in this section the heat source group will be represented by

$$\frac{\theta^*}{v\pi} = (HS)\ \mu_I W_I \quad (6.13)$$

where (HS) represents those parameters in the heat source strength group, (eqn.(6.6)), which do not vary with time and the subscript I refers to values in the Ith increment. The change in the heat source group in terms of $\mu_I W_I$ for a typical scuffing test is shown in Fig.6.4. If it is

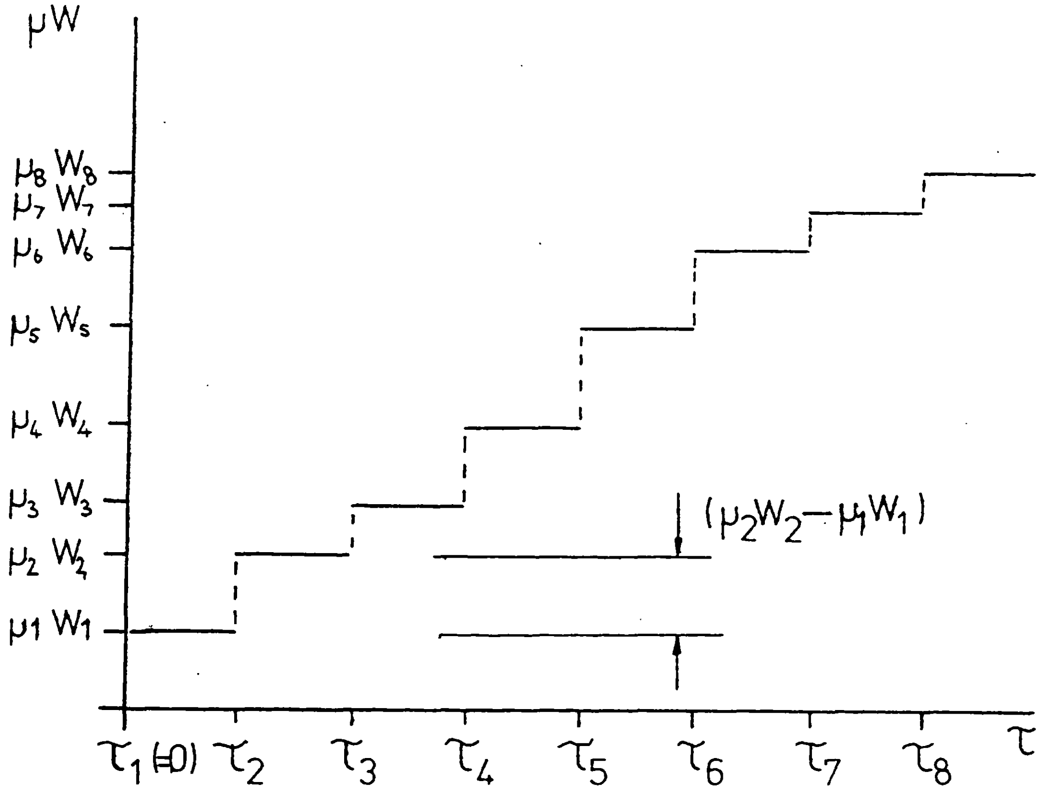

Figure 6.4 Incremental variation of heat source strength for a two disc scuffing test.

assumed that μ is constant during an increment and only changes from increment to increment, then $d(BC(\tau))/d\tau = 0$. In this case only the second term on the right hand side in eqn.(6.11), that for finite jumps, need be considered. Errors resulting from the assumption that μ is constant during an increment are discussed in Section 6.7.3.

Combining eqns.(6.11), (6.12) and (6.13), gives the response for the Ith increment of a two disc test as

$$T^*(y,\theta,z,\tau) = (HS).\left\{ \left[(\mu_1 W_1) \sum_{m=1}^{\infty} \left(C_m - \sum_{n=1}^{\infty} D_{mn}.e^{-d_{mn}\tau}\right)\right] + \left[(\mu_2 W_2 - \mu_1 W_1) \sum_{m=1}^{\infty} \left(C_m - \sum_{n=1}^{\infty} D_{mn}.e^{-d_{mn}(\tau-\tau_2)}\right)\right] + \left[(\mu_I W_I - \mu_{I-1} W_{I-1}) \sum_{m=1}^{\infty} \left(C_m - \sum_{n=1}^{\infty} D_{mn}.e^{-d_{mn}(\tau-\tau_I)}\right)\right]\right\}$$

which reduces to

$$T^*(y,\theta,z,\tau) = (HS) \left\{\left[\mu_I W_I \sum_{m=1}^{\infty} C_m\right] - \left[\mu_1 W_1 \sum_{m=1}^{\infty} \sum_{n=1}^{\infty} D_{mn}.e^{-d_{mn}\tau}\right] - \left[(\mu_2 W_2 - \mu_1 W_1) \sum_{m=1}^{\infty} \sum_{n=1}^{\infty} D_{mn}.e^{-d_{mn}(\tau-\tau_2)}\right] - \left[(\mu_I W_I - \mu_{I-1} W_{I-1}) \sum_{m=1}^{\infty} \sum_{n=1}^{\infty} D_{mn}.e^{-d_{mn}(\tau-\tau_I)}\right]\right\}$$

The steady state temperature at the end in the Ith increment is therefore a function of the heat source strength in that increment and is independent of the previous increments. The transient in the Ith increment is a combination of that from previous increments, although the exponential rate of decay for each transient term is still d_{mn} and the radial variation of the steady state temperature is still a function of $I_o(\gamma_m.y)$.

When the increments are sufficiently long for the transient terms to decay to a negligible value before the application of the next load, the response in the Ith increment can be simplified further to

$$T^*(y,\theta,z,\tau)\Big|_{Ith} - (HS)\left\{\left[\mu_I W_I \sum_{m=1}^{\infty} C_m\right] - \left[(\mu_I W_I - \mu_{I-1} W_{I-1}) \sum_{m=1}^{\infty} \sum_{n=1}^{\infty} D_{mn} . e^{-d_{mn}(\tau-\tau_I)}\right]\right\} \tag{6.14}$$

which is the case in the two discs tests examined in Section 6.7.

Expressions for the heat source strength, its division between the discs, the effect on temperature of a time varying heat source of reduced length have been found. Only the convective heat transfer coefficients appropriate to the discs rotating in the two disc machine environment need to be determined before the expressions for the bulk temperature, (eqn.(5.12)), can be used to predict temperatures in a scuffing test. Determining the heat transfer coefficients is the subject of the next two sections.

6.5 Evaluation of limiting values of the heat transfer coefficients

The axial and radial Biot numbers, Ha and Hr , depend on the dimensions of the cylinder, the thermal conductivity and the convective heat transfer coefficients, h_a and h_r .

The convective heat transfer coefficients for the surface and side-faces of a rotating body can be influenced by many factors. These include the shape, orientation and rotational speed of the bodies, the proximity of an enclosure, the cross flow of the surrounding medium and, most importantly here, the temperature and properties of the surrounding medium. The problem is that for the two disc machine the exact nature of the environment is unknown.

In the two disc machine the discs and part of their shafts are enclosed in a perspex box. (Fig.6.5). The oil is fed from outlets, one above each disc, onto the disc surfaces, upstream of the contact. Most of the oil supplied to the discs is slung off as they rotate, only a thin layer being retained on the surfaces. The replenishment of this thin layer of oil with fresh oil from the supply has been shown by Crook (1957) to be slow. The environment surrounding the discs is a dispersion of hot

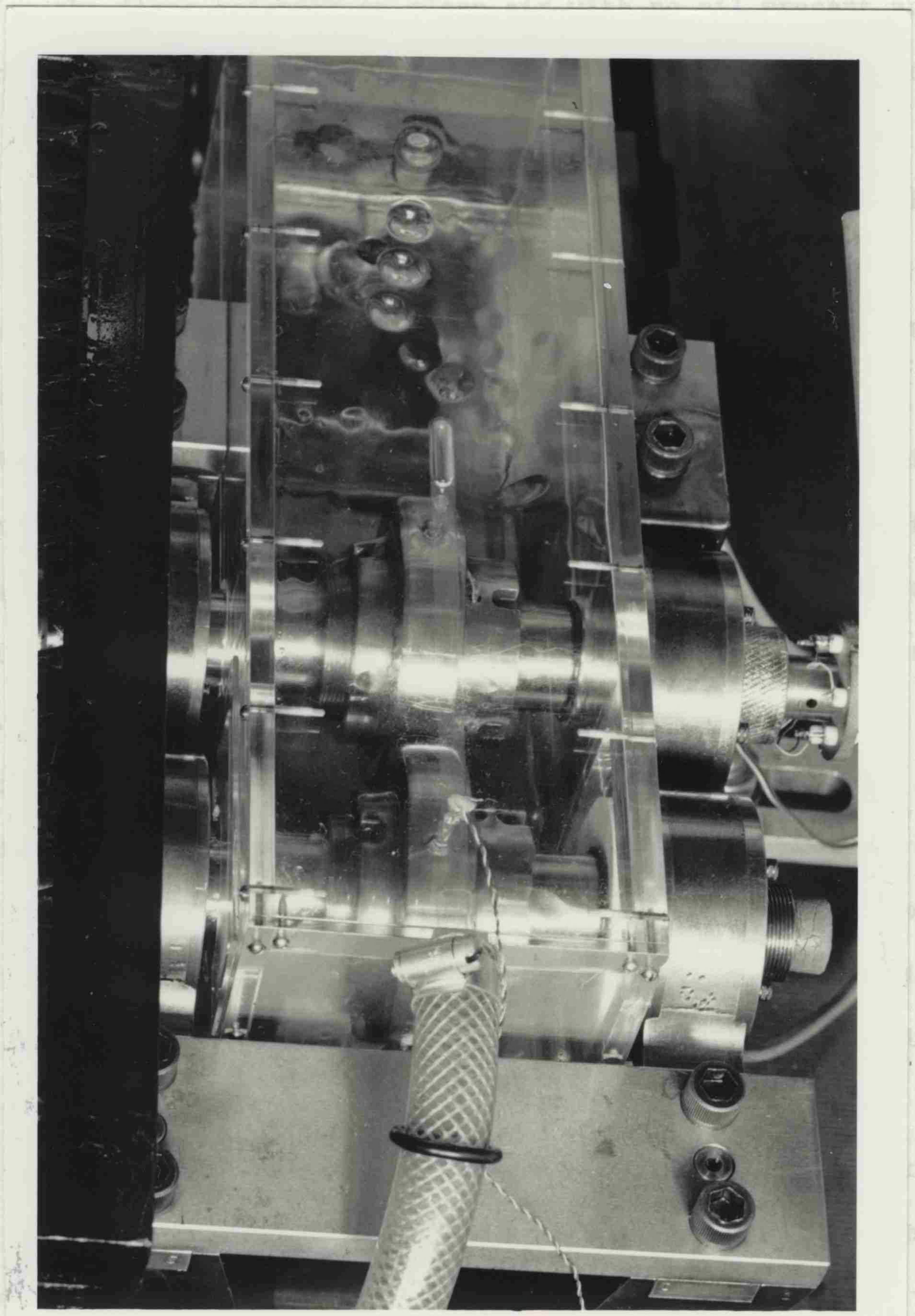

Figure 6.5 Enviroment of discs in test machine.

oil in air.

It is likely that limits for the heat transfer coefficient would be those for the discs rotating in clean air with no oil present and for the discs rotating fully submerged in oil. The presence of the thin oil film on the disc, the oil flung off the disc and the fine dispersion of oil droplets in the air are expected to result in heat transfer coefficients within these limits. Heat transfer coefficients appropriate to the system for these two limiting cases can be determined from existing literature to show the conceivable range of h_a and h_r .

Kays and Bjorkland (1958) found the heat transfer coefficients for rotating heated cylinders in air with varying degrees of cross flow. The results were presented in terms of non-dimensional groups and were limited to fluids with Prandtl numbers in the range 0 to 15 , where the Prandtl number, $Pr = Cp.\eta/\kappa$, and Cp is the specific heat capacity, η , the dynamic viscosity and κ the thermal conductivity of the fluid.

Story used the results of Kays and Bjorkland to find h_r for air (Pr of air ~ 0.7) and also grossly extrapolated the results to find h_r for cylinders submerged in oil (Pr of oil ~ 100 to 1000). Similar values of the heat transfer coefficient were obtained (at 30°C) for oil (and air with the value for oil) being slightly higher than that for air at 70°C. Story argued that as the values were similar at 30°C , the controlling medium is not crucial and so compared the theoretical predictions of her model with experimental values at this temperature.

Much of the published literature on heat transfer has been combined and summarised in 'Heat Transfer and Fluid Flow Data Book' (1984) (no author). This reference provides a unified approach to the determination of heat transfer properties for a broad range of situations. Section G.511 of this reference is concerned with rotating discs and has been followed to find heat transfer coefficients, for oil and air. The steps are outlined below. As this is only intended as a guide to the possible range of values, several simplifying assumptions have been made.

1) The discs are treated as shaftless rotating discs without an enclosure.

2) There is no cross flow of fluid.

3) The disc temperature at the side face is constant with radius.

Eqn.(5.11) predicts a radial temperature variation in finite width discs but experiment has shown this to be a variation of only several degrees for the range of conditions in the disc tests, which should not significantly affect the fluid properties.

Table 6.1 gives the properties and Prandtl numbers of oil - OM100 and air at 30°C, 50°C and 70°C. The way in which the heat transfer coefficients are calculated depends on the Prandtl number.

<u>To find h_a for air</u>

For fluids with $Pr < 4$, the gas range, and the case for the discs rotating in air, the rotational Reynolds number of the fluid determines whether the flow is laminar or turbulent. The criteria quoted for rotating discs are,

0 < rotational Reynolds number	180000 <	laminar flow
180000 < rotational Reynolds number	310000 <	transitional flow
350000 < rotational Reynolds number		turbulent flow

where the rotational Reynolds number = $\rho\omega r^2/\eta$.

Values of the rotational Reynolds number are given in Table 6.2 for the discs in air at 30°C, 50°C and 70°C and for the three rotational speeds used on the two disc machine. These values are for the outer edge, $r = R$, of the discs, i.e. for the maximum value, and are all in the laminar range.

For a uniform radial temperature, the heat transfer coefficient from the side face of a rotating disc, h_a , at radius r is given as a/ AIR

TEMPERATURE	30°C	50°C	70°C
DENSITY - ρ kg/ m^3	1.17	1.09	1.03
VISCOSITY - η kg/sm	18.7 $\times 10^{-6}$	19.6 $\times 10^{-6}$	20.5 $\times 10^{-6}$
THERMAL CONDUCTIVITY - k J/ms°C	0.0264	0.0278	0.0292
SPECIFIC HEAT CAPACITY - C_p J/kg°C	1.006 $\times 10^3$	1.007 $\times 10^3$	1.008 $\times 10^3$
PRANDTL No. - P_r = $C_p.\eta/k$	0.713	0.71	0.708

b/ OIL - OM100

TEMPERATURE	30°C	50°C	70°C
DENSITY - ρ kg/ m^3	873	861	848
VISCOSITY - η kg/sm	0.132	0.045	0.019
THERMAL CONDUCTIVITY - k J/ms°C	0.132	0.13	0.129
SPECIFIC HEAT CAPACITY - C_p J/kg°C	1940	2015	2160
PRANDTL No. = $C_p.\eta/k$	1940	698	318

Table 6.1

Physical properties and Prandtl numbers of oil (OM100) and air.

DISC ANGULAR VELOCITY	TEMPERATURE		
	30 °C	50 °C	70 °C
$\omega 1 = 78.5\ ^{c}/s$ = 750 rev/min	7150	6345	5733
$\omega 2 = 157\ ^{c}/s$ = 1500 rev/min	14300	12691	11466
$\omega 2 = 235.5\ ^{c}/s$ = 2250 rev/min	21450	19036	17198

Table 6.2 Rotating Reynolds numbers for discs in air.

$$h_a = a_1 \cdot \frac{k}{r} \left(\frac{\rho\omega r^2}{\eta}\right)^{a_2} \left(\frac{Pr}{0.7}\right)^{a_3}$$

where ρ , η , Cp and k are the values for air.

For laminar flow, the coefficients are $a_1 = 0.35$, $a_2 = 0.5$ and $a_3 = 0.33$ which gives

$$h_a = 0.41\ k\left(\frac{\rho\omega}{\eta}\right)^{0.5} (Pr)^{0.44} \qquad (6.15)$$

as $a_2 = 0.5$, h_a is independent of the radius.

<u>To find h_a for oil</u>

For fluids with higher Prandtl numbers, the case for the discs rotating in oil, the GE Fluid Data book directs the user to further references. That by Sparrow and Gregg (1959), an analytical determination of convective heat transfer values for rotating discs with a radially uniform temperature, has been used here. They presented a non-dimensional heat transfer coefficient graphically for Prandtl numbers in the range .01 to 100, and gave asymptotic expressions for $Pr \rightarrow \infty$ and $Pr \rightarrow 0$.

The Prandtl numbers the oil OM100, are all > 100 (Table 6.1). The asymptotic expression for heat transfer coefficients at higher Prandtl numbers when rearranged gives

$$h_a = 0.62.k\left(\frac{\rho\omega}{\eta}\right)^{1/2} .Pr^{1/3} \qquad \text{as} \quad Pr \rightarrow \infty \qquad (6.16)$$

This expression has the same form as that for air (eqn.(6.15)), but has different coefficients and power dependence for the Prandtl number. h_a is again independent of r .

h_a values for air and oil calculated using eqns.(6.15) and (6.16) are given in Table 6.3 and have been used to calculate the axial and radial Biot numbers given in Table 6.4. It has been assumed that the axial and radial heat transfer coefficients are the same, i.e. $h_a = h_r$.

For air, there is little variation in Ha and Hr with temperature whereas for oil they increase with temperature due to the change in η and ρ . In all cases Ha and Hr are proportional to the square root

h_a air - J/ (m²s °C)

DISC ANGULAR VELOCITY	TEMPERATURE OF MEDIUM		
	30 °C	50 °C	70 °C
ω1	20.6	20.5	20.4
ω2	29.1	29.0	28.8
ω3	35.6	35.4	35.3

h_a oil (OM100) - J/ (m²s °C)

ω1	735	876	1022
ω2	1040	1239	1445
ω3	1274	1517	1770

Table 6.3

Heat transfer coefficients for disc rotating in air and in oil (OM100)

H_r air

DISC ANGULAR VELOCITY	TEMPERATURE OF MEDIUM		
	30 °C	50 °C	70 °C
ω1	0.0151	0.0150	0.0149
ω2	0.0213	0.0213	0.0211
ω3	0.0261	0.026	0.0259

H_r oil (OM100)

ω1	0.539	0.642	0.749
ω2	0.762	0.908	1.059
ω3	0.934	1.112	1.3

H_a air

ω1	0.00315	0.00313	0.00312
ω2	0.00445	0.00443	0.0044
ω3	0.00544	0.00542	0.0054

H_a oil (OM100)

ω1	0.112	0.134	0.156
ω2	0.159	0.189	0.221
ω3	0.195	0.232	0.271

$H_r = \frac{R.h_r}{k_{steel}}$ $\qquad H_a = \frac{L.h_a}{k_{steel}}$

Table 6.4

Axial and radial Biot numbers for oil (OM100) and for air.

of the angular velocity, $\omega^{1/2}$. Comparing the Biot numbers for oil to those for air at the same speed and temperature, the effect of the medium is apparent. For example, at 30°C the Biot numbers for oil are approximately 35 times those for air, rising to 50 times greater at 70°C. At 30°C Story found the heat transfer coefficients to be similar for oil and air. This shows that the extrapolation of the results of Kays and Bjorkland to fluids with a high Prandtl number was not valid.

The effect of the media on operating temperatures is shown in Fig.6.6. This figure shows, for a L/R ratio in the disc machine, 0.208, the steady state bulk temperature rise above ambient, made non-dimensional by the heat source strength group, i.e. $\frac{v\pi}{\theta^*} . T_s^*$ at y= 1, z = 0 , against Hr for a range of Ha . The regions of operation for oil and for air environments are shown. The choice of medium can make up to a twenty-fold difference in T_s^*.

Ha and Hr, for the environment in the two disc machine, are expected to lie within these limiting values for oil and air. As the possible range is large a more accurate method to find Ha and Hr is needed if the model of the previous chapter is to be used to predict temperature rises in the disc machine with any degree of accuracy. The experimental method described in the next section was used to determine working values for the coefficients.

6.6. Experimental determination of Hr and Ha.

6.6.1. Theory

In the model for finite cylinders the only losses from the system were by convection from the surface and the side faces of the discs. In the two disc machine the discs are mounted on tapered shafts. Conduction is to be expected along the shafts to cooler parts of the machine, whilst the area of the side faces available for convection losses and the volume of the discs is reduced. Both factors are expected to affect the bulk temperature. In effect there are three unknowns; the heat transfer coefficients h_a and h_r , the shaft losses and the effect on the temperature of the reduced side-face area and volume, Fig.6.7a.

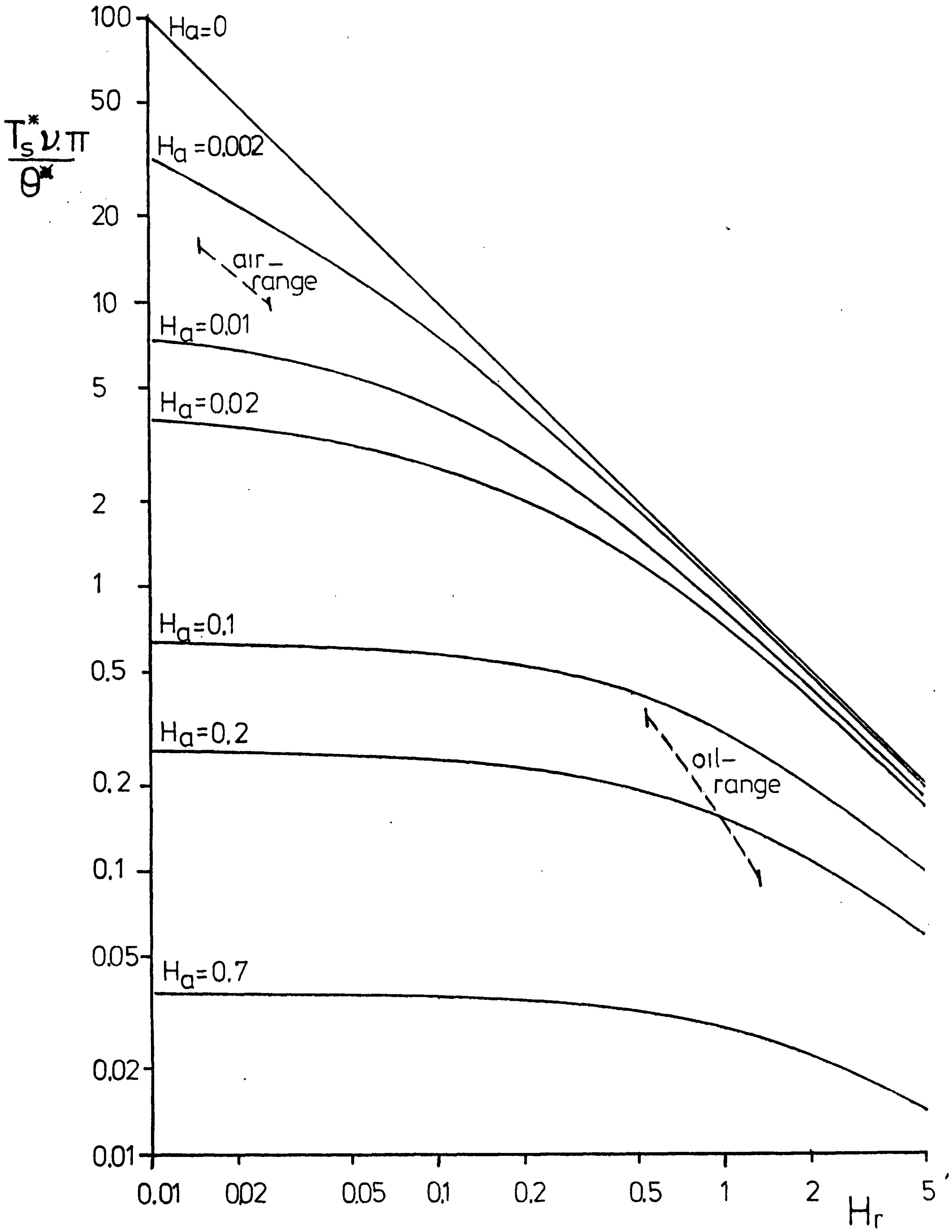

Figure 6.6 Variation of steady state temperature in a disc with Ha and Hr. (L/R = 0.208, y = 1, z = 0)

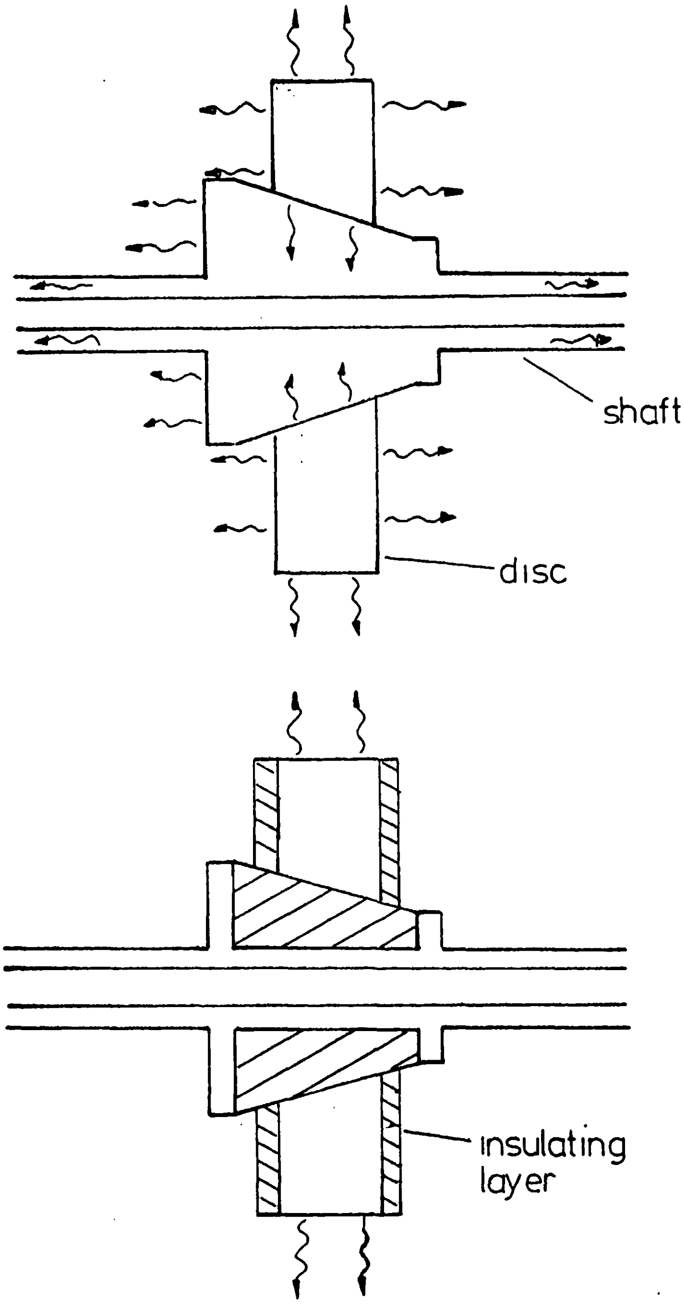

Figure 6.7 Heat losses from a standard disc/shaft arrangement and from an insulated disc.

Attempts have been previously made to model the effect of a shaft. Story (1984) introduced a shaft in a modification to her infinitely long cylinder solution. by assuming that the shaft acted as a heat sink, which held the temperature at the interface between the cylinder and the shaft at the ambient value. This boundary condition for the shaft cylinder interface is, in the light of practical experience, not applicable in this case.

Gecim and Winer (1986a) chose a more flexible boundary condition for the shaft/cylinder interface. By allowing heat to pass either way across the interface, their shaft could act as a heat source or a heat sink and the effect of varying the heat flow across the interface on the steady state bulk temperature in an infinitely long cylinder was shown. The solution for no heat flow across the interface was likened to an insulating layer at the cylinder/shaft boundary. The resulting steady state bulk temperature was the same as for a solid long cylinder. The transient solution was not attempted but it is probable that the rate of change of temperature will be altered by an insulated centre and the reduced volume of the discs.

For the experimental method to find H_r, the losses from the discs are reduced by insulating the side faces and the disc/shaft interface. The convective heat transfer from the sidefaces and the losses by conduction along the shaft are then assumed to be negligible, so that the only losses are those by convection from the surface (Fig.6.7b). Both the steady state and transient of the bulk temperature for a disc with insulation at the disc sides and in the centre must be known. The solution for this case is similar to that for an infinitely long cylinder as given by Story, i.e. no axial variation in the temperature (as $h_a \to 0$) but it has the additional boundary condition

$$k \frac{\partial T}{\partial y} = 0$$

at $y = y_1$, the shaft/cylinder interface. The solution is given in Appendix A7.

The resulting steady state bulk temperature in an insulated disc is, as shown by Gecim and Winer, the same as that in a solid infinitely long cylinder, i.e.

$$T_s^* = \frac{\theta^*}{\nu\pi} \cdot \frac{1}{H_r} \times v' \tag{6.17}$$

where v' is the correction factor due to the disc chamfer (Section 6.3).

The rate of decay of each term in the bulk transient series is determined, for both the solid infinitely long cylinder and the insulated disc by $e^{-\Lambda n^2 . \tau}$. For the insulated disc Λn is the nth root of

$$Hr = \Lambda n \frac{[\{J_1(\Lambda n y_1).Y_1(\Lambda n)\} - \{Y_1(\Lambda n y_1).J_1(\Lambda n)\}]}{[\{J_1(\Lambda n y_1).Y_0(\Lambda n)\} - \{Y_1(\Lambda n y_1).J_0(\Lambda n)\}]} \tag{6.18}$$

which is a function of Hr and the radius of the central insulating layer y_1. Whereas for a solid cylinder with no end losses Λn is the nth root of the simpler eigen condition

$$Hr = \frac{\Lambda n J_1(\Lambda n)}{J_0(\Lambda n)}$$

Therefore, although the steady state bulk temperature is the same as that for an infinitely long cylinder, the rate of change of the temperature is altered by the central insulating layer.

6.6.2. Method to determine Hr

Hr is the only unknown in the expressions for both the steady state bulk temperature and the exponential power term for an insulated disc. The experiment to find working values of Hr (and Ha) makes use of this condition.

An idealised experimental temperature/time response for an insulated disc, in a two disc machine, following the application of a load, is shown in Fig.6.8a. The temperature of the disc is initially at the ambient and rises in an exponential fashion to its equilibrium value. The response can be represented by the function

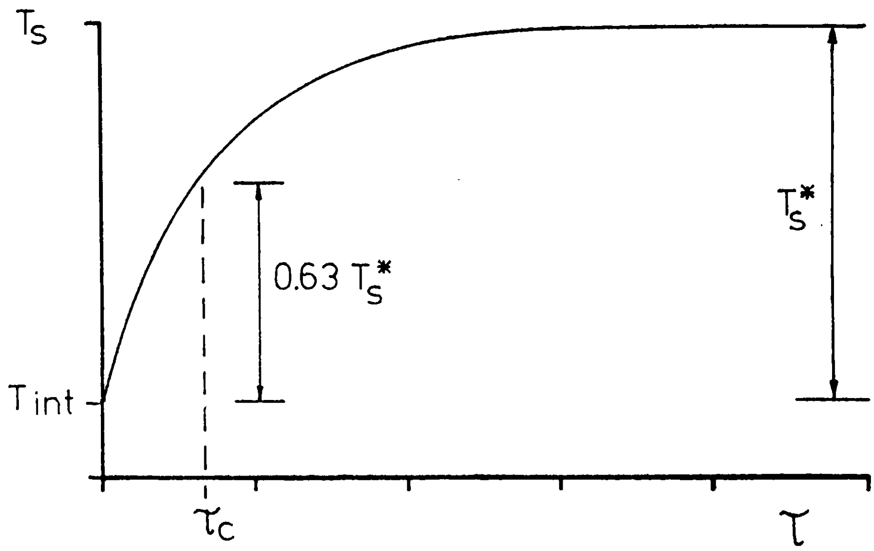

Figure 6.8a Ideal variation of disc bulk temperature with time following the application of a load.

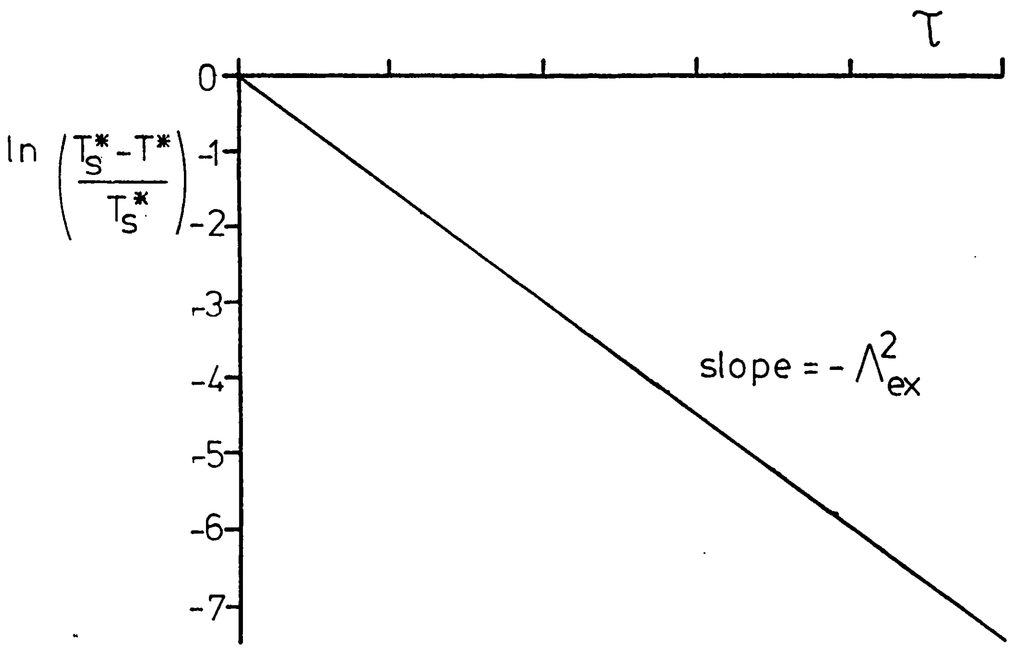

Figure 6.8b $\ln\left(\frac{T_s^* - T^*}{T_s^*}\right)$ with τ for an ideal rise in bulk temperature.

$$T^*(ex) = T_s^*(ex)\left(1 - e^{-\Lambda^2(ex).\tau}\right) \qquad (6.19)$$

where $T_s^*(ex)$ is the measured steady state temperature rise above the ambient and $\Lambda^2(ex)$ is the experimental exponential power term. The (ex) is used to differentiate the measured from the predicted values.

The time constant $\tau c(ex)$ of the system is defined such that or $\tau c(ex) = 1/\Lambda^2(ex)$. At this time

$$T^*(ex) = T_s^*(ex)\left(1 - e^{-1}\right) \quad \text{or} \quad T^*(ex) = 0.632\ T_s^*(ex) \qquad (6.20)$$

i.e. the time constant is the time taken for the temperature to rise to 63.2% of the steady state value above the ambient and is independent of the size of the temperature rise. τ is the non-dimensional time where $\tau = \kappa t/R^2$. For the material and dimensions of the discs this gives the time in seconds as $\sim 100\,\tau$.

In the experiments to determine Hr , a load is applied between the discs which are initially at ambient temperature. The friction between the discs and the temperature in the faster disc is measured. From the load, the friction coefficient and the surface speeds, the heat source group $\theta^*/\nu\pi$, appropriate to the disc is calculated. The steady state bulk temperature rise and the corresponding value of $\theta^*/\nu\pi$, is used with eqns.(6.17) to give one value of Hr .

The time constant, $\tau c(ex)$ and $\Lambda(ex)$ can be found from the measured bulk temperature variation using the relationship given in eqn.(6.20). The bulk temperature transient is a series solution. To find Hr from the experimental time constant, it is assumed that the first term in the series for the bulk temperature transient is dominant. The exponential rate of decay of the first term in the transient series, is determined by Λ_1 , which for an insulated disc is the first root of the eigen condition given by eqn.(6.18). This can be shown to be a reasonable approximation once values for the heat transfer coefficients have been found. Λ_1 and $\Lambda(ex)$ can be equated and the corresponding value of Hr found from eqn.(6.18).

If these two values for Hr found a) from the steady state temperature and b) from the time constant, are in reasonable accord and lie within the limiting values for Hr for the discs completely submerged in oil or in air, then the average of the two values can be taken as working value of Hr for the oil/air environment around the discs in the machine at that ambient temperature.

6.6.3. Experiments to determine Hr

The shafts used with the insulated discs are shown in Fig.6.9. They are the same as the original shafts, except for the cutout over the tapered section. This is replaced by the tufnol pieces. The discs have tufnol washers glued to their side faces and are mounted on the tufnol tapered pieces, and located with key ways. The locking ring is used to hold the disc on the tapered section.

Tests were conducted with a single load increment of 2 kgf applied for 15 mins. The experimental procedure was otherwise as described in Chapter 3. The tests were run at the 3:1 speed ratio and the temperature monitored in the faster disc.

Three tests were run, with initial temperatures of 30°C, 50°C and 70°C. The variation of the temperature and coefficient of friction with time for the 30°C and 50°C tests are plotted in Figs.6.10a and b. There was a larger temperature rise in the 30°C and 50°C tests than in the first increment of the equivalent tests reported in Chapter 3, tests D and E. There was also a larger temperature rise in the 70°C test than in test F but this test failed in the first increment before equilibrium had been established. Consequently a heat transfer coefficient was not found at this temperature.

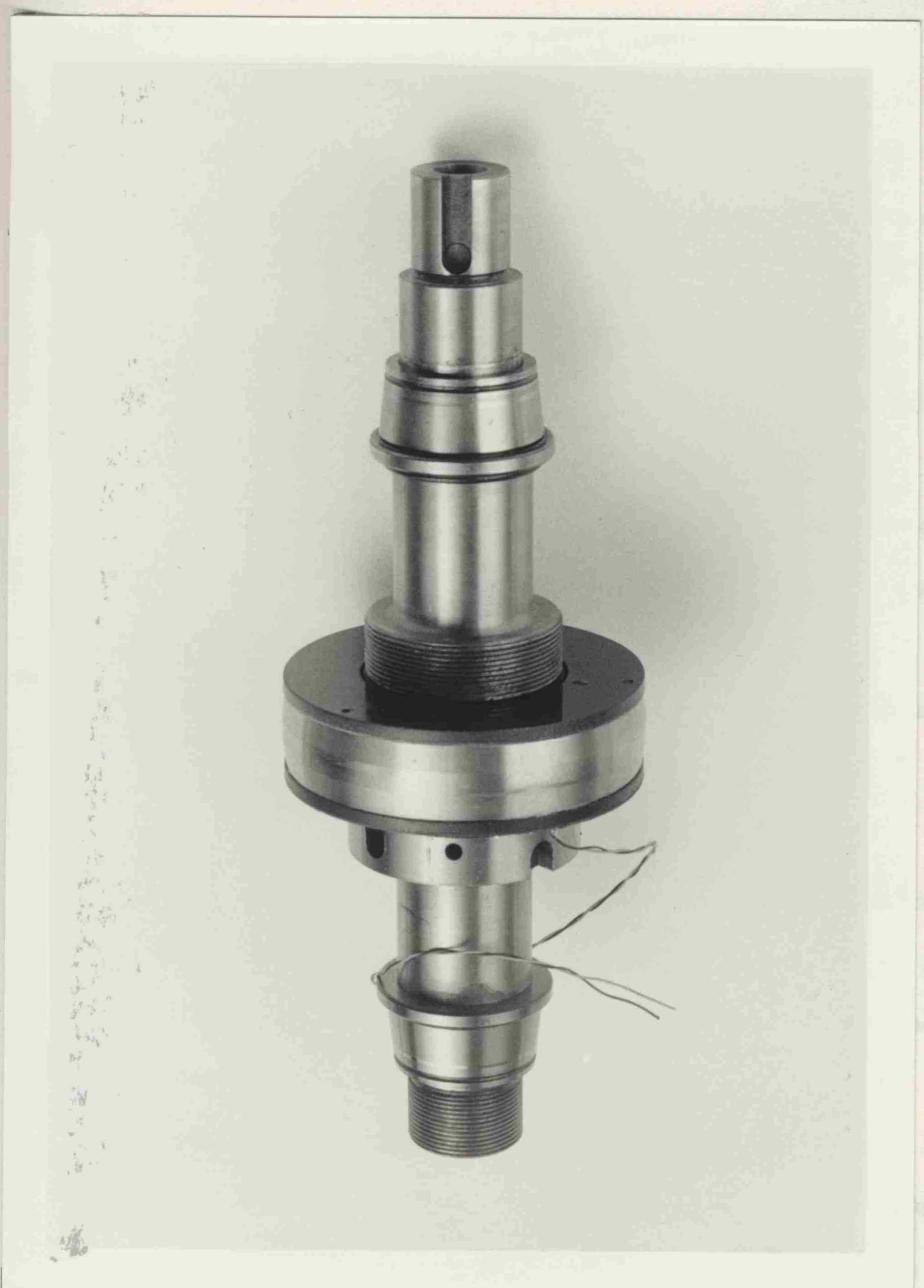

Figure 6.9 Insulated discs mounted on their shafts.

In Table 6.5 the heat source group $\theta^*/\nu\pi$, calculated from eqn.(6.10) is given for both discs at the 2:1 and 3:1 ratio. The expressions are in terms of the applied load and the coefficient of friction. The coefficient of friction in the 50°C test rose slightly in the first minute but was then steady for the rest of the test. The steady value has been used in the calculations of Hr . In the 30°C test, the friction was more random. An averaged value has been used in the calculations. The errors arising from this are discussed in Section 6.7.3. The steady state temperature, the coefficient of friction and the heat source strength term and the corresponding value of Hr are given in Table 6.6.

Due to the scatter of the temperature data points shown in Fig.6.10, the error in finding $\tau c(ex)$ by drawing a best fit curve through the points is $\pm$ 10 seconds.

Rearranging eqn.(6.19) and taking logarithms of both sides gives

$$\ell n \left(\frac{T_s^*-T^*}{T_s^*}\right)(ex) = -\Lambda^2(ex).\tau$$

$\ell n\left(\frac{T_s^*-T^*}{T_s^*}\right)$ (ex) plotted against $\tau(t/100)$ gives a straight line of gradient $-\Lambda^2(ex)$ as shown in Fig.6.8b. A more accurate value for $\Lambda(ex)$ was obtained by plotting the test data in this way and taking the slope of the best fit straight line through the points.

The relationships between $\Lambda_1(=\Lambda(ex))$ and Hr , eqn.(6.18) is plotted in Fig.6.11. Values of $\Lambda(ex)$, $\tau c(ex)$ and the corresponding values of Hr found from this figure for the 30°C and 50°C tests are given in Table 6.6.

The radial Biot numbers, Hr , given in Table 6.6 at each initial temperature obtained by the two routes, i.e. form the steady state temperature and from the time constant, are in reasonable agreement (15%). At each temperature the average of the two results is taken as Hr . The axial heat transfer coefficient, Ha , for finite discs at the same temperature was found by assuming that $h_r(R) = h_a(r)$, and hence Ha = Hr x L/R . The axial Biots numbers are also given in Table 6.6.

GEAR RATIO	3:1	2:1
SURFACE SPEEDS - m/sec FAST DISC u_1 SLOW DISC u_2	 9 3	 6 3
SLIDING SPEED u_s - m/sec	6	3
$\frac{u_1^{1/2}}{u_1^{1/2} + u_2^{1/2}}$	0.634	0.586
$\frac{u_2^{1/2}}{u_1^{1/2} + u_2^{1/2}}$	0.366	0.414
$\frac{\theta^*}{\nu\pi}$ | 1 a b	μ x W x 2.29 μ x kgf x 224.4	μ x W x 1.06 μ x kgf x 103.8
$\frac{\theta^*}{\nu\pi}$ | 2 a b	μ x W x 1.32 μ x kgf x 129.7	μ x W x 0.75 μ x kgf x 73.1

a - in terms of load in Newtons at disc and
b - in terms of load in kgf at 10:1 hanger ratio.

$\nu' = 0.32$

Table 6.5 Heat source strength terms.

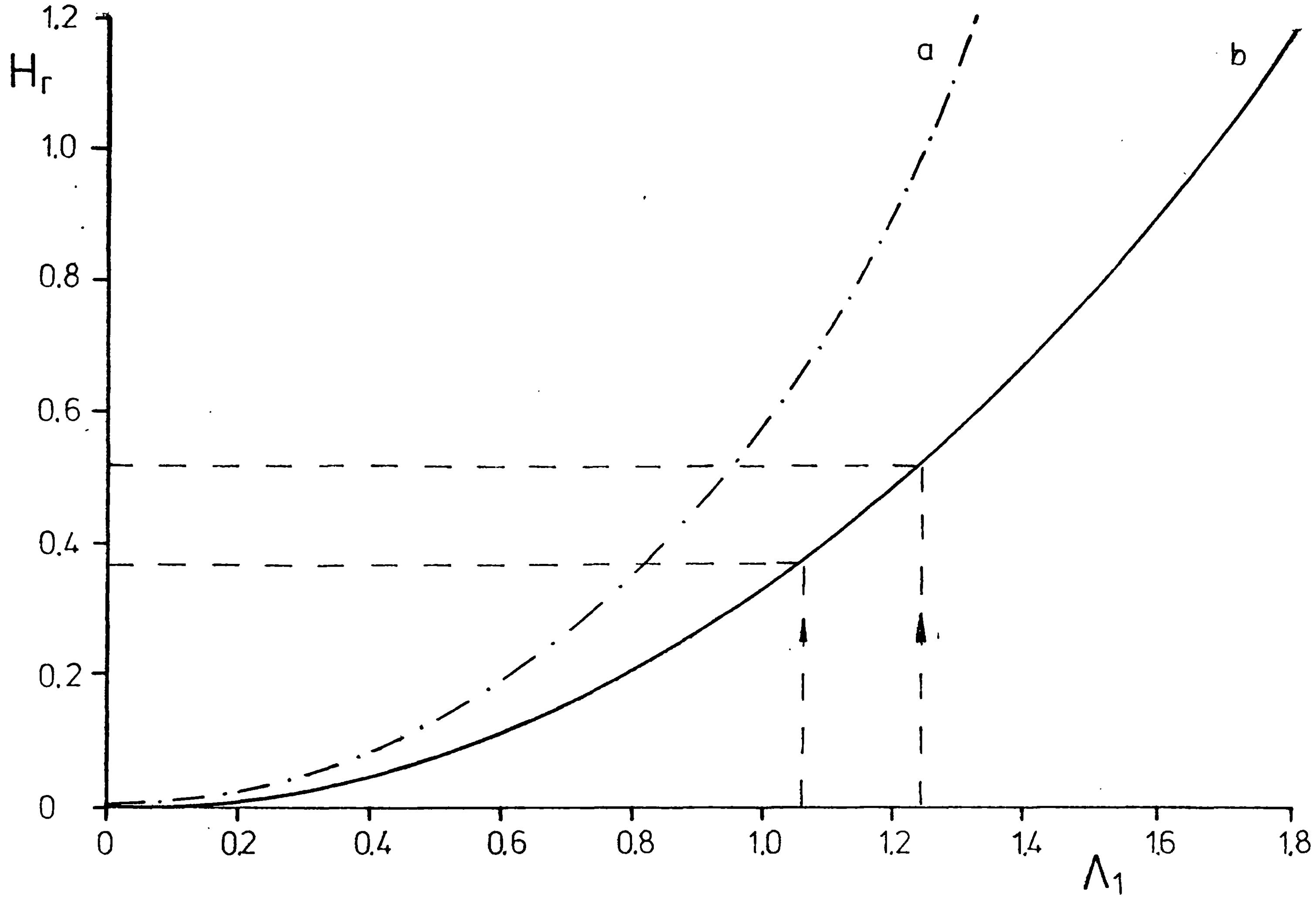

Figure 6.11 Relationship between Hr and Λ_1 for a/ normal and b/ insulated discs.

TEST	30'C TEST	50'C TEST
μ	0.033	0.031
T^*s - °C	12	10.2
$\frac{\theta^*}{\nu\pi}\Big\vert_1$	μ x kgf x 71.8 = 4.74	μ x kgf x 71.8 = 4.45
Hr (from steady state values)	0.395	0.436
$\Lambda_{ex}{}^2$	1.11	1.54
τ_c (ex)	0.89	0.65
t_c $(=\tau_c x100)$ - secs	89	65
Λ_1 (assumed = Λ_{ex})	1.06	1.24
Hr (from time constant)	0.37	0.51
Hr (average value)	0.383	0.476
Ha (=0.208 x Hr)	0.08	0.1

Table 6.6 Results of hr determination tests and resulting Biot numbers Hr and Ha.

As expected, the values of Hr found experimentally lie within the limiting cases for the disc rotating in oil or air. In Fig.6.12, the operating positions at 30°C and 50°C ambient temperatures are compared to the ranges for the limiting cases of oil and of air. The experimentally determined values tend to those for oil, the differences in non-dimensional steady state temperature for oil and the experimental conditions being approximately twofold.

The theoretical values for oil were found to vary with the temperature due to their dependence on the viscosity and the density of the oil. The ratio of the Biot numbers found experimentally at the two temperatures is similar to that for the theoretical values, i.e.

$$\text{For oil} \quad \frac{Hr(50°C)}{Hr(30°C)} = 1.19$$

and for the two disc machine environment

$$\frac{Hr(50°C)}{Hr(30°C)} = 1.24$$

This also indicates that the oil is the controlling medium and that the relationship between Biot number and the oil properties is similar to that predicted.

6.7. Comparison of theoretical and experimental values for finite discs

The values of Hr and Ha found in the previous section and the expressions for heat source strength, effect of a chamfer and the second and successive increment analysis can be combined with eqn.(5.12) to predict the temperature and the time constants in the two disc machine. Section 6.7.1 compares the steady state temperatures in the discs and the time constants and Section 6.7.2 compares the radial variation of the temperature in the discs. Section 6.7.3 discusses possible sources of errors in the results, for example the still unknown effect of shaft losses and suggests further modifications to the model which could be made.

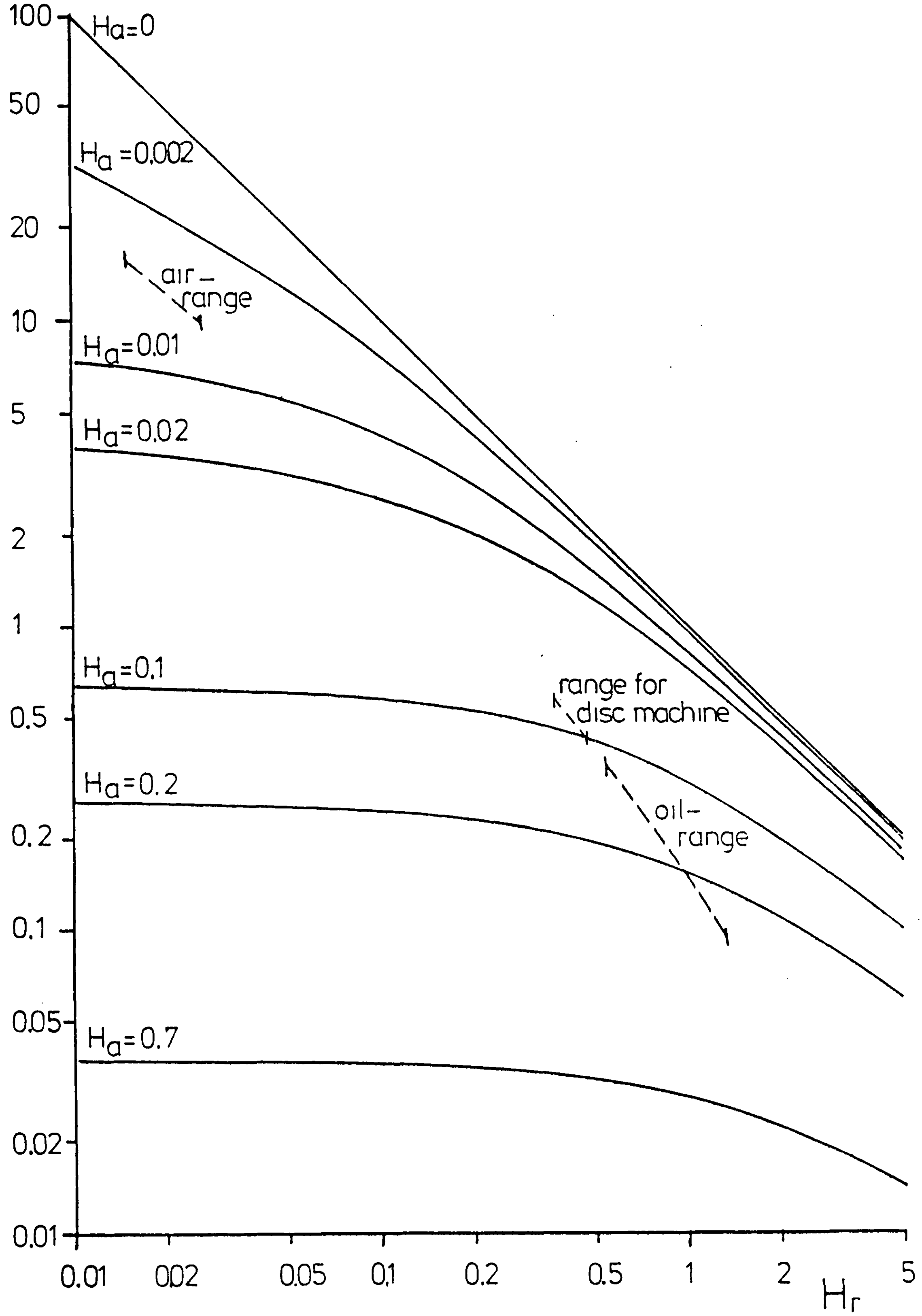

<u>Figure 6.12</u> <u>Variation of steady state temperature in a disc with Ha and Hr. (L/R = 0.208, y = 1, z = 0)</u>

(Operating condition for oil /air mixture shown.)

6.7.1. Steady state and transient values

Table 6.7 gives the experimental and predicted values of the steady state temperatures (at y=0 and 1, z=0) and time constants, for the first increment of six of the tests reported in Chapter 3. The predicted values are given for both finite and 'infinite' cylinders to show the effect of axial losses. All values are for the faster disc of the pair.

In tests D and E there was some doubt about the friction values so the steady state temperature has been calculated using both the measured value of μ and a more 'reasonable' value of 0.03 in these tests.

The values for the 2:1 ratio tests J and K have been calculated using the Biot numbers found for the fast disc at the 3:1 ratio ($\omega 3$ - Table 6.2). The limiting Biot numbers for oil and air varied with the square root of the angular velocity, ω, (Section 6.5). If it is assumed that the Biot numbers for the two disc machine environment have the same variation with angular velocity as the limiting values, then the Biot numbers found for the fast disc at the 3:1 ratio can be 'corrected' for the other speeds.

$$\frac{Hr(\omega 2)}{Hr(\omega 3)} = \frac{(\omega 2)^{\frac{1}{2}}}{(\omega 3)^{\frac{1}{2}}}$$

The temperature rises and time constants using the corrected values for the 2:1 tests are also given in Table 6.7. The corrected Biot number values for the faster disc speed at the 2:1 ratio, $\omega 2$, increase the predicted temperature at the disc surface by 16% at 30°C and 18% at 50°C.

The predicted temperatures have been calculated at y=1 and at y=0 , to show the range of the radial variation. The experimental temperatures are those measured by the thermocouple 2 mm below the surface, i.e. at y=0.95. The error in using the predicted temperature at y=1 rather than that predicted for y=0.95 is shown in the next section to be approximately 4%. Therefore the experimental temperatures are compared here to the predicted temperatures at y=1 .

TEST	E	E_1	B	D	K	J
AMBIENT TEMPERATURE °C	50	50	50	30	50	30
GEAR RATIO	3:1	3:1	3:1	3:1	2:1	2:1
EXPERIMENTAL VALUES						
μ	0.009	0.042	0.077	0.01	0.033	0.033
T_s^* °C	4.8	5.2	1.1	3.8	2.9	3.4
t_c (τ_cx100) secs	54$\pm$5	72$\pm$5	68$\pm$5	38$\pm$5	58$\pm$5	40$\pm$5
PREDICTED VALUES -FINITE DISCS						
T_s^* °C y=1	1 3.2#	4.5	0.8	1.3 3.9#	1.6 1.9*	2 2.3*
y=0	0.6 1.9#	2.7	0.5	0.9 2.6#	1	1.3 1.7*
t_c (τ_cx100) secs	32	32	32	40	32 39	40 48
PREDICTED VALUES -INFINITE DISCS						
T_s^*	2.7 9#	12.7	2.3	3.8 11.3#	4.6	5.7
τc x100 - secs	118	118	118	144	118	144

- using μ = 0.03
* - using Biot numbers corrected for 2:1 disc speed.

Table 6.7 Predicted and experimental values of steady state bulk temperature and time constant for two disc tests (first increment only).

The measured steady state temperatures above ambient, T_s^* , lie between the finite and infinite predicted values, except in test D, where using the assumed value of μ=0.03 gives a finite predicted value slightly greater than that measured. Tests E_1 and B , for which no corrections to the values were necessary, have the best agreement between the finite and measured T_s^* , the finite values being 86% and 73% of the measured values respectively. Using the assumed value of μ=0.03 and the Biot numbers corrected for speed in the 2:1 tests improves the correlation between the values. The time constants are approximately equal to or greater than the finite values but are in all cases less than the infinite predicted value.

In Figs.6.13a and b the predicted and experimental temperatures for test B and test K are compared. For test K both the original (i.e. that for ω3) and corrected (for ω2) Biot numbers have been used. The experimental temperatures and time constants for both tests lie between the predicted values for intinitely long and finite width cylinders. In test K, T^* for the finite disc using the original Biot numbers are approximately 60% of the measured values and for the corrected Biot numbers approximately 70% of the measured values. In test B, T^* for the finite disc is apprxoimately 80% of the measured values at the beginning of the test falling to 60% by the end of the test.

6.7.2. Radial distribution of temperature

The disc bulk temperature given for the tests reported in Chapter 3 was that measured by a thermocouple embedded 2 mm below the disc surface. This temperature was used in place of the surface temperature to calculate the film thickness and in the previous section was compared to the predicted temperature at the surface. This section examines the experimental and predicted radial variation in the bulk temperature and assesses the error in using the measured temperature 2 mm below the surface in place of the surface temperature.

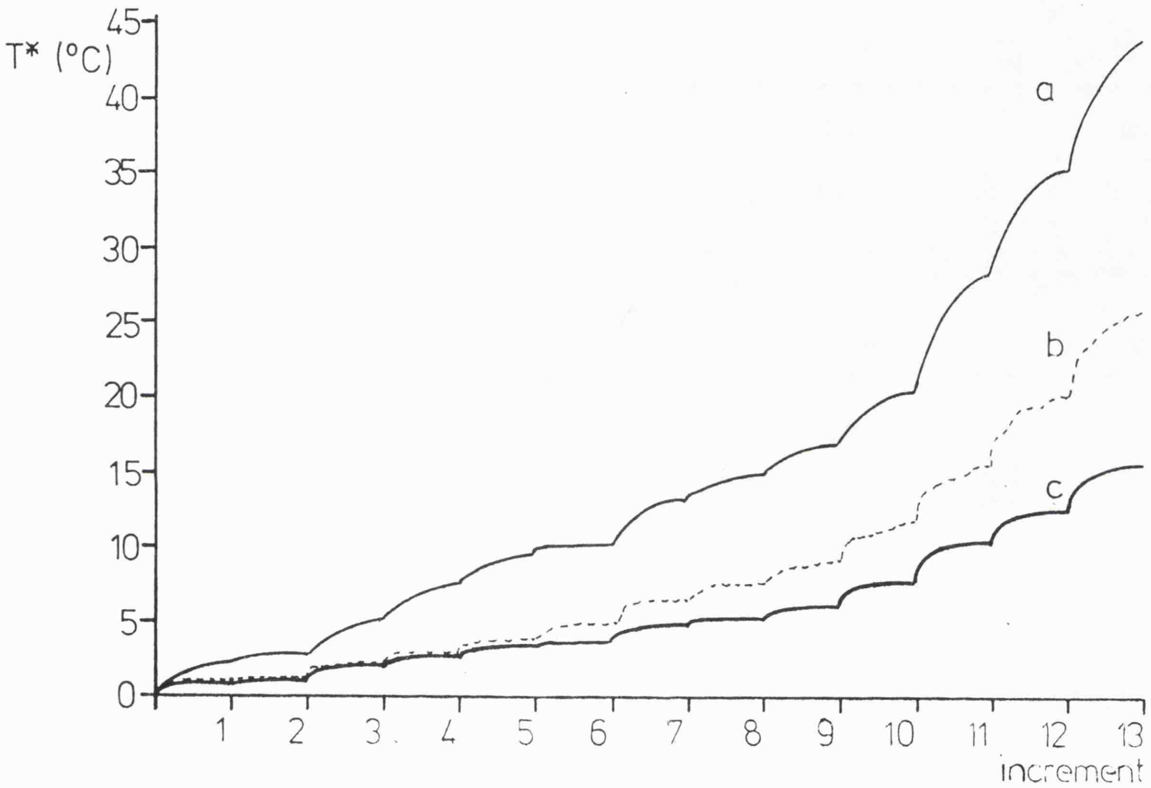

Figure 6.13a Variation of disc bulk temperature for test B, (fast disc).
i/ predicted for infinite length disc,
ii/ experimental and
iii/ predicted for finite length disc, (L/R = 0.208).

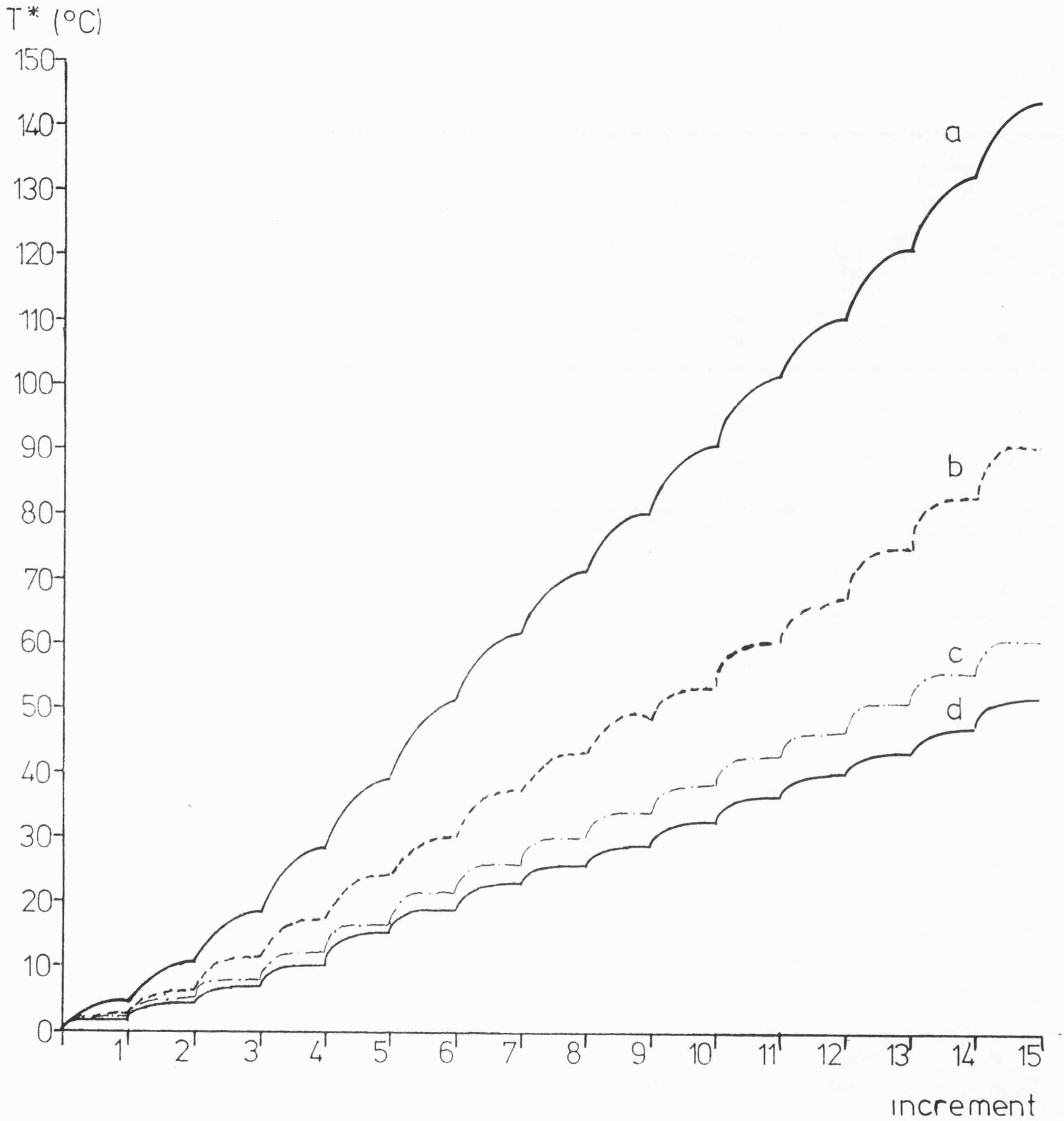

Figure 6.13b Variation of disc bulk temperature for test K, (fast disc).
i/ predicted for infinite length disc,
ii/ experimental,
iii/ predicted for finite length disc with Biot numbers adjusted for 2:1 speed.
iv/ predicted value for finite discs with Biot numbers found for 3:1 speed.

Work on a method to measure the disc surface temperature directly was carried out by the author (Finnis (1984)), near the start of this project. The work was carried out at the Petroleum, Chemistry and Technology Division of the Royal Aerospace Establishment, Farnborough [N and T Div.] on a two disc machine of the same design as that described in Chapter 3. The purpose of the work was to calibrate an infra-red thermal imaging temperature measuring device to measure the disc surface temperature. The emissivity setting for the device, appropriate to the disc surface, had to be found.

Four thermocouples were embedded, 2 , 4 , 8 and 13 mm below the surface of the disc.

Ku and Li (1977) reported that the variation of the temperature with depth below the disc surface on a two disc machine followed a logarithmic/linear relationship. The radial temperature profiles from the four thermocouple readings, when plotted as ℓn(temperature)/distance from the surface of the discs were, as reported by Ku and Li, linear. The line through the data points could therefore be extrapolated to give the surface temperature. Fig.6.14 shows profiles, plotted in this way for steady state conditions at the end of the increments of a scuffing test.

The surface temperatures were measured with the infra red temperature measuring device for a range of emissivity settings. These were compared to the surface temperatures found by extrapolating the four thermocouple readings to find the appropriate emissivity value for the disc surface.

The emissivity varied with disc temperature and with load. As there were several problems encountered in using the infra red device with the two disc machine, it was not adopted for use in the present project.

Using embedded thermocouples was thought to be the more reliable method and this method was therefore used to measure the disc bulk temperature for the tests reported in this thesis. Due to the instrumentation, there was a greater scatter of data points so the temperature profiles were

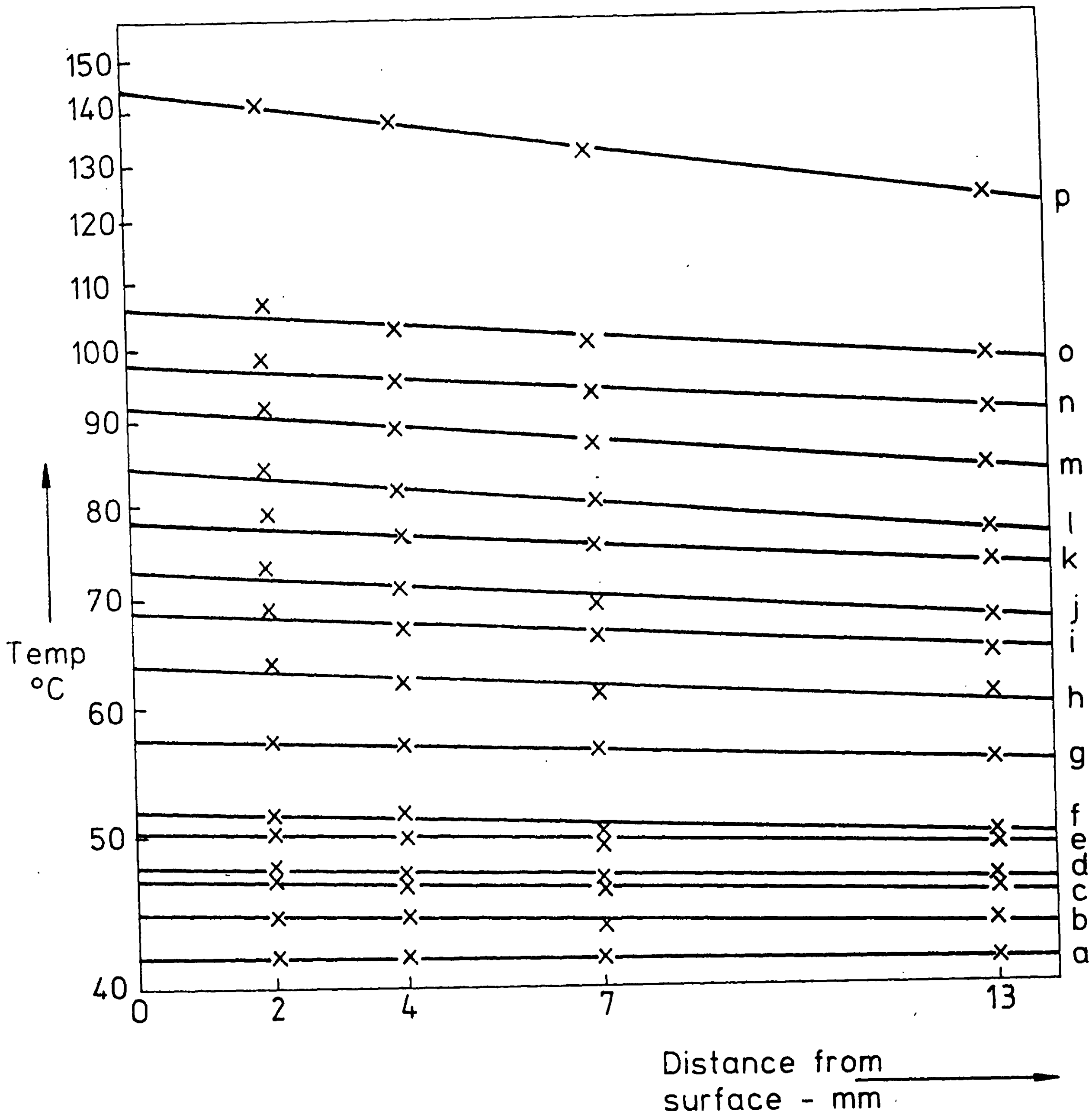

$T_j \simeq 50°C\ \bar{u} = 4m/s$
Profiles taken 5mins after load increase
Loads added in stages below at 5min. intervals

a = 00·00 kN/m	i = 169·28 kN/m
b = 29·76 "	j = 196·54 "
c = 53·34 "	k = 227·12 "
d = 60·33 "	l = 252·15 "
e = 83·91 "	m = 279·64 "
f = 86·18 "	n = 310·21 "
g = 113·66 "	o = 365·82 "
h = 138·70 "	p = 393·09 "

Figure 6.14 Radial variation of steady state temperature for two disc test.
(Test performed on two disc machine at NPC and T Division, Pyestock.)

inferior to those obtained for the tests at the NP & CT.D. The temperature profiles obtained during the project at the NP & CT.D will therefore be used to compare the predicted radial distribution.

The predicted radial profile for each term in the series for the steady state bulk temperature in finite length cylinders, eqn.(5.12) has the form $I_o(\gamma_m.y)$. This is a function of Ha only. The steady state bulk temperature at the end of each increment, given by eqn.(6.12) has the same form of radial variation.

For the low axial Biot numbers found for the two disc machine environment in Section 6.6, the first term in the steady state series dominates. The radial variation of this first term has the form $I_o(\gamma_1 y)$ and is shown in Fig.6.15 for the values of Ha found in Section 6.6. The temperature increases with radius, with T_s^* at the surface being approximately 1.6 times that at the centre.

To compare the experimental and predicted temperature variation the points from Fig.6.14 are replotted on a graph of T_s^* against y in Fig. 6.16. Lines of $I_o(\gamma_1.y) \times T_s^*(y=0)$ - the predicted radial variation, for the Ha value found for the ambient temperature of 50°C are also shown. The friction was not measured in this test and so it is not possible to predict T_s^*. Even if it were possible the errors in predicting the temperature rise would hinder the comparison between the predicted and measured radial variation in the steady state temperature, which is the function of interest here. To overcome this problem the lines of the predicted radial variation are for the values of T_s^* at y=1 at the end of each increment found by extrapolating the lines through the four thermocouple readings in Fig.6.14. The lines for the variation of the steady state temperature are not therefore a complete prediction of T_s^*, but only of its variation with y for a given surface temperature.

The predicted radial temperature profiles obtained in this way are an excellent representation of the experimental temperature profile throughout the test even when the difference between the centre and the surface

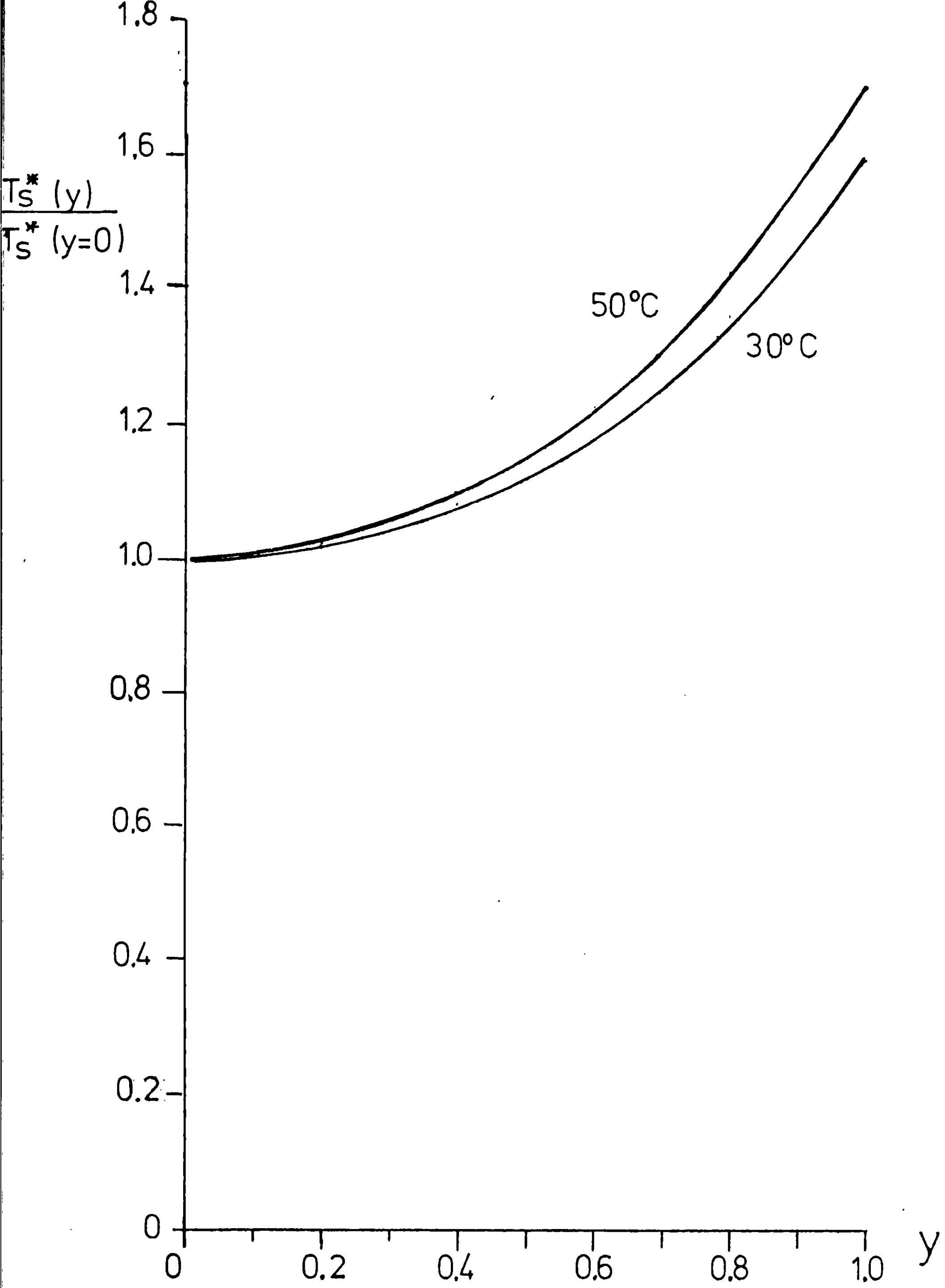

Figure 6.15 The radial steady state temperature distributions in discs with L/R = 0.208 and at ambient temperatures of 30°C and 50°C.

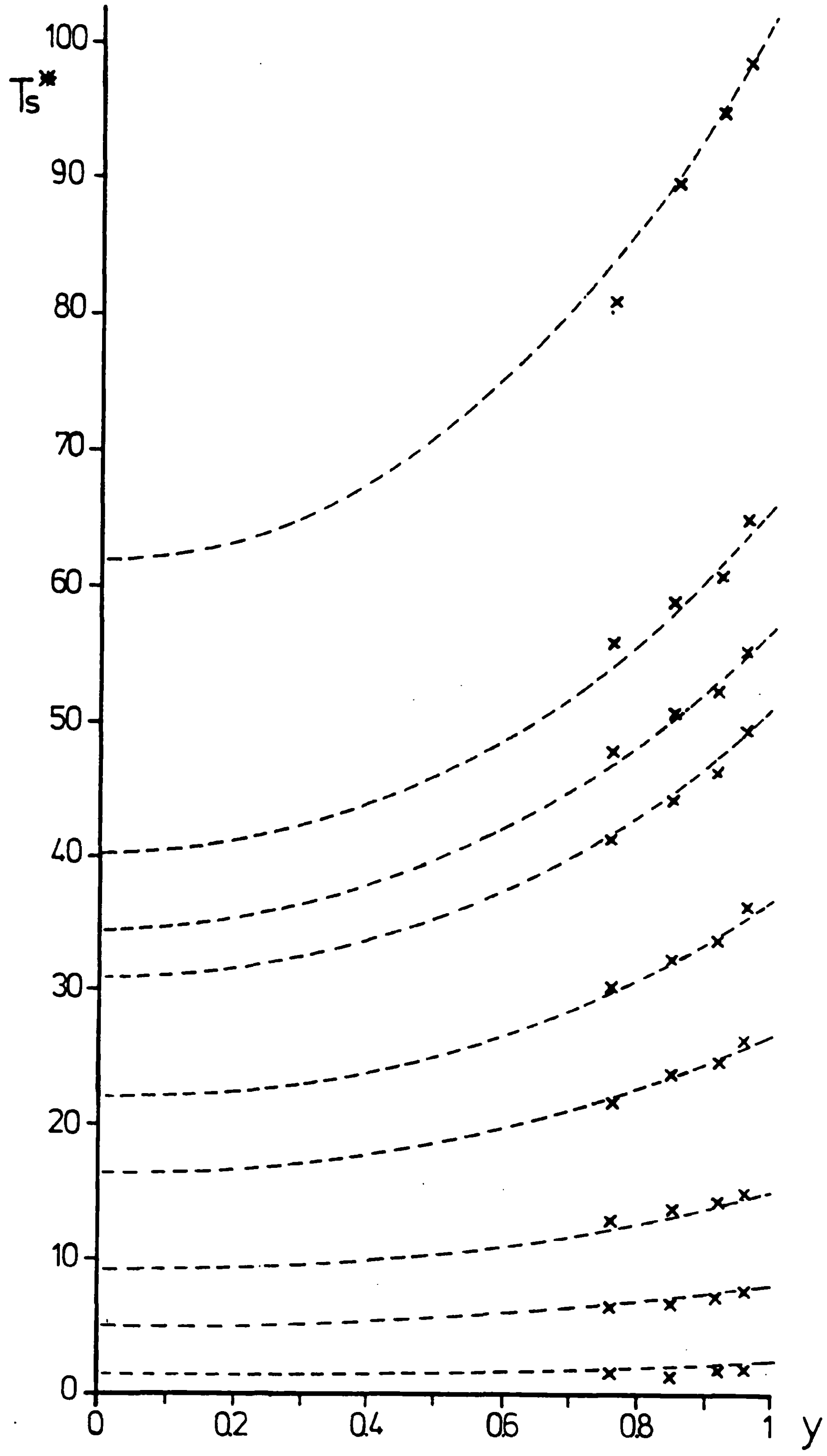

Figure 6.16 Comparison of predicted and experimental radial steady state temperature distribution for two disc scuffing test.

temperature is large, that is up to 40°C.

It is now possible to waylay some of the queries which arose earlier of the inaccuracy in taking the properties of the oil at the 2 mm thermocouple temperature to calculate film thickness values.

It is the surface temperature of the disc in the inlet zone which determines the viscosity of the oil and hence the film thickness. A large radial temperature gradient in the discs could result in a 2 mm thermocouple temperature considerably less than the quasi-stationary surface temperature, and an over-estimation of the film thickness. For tests A, D and J, contact was indicated by the count rate monitor at thicker films than expected. A suspected cause for this was the difference between the surface and 2 mm thermocouple temperature.

Using the predicted radial temperature variation, the ratio of the steady state temperature 2 mm below the surface, that is at $y=0.95$, to that at the surface is

$$\frac{T^*(y=0.95)}{T^*(y=1)} = \frac{I_0(y_1 . 0.95)}{I_0(y_1)}$$

Using the Ha values found in Section 6.6 gives the ratio of the temperature at the 2 mm thermocouple to that at the surface as

$$\frac{T^*(y=0.95)}{T^*(y=1)} \approx 0.96$$

at both operating temperatures. The maximum rise in temperature above the ambient value observed in the first test series was ~ 100°C. This would give a 4°C difference between the surface temperature and the 2 mm temperature. In tests A, D and E first contact was at 2 mm thermocouple temperatures in the range 40-50°C, which is equivalent to T^* the temperature rise above ambient, of 10-20°C. The error between the surface temperature and that 2 mm below the surface at these conditions would be ~ 0.5-1°C. This difference is too small to account for the early contact results in these tests. The error in using the 2 mm thermocouple temperature to find the film thickness is therefore negligible at low T^*

and rises to only a few degrees at the highest temperatures reached in the scuffing tests.

6.7.3. Discussion

Section 6.7.1 has shown that in general experimental temperatures lie between those predicted for finite and infinite cylinders. Section 6.7.2 shows that there is good agreement between experimental and theory for the radial variation in the temperature. There are several possible causes for the discrepancies in magnitude of the predicted and experimental temperatures and time constants. These include

a) the effect of shaft losses,

b) the effect of the reduced central volume and side face area due to the shaft through the centre,

c) the assumption that $h_a = h_r$,

d) the method used to find h_r ,

e) the effect of non-constant μ during an increment, and

f) the assumption that the bulk temperatures of the discs are equal when calculating the division of heat for all the increments.

a) The effect of heat loss along the shaft to cooler parts of the machine has not been included in the analysis. The effect on the steady state temperature of a shaft acting as a heat source or sink through the centre of an infinitely long cylinder was given by Gecim & Winer (1986a).

The shaft acting as a heat sink reduced the steady state temperature in the cylinder. The amount of heat conducted along the shafts was expressed in relation to the heat source strength. The amount of heat lost along the shafts is not known for the present machine, but the results of Gecim & Winer suggest that it would lower the predicted temperatures. Modifying the solution to include shaft losses is therefore likely to increase the discrepancy between the predicted values for the finite disc and the experimental values.

Gecim & Winer only examined the steady state solution for the effect of shaft losses. The predicted and measured time constants here were in excellent agreement at 30°C but at 50°C the time constants were up to 40 secs longer than predicted. This could be another effect of the shaft. Heat losses to cooler parts of the machine would be expected to increase at higher disc temperatures, in which case the disc temperature would take longer to reach equilibrium.

b) The model assumes a solid cylinder and does not account for the effect of the reduced volume and side face area at the centre of the discs. A simple analysis can be used to show expected effect of this on the bulk temperature. A heat source of known strength was applied in a disc with no centre and to a solid finite disc both initially at ambient temperature. It was assumed that there was no heat loss along the shaft and that the system was lumpable, that is the Biot numbers for both the axial and radial directions were sufficiently low for the variation of the temperature with position in the discs to be ignored. The results showed that the reduced volume and side face area would increase the predicted temperatures by a factor of 1.3 compared to solid finite discs. For example, if the predicted temperatures for test B were increased by a factor of 1.3, they would be approximately equal to the experimental values for the first five increments, falling to 80% by the end of the test. This result is an encouraging indication that a similar modification to the full solution would improve the correlation between the predicted temperatures and experimental values.

c) It was assumed that the heat transfer coefficient from the side faces of the discs h_a was the same as that found experimentally for the surface, h_r. There is a direct jet on to the surface of the discs whilst the side faces are only rotating in the oil/air suspension which could have resulted in an over-estimation of h_a. This would reduce the predicted temperatures and time constants. From eqn.(5.12) to Fig.6.12 it can be shown that a reduction of h_a to $h_a = h_r/3$ would increase the predicted temperature in the finite disc to the order of the measured temperatures. This would cause the predicted time constants to increase to 87 secs at 30°C , which increases the discrepancy to the experimental value. The time constant for an ambient temperature of 50°C would increase to 62 secs , which is an improvement.

The radial variation in the temperature is a function of Ha only. A reduction of Ha to Ha/3, would reduce the radial variation from the temperature at the surface being 1.6 times that at the centre to 1.2 times that atthe centre. However, there was excellent agreement between the predicted and measured results radial variation (Fig.6.16), in the temperature using the assumed value of $h_a = h_r$, which suggests that this assumed value for h_a is reasonable.

d) The determination of h_r (Section 6.6) is dependent upon the expressions chosen to model the heat source, (Section 6.2). The determination of h_r and h_a should ideally not depend on any of the assumptions used in developing the temperature model or on the expressions for the heat source strength and should be capable of separately determining h_a and h_r . This would avoid the need for the assumption that $h_a = h_r$. This suggests that a separate calibration rig is needed in which the environment in the two disc machine could be simulated but with an independent known heat source to the specimen.

e) For the analysis it has been assumed that μ was constant during each increment. For constant μ , when the first term in the series for the transient terms dominates, a near exponential rise in the bulk temperature was predicted. τc was defined as the time for the temperature to rise to 0.632 T_s^* . Using the same definition when μ was not constant and the response not exponential could be a possible source of error in the determination of h_r .

Examination of the friction traces for the tests reported in Chapter 3 (Fig.3.15), and the h_r determination tests (Fig.6.10), shows that μ more often than not varies within an increment. In the 30°C, h_r determination test there was no definite pattern but quite random variation of the μ data points.

For non-constant μ, providing the variation could be expressed analytically, Duhamels theorem could be used to show the effect on the temperature variation. The effect of varying μ on the determination of h_r can be examined using the simple case shown in Fig.6.17. $\mu = 0.025$ for the first 30 secs of the increment and then jumps to $\mu = 0.035$ for the remainder. The time constant of the system is 60 secs. The dotted line shows the response for the lower value of μ acting for the whole of the increment which would result in a steady state temperature of, say, 5°C . The dashed line is for the higher value of μ acting for the whole of the increment which gives a steady state temperature of 7°C. The response to the varying μ found using Duhamels theorem is that of the dotted line for the first 30 secs, i.e. that for $\mu = 0.025$ and thereafter follows the solid line with the steady state temperature determined by $\mu = 0.035$. If the time constant is taken as the time to $0.632\ T_s^*$, an inaccurate value of the time constant of 74 secs is obtained. The corresponding value of Hr for an insulated disc, from eqn.(6.16) or Fig.6.11, is 0.44 compared to 0.52 for the true time constant of 60 secs. The value of Hr obtained by the other method, i.e. from the steady state temperature and $\mu = 0.035$ will be correct. This form of non-constant μ would therefore result in an underestimation of Hr .

In the h_r determination test at 50°C, $\mu = 0.024$ for the first 20 secs, jumps to $\mu = 0.028 \pm 0.002$ for the next 40 secs and then increases gradually to 0.032 by the end of the fifth minute and is thereafter almost constant for the rest of the increment, although only the first five minutes of the test are shown in Fig.6.10. To calculate Hr from the

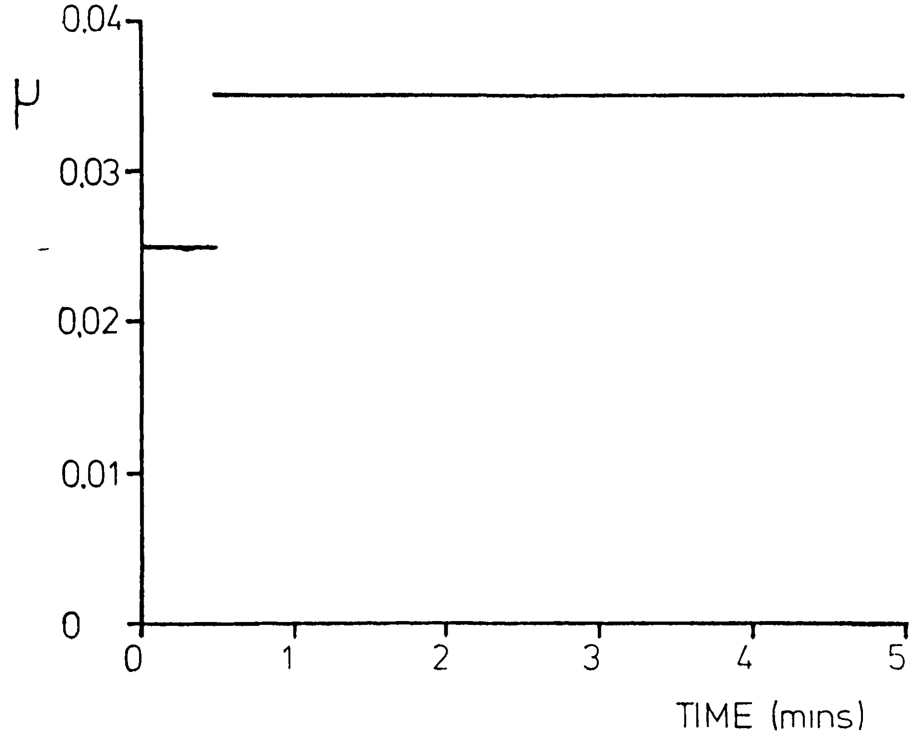

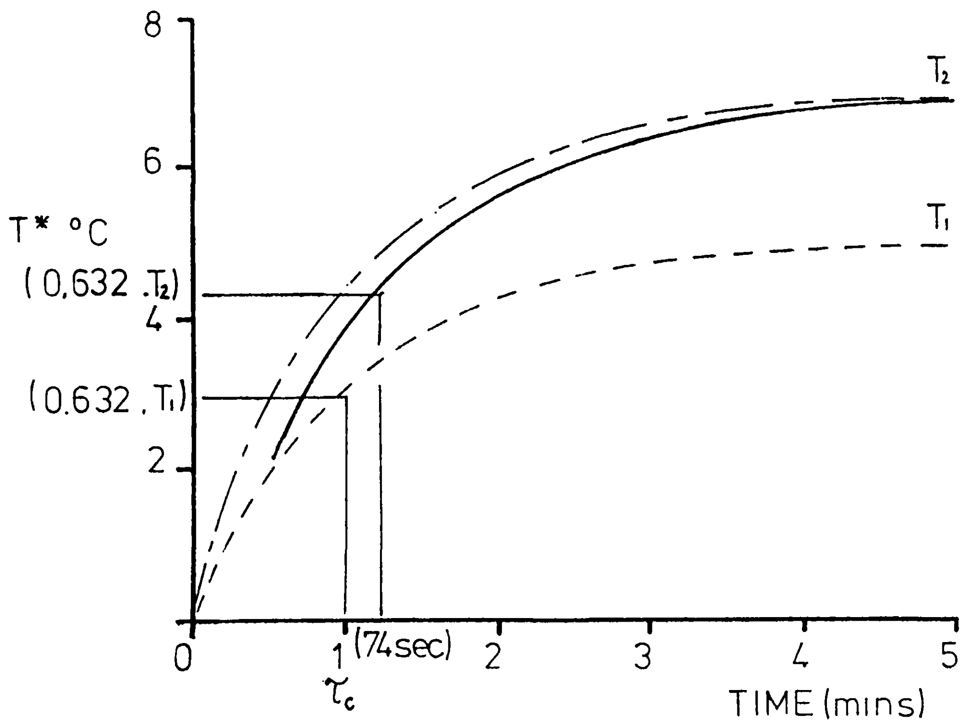

Figure 6.17 Effect of a step change in friction coefficient during an increment on bulk temperature variation.

steady state temperature an average value of μ (0.031) from the third minute to the end of the test was used.

In the 30°C h_r determination test, μ fell from 0.03 to 0.021 over the first minute. The remaining values were higher but had considerable scatter. μ was again taken as an average from the third minute on, i.e. from when the temperature stabilised. The variation in μ for both these tests is similar to the simplified form of μ in the example. The initial response in both tests was probably that to the initial values of μ and as has been seen with the simpler example, this results in values of H_r lower than the real value. Allowing for the effect of the variation in μ would reduce the predicted temperatures, i.e. increase the discrepancy between the results.

f) The difference in the bulk temperatures of the discs should be taken into account when calculating the division of the heat between the discs. If the bulk temperature had been measured in both the discs, the division of heat could have calculated using eqn.(6.7). Unfortunately the experimental set-up was such that the temperature could only be measured in the faster disc. As the difference in the disc bulk temperatures was not known, the division of heat has been calculated using the simpler expression for discs with equal bulk temperatures, (eqn.(6.5)). This assumption is valid for the first increment of a test as the initial bulk temperatures should be approximately equal. Rossides measured the bulk temperature in both discs during scuffing tests run at a 3:1 speed ratio. The discs temperatures prior to scuffing ranged from being approximately the same to a fast disc temperature of 169°C being 35°C above the slower disc temperature. The proportion of heat into the hotter disc would be reduced compared to that for the discs at the same temperature. For example, β_1, the proportion of the heat into the faster disc at a load of 20 kg f, where the faster disc is 20°C hotter than the slower disc would be $\beta_1 = 0.543\beta$, compared to $\beta_1 = 0.634\beta$ if the temperatures are the same. This would reduce the predicted temperatures for the faster disc in tests B and K and so increase the discrepancy between the values.

Although there is a discrepancy between predicted and experimental values and various modifications to the solution could be made, it is nevertheless in a suitable form to predict the relative effects of various parameters on the temperature and time constant. In the next section it is used to assess the differences of thermal response noted for test machines used by earlier workers.

6.8. Using the analysis to compare the thermal response to those of earlier workers

The differences in the thermal response of the Story and Rossides tests were thought to be a result of the different two disc machines used for the tests. This differences were reported in Chapter 2. Briefly they were that the temperature in the Rossides discs following an increase in load was quicker to stabilise than that in the Story discs, which in some increments did not stabilise. The Story machine was also thought to be a more efficient heat sink, (Story et al (1980)).

As the tests were also run with different operating temperatures, loading sequences, rolling and sliding speeds and oil supply configurations, it was difficult to quantify the effect of the machine on the temperature. By running tests with similar conditions these parameters were shown to effect the regime of lubrication in which the tests were run (Chapter 3). The results of this and the previous chapter can be used to estimate to what extent the machine design and the other factors could effect the differences in temperature rise and rate of change observed.

There were differences in the length (2L) of the discs, the dimensions of the shafts and the operating temperatures used by the groups. The length of a cylinder or disc has been shown to have a large effect on the temperature, particularly when the cylinders are 'short' and it is this point that it is examined here.

Both types of disc were 3 in. diameter. For the discs used by Rossides, 2L = 1/4 in. and those used by Story, 2L = 5/8 in. Both discs types were chamfered to give similar track widths of 3/16 in for the Rossides test and 5 mm for the Story tests, which makes the ratio of the track length to 2L , v' = 0.75 and 0.32 respectively. The dimensions of the Story discs were the same as those for the discs used for the tests reported in this thesis. The heat source strength group $\theta^*/\nu\pi$ for a chamfered disc is given by (eqn.6.6) as

$$\frac{\theta^*}{\nu\pi} = \frac{U_1^{1/2}}{U_1^{1/2}+U_2^{1/2}} \cdot \frac{\mu W U_s}{4\pi k v'.L}$$

where W = the total load.

It is customary to compare two disc tests at the same hydrodynamic conditions, i.e. in kN/m or maximum Hertzian pressure Po . The load/unit length of the track is W/2v'L. As the track length, 2v'L , is approximately the same for each disc type, then for the same hydrodynamic conditions the total load W (N) , is also the same. Using the appropriate speeds, disc widths and values of v' for each disc type, the heat source strengths groups have been calculated, in terms of the friction coefficient and the load W (N) .

The bulk temperature for a chamfered disc is given by combining eqn.(5.12), the expression for a plain disc, with the adjustment series for a chamfered disc given in eqn.(6.8). The heat transfer coefficients for the Story and Rossides test machines are not known, so those found in Section 6.6 for the present machine have been used. It was shown in Section 6.3 that for low Biot numbers the adjustment series for a chamfered disc reduces to $\frac{4\,v'.\sin\Gamma_m}{2\Gamma_m + \sin 2\Gamma_m}$ and the series for the bulk temperature terms can be reduced to the first term for both the steady state and the transient series. The bulk temperature is therefore for a single increment - using the notation of Section 5.4

$$T^* = \frac{\theta^*}{\nu\pi} \cdot v' \left(C_1 - D_1\, e^{-d_1\tau}\right)$$

The predicted changes in bulk temperature for the different disc types and surface speeds, but for the same load and coefficient of friction, are plotted in Fig.6.18. Rossides used a range of surface speeds which were all in a 3:1 ratio. The plotted examples are for sliding speeds of 6 m/s, 4.95 m/s and 3.9 m/s for the present, the Story and Rossides test respectively. The steady state temperature in the Rossides discs is similar to the present 3:1 tests but larger than in the Story discs, although the Story tests a higher sliding speed. The Rossides tests have the smallest time constant,that is the temperatures are quicker to stabilise. The form of these curves are consistent with the original observations; the Rossides discs were quicker to equilibrium but the Story discs were a better heat sink.

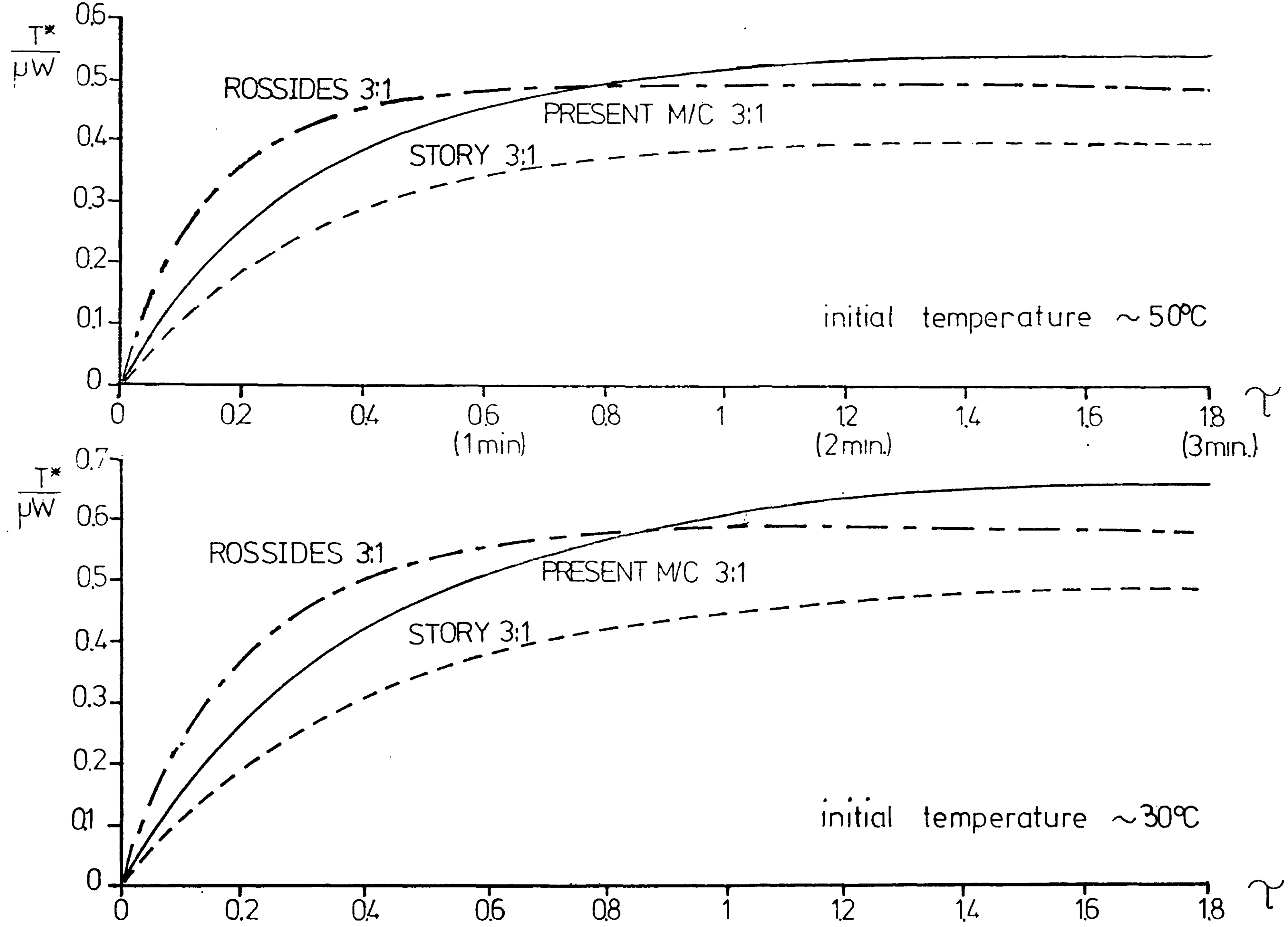

Figure 6.18 Predicted variation in disc bulk temperature for the disc speeds and widths for the present, Story and Rossides tests.

CHAPTER 7

VARYING THE THERMAL RESPONSE OF THE TEST MACHINE AND THE SECOND TEST SERIES

7.1 Introduction

There were two suggested reasons for the differences in the scuffing conditions of tests run by Story (1980) on the one hand and by Bell and Dyson (1972) and Rossides (1980) on the other. The first of these suggested reasons, the role of operating conditions, was investigated in Chapter 3. It was shown that the operating conditions determined the regime of elastohydrodynamic lubrication in which the system operated and at high sliding speed; this determined whether or not the surfaces ran-in.

The second suggested reason arose from observations of the thermal responses of the test machines used by Story and Rossides and of the differing degree of running-in in the test types. A scuffing criterion proposed by Crook and Shotter (1957) seemed to have some relevance in the light of these observations. Their hypothesis was that a system survives a change in conditions if the rate at which the surfaces are able to run-in exceeds the rate of change of film thickness, and was reviewed in Section 2.

The rate of change of film thickness is related to the rate of change in bulk temperature due to the effect of the bulk temperature on the oil viscosity. The Dowson and Higginson film thickness formula gives the relationship between the film thickness h^*, and the fluid viscosity at the bulk temperature of the discs η, as

$$h^* \propto \eta^{0.7} \qquad (7.1)$$

The variation of η with the bulk temperature, T, can conveniently be expressed

$$\eta = \eta_o e^{-\gamma T} \qquad (7.2)$$

where γ is the temperature coefficient of viscosity and η_o is the viscosity at ambient temperature and pressure.

If the axial Biot number for the discs in a two disc machine is low, the bulk temperature rise, following an increase in load, can be assumed to be exponential, as shown in Fig.7.1. The temperature at time t is

$$T = T_{int} + T_s^* (1 - e^{-Kt}) \qquad (7.3)$$

where K is the decay exponent of the system.

The rate of change of film thickness during an increment can be found by differentiating equations (7.1), (7.2) and (7.3) and combining in the expression

$$\frac{dh}{dt} = \frac{dh}{d\eta} \cdot \frac{\partial\eta}{dT} \cdot \frac{dT}{dt}$$

to give

$$\frac{dh}{dt} \propto - \eta^{0.7} . K . T_s^* . e^{-Kt} \qquad (7.4)$$

$\frac{dh}{dt}$ is a maximum when $t = 0$. $\eta^{0.7}$ is then proportional to h_i , the initial film thickness and eqn.(7.4) reduces to

$$\frac{dh}{dt} \propto - h_i . K . T_s^* \quad (\text{at } t = 0) \qquad (7.5)$$

This expression shows that the maximum value of $\frac{dh}{dt}$ during an increment is proportional to h_i , the decay exponent K , and the incremental temperature rise T_s^* . Chapters 5 and 6 have developed expressions to predict both the temperature rise and the decay exponent for a two disc system. Although the agreement between theoretical and experimental temperature response is not yet exact it is sufficient to indicate the ways in which the thermal response might be changed and the Crook and Shotter hypothesis tested. Attempts to alter the thermal response of the test machine and the effect of these changes on scuffing conditions are the subjects of this chapter.

The design of the discs and the machine described in Chapter 3 is taken as the 'normal' case. Changes in the temperature rise during any increment, ΔT_s^*, and the decay exponent, K , about the normal level are required. Various methods of changing the thermal response are discussed in Section 7.2 and assessed in the light of the results of Chapters 5 and 6.

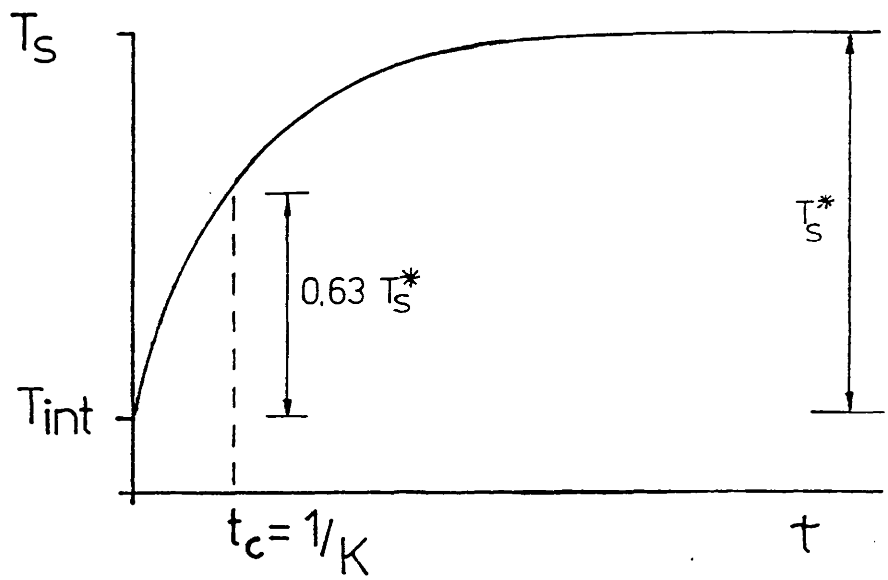

Figure 7.1 Exponential disc bulk temperature rise following the application of a load.

The method adopted to increase the temperature rise was to insulate the discs, as in the tests to determine h_r (Section 6.6) . The results of a series of six tests, in this mode, are reported in Section 7.3.

Exploratory tests of a method to reduce the rise in bulk temperature are described in Section 7.4. Recommendations for improvements in this method are made.

Section 7.5 discusses the extent to which the thermal response has been altered.

7.2 Methods to change thermal response of the test machine

Various methods were considered to alter the thermal response of the test machine. These included

a) additional sources of heating or cooling to the discs

b) changing the dimensions of the discs and/or of the disc chamfer

c) changing the heat transfer coefficients.

Feasible methods were limited by the existing design of the discs and shafts and by the possibility that any substantial changes to the discs or to the machine could be a potential source of unforeseen variation in the results. Some of the methods which were thought suitable could not be implemented for this project due to additional equipment required and lack of time. These could be adopted in the future and so are discussed here.

7.2.1. Additional sources of heating and cooling

Internal heating and cooling of the discs was first considered as this would provide a controllable method of altering the thermal response. Various methods have been employed to do this by other workers. In a crossed cylinders machine used by Archard and Kirk (1961) to study the effect of body temperature on film thickness, oil at a different temperature to the supply oil was pumped around a pipe network within the cylinder body.

The surface was made of a separate thin sleeve which was responsive to changes in the internal oil supply temperature.

Although the shafts in the present discs have a hollow centre portion they were not suitable for internal oil circulation. As the bulk of the discs was large it is expected that they would not be very responsive to changes in the temperature cooling oil even if this were possible. To adopt this method of cooling would therefore require a new shaft/disc arrangement such that the heated or cooled oil could flow close to the surface of the discs. It would also require fittings for the oil to enter and leave the shafts but still be compatible with the existing bearing, cantilever housing and disc drive system. A secondary oil circulation system would also be needed. In short this system is not very convenient in a non purpose-built machine.

Other workers have used electric heating elements to provide an additional source of heating to the discs. For example, Hirst and Moore (1980) and Conry, Johnson and Owen (1979), made traction measurements on a two disc machine, with electrically heated discs. Heating elements were located in holes drilled axially through the disc and a voltage supplied via slip rings. This potentially useful and comparatively simple method could not be adopted due to the lack of suitable slip rings both to supply the voltage to heating elements and to transmit the thermocouple signals used to measure the bulk temperature of the discs.

As the methods of controllable additional sources of heating or cooling were not feasible, simpler methods of altering the thermal response were considered.

7.2.2. Changing the disc dimensions

The previous two chapters have studied factors which influence the temperature changes and rates of change in two disc machines. It has been shown that T^* and τ_c (1/K) are functions of the heat transfer coefficients h_a and h_r, the dimensions of the discs, L and R, and the size of the chamfer of the disc, $2v'.L$. Altering T^* and τ_c by changing the disc dimensions is discussed in this section and by changing h_r and h_a in the next.

The radius of the discs is set by the machine design. A change in the length of the discs or the length of the chamfer is a feasible method to change the response. The primary requirement of any such change for tests using discs of different dimensions to be comparable is that the hydrodynamic conditions, i.e. the load/unit length of the track, be the same. There is a limit to the extent of any such changes set by, for example, the distance between the bearing housings and the limit of the loading system.

The effect of the length of a cylinder with a heat source extending along its full length on the bulk temperature was examined in Section 5.4.4. Increasing L increases the axial Biot number $Ha = h_a L/k$, and from Biot number considerations alone should reduce the temperature. However, it was shown in Section 5.4.4 that the temperature would increase under these conditions. This was due to the increase of the heat source length with the cylinder length, whilst the heat loss from the ends of the shaft remained constant.

It was shown in Section 6.3 that when the heat source extends only over the centre portion of a disc, $2v'L$, for a low axial Biot number, the bulk temperature above ambient, T^* , was reduced to v' times that in a disc with a heat source of the same strength, β , extending over its full length. Varying the length of the heat source in proportion to the disc length would be a simple method of altering the response. For example, using two plain discs of the same length as the normal discs should, for the same heat source strength, increase the centre temperature of the discs approximately threefold.

Alternatively the track length, $2v'L$, could be held constant and the length of the discs changed. This was the difference between the Rossides and the Story type discs; they had the same track length but the Story discs were over twice as long. The predicted temperature response of the two disc types was examined in Section 6.8. For the Rossides discs it was found that the shorter discs acted to reduce T* and τ_c , but the heat source extending over a greater proportion of the disc length acted to increase T*. The net effect was that the temperature rise for the Rossides discs for a given heat source strength was slightly greater than that for the Story discs but that they had a smaller time constant, i.e. the temperatures were quicker to stabilise. The true effect of any such changes in the discs dimensions should be carefully analysed before being implemented.

Of the three options for varying the disc axial dimensions the second, altering the track width while the disc width is constant, would be the most practical, as the existing shafts could be used. It could not, however, be adopted for this investigation as all the discs, which were supplied by the sponsoring body (the NPC & T Division of the RAE) were manufactured prior to this investigation, with all the rough discs being chamfered. This method should be considered for any future work along these lines.

7.2.3. Changes in heat transfer coefficients

The maximum possible changes in T* resulting from changes in either heat transfer coefficient can be shown by reference to Fig.7.2. This shows, for an L/R ratio of 0.208 , the bulk temperature T_s^* normalised with respect to the heat source strength, for a range of Hr and Ha .

In Section 6.6, Biot numbers were determined for the two discs machine environment. It was assumed that the radial and axial heat transfer coefficients were the same, i.e. that Ha = 0.208 Hr . The operating condition for these Biot numbers are shown by crosses, (condition A).

The predicted bulk temperature in a finite disc, using these values were less than those measured in experiments. One possible reason for this was that $h_a \neq h_r$. The approximate range of operation for the tests using the same value of Hr but an adjusted value of Ha to match the predicted and experimental temperatures is also shown, (condition B) .

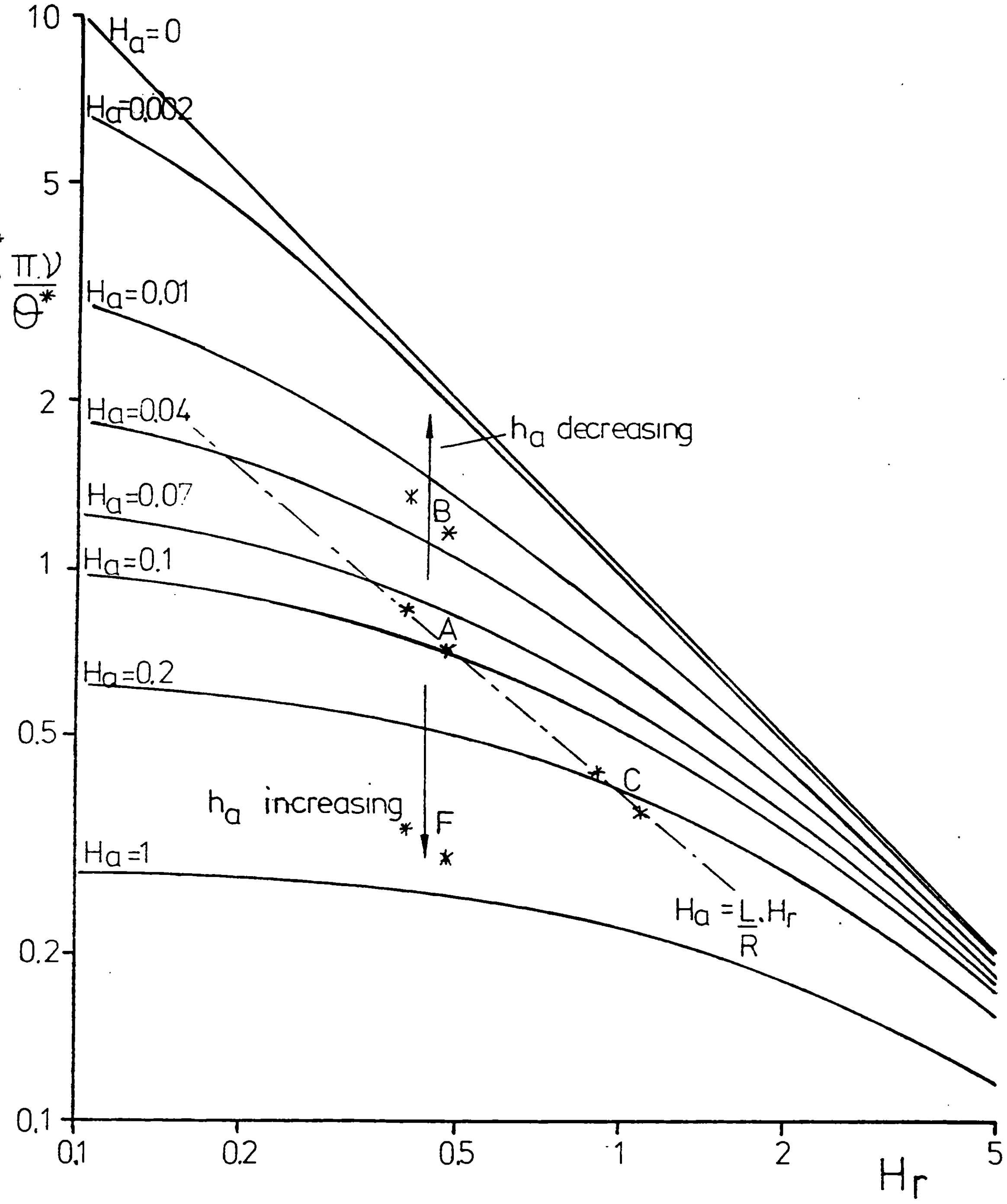

Figure 7.2 Effect of altering the heat transfer coefficients on the steady state temperature.

The chain line through condition A shows the operating temperatures when the heat transfer coefficients h_r and h_a, are changed but as in the previous chapter still assume equal, i.e. the range for Ha = 0208 x Hr . The maximum heat transfer coefficient is expected to be that for the disc completely submerged in oil. Theoretical values of h_a and h_r for this case were found in the previous chapter and this operating condition (condition C) is also shown. The predicted rise in temperature for a disc fully submerged in oil is approximately one half that for condition A and one third that for condition B. The other extreme of heat transfer coefficient is for the discs rotating in air (not shown on figure) and give a temperature rise of approximately 20 times that for the discs completely submerged in oil.

An obvious way to change the heat transfer coefficients is to change the oil flow rate. The relationship between the oil flow rate and heat transfer coefficients has not been investigated here. Ku and Li (1977) investigated the effect of oil supply on the surface temperature. They gave a simple expression relating the surface and oil supply temperatures and the frictional heating in the contact,

$$T_{surface} - T_{oil\ supply} = C.(\beta.A)^n$$

where $\beta.A$ represents the frictional heating in the contact and C was a parameter which was partly a function of the oil supply rate. The variation of C with oil supply rate for three different test machines is shown in Fig.7.3, and is relatively insensitive to the supply rate in each case. If the effect of supply rate on temperature for the present machine is similar to that shown in Fig.7.3, doubling the supply rate, would only reduce the temperature rise by approximately 10%.

This apparently simple method of altering the heat transfer coefficient was not adopted as the effect of the supply rate was expected to be small, the pump setting was already near maximum and there was a possibility

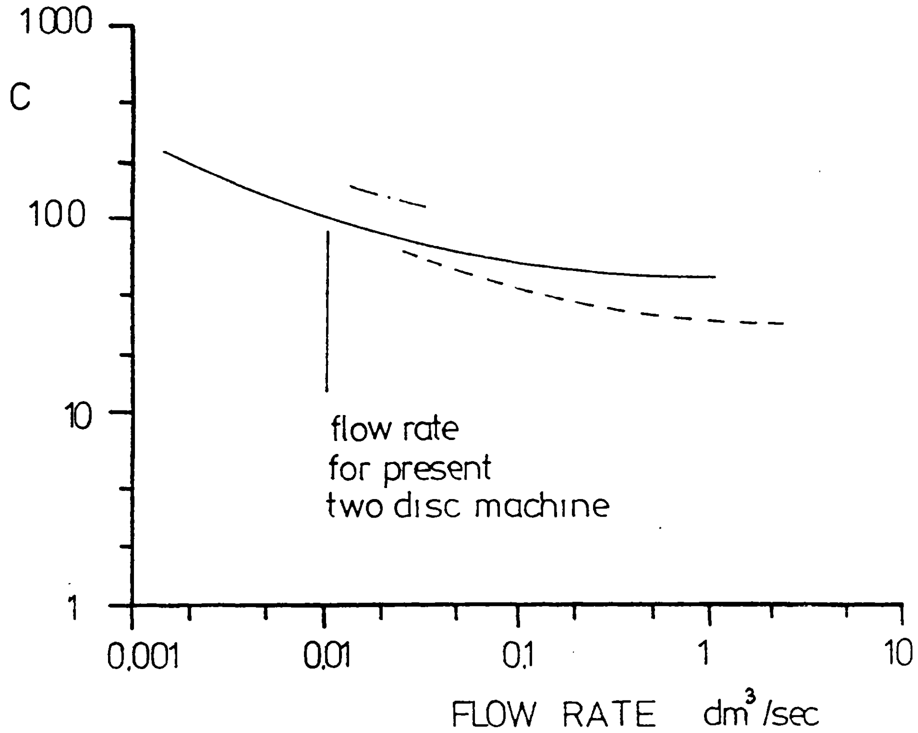

Figure 7.3 Effect of oil flow rate on disc bulk temperature for three test machines.
(after Ku and Li (1977))

that severely reducing the flow rate could have a hydrodynamic effect, for example starvation.

Methods by which h_a can be altered independent of the oil flow rate are next considered. The variation in h_a at constant h_r gives a vertical line on Fig.7.2. In the previous chapter it was assumed that by insulating the side faces of the discs and the disc centre, h_a and the losses along the shaft were reduced to a negligible value. The disc temperatures were then taken as tending to those predicted for an infinite length cylinder, corrected for the effect of a reduced chamfer, i.e.

$$T_s^* = \frac{\theta^*}{\sqrt{\pi}} \cdot \frac{v'}{Hr}$$

This operating condition (condition E) is also shown in Fig.7.2. This is the maximum temperature which could be achieved by changing h_a alone. The predicted temperature rise is 3 to 4 times that for a normal finite disc, (condition A) or twice that for the adjusted values of Ha (condition B), which matches the experimental conditions for finite discs in Chapter 3. Due to the ease of this method which had already been shown to be effective, it was adopted as the one extreme of the range of thermal response which could be achieved without major modifications to the test machine.

The method adopted to increase the axial heat loss and hence T* was to increase the surface area available for convection at the side of the discs with fins and to force the convection from these fins by directing air jets onto them.

Fig. 7.2 shows that around the normal operating condition, T* is not very sensitive to a reduction in h_a. For example, to reduce T* to a quarter of that for normal discs, ie. condition B to condition F, h_a has to be increased approximately 20 fold. It was doubtful that such a large increase in h_a would be achieved. A prototype fin arrangement in the form of collars was made which could be used with the existing discs and shafts.

A short series of exploratory tests were run using the collars to provide an insight into the effectiveness of the method and the problems of running these tests.

The three modes of operation will be referred to as 'insulated', 'normal' and 'cooled', the 'normal' mode being that of the machine operating as described in Chapter 3. The results of the insulated and the exploratory cooled tests are reported in Sections 7.3 and 7.4 respectively.

7.3. Insulated tests

7.3.1. Test procedure

The insulated tests were run at the 3:1 speed ratio. This should produce larger temperature changes than at the 2:1 ratio, due to the greater sliding speed and it was envisaged that any resulting differences in behaviour between the insulated and normal tests due to the change in the thermal response would therefore be more defined at this ratio.

Six insulated tests were run with initial and operating conditions to match as closely as possible those of the 3:1 normal tests A-F.

The disc/shaft configuration for the insulated mode was described in Chapter 6. The test preparation and running procedure was essentially as detailed in Chapter 3 except for the following modifications.

In the tests to determine the heat transfer coefficients (Section 6.6), the temperatures in the insulated discs did not stabilise until approximately the fifth minute. The increment length was therefore extended to ten minutes for the insulated scuffing tests to ensure that equilibrium was established within an increment. Two strain gauged cantilevers were used in the insulated tests. There was an imbalance of up to 2.5 N in all of the tests. At low values of load this discrepancy has a large effect on the resulting values of μ for the two cantilevers but this is reduced at higher values of load and friction. For example, in test B' in the first increment values of friction of 1.8 and 0.93 N results in coefficients of friction of 0.233 and 0.12 respectively. In the ninth increment of the same test friction values of 9.54 N and 8.23 N give μ values of 0.056 and 0.048, i.e. the difference in μ is reduced. This again highlights the errors in measurement of friction particularly at low load.

For the normal tests the Talysurf profilometer was used to measure surface roughness of the discs 'in-situ' on the machine test bed. This arrangement was adopted as it was originally intended to take surface roughness measurements at intermediary stages of the test. Although this was not in the end the case, the Talysurf was used in this position. Measurements of surface roughness taken with the Talysurf mounted on the test bed were sensitive to background vibrations which limited the times at which the apparatus could be used. For the insulated tests the Talysurf was used on its standard base, with the discs mounted on a shaft held in position by V-blocks on the Talysurf base. Four relocated traces of each disc were taken by aligning the eyepiece graticule with the centre of the diamond indentation as before.

Tufnol pieces electrically insulated the discs from the shafts. So that the count rate monitor could still function, a wire connected the shaft to the discs, through a hole in one of the Tufnol side pieces.

7.3.2. General observations

Six insulated tests, A'-F', were run at the 3:1 speed ratio, with initial temperatures of 30°C, 50°C and 70°C for both loading sequences.

All the tests were run until failure. The surface was scuffed on the free side in tests A', B' and E' and on both sides in tests E' and F'. In test C' the scuff covered the whole surface so no post-run surface data was available for this test.

The initial and failure conditions for tests A'-F' are given in Table 7.1a and those of the normal 3:1 tests A-F, are repeated in Table 7.1b for comparison.

TEST	A′	B′	C′	D′	E′	F′
LOADING SEQUENCE	LOG	LOG	LOG	LIN	LIN	LIN
OIL SUPPLY TEMPERATURE °C	29	50	73	33	52	74
INITIAL DISC BULK (2mm) TEMPERATURE °C	29	48	70	32	51	72
FAILURE INCREMENT	10	10	6	3	2	1
FAILURE LOAD - kgf (10:1)	4.9	4.9	2.4	6	4	2
Po at FAILURE $N/m^2 x 10^6$	431	431	301	476	389	275
DISC BULK (2mm) TEMPERATURE AT FAILURE °C	68	76	95	61	68	108
COEFFICIENT OF FRICTION AT FAILURE - μ	.042	.057	.114	.060	.041	.128
FLASH TEMPERATURE AT FAILURE °C	34	46	53	57	28	40
TIME TO FAILURE IN LAST INCREMENT -SECS	134	39	114	37	31	109

Table 7.1a Initial and failure conditions - 3:1 insulated tests.

TEST	A	B	C	D	E	F
LOADING SEQUENCE	LOG	LOG	LOG	LIN	LIN	LIN
OIL SUPPLY TEMPERATURE °C	29	53	77	25	52	72
INITIAL DISC TEMPERATURE °C	28	46	71	24	49	68
FAILURE INCREMENT	15	14	10	6	3	3
FAILURE LOAD - kgf (10:1)	11.9	9.9	4.9	12	6	6
p_o AT FAILURE $N/m^2 \times 10^6$	671	612	431	674	476	476
DISC BULK (2mm) TEMPERATURE AT FAILURE °C	55	76	86	62	67	88
COEFFICIENT OF FRICTION AT FAILURE	.016	.045	.027	.022	.022	.027
FLASH TEMPERATURE AT FAILURE °C	25	62	22	34	21	28
TIME TO FAILURE IN LAST INCREMENT SECS	84	17	13	53	84	9

Table 7.1b Initial and failure conditions - 3:1 normal tests.

The initial bulk temperatures were within $\pm$ 4'C of the corresponding normal tests except for test D' where it was 7'C higher than in test D .

Tests B', D' and E' failed within the first 40 secs. of the final increment whilst A', C' and F' failed between 100 and 140 secs. In test C', the coefficient of friction was very high in the first increment and this was accompanied by a very large rise in temperature. The friction coefficient remained high for the rest of the test and there was extensive post-run surface damage. These factors suggested that the discs may have scuffed (and 'healed') in the first increment. There was no noticeable sudden increase in the levels of noise and vibration of the machine indicative of scuffing during the first increment and examination of the detailed friction and temperature results for the increment showed no sudden increase in friction or temperature. The failure conditions for this test are therefore taken as those in the sixth increment.

In test F' , there was also a high initial coefficient of friction, although not as high as that in test C' . There was a rapid increase in friction and temperature from the beginning of the first increment, but failure occurred after 109 secs. with a definite sharp increase in friction and temperature that is characteristic of scuffing failure.

The tests failed at loads in the range, 2 kgf to 6 kgf and at bulk temperatures in the range, 61'C to 108'C . There was a tendency for the failure load to decrease and the bulk failure temperature to increase with increasing initial bulk temperature with no apparent benefit in using the LOG or LIN loading sequence over the three temperatures.

The failure loads are less than in the equivalent normal tests. They ranged from 2/3 of the normal test load in tests E/E' to 1/3 in tests F/F'.

The bulk temperatures at failure for the test pairs B/B' , D/D' and E/E' were approximately the same ($\pm$ 1'C). In tests A/A' , C/C' and F/F', the insulated tests failed at higher bulk temperatures than the normal tests, the greatest difference being 20'C in tests F/F' .

The pre- and post-run surface roughness data is given in Table 7.2. There was no post-run surface data available for test C' as the surface was completely scuffed. The degree of running-in will be expressed, as before, in terms of ΔRa , the difference between the pre- and post-run surface roughness.

The range of ΔRa for the insulated tests was $\Delta Ra \sim 0.025\text{-}0.038$, which is smaller than that for the normal 3:1 test, $\Delta Ra \sim 0.011\text{-}0.06$. In the 'normal' tests, A , D and E had the least reduction. In the equivalent insulated tests, ΔRa values in these three tests have increased slightly. Conversely tests B , C and F had moderate running-in but in B' and F' these values are reduced.

7.3.3. Incremental changes in friction and temperature

The coefficient of friction and the bulk temperatures for tests A'-F' are plotted in Fig.7.4. The coefficient of friction and the bulk temperatures for each increment are replotted against p_o , in Figs.7.5 and 7.6 respectively, using the same conventions as described in Section 3.3.4. It was noted in Section 7.3.1 that two strain gauged cantilevers were used in three tests and that there was some imbalance in the values. The values of in Figs.7.4 and 7.5 are the lowest value in each case.

In the tests starting at 30°C and 50°C , tests A' , B' , D' and E' , the coefficient of friction patterns are similar to those for the early stages of the normal tests. The LOG tests start with a high coefficient of friction, consistent with classical lubrication; the LIN tests starting with a higher load and lower coefficient of friction in the ehl regime. Both the LOG and LIN tests fail at lower loads than the normal tests, before a full pattern of friction coefficient against p_o emerges.

In the normal 3:1 tests, the friction coefficients throughout tests A , C , D , E and F were consistently lower than in test B , the repeat 3:1 tests B1 , B2 , E1 and E2 , and all the 2:1 tests. The friction

TEST	A′	B′	C′	D′	E′	F′
PRE - RUN						
ROUGH DISC Ra- μm	0.375	0.365	0.383	0.356	0.322	0.273
SMOOTH DISC Ra- μm	0.044	0.045	0.046	0.051	0.046	0.031
do	0.668	0.650	0.683	0.637	0.554	0.486
POST - RUN						
ROUGH DISC Ra- μm	0.343	0.327	*	0.332	0.297	0.242
SMOOTH DISC Ra- μm	0.044	0.051	*	0.053	0.046	0.030
ΔRa ROUGH DISC	0.032	0.038	*	0.024	0.025	0.031

* insufficient unscuffed surface for measurement

Table 7.2 Surface roughness values - insulated tests (3:1).

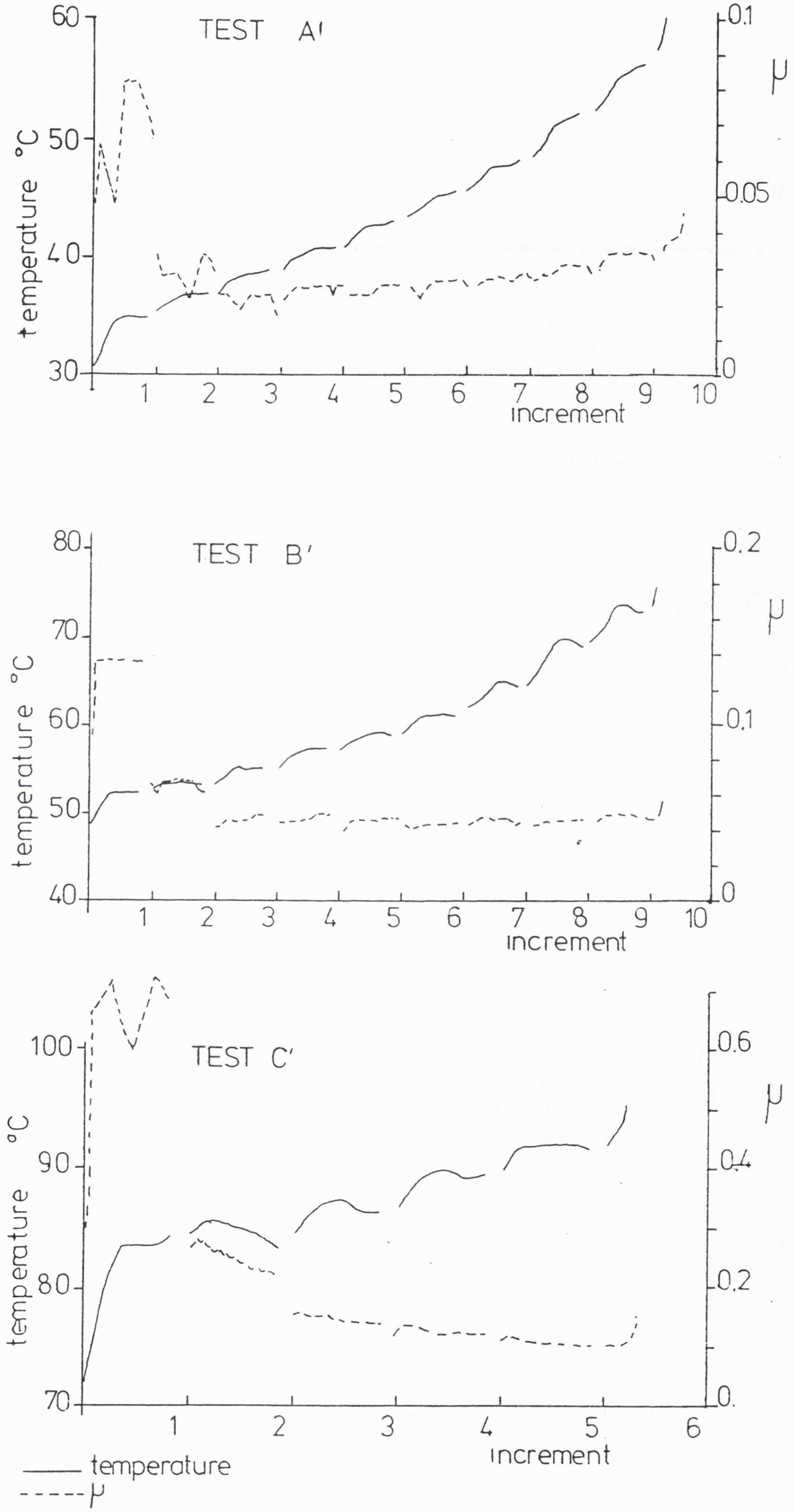

Figure 7.4a   Incremental changes in bulk temperature and friction - 3:1 insulated tests. (A' B' and C')

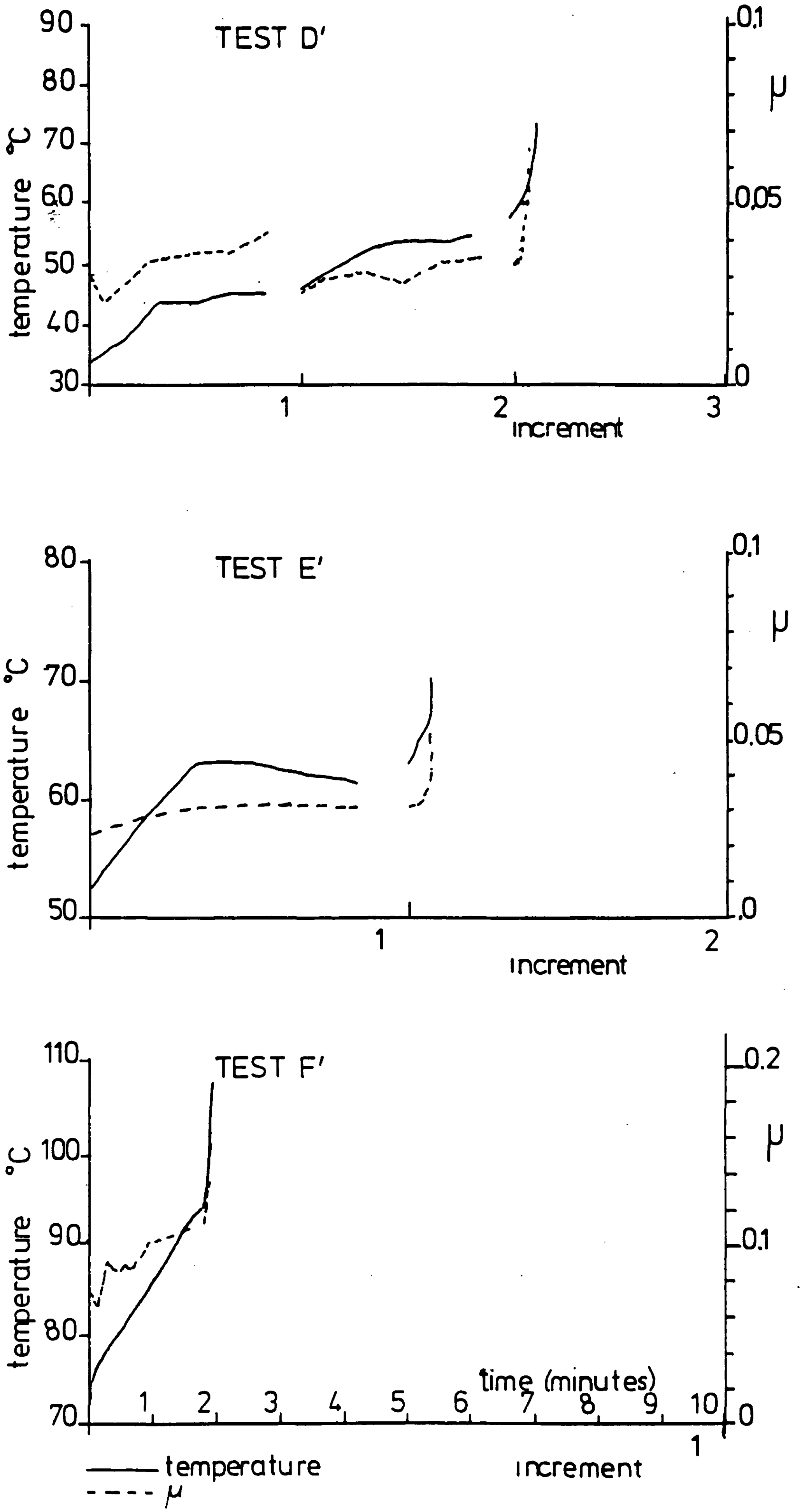

Figure 7.4b Incremental changes in bulk temperature and friction - 3:1 insulated tests. (D' E' and F')

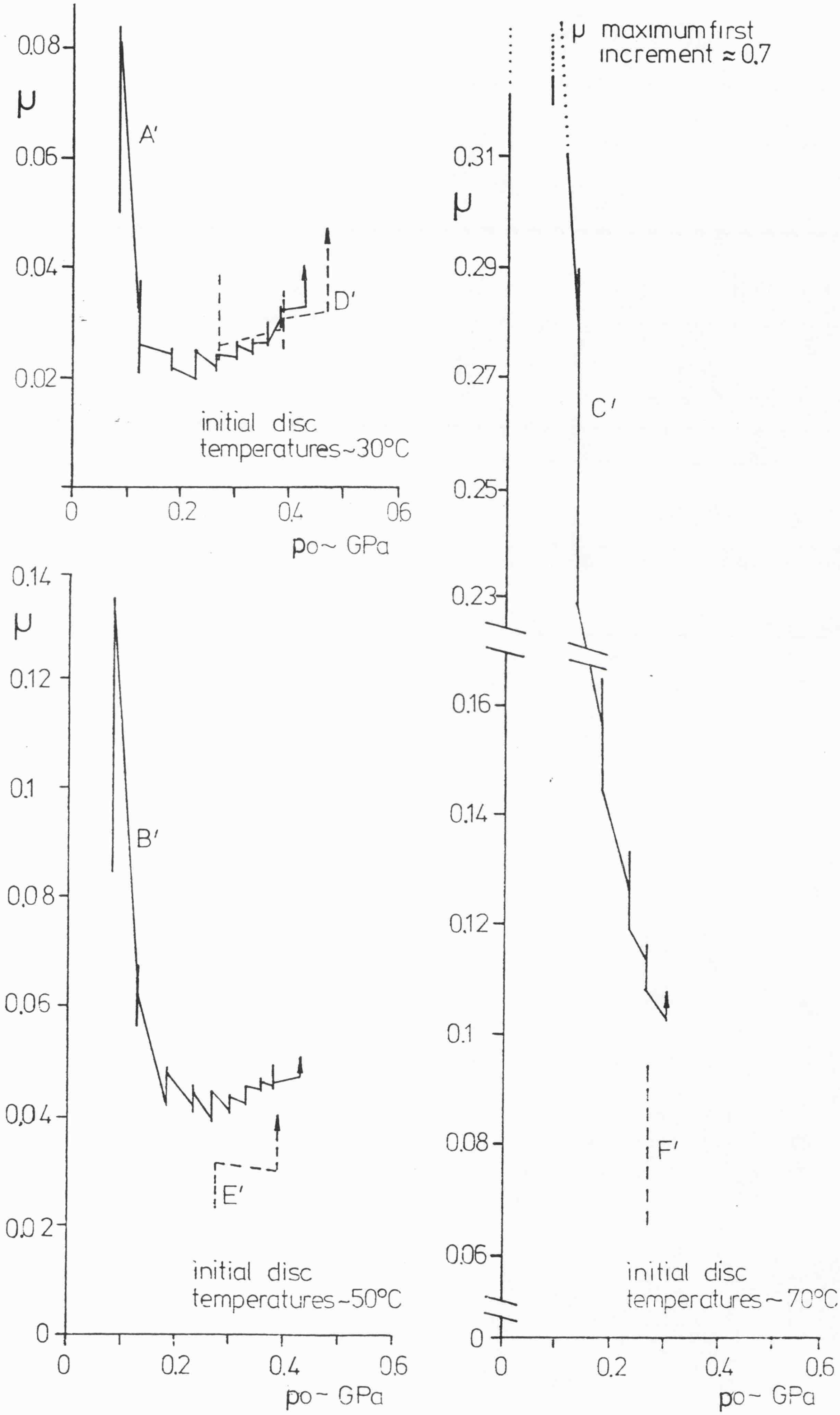

Figure 7.5 Coefficient of friction / p_0

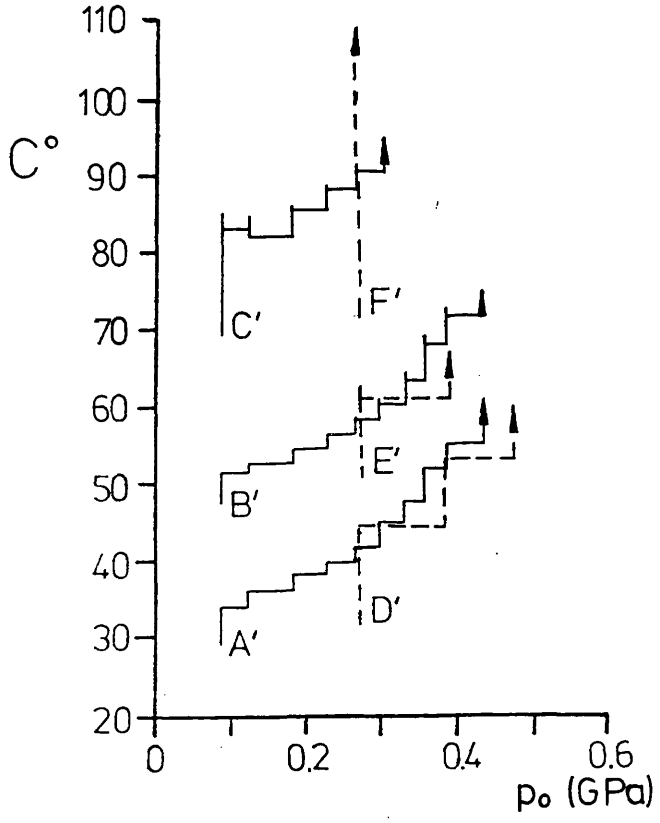

Figure 7.6 Disc bulk temperature/p_o

levels in tests A' , B' , D' and E' are all similar and are comparable to the higher levels in the normal tests.

In the high temperature insulated tests, C' and F' , there are noteworthy differences in the coefficient of friction results. The initial coefficient of friction in test F' is much higher than that in test F , but is similar to that in the 2:1 test, L . The coefficient friction in the first increment of test F' rises rapidly from 0.065 to 0.095 during the first 109 secs. at which time the discs failed.

In test C' , the initial value of μ is much higher than in any other test. As already noted it was suspected that failure could have occurred in the first increment but although both μ and the temperature rose throughout the increment the rise was gradual, i.e. there was no sudden change in conditions. In the following increments the classical/ehl friction coefficient pattern began to emerge, with μ falling towards a minimum value of 0.1 in the failure increment, which is still higher than that during any other test. The predicted temperature rise using this value of friction coefficient was ~ 8 C compared to a measured value of 14 C, which suggests that the high values were not a fault in the instrumentation. No obvious source of error could be found to explain these very high values. They are discussed in more detail in the final chapter.

The steady state temperatures, T_s^* , for each increment of each test are plotted against p_o in Fig.7.6. Insulation of the discs gives gradients of T^*/p_o greater than in the normal tests over the same p_o range. In the LOG tests there is a larger temperature rise in the first than in the second increments. This was especially pronounced in test C' where the temperature rose by 14°C in the first increment and fell by 1° during the second increment. In this test the decrease in friction coefficient from the first to the second increments is proportionally larger than the increase in load and hence the heat source strength decreases.

7.3.4. Total contact temperatures and frictional power intensity at failure

The total contact temperature of the six insulated tests prior to failure are given in Table 7.3. The values range from 96°C to 148°C , the highest value being that for test C' . This range is similar to that for the 3:1 normal tests but the problems of friction measurement in those tests makes a direct comparison for equivalent 3:1 tests in the two modes difficult.

For the total temperature at failure to remain constant, an increase in the bulk temperature must be accompanied by a reduction in the flash temperature. In tests A' , C' and F' , the bulk temperatures at failure are higher than tests A , C and F respectively. Even though the friction is uncertain, a higher failure load in the normal tests would suggest a higher flash temperature, which shows some trend towards the inverse relationship between the temperatures.

The criterion for total contact temperature at failure should be independent of sliding speed. The range of total contact temperature for the 3:1 insulated tests is lower than that for the normal 2:1 tests (232-295°C) which offers little support to the criterion.

The values of frictional power intensity at failure for the insulated tests are given in Table 7.4. The values range from 75.2×10^6 watts/m^2 to 161.7×10^6 watts/m^2 . Excluding the highest value, which was again that for test C' , the range is higher than tests A , C , D , E and F , similar to the normal 3:1 repeat tests B , B1 , B2 , E1 and E2 (50.6×10^6-129×10^6) but lower than the 2:1 normal tests.

7.3.5. Regimes of lubrication

In this section the results of the insulated tests are discussed in terms of both the effect of the change of the thermal response and, as in the normal tests, in terms of the regimes of lubrication. The six insulated tests are shown on the micro-ehl onset plot in Fig.7.7. The count rate

TEST	A′	B′	C′	D′	E′	F′
BULK TEMPERATURE °C	68	76	95	61	68	108
FLASH TEMPERATURE °C	34	46	53	57	28	40
TOTAL CONTACT TEMPERATURE °C	102	122	148	118	96	148

Table 7.3 Total Contact temperature at failure - 3:1 insulated tests.

TEST	A′	B′	C′	D′	E′	F′
μ	0.042	0.057	0.114	0.06	0.041	0.128
P_{av} ($N/m^2 x10^6$)	338.5	338.5	236.4	373	305.5	216
FRICTIONAL POWER INTENSITY - $x10^6$ watts/m^2	85.3	115.8	161.7	134.3	75.2	123.1

Table 7.4 Frictional power intensity at failure- insulated tests.

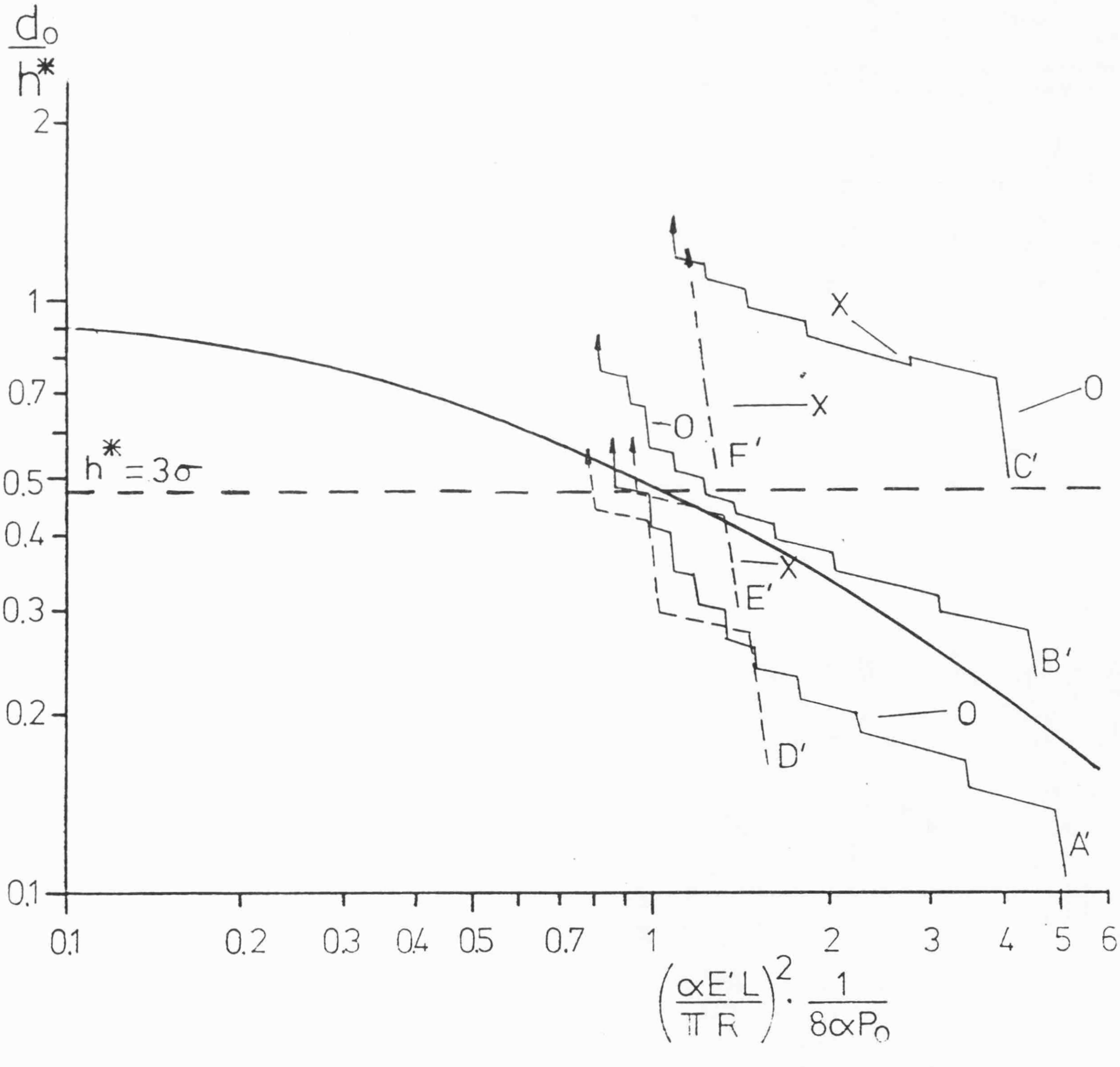

Figure 7.7 Test histories of 3:1 insulated tests on micro - ehl onset plot.

information is displayed as before on the tests histories, by an 'O' for the decaying pattern and an 'X' for a sustained count rate pattern.

The insulated tests start with values of the load group and do/h* similar to the equivalent normal tests; tests A' , D' and E' start operation in the ehl region and tests B' , C' and F' in the micro-ehl region. The larger temperature rise per load stage is reflected in larger vertical steps and hence the steeper slope of the plotted test histories compared to the normal tests.

In tests A' , D' and E' , the steeper paths result in the test histories lying closer to the transition band to micro-ehl than the equivalent normal tests, although they do not cross it. It also causes the tests to cross the mixed lubrication boundary ($h^* = 3\sigma$) at lower loads than the normal tests.

All three tests fail during the increment of transition to mixed lubrication, as predicted by $h^* = 3\sigma$. As such the do/h* level for these three tests at failure is more similar than in the equivalent normal tests.

Tests B' , C' and F' which start in the micro-ehl region, each fail with a nominal degree of interaction do/h* similar to the equivalent normal test. Again, due to the steeper paths, each insulated test fails at a lower value of the load group than the equivalent normal test.

In the normal mode at the 3:1 ratio, the nominal interaction at failure, the nominal interaction at which the contact patterns emerged and the degree of running-in in the tests, were all taken as indications of different regimes of lubrication.

Tests C' and B' ran to higher do/h* levels than A' , D' and E' before failing, which is again indicative of different regimes of lubrication. Although test F' failed in the first increment, the nominal interaction level, do/h* , at which the discs scuffed was also higher than in the ehl/mixed tests.

There is no count rate data available for test D' . In test A' , the first pattern is observed at do/h* ~ 0.2 , that is at a thicker film than predicted, although there was very little activity thereafter and the test failed before the X pattern emerged. As both tests failed at $h^* > 3\sigma$ there should have been little contact before failure. The early contact in test A' , and the running-in in both the tests, suggests that h^* is again an overestimate. Possible causes for the count rate at thicker values of film thickness than expected for the normal tests were discussed in Section 4.5 and will not be reiterated here.

In tests E' the 50°C LIN test, which started operation at $do/h^* \sim 0.3$ and failed in the second increment, there was sustained count rate activity throughout the test. In contrast in test B' , the decaying pattern was delayed to the eighth increment, $do/h^* \sim 0.65$. This difference in the count rate patterns in the two 50°C tests is consistent with ehl/mixed behaviour in test E and micro-ehl behviour delaying contact to thinner nominal films in test B' . As such, this is a more positive indicator of different regimes of behaviour than in the normal tests at this temperature.

In the high temperature tests C' and F' there was contact from the start of the test. Although these tests started with similar do/h^* levels to those in the normal tests, C and F , the very large rise in the bulk temperature in the first increment of both insulated tests resulted in a change in do/h^* to 0.73 , by the end of the first increment in test C' and to 0.95 before failure in test F' . These values are greater than those at which contact first occurred in the normal tests. It is probable if micro-ehl did take place in these tests that the deformation of the main-scale asperities was not sufficient to delay contact at these high levels of do/h^* .

In the 3:1 normal tests, ΔRa was larger in the tests which started in the micro-ehl region than in those which moved from the ehl to mixed lubrication regimes. The difference in ΔRa between the two test types has been reduced in the insulated test and is not therefore an indicator of different regimes.

The larger temperature rise in each increment of the insulated tests implies an increase in the value of $\partial h/\partial t$. If the Crook and Shotter hypothesis is correct, then a larger value of $\partial h/\partial t$ should result in earlier failure of the surfaces with presumably less surface modification.

In tests A' , D' and E' failure was indeed earlier than in the normal case (lower values of do/h^*) but ΔRa was increased. ΔRa was reduced in tests B' , C' and F' and here the values of do/h^* at failure were similar to those in the normal tests. In all cases the failure load was lower than normal. Support for the Crook and Shotter hypothesis seems contradictory and it is not possible to determine from these tests whether early failure was due to a greater $\partial h/\partial t$ or a larger temperature rise per se.

The 2:1 normal tests were able to survive the transition from ehl to mixed lubrication and could also continue to run in the micro-ehl regime when there was significant contact. If 2:1 insulated tests had been run and if the tests failed earlier, i.e. if they did not survive the transition to mixed lubrication, then this would have been a more direct indication that the rate of film thinning was of importance. For this reason in retrospect it would have been useful to run some insulated 2:1 tests.

7.3.6 Conclusions

Some of the indications of different regimes of lubrication found previously were not repeated in the insulated tests. Only the successful operation of tests B' and C' to thinner nominal films than in tests A' , D' and E' and the difference in the levels at which the count rate patterns emerged in tests B' and E' pointed to different regimes.

The nominal interaction at failure for each insulated/normal test pair was similar although failure was at lower loads in the insulated tests. This suggests that the degree of interaction may be of relevance to failure within the different regimes.

Significantly larger temperature increases were achieved compared to the normal tests so that insulating the discs can be regarded as a successful method of altering the heat transfer of the discs. The insulated tests failing at lower loads due to the increased temperature rises, shows the importance of the thermal characteristics of test machines which are being used to simulate conditions in machinery. If load is used as an operation limit, the thermal response of the test machine and the full scale machinery should be similar for the results to be applicable.

More controlled tests are required if the effect of the rate of change of film thickness is to be explored fully. It is not easy to achieve this level of sophistication on a two disc scuffing machine.

7.4. Exploratory cooled tests

7.4.1. Cooling system

The aim of the cooled mode of operation was to reduce the rate of change of film thickness during an increment compared to that for the normal tests. Eqn.(7.5) showed that a reduction in either T^* or K ($K = 1/\tau_C$) will reduce dh/dt .

The system adopted was to use cooling fins on the sides of the discs, with the aim of increasing the axial heat transfer coefficient and hence reducing T^* . The fins, in the form of copper collars, fitted on the existing shafts on both sides of the discs. The assembled unit is shown in Fig.7.8. An air supply of ~ 80 litres/min was directed on to the fins through fittings in the lid of the box which surrounded the discs. The air rate was controlled by a valve and measured with a flow metre in the supply line.

7.4.2. Trial procedures and discussion

In the first procedure considered, the machine was run for two hours prior to testing, with both the air and the oil supply on. The increments

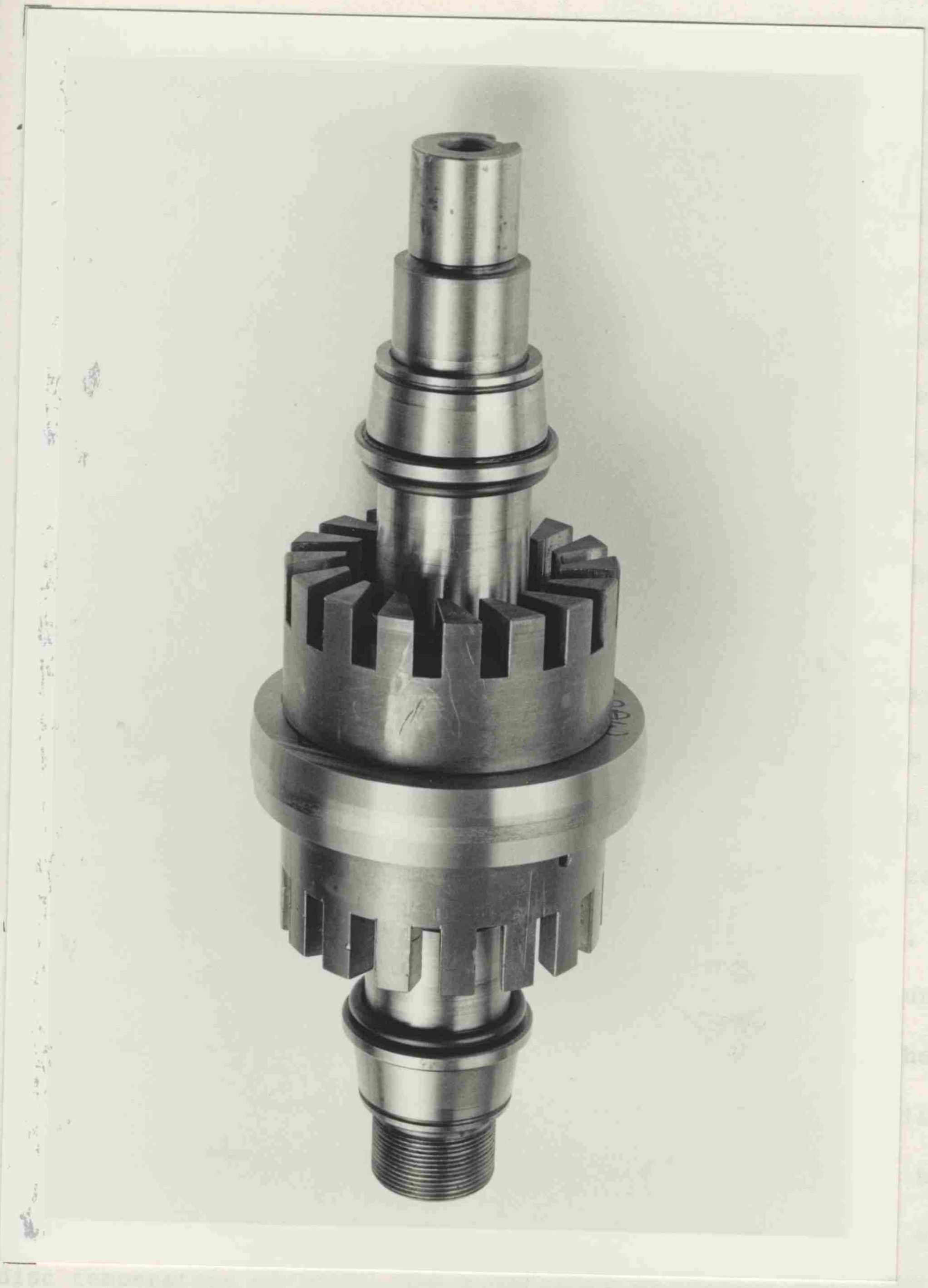

Figure 7.8 Discs and shafts with cooling collars.

were ten minutes long. The test procedure was otherwise as described in Section 3.2.

Two such tests with an oil supply temperature of $\sim 30^\circ C$ were run, one with the LOG and one with the LIN loading sequence. Both tests were run until failure. The oil supply, initial and failure disc temperatures and the failure loads for these and the equivalent normal tests are given in Table 7.5. Due to the similarity of the results for the different modes, there was some doubt as to whether any additional cooling was taking place.

It was attempted to run a similar test with an oil supply temperature of $50^\circ C$, but it was unsuccessful as the collars became loose during the tests. There was a $12^\circ C$ difference in the oil supply and initial disc temperature, which is greater than in the normal tests at this temperature. The effect of the air on the disc temperature at the three thermocouple locations, with the discs at zero load, is shown in Fig.7.9.

The reduction in the disc temperature caused by the air supply is an indication of increased cooling. However, it also raised the question of whether the oil supply or the initial disc temperature should be the same as in the normal tests and cooled modes for the tests to be comparable. It is the disc temperature which controls the film thickness, which suggests that tests should be run with the same initial disc temperature. To do this the oil supply temperature would have to be considerably higher than the required initial disc temperature, for example, an initial disc temperature of $50^\circ C$ required an oil supply temperature of $65^\circ C$. The oil bath could not raise the oil temperature sufficiently to run a similar test with an initial disc temperature of $70^\circ C$. The problem of an initial disc temperature far lower than the oil supply temperature was not so apparent when the oil supply temperature was similar to the ambient.

It was noted that in a test run in this way with an initial disc temperature of $50^\circ C$, the size of the temperature increases per load stage were similar to those in the normal tests. A discs temperature far lower than the oil supply temperature for zero applied load was indicative of an

TEST	A	LOG COOLED	D	LIN COOLED
OIL SUPPLY TEMPERATURE °C	29	33	25	29
INITIAL DISC TEMPERATURE °C	28	29	24	26
FAILURE LOAD kgf	11.9	11.9	12	12
DISC FAILURE TEMPERATURE °C	55	63	62	49

Table 7.5 <u>Comparison of test conditions for continuously cooled tests and equivalent normal tests.</u>

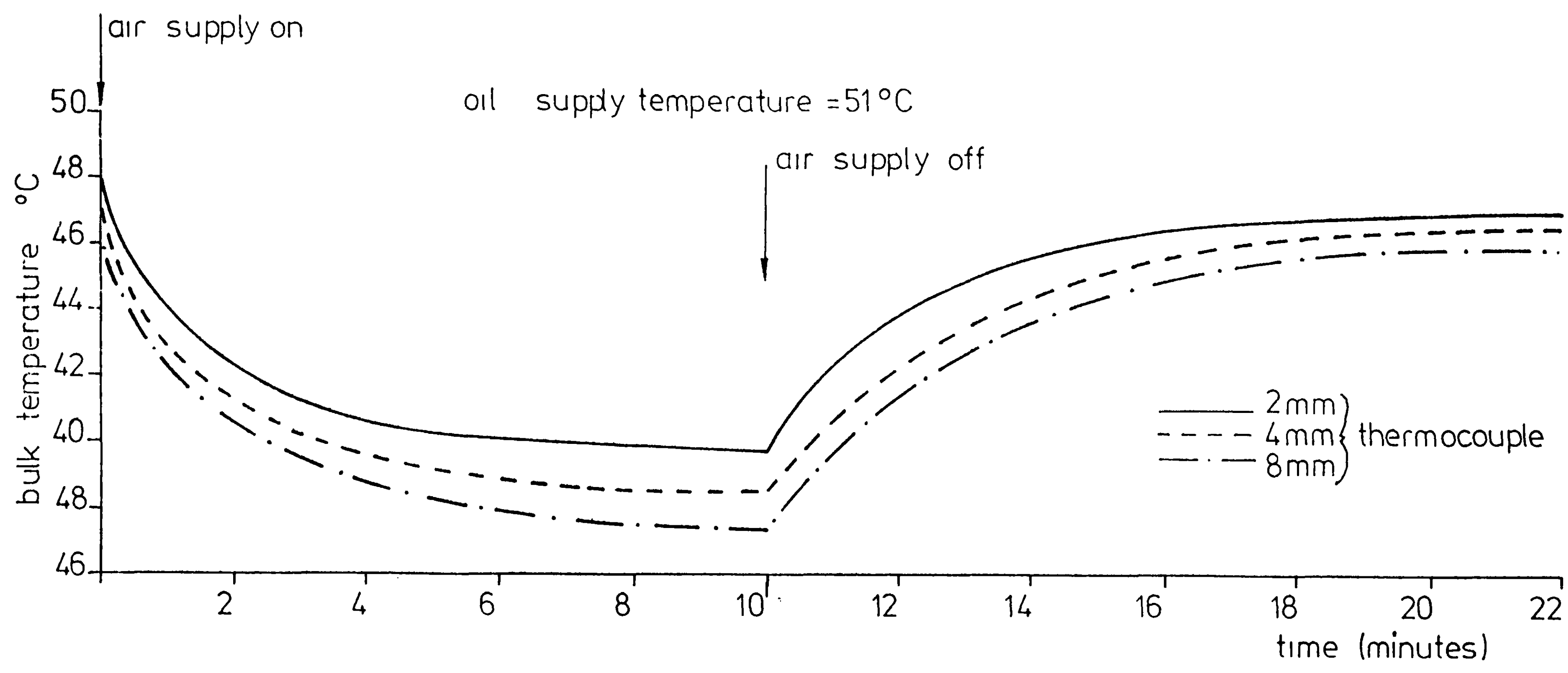

Figure 7.9 Effect of air supply on disc temperature at zero load.

increased axial heat loss due to the forced convection from the fins. The net cooling effect, however, on the discs temperature during a scuffing test run was questioned as the radial heat transfer would be from the hotter oil into the cooler discs, which is removed by the increased axial heat loss. A different method of running the tests was therefore required.

An improved procedure would be for the machine to run prior to the tests up to the initial temperature with the air supply OFF, and for the air supply to be gradually increased during the test. This would gradually raise the axial heat loss and so control the rise in temperature. To run tests in this way would require a control system for the air supply rate which would respond to the temperature rise. Before any such system was devised the feasibility of this method was tested by running two further tests, again a LOG and LIN test with initial disc temperatures of 30°C. The air supply was initially OFF and was gradually increased by the operator via the control valve during the test. The change in temperature with time is shown in Fig.7.10. Although the change in temperature with time, following each increase in load was somewhat erratic, the overall increase in the bulk temperature were less than those in the normal tests up to a load of about 8 kgf. At this stage in both tests the air supply rate reached a maximum and the temperatures thereafter began to rise in a normal fashion. Both tests were stopped before failure.

This, in theory, would be the best way to run these tests but several major adaptions to the cooling system would have to be made. These include

1) a greater air supply,
2) a more efficient fin/air jet arrangement, and
3) an automatic air flow control system, which operates in response to changes in the temperature.

To commission such a system would require a full series of calibration tests to establish the relationship between air supply, the effective forced axial heat transfer coefficients and the disc temperature. This program

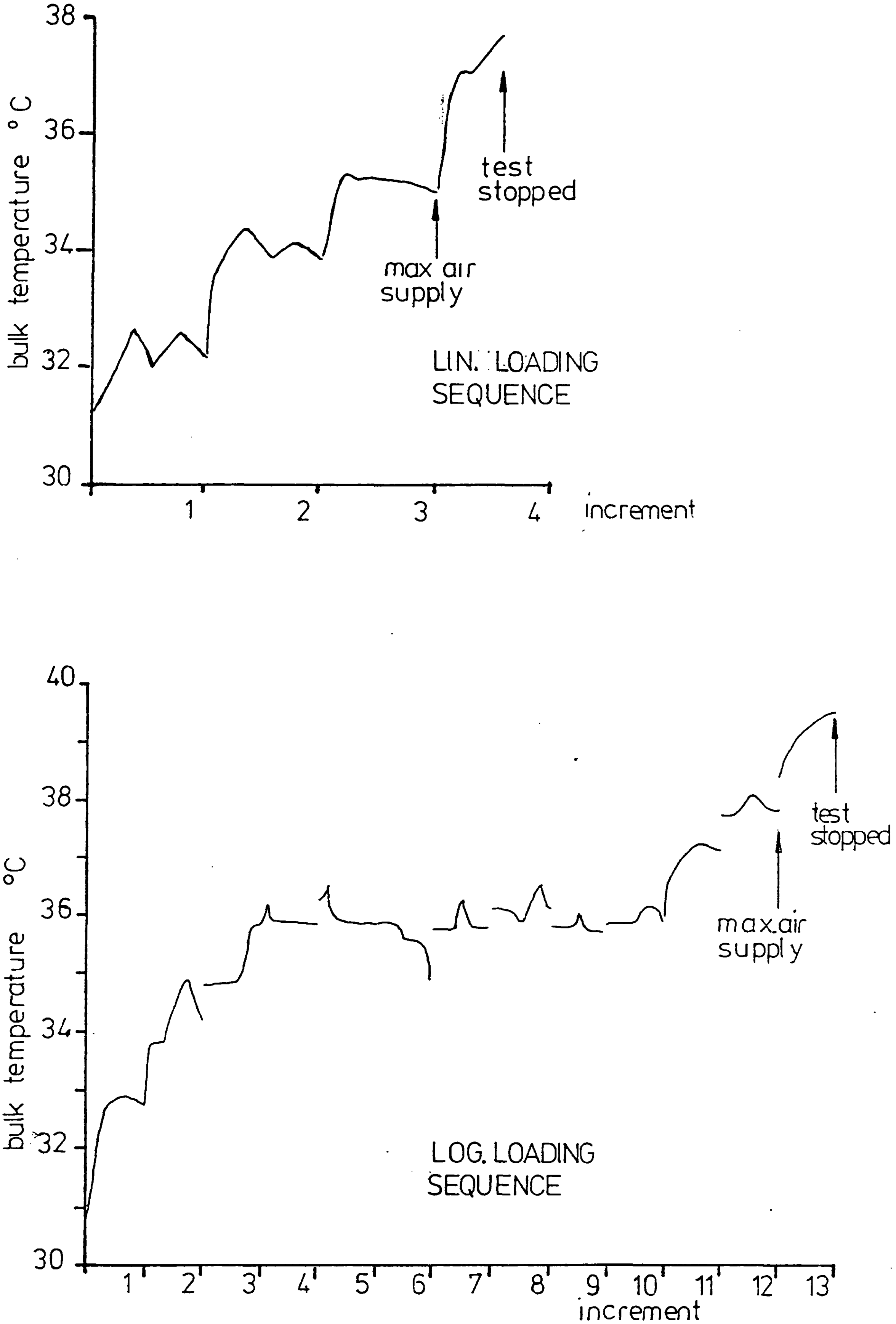

Figure 7.10 Incremental changes in bulk temperature for a gradually cooled test.

could not be implemented in the time of the project so this line of investigation is left to some later project.

It was not possible to calculate the true axial heat transfer coefficient for the cooled mode as the temperature, as the fin/air interface had not been measured. By assuming that, as in the normal mode, the side faces were at the oil supply temperature, an effective value of h_a for the cooled mode can be calculated. The value for the maximum air supply rate thus found was $h_a \approx h_r$. It was found in Section 6.7 that a value of $h_a \approx h_r/3$ gave the best agreement between predicted and experimental temperatures. An effective value of $h_a = h_r$ for the cooled tests is therefore three times that for the normal tests. The temperature rise, T^*, would in turn be reduced to ~ 0.9 compared to 1.4 for the normal tests.

7.5. Discussion and Conclusions

The differences in the thermal response of the Rossides and Story tests was one of the suggested reasons for the differences in the results of the two test series. This chapter has reported the attempts to alter the thermal response of the test machine described in Chapter 3 by insulating and cooling the discs.

Six tests were run in the insulated mode. The increase in the bulk temperature per load stage was increased significantly compared to the normal mode, whilst the failure loads were reduced. Due consideration must therefore be given to the thermal response of the test machine when results are used to predict behaviour in machinery.

The experiments in the cooled mode, with a gradually increasing air flow rate, showed a decrease in the temperature rise per load stage for a limited number of load stages. A number of problems in running tests in this way, such as an insufficient air supply, prevented a full series of tests being run in this mode.

The range of T^*, the temperature rise above ambient, that has been achieved with the three modes of operation is shown in Fig.7.11. The steady

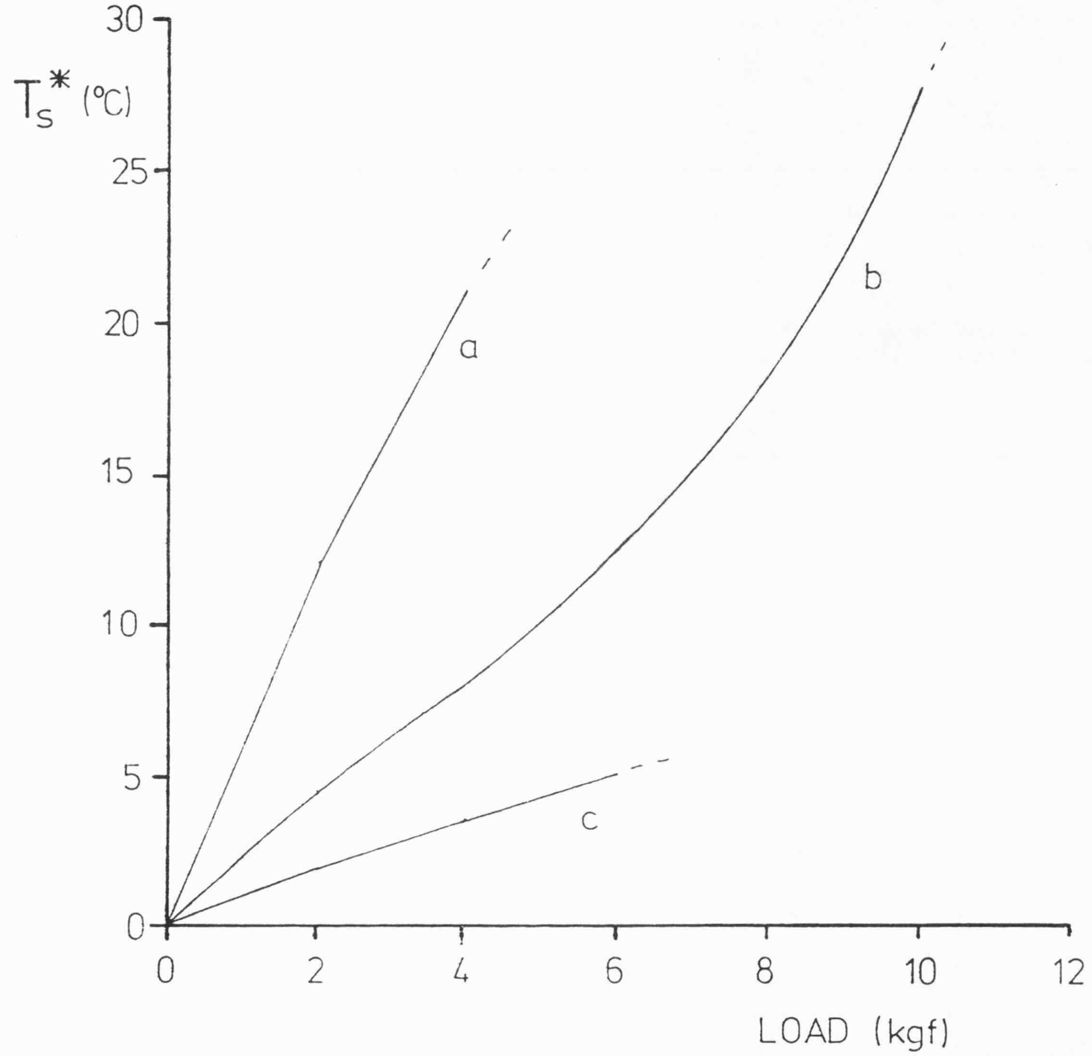

Figure 7.11 Range of steady state temperatures achieved with the three modes of operation.
a/ insulated
b/normal
c/ gradually cooled.

state value of T^* for each load stage is plotted for the three 30 °C LIN tests. At the end of the second increment T^*_s for the insulated test is approximately 7 times that for the cooled mode. The air supply rate for the cooled test reached a maximum in the third increment and thereafter T^* per load stage was similar to that in the normal tests.

The variation in the thermal response has been discussed in terms of T^*. In Section 7.1 it was shown that the rate of change of film thickness, dh/dt, which results from the change in bulk temperature during an increment is proportional to both T^*, and K, the decay exponent. Changing the thermal response of the test machine should, therefore, make it possible to explore the Crook and Shotter failure mechanism experimentally. However, comparing the insulated to the normal tests, it was found that more sophisticated experiments are needed to separate the effects of a change in dh/dt from that of a change in T^* per se. Nevertheless it is worth noting the relative size of KT^* $\left(\propto \frac{dh}{dt}\right)$ caused by the changes in the thermal response.

Table 7.11 gives the appropriate values for h_a, K, T^* and KT^* $\left(\propto \frac{dh}{dt}\right)$ for the three modes. The values for the axial heat transfer coefficients are assumed to be $h_a \to 0$ for the insulated tests, $h_a = h_r/3$ for the normal mode (Section 6.7) and $h_a = h_r$ for the cooled mode (Section 7.4). Increasing values of h_a decrease T^* and increase K. In the insulated tests K is also affected by the central insulated layer. The net effect is that, like T^*, dh/dt is greatest in the insulated tests but dh/dt is less in the normal than in the cooled tests. Further experimentation in the cooled and normal modes would therefore seem to offer the opportunity of distinguishing between the effects of $\partial h/\partial t$ and T^*.

MODE	INSULATED	NORMAL	COOLED
$T_{\varsigma}^{*} \cdot \left(\frac{\upsilon\pi}{\theta^{*}}\right)$	2.6	1.4	0.9
K	1.16	1.3	2.5
$\frac{dh}{dt}$	3.0	1.8	2.25
ha	0	hr/3	hr

Table 7.6 Relative values of dh/dt for the three modes of operation at ambient temperature of 30'C.

CHAPTER 8

DISCUSSION, CONCLUSION AND SUGGESTIONS FOR FURTHER WORK

8.1 Introduction

This chapter reviews the work of the thesis in the light of more recent developments and suggests further work where applicable. This work arose from earlier investigations of scuffing failure using rough, circumferentially finished discs.

This background is reviewed in detail in Chapter 2. In brief: Bell and Dyson (1972) and Bell, Dyson and Hadley (1974) carried out a programme of two disc machine tests covering a wide range of rolling and sliding speeds. Many of these tests reached considerable degrees of surface interaction before failure. This stimulated Dyson (1976) to determine the dry contact separation of the surfaces just before failure for which he used real, run-in surface data taken from unscuffed portions of a pair of failed discs, (Archard, Hunt and Onions (1975)). He suggested that lubrication would fail and scuffing occur when the discs became too hot for the system to generate an elastohydrodynamic film thickness greater than the dry contact separation of the surfaces.

Workers at University College Cardiff and Leicester University set out to test Dyson's hypothesis. They compared theoretical and experimental failure temperatures under apparently similar operating conditions of oil, speed and roughness. Cardiff's comparison was a great success, whilst the failure temperatures in the Leicester tests fell below those predicted and many of the surfaces failed without running-in, (Figs.2.8, 2.9 and 2.10). Comparison of the test programmes (Story et al (1981)), showed that the Leicester tests started with a higher load increment and a lower oil temperature than the Cardiff tests and that the Leicester machine was more robust which could possibly cause differences in the thermal response. A study by Story (1984) on the literature on scuffing showed that similar anomalies in test results had previously been noted. Fein (1967) had found that longer run-ins with thinner films enhanced successful running-in.

Crook and Shotter (1957) showed that earlier failure could be induced if the thermal characteristics of the disc were changed by insulation.

Fein's observations, caused Baglin (1986) to ask, "Why should test history matter?". This question led to the development of the chart shown in Fig.2.18, which predicts that more than one form of elastohydrodynamic lubrication occurs with circumferentially finished surfaces. The tests of Cardiff and Leicester apparently operated in different regimes (Fig.2.18) and this was suspected to be the cause of the differences in failure.

An alternative possible explanation was that the different machines caused different thermal response patterns. Crook and Shotter had argued from their results that scuffing could result from an uneasy balance between the rate at which the surfaces were able to run-in and the rate of change of film thickness caused by increasing temperature. Could changing the thermal response therefore be a cause of earlier failure?

A machine with variable thermal characteristics was designed by Kelly (Williams, Finnis and Kelly (1987)) and is described in Sections 3.2. A detailed thermal analysis of its behaviour was required. The first stages in the analysis had been carried out by Story (1984) but further work was required before the appropriateness of the Crook and Shotter failure mechanism could be investigated.

8.2 Reproduction of the Cardiff and Leicester Tests

This was the general background to the work in this thesis. The first detailed problem was to attempt to reproduce the differences between the Leicester and Cardiff tests on one machine. It was shown in Chapter 3 that, by using the loading sequences and temperatures appropriate to the test type, broadly speaking the failures could be reproduced although some finer aspects of the differences were not replicated.

1. The tests with the Story conditions resulted in early failure with no running-in at the 3:1 ratio, whereas later failure in the Rossides type test was accompanied by running-in.

2. There was no marked difference in the thermal response following an increase in the load when the two test types were produced on one machine, although differences existed in the original tests.

3. Although the Rossides type tests had more severe failure conditions than the Story type tests, they did not run as far as the original Rossides tests and the running-in was not so marked.

The question of a different thermal response was addressed in Chapter 6 where it was shown that thinner discs of the Rossides tests would account for the smaller time constant observed.

The reasons for the earlier failure in the reproduced than the original Rossides type tests was not addressed directly. It was later determined that Rossides discs were through hardened to 575 VPN whereas the present discs were case hardened to 700 $\pm$ 25 VPN. The effect of metallurgy is an obvious area for further work. This aspect is touched on briefly in Section 8.5.3 which describes running-in.

8.3 Regimes of lubrication versus operating conditions

Having broadly reproduced the results of the Story and Rossides test types the next question was whether the differences in test types were due to the operating conditions per se or that, as suggested by Baglin, the operating conditions give rise to different forms of lubrication. An experimental programme was set up which covered a range of initial temperatures using both loading sequences and two slide/roll ratios, such that the tests started over a range of locations on the micro-ehl onset plot, Figs.3.20a and 3.20b. The results were detailed in Chapter 3.

The major conclusions reached were:

For the 3:1 tests the failure conditions, (Table 3.5a), degree of running-in, (Table 3.6a) and levels of emergence of count rate resistance patterns (Fig.3.20a), indicated that at least two regimes of operation did exist.

At the 2:1 test speed the results were not so definite, as all the tests had similar failure conditions and degrees of running-in (Tables 3.5b and 3.6b). However, there was some indication from the countrate levels (Fig.3.20b) and from the friction and thermal patterns for the complete test (Figs.3.15b and 3.16), that the tests operated in different regimes.

Although when viewed as a whole results led to these conclusions, there was some variability in the 50 °C tests. This was not unexpected as:

1. The initial conditions of these tests lay close to the boundary, the position of which was not thought to be exact due to several simplifying assumptions made in its derivation.

2. The exact placing of the points is dubious because the film thickness was not measured but inferred from the temperature using Dowson and Higginson film thickness formula.

Factors which can influence film thickness were discussed in Chapter 4. It was shown that the difference in the film thickness results were consistent with the effects of roughness and the degree of starvation determined by the zero reverse flow inlet boundary conditions. Further work is required to determine the true degree of starvation of the system by runnimg the machine with the present feed rates and temperatures but using smooth discs with the film thickness measured directly by capacitance techniques.

The Baglin model to determine the conditions for the onset of micro-ehl was simplified in several ways. A simple sine wave was used to represent the surface roughness. In applying this to an equivalent real surface it was assumed that the secondary roughness components would have no effect on the generation of the pressure ripples. The criterion for micro-ehl formation was taken as that where the hydrodynamic pressure ripple, generated by rigid asperities, became equal to the elastic pressure distribution necessary to flatten the asperities under the same load. As in the transition from the classical regime to ehl on the macro-scale, some asperity deformation should occur before the micro-ehl condition is reached so the change from rigid asperity behaviour to fully developed micro-ehl is expected to be gradual.

It was also assumed that the properties of the fluid, even in regions of high localised pressure, would be Newtonian. Due to the various assumptions there was expected to be some inaccuracy in the predicted transition boundary position.

The initial locations of the low and high temperature tests on the micro-ehl onset model were well removed from the predicted position of the transition boundary. The 50°C tests straddled, and lay close to the transition line. Test B showed some of the characteristics of the micro-ehl tests but these were not so pronounced as in the high temperature tests.

The test histories of test B, the repeat tests B1 and B2 and the insulated test B' are shown on the micro-ehl onset plot in Fig.8.1. The initial conditions of the four tests are such that their starting locations and subsequent paths, based on the nominal conditions, are slightly separated. B and B1 cross the boundary into the mixed lubrication whilst B2 and B' remain in the micro-ehl region. The countrate data for the four tests is also shown. The '0' countrate pattern is observed immediately in test B1 and in the second increment in test B. Conversely in B2 there was only random activity until the failure increment, with less activity again

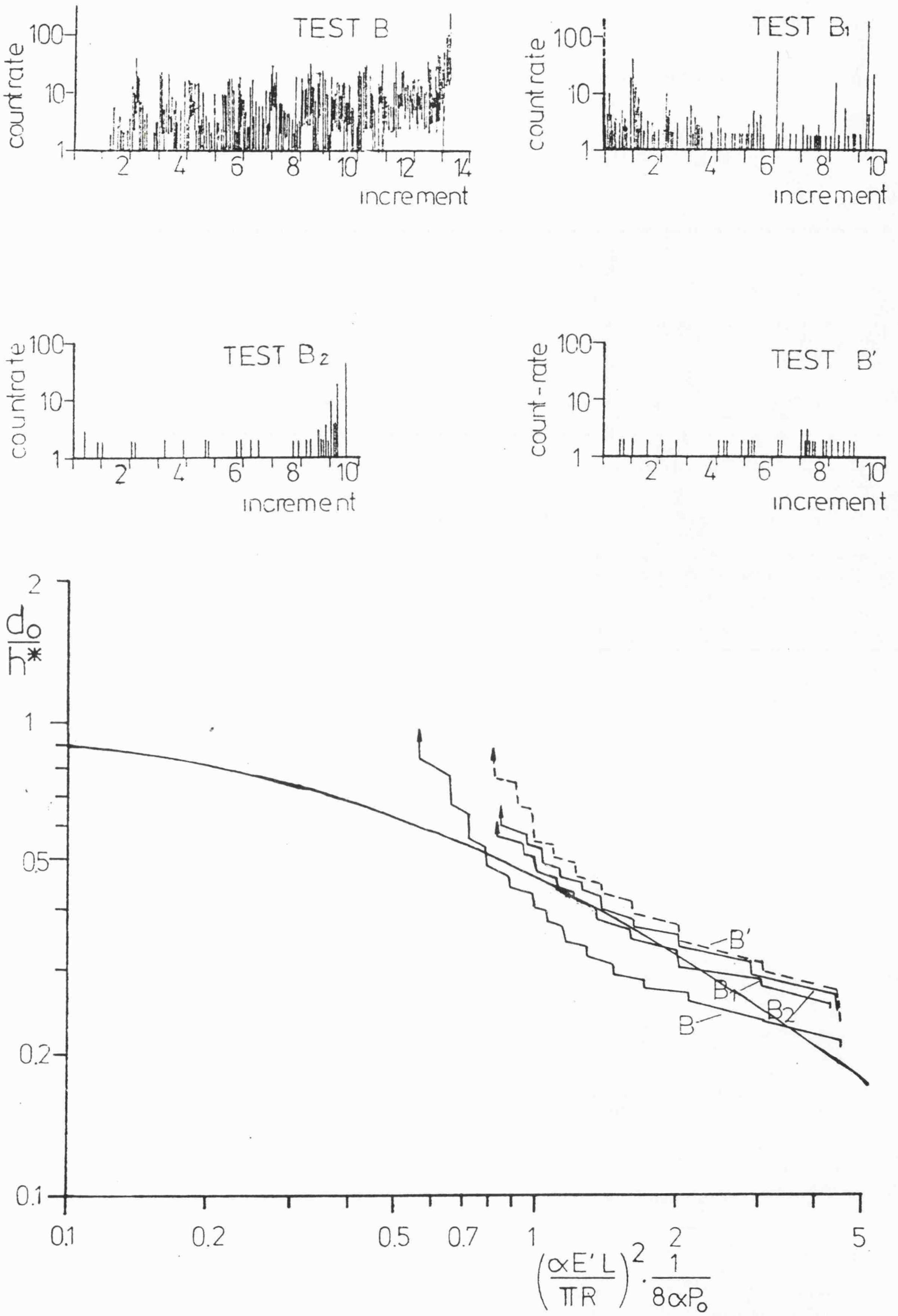

<u>Figure 8.1</u> <u>Comparison of test histories and countrate data of tests B, B1, B2 and B'.</u>

in B'. This variation in behaviour over such a small range of operating conditions suggests that the boundary position may be more accurately positioned than originally thought, possibly with the main scale asperities in tests B and B1 only undergoing partial deformation.

8.4 Further developments in micro-ehl theory

Since the onset of this project there have been further developments in predicting behaviour within the micro-ehl regime. These developments throw some light on the test results. The recent developments will be outlined and some aspects of the test results discussed in terms of this new work.

8.4.1. Numerical solution for micro-ehl

Computer based numerical solutions have been developed to predict behaviour in the micro-ehl region by workers at University College, Cardiff [Karami, Evans and Snidle (1986, 1987), Barragan de Ling, Evans and Snidle (1989)]. Like the Baglin onset model, the solution was for a longitudinal simple sine wave form. A number of solutions were presented covering a rage of sinewave amplitudes, loads and temperatures. In a non-dimensional form, the solutions covered a similar range to the tests reported in this thesis. The locations of the solutions are shown on the micro-ehl onset model in Fig.8.2. Deformed asperity shapes and pressure ripple distributions for some of the positions are also shown.

The following points are worth noting. With increasing values of d_o/h^* and with decreasing values of the load parameter, the pressure ripple becomes more concentrated about the asperity tips, with the valley pressure tending to zero at the most extreme conditions. At the same time, the deformation of the asperity increases and the asperity tip becomes indented.

All the computed points, except one, lie above the transition line. For the point below the line the deformation is small and the peak remains

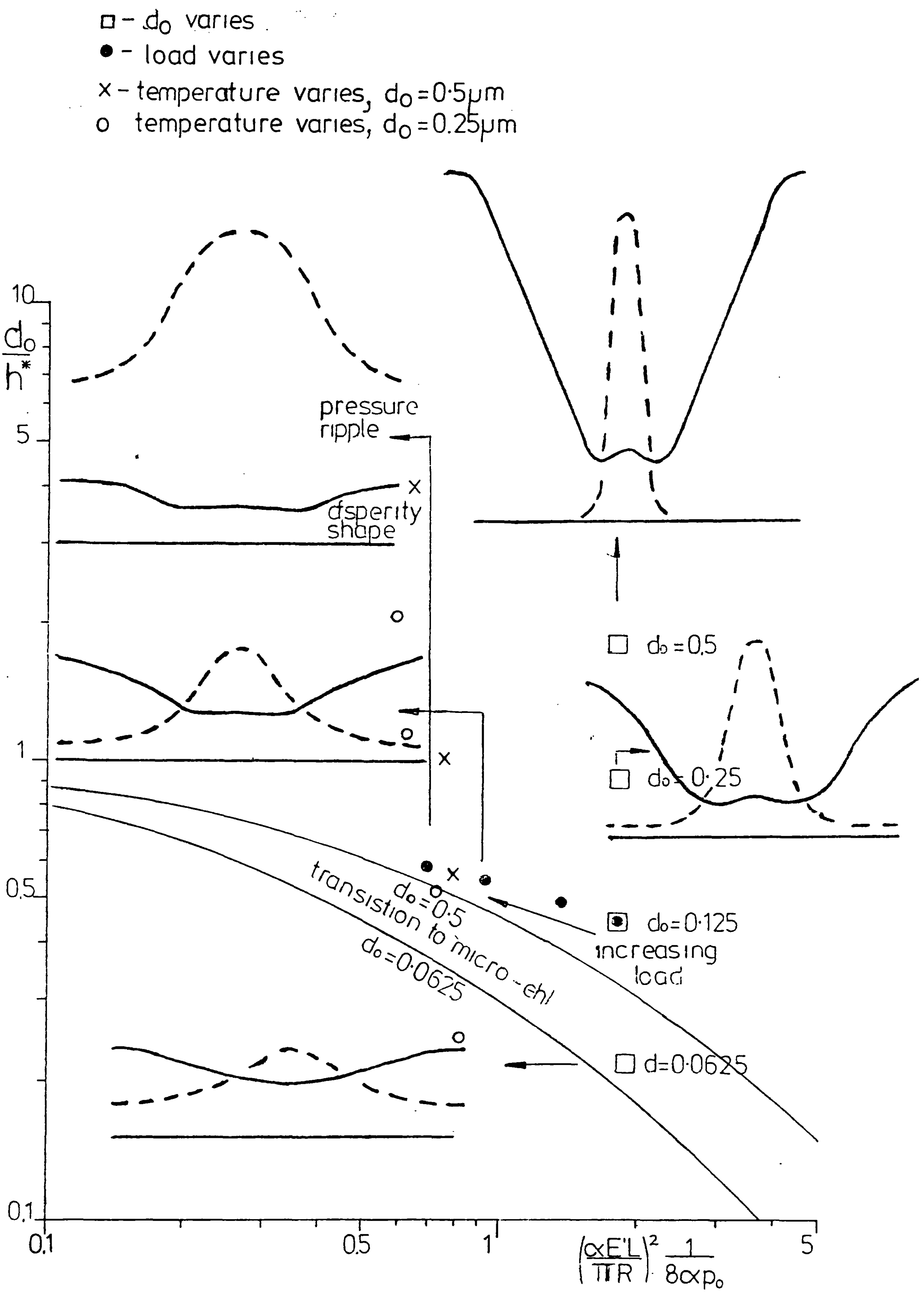

Figure 8.2 Locations, pressure ripple distributions, and deformed asperity shapes of numerical solutions by Karami et al.

rounded and is not flattened. This may be within the conditions for a gradual change from rigid to deformed asperities, for which the onset condition assumed by Baglin, acts as an upper limit.

8.4.2. Analytic solutions to micro-ehl regime

Analytic solutions for behaviour in the micro-ehl regime have been developed by Baglin (1988). The simple sinusoid waveform was retained. The numerical conditions had predicted that, considered in extremes, two types of micro-ehl would exist - "cooperative", in which valley pressures remain large and "isolated" where there is virtually zero pressure in the valleys. In the analytical model both the predicted types were initially considered. For the cooperative form the average pressure was assumed to deform the body on a macro scale, (effectively removing the curvature in the rolling direction), whilst the pressure ripples would deform the asperities on the micro-scale.

In the isolated form, with the valley pressure tending to zero, it was assumed that each sinusoidal rib would act as an individually lubricated contact.

The method of solution for both configurations is along similar lines to the original onset analysis. The dry contact configuration under a given load was first found. For the cooperative type, a solution by Westergaard (1939) was used. This gave the deformation of sinewave asperities superimposed on a plane surface. No existing solution was available for a cylinder ribbed with a sinewave form, each asperity for the isolated form was therefore treated as an individual elliptical Hertzian contact. The resulting dry contact shapes were used in the hydrodynamic part of the problem to give the hydrodynamic pressures against surface separation. For a fixed load the separation at which the elastic and hydrodynamic pressures were compatible was the required solution.

The analytic solutions showed that the occurrence of 'isolated' micro-ehl was dependent upon the asperity sharpness parameter $\pi \alpha E' d_o/L$.

For low values of the parameter, appropriate to roller bearings for example, Westergaard type macro-ehl would occur for all values of the operating variables. For typical gear surfaces, both forms of micro-ehl can occur as shown in Fig.8.3. The axes parameters are the same as for the original onset plot. The Westergaard type asperity shape is formed at smaller values of d_o/h^* and at lower values of the load group, i.e. at higher loads. The boundary between the regions has tentatively been placed as the position where the deformation resulting from each type of micro-ehl is the same and it depends on d_o, L , and R the radius of the cylinder. Behaviour to the left of the boundary is dominated by the macro distribution with the asperities locally flattened. Moving to the right of the plot the asperities act more as individual elliptical contacts.

The contours are for constant values of $\frac{h_{micro}}{d_o}$, that is the ratio of the film thickness beneath the deformed asperity tip to the undeformed asperity amplitude. It can be seen that a protective film exists beneath the deformed asperities although in terms of the nominal d_o/h^* levels there is considerable asperity overlap. The maximum benefit is in the region of cooperative micro-ehl. For example, when the load group ≈ 0.3, at a nominal d_o/h^* of ~ 1 , then $h_{micro} = 0.5\ d_o$; that is, at conditions which would result in contact for an undeformed asperity the film thickness beneath the deformed asperity is half the asperity amplitude. At the more severe conditions of $d_o/h^* = 6$, then $h_{micro} = 0.1 \times d_o$, which still prevents contact.

Also shown in the figure are the locations and $\frac{h_{micro}}{d_o}$ values for some of the Karami et al. solutions. The $\frac{h_{micro}}{d_o}$ values from the two types of solution are in reasonable agreement.

As in the original model for micro-ehl onset, the results for a simple sinusoid were extended to apply to a real surface by using the relationships between the sinewave form and a Gaussian distribution of surface heights (Section 3.4.1.). This assumes that the secondary roughness can be superimposed on the mainscale with no effect on pressure ripple

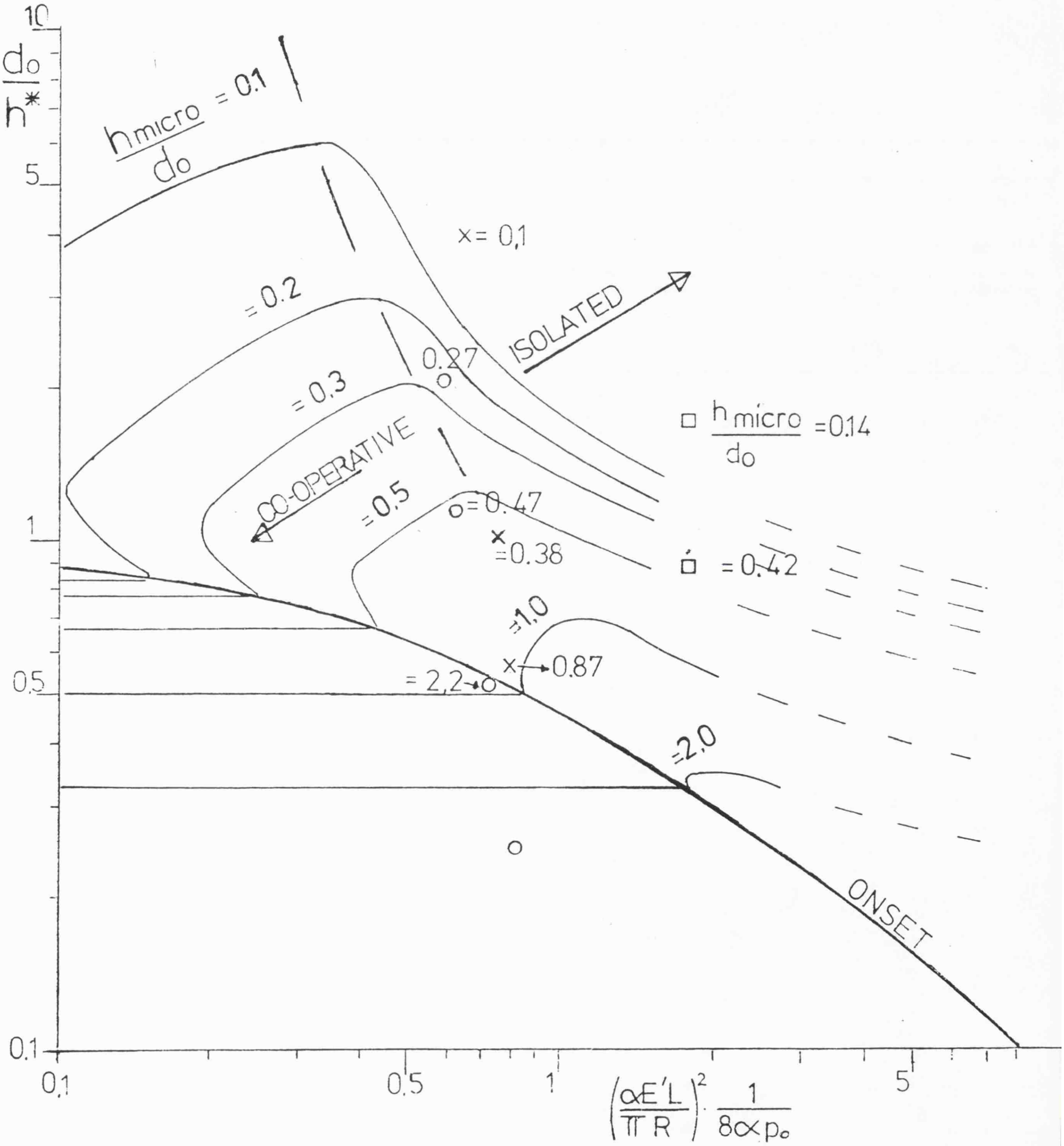

Figure 8.3 Analytical solution by Baglin for micro-ehl film thickness for a sine wave form asperity, for conditions of present tests.

formation. Baglin (1988) has shown that this is a valid assumption for secondary asperities with a wavelength of ~ L/10.

The plot converted to deal with real surfaces is shown in Fig.8.4. The lines are for values of surface interaction expressed in terms of ξ' as defined in the figure. In the mixed lubrication region the $\xi' = 0$ line corresponds to the first contact of the secondary asperities, whilst the mainscale remains rigid, i.e. $h^* = 3\sigma$.

In the micro-ehl regime, the first contact level is raised for load group values between 1 and 3 . For example, the maximum nominal d_o/h^* for first contact being 0.64 compared to 0.47 for an undeformed mainscale. At higher values of the load group the benefit is negligible. For increasing degrees of overlap, the maximum benefit is achieved in the area of cooperative micro-ehl.

8.4.3. Oil rheology

Both the numerical and analytical models for micro-ehl behaviour assumed that the oil was Newtonian, i.e. shear stress $\propto$ shear strain rate. In fact the rheological behaviour of a lubricant depends on:- the fluid properties, the load, rate of shear or sliding speed and the temperature and this can markedly affect the frictional traction.

Evans and Johnson (1986a,b) constructed traction maps for three different lubricants, with coordinates which were a function of a load parameter, and a parameter related to the film thickness. The maps were split into areas and for each area a relationship between friction and shear rate was derived from fundamental lubrication principles. The predicted traction in each area was supported by experiments, with viscometers at the lower pressure and, at high pressure, with smooth discs on a two discs machine. Fig.8.5a shows such a map for a mineral oil, HVI 650 (η_o = 0.09 N s/m^2, α_o = 3.02 x 10^{-8} m^2/N at 30°C). Typical changes in the frictional traction pattern with sliding speed for different areas of the map, are also shown in the figure. Higher coefficients of friction were associated with the areas of higher pressure and increased sliding speed.

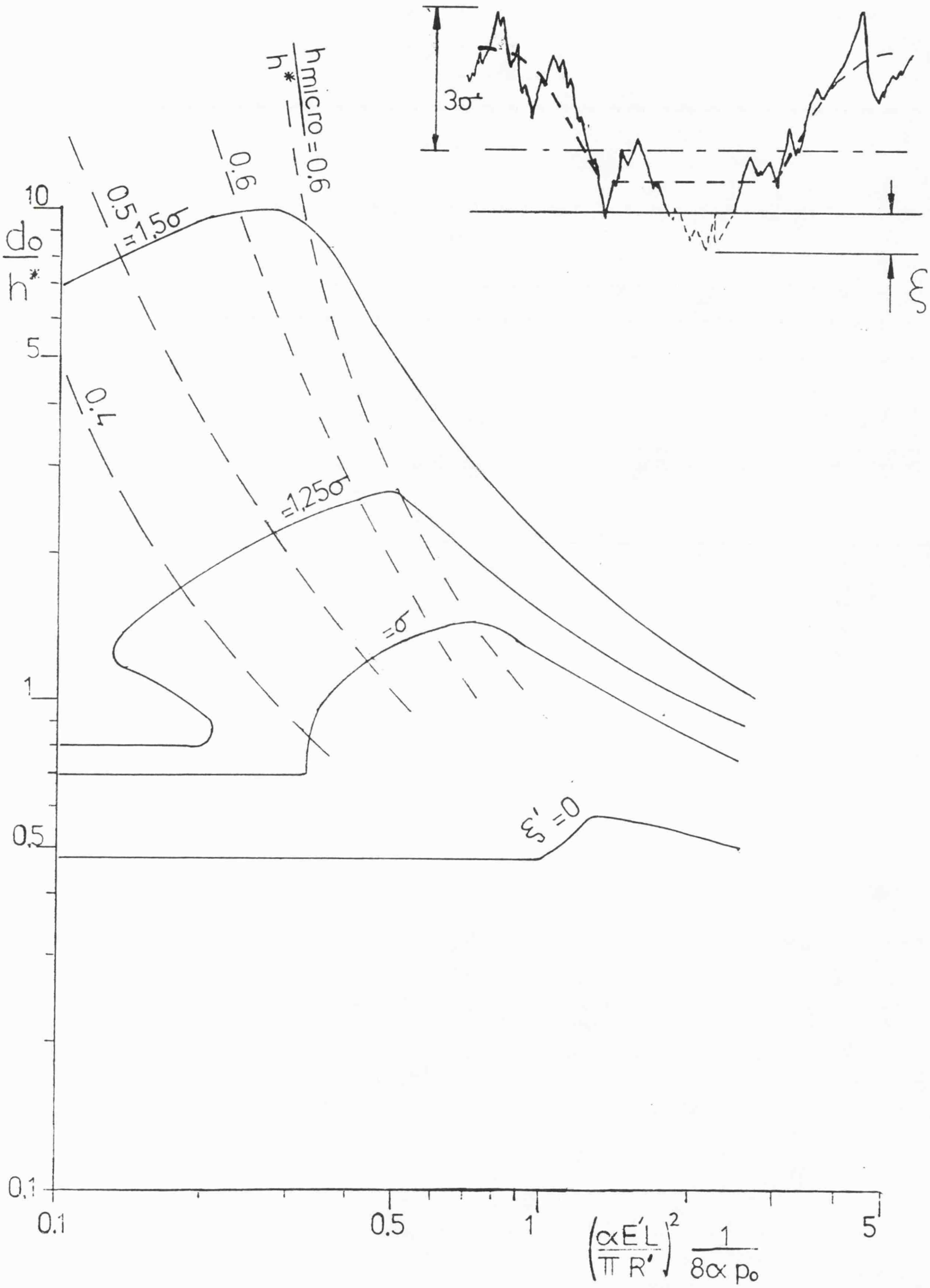

Figure 8.4 Asperity interaction for a real surface by Baglin for conditions of present tests.

Evans and Johnson (1987) then proposed that the same maps could be used with rough surfaces provided the pressure enhancing effects of micro-ehl were taken into account.

Two discs machine experiments were run with rough surfaced discs to give various d_o/h^* ratios. With decreasing h^* but a constant value of $\alpha_o p_{av}$, the traction form shifted from that associated with a low pressure area to a higher coefficient associated with higher average pressures. This change of behaviour was accredited to the increasing local pressures around the asperity tips. The location of these tests are shown on the traction map, Fig.8.5a, and on the micro-ehl onset plot in Fig.8.5b.

The greatest shift of frictional traction behaviour compared to that with the same $\alpha_o p_{av}$, but with smooth surfaces, was achieved with the isolated regime, (test 1). Both the numerical and analytical solutions to micro-ehl, indicate that this form of lubrication produces more concentrated pressure ripples about the asperity tip.

The present tests use a different mineral oil from that used by Evans and Johnson and were at a higher sliding speed. Similar data is needed for OM100 if the predictions of Evans and Johnson are to be applied to the present tests. However, it is reasonable to expect a similar shift in traction behaviour on moving into micro-ehl and, more particularly, in the isolated micro-ehl regime with other oils. The work of Evans and Johnson shows that for the asperity pressures generated with rough surface lubrication, some allowance for the oil rheology needs to be made and that high friction coefficients of a level usually associated with asperity contact may also be produced by these effects.

Both Baglin and Karami et al. assumed Newtonian fluids in their analyses. The inclusion of rheology effects in any future model may introduce the effects of sliding which have hitherto been ignored.

We shall now examine some of the tests of the earlier chapters with respect to these recent developments in micro-ehl behaviour.

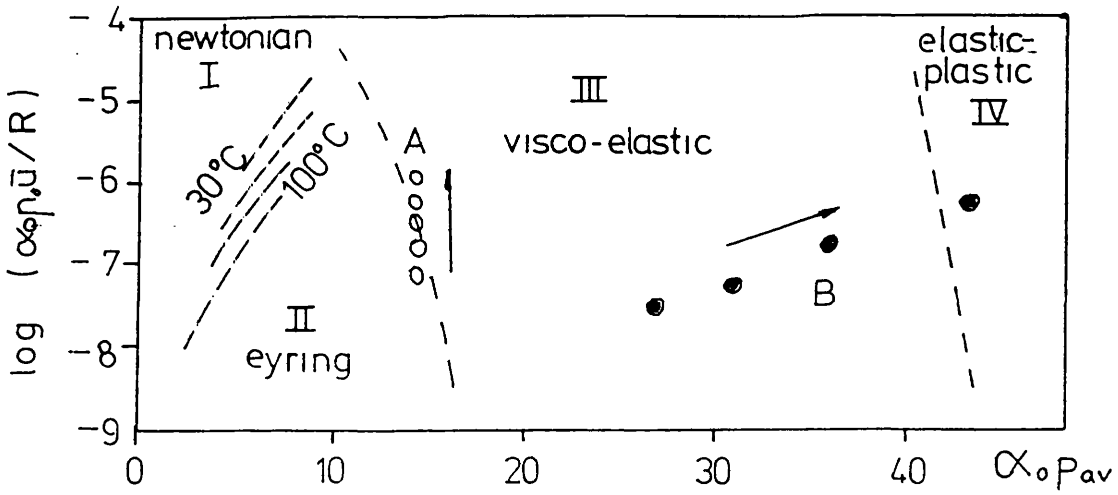

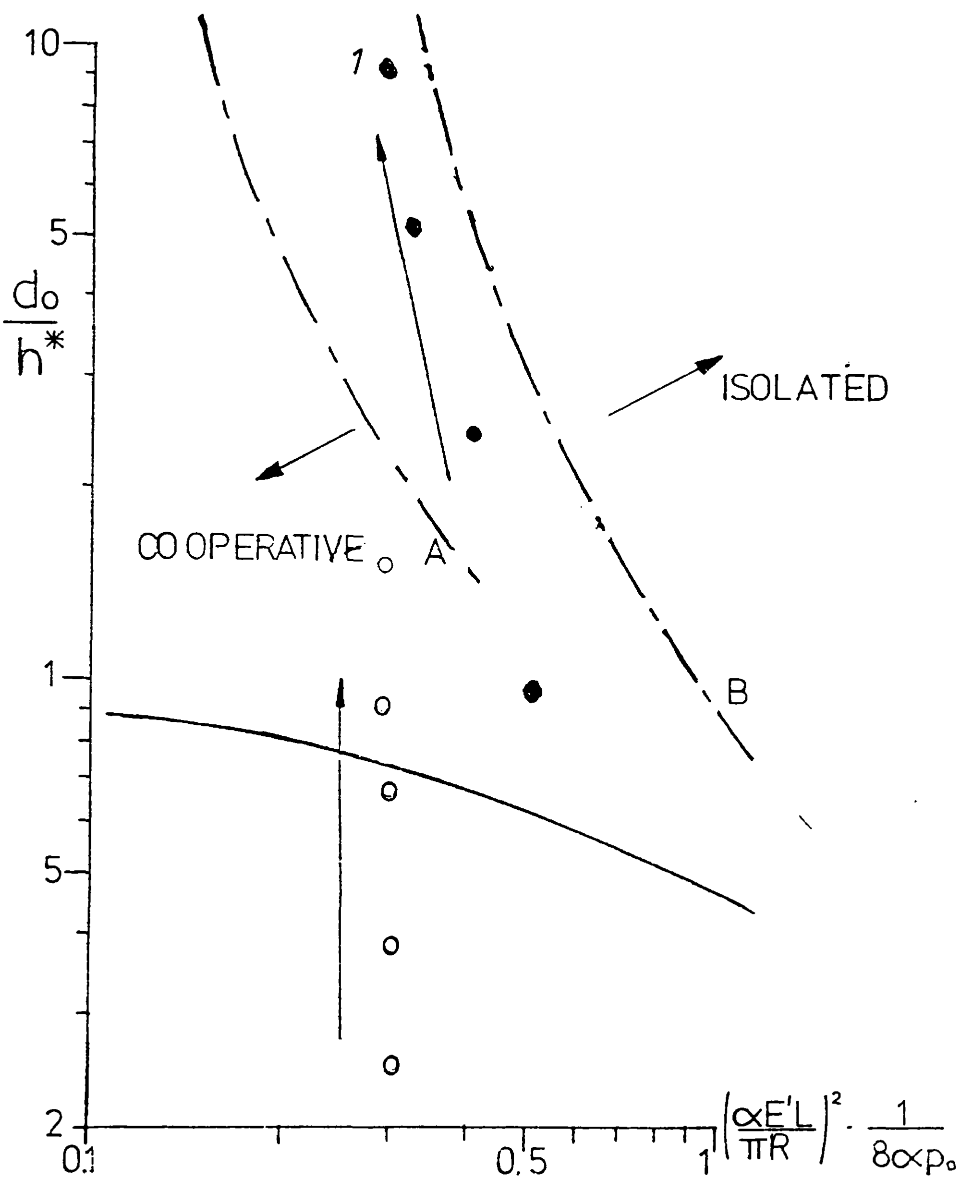

Figure 8.5 Test results of Evans and Johnson on a/regimes of traction behaviour chart and b/micro-ehl map.

8.5 Further discussion

Figure 8.6 shows tests D, J, C, I, C' and F' on a micro-ehl plot. The boundaries to the different regions, contours for various degrees of overlap and lines of constant values of h_{micro}/h^* are shown.

8.5.1. Levels of contact

The levels at which the first significant contact or 'O' pattern occurred were previously discussed in terms of the nominal d_o/h^* value. The first contact in tests J and D was below the $d_o/h^* = 0.47$ line. Possible causes for this were discussed in Chapter 4 and Section 8.3.

The first contact in the micro-ehl tests occurred above the nominal contact line. The recent analysis has shown the conditions at which contact should occur in this region. The maximum nominal conditions to which contact of the secondary asperities is prevented by micro-ehl is $d_o/h^* = 0.64$ when the load parameter is approximately 2.

First contact was indicated in tests C and I at $d_o/h^* = 0.64$ and 0.7 respectively. This is at a similar level to the possible maximum but at a higher value of load. It is worth noting that at higher values of the load group, the position of the degree of overlap lines has been estimated, (dotted portion).

8.5.2. Frictional traction differences

At the 2:1 test speed, differences in the frictional traction were identified between the ehl/mixed tests and those starting in the micro-ehl region. Fig.8.7 shows the incremental changes in friction plotted against the load for two such tests. In test J , the initial coefficient of friction is low, around 0.03, which is typical for the shearing of an oil film. On increasing severity of conditions μ increases, most likely due

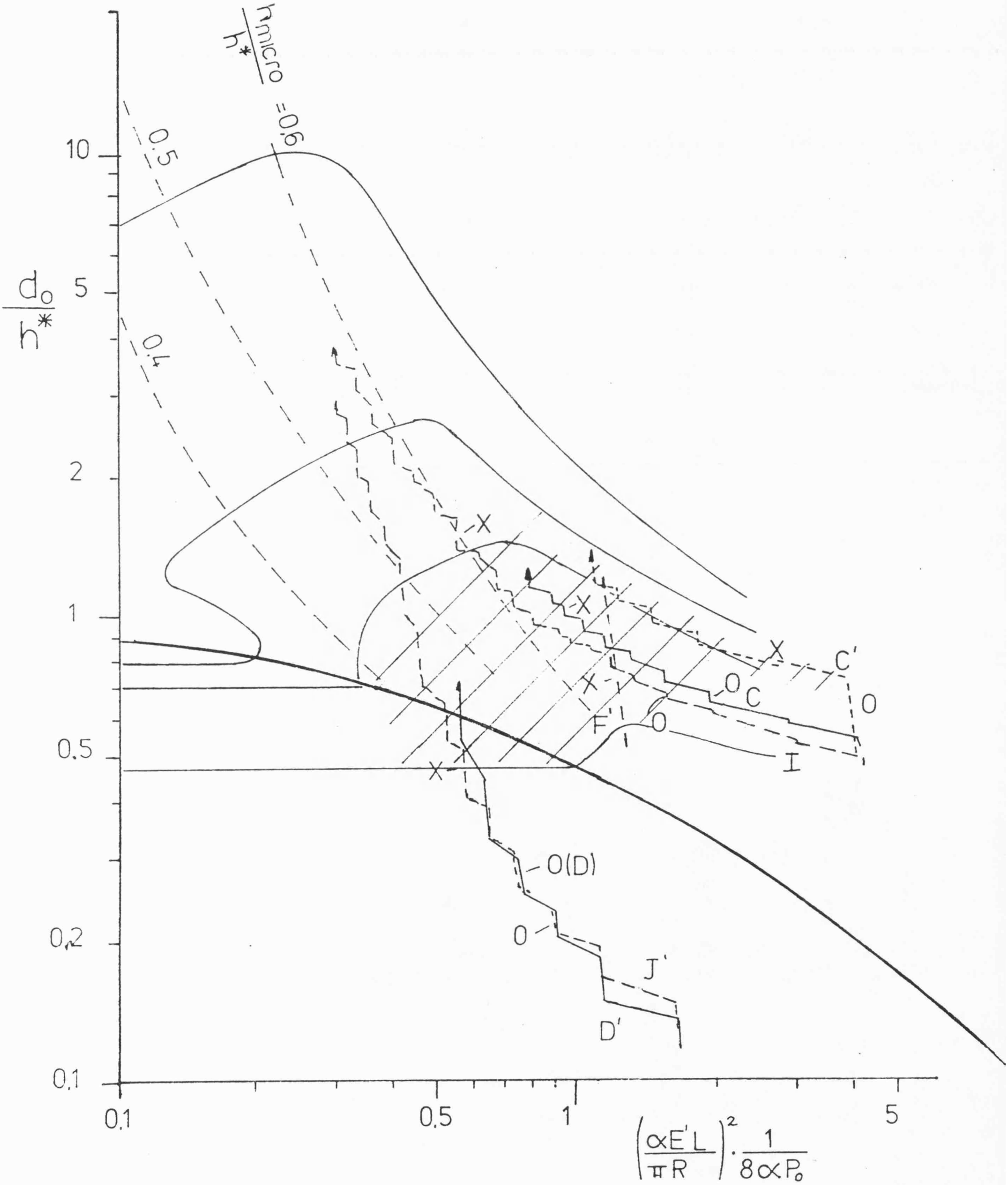

Figure 8.6 Two disc tests on asperity interaction map.

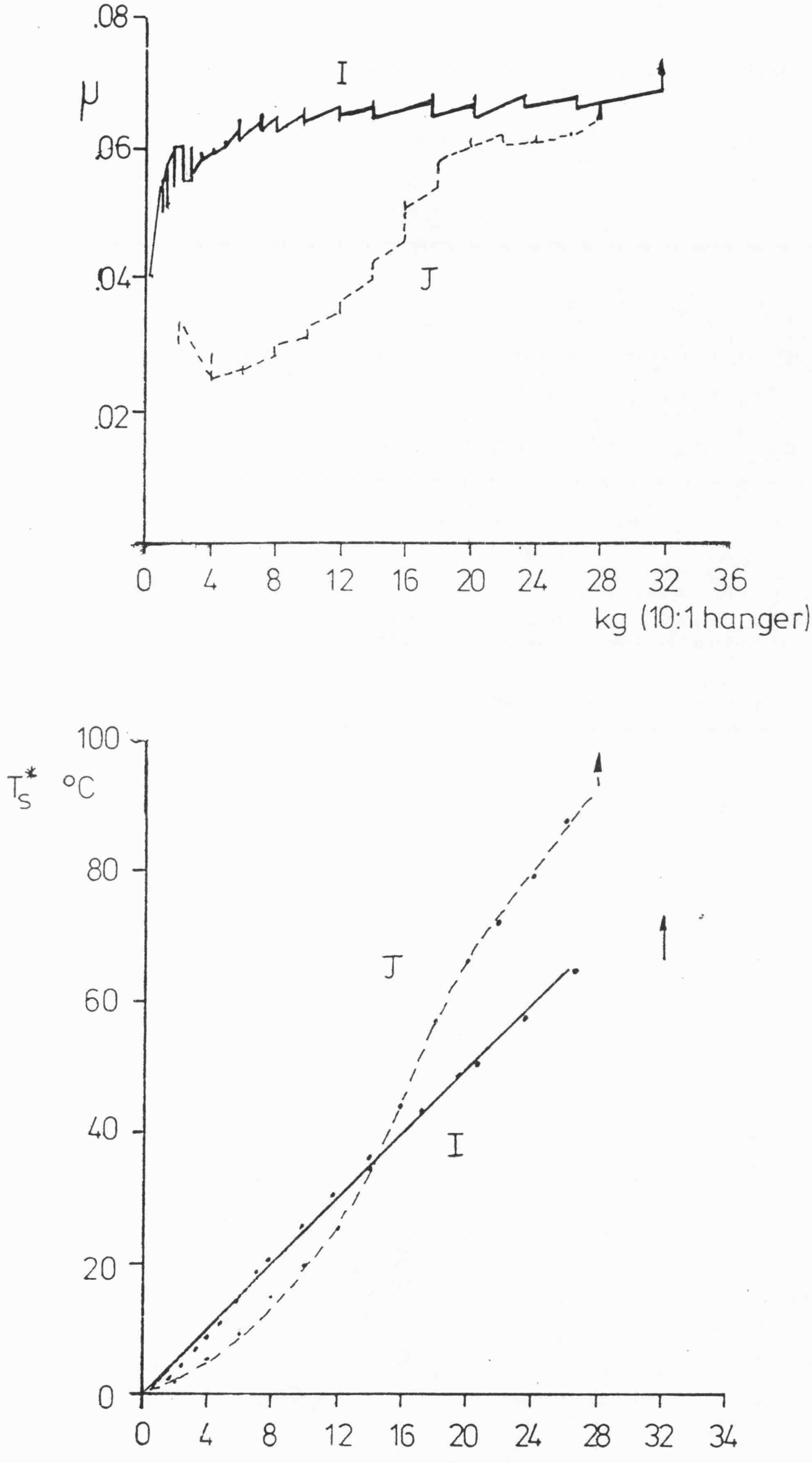

Figure 8.7 Incremental changes in friction and steady state temperature for tests J and I.

to the increasing asperity interaction as the test moves into the mixed lubrication regime. In tests I , the μ was initially high, ~0.065, rose over the next two increments to 0.07, and remained around this level for the remainder of the test.

There are several possible causes for the higher friction over the earlier stages of test I . The nominal d_o/h^* values suggest asperity overlap from the start of the test which would result in higher friction but there was no contact indicated by the countrate until the third load stage. The initial load for the LOG sequence is low enough for the lubrication to tend towards classical on the macro scale. Higher values of μ are associated with this form of lubrication. In test L , the LIN test, the initial load was sufficiently high for the system to be operating in ehl on the macro-scale from the start of the test but there was also a high initial μ in this test.

The work of Johnson and Evans has provided another possible cause for the high friction in the micro-ehl region. This is that the increased pressure and shear rate beneath the asperity tips changes the properties of the oil to those which give a higher value of frictional traction. This effect increases with more isolated behaviour.

Although the effect of very high pressure on the frictional traction is not known for the oil used in these tests it is possible that a similar effect could partly be the cause of the high friction in these tests, which initially run in conditions tending to be isolated.

8.5.3. Running-in differences

Fein (1967) observed that longer run-ins with thinner films promoted running-in. This statement implies 1) conditions which give rise to micro-ehl, i.e. low loads at high temperatures, and 2) that the initial stages of running-in is a gradual process.

Bishop (1981) on the other hand, by interrupting Rossides type tests, at various stages found that the majority of the running-in occurred in the initial stages of the tests and within 15 seconds of the application of the load, i.e. that it is a rapid process.

From the ΔR_a values of the tests it is possible to speculate at what stage of the tests the running-in has taken place.

ΔR_a for test C was 0.61 μm. If it is assumed that running-in is a contact process, this must have occurred between first contact and failure. Test I initially followed a similar path to test C but ran to far more severe conditions. The running-in was similar to that for test C i.e. $\Delta R_a = 0.68$ μm . If it is assumed that the running-in was due to the same process as that in test C , then it can be assumed that the majority of the running-in in test I took place over the similar range of conditions as in test C , i.e. between first contact and the tenth increment.

During the later stages of test I , i.e. after the failure of test C , ξ' arose from σ to 1.25σ . Additional running-in may have occurred in these stages which could not be detected from R_a measurements. Alternative parameters to R_a which are more sensitive to changes in surfaces topography caused by running-in, for example radii of asperity tips, could not be measured on the apparatus available.

Test D failed soon after crossing the mixed lubrication boundary with little prior contact and there was little surface modification. Test J which initially followed a similar path to that of test D , continued in the mixed lubrication regime. The nominal conditions then indicate that it passed into the cooperative micro-ehl region, although whether this transition is possible is not known. Test J had significant running-in and comparison to test D suggests that this occurred over the later stages of the test. By similar comparisons for other test pairs, an area within which the majority of the change in ΔR_a is thought to occur can be determined. This area is shown shaded in Fig.8.6, the lower bound being the zero contact line and the upper boundary around the line for an overlap of $\xi' = 1\sigma$

Test results show a clear correlation between running-in and successful operation to more severe conditions before scuffing occurs. Whether running-in is a necessary pre-requisite for successful operation or whether the conditions which optimise running-in are also those which retard scuffing is not clear.

In the 2:1 and 3:1 test series those tests at the lower slide/roll ratio, and those in the micro-ehl region at the higher slide/roll ratio exhibited running-in but not to such an extent as noted in some of the Rossides tests. The Rossides discs were through hardened to ~570 VPN compared with the 700 VPN hardness of the present discs. Experimental comparison suggests that the softer discs were more able to run-in than their harder counterparts and the tests proceeded further. This is, perhaps, evidence of the appropriateness of the Crook and Shotter hypothesis.

Another factor which is known to give longer life is the use of oil additives. Rossides and Bishop have both shown that additives lead to more surface modification in tests which start in micro-ehl and the question naturally arises - is the same true of tests which start in the rigid asperity regime?

A series of tests using additive oils were run by Williams, Finnis and Kelly (1988), using the linear loading sequence and the three initial temperatures of 30 °C, 50 °C and 70 °C. All these tests, except one, were at the 3:1 speed ratio. Unlike the OM100 tests, those starting in both regimes exhibited running-in. Those starting in the ehl regime passed into the mixed lubrication regime without failing and ran to more severe conditions than the 3:1 OM100 tests, although not as severe as the 2:1 tests with the plain mineral oil.

Several factors therefore seem to enhance the ability of the surfaces to run-in; surface speeds, regime of operation, use of additives and disc hardness. Regardless of the process by which running-in occurs, or whatever protects the system while promoting running-in, then the system can run to more severe conditions before failure. Altering the initial operating conditions to utilise this aspect of micro-ehl behaviour would be beneficial in avoiding scuffing failure. Further work is needed to pinpoint the exact regions in which the running-in occurs within the framework suggested by these tests and the proposed subdivisions of the micro-ehl regime.

8.5.4. Scuffing failure - and its prevention

The aim of the Story and of the Rossides test series was to examine the validity of the scuffing failure criterion proposed by Dyson (1976) (Chapter 2). This proposed that lubrication would fail and scuffing occur when the system became too hot to generate an elastohydrodynamic film thickness greater than the dry contact separation. Failure was predicted in terms of, amongst other parameters, a critical bulk temperature.

The failure conditions of the Rossides, the Story and the present test series are shown in Fig.8.8. The failure conditions can be grouped as shown in the figure.

In the Rossides tests the surfaces ran-in and the bulk temperatures at failure were in good agreement with those predicted by the Dyson analysis. (Snidle, Rossides and Dyson (1984)). These tests started in the micro-ehl region and the failure conditions of the tests lie close to the line of maximum h_{micro}/h^*. The 2:1 tests which start operation in the micro-ehl region follow a similar path and had failure temperatures in the same range as the Rossides tests and also exhibited running-in. The failure conditions of these tests tend to lie along the same locus as the Rossides tests. Due to the similarities between the two test groups it is likely that the 2:1 micro-ehl tests also failed in accordance with the Dyson criterion.

The 2:1 tests in this group, which start operation in the ehl region, have similar failure conditions (the Rossides and micro-ehl tests) in this group and also ran in, but have a different history. They passed

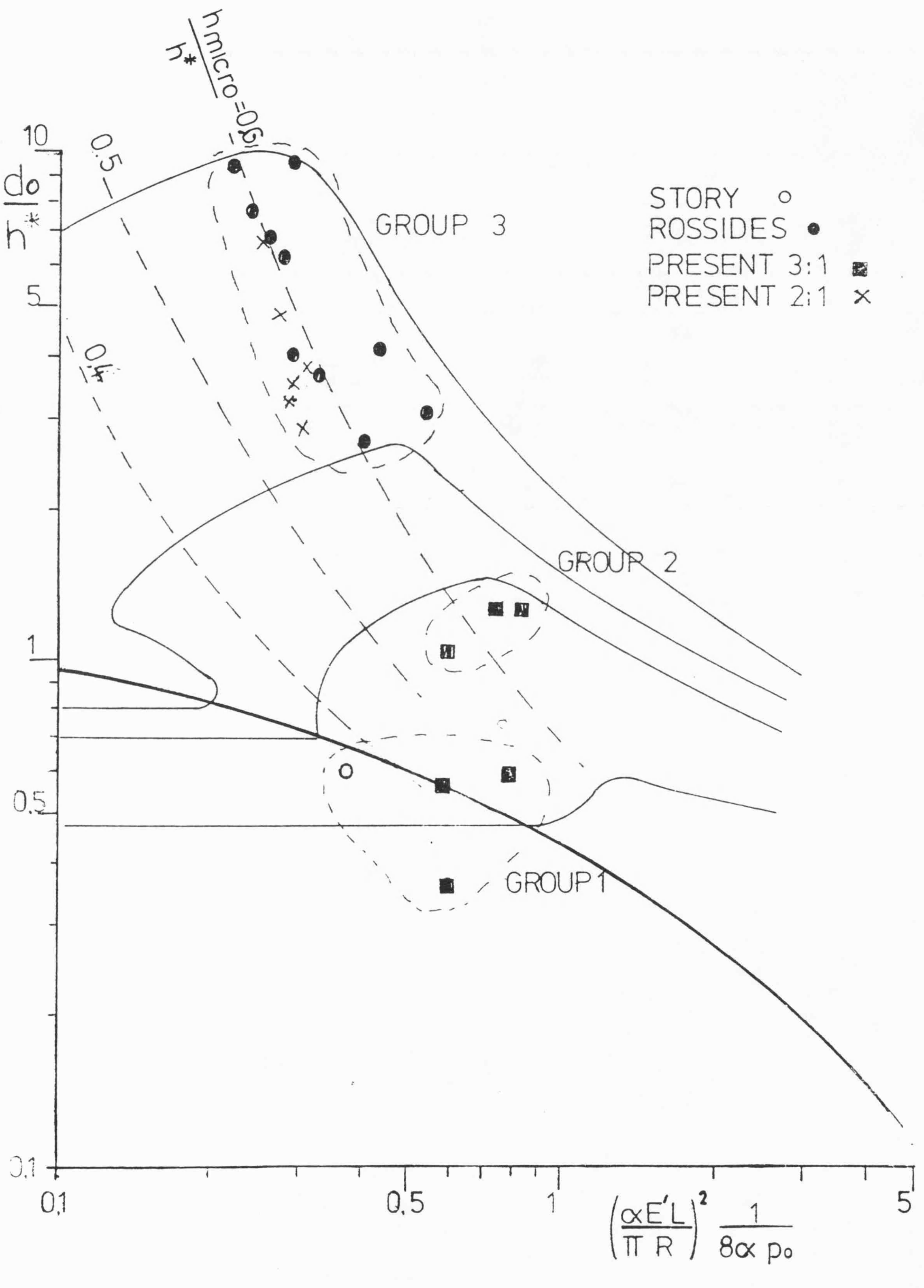

Figure 8.8 Failure conditions of the Rossides, Story and the present tests on the asperity interaction map.

from the ehl regime into mixed lubrication. As plotted they have obtained conditions which predict micro-ehl, but it is not known whether this transition can occur. Whether these tests, which are probably operating in a different regime to the rest of the tests in group 3, failed in accordance with the Dysn criterion is less predictable. The results of both test types in this group should be analysed to show whether the Dyson criterion is only applicable to those operating in micro-ehl.

Group 1 includes the Story 3:1 tests and the present 3:1 tests. They start operation in the ehl regime and fail in conditions of mixed lubrication. In this group the failure temperatures were again similar, and the surfaces did not run-in. The Story tests failed at temperatures less than those predicted by the Dyson analysis which implies that it does not hold for mixed lubrication conditions. It is expected that if tested the failure temperatures of the present tests in this group would also be less than those predicted by the Dyson criterion.

The tests in Group 2 are the 3:1 micro-ehl tests. These tests exhibited similar running-in to some of the Group 1 tests, but the failure condition was less severe than the Group 1 tests, even though the friction was lower.

This suggests a different type of failure to the other two groups, possibly as a result of the higher sliding or oil rheology (Section 8.4.3.).

The failure conditions of Group 3 tests lie along the line of h_{micro}/h^*. This is close to the maximum values of $h_{micro}/h^* = 0.6$ which is in terms of film thickness beneath the asperities, can be viewed as the optimum operating conditions for the system. The histories of the 2:1 micro-ehl tests run along the failure locus for the majority of the test. The 2:1 tests which come through the mixed regime initially have a steeper path than the micro-ehl tests but also tend to follow the locus in their later stages. These differences are reflected in the temperature changes per increment which were discussed in Section 3.4. The temperature changes and friction for tests I and J are shown in Fig.8.7. The slope of steady state temperature/load in test I is almost linear throughout the test. The temperature changes in test J are initially low when operation is in the ehl reion and increase in the mixed regime. As the test history approaches the $h_{micro} = 0.5\ h^*$ line, the slope of the temperature/load curve decreases and the coefficient of friction thereafter remains constant. The system appears to have the ability to self-adjust to obtain this optimum condition. Simple viscous systems have been shown to be able to do this in order to minimise energy dissipation. (Christophersen and Dowson (1959)).

At the initial conditions of the micro-ehl tests, the lines of degree of overlap, Σ', are close together such that small changes in nominal d_o/h^* gives a larger change in asperity interaction. Insulating the discs for tests, in this regime, causing more interaction, may effect the system's ability to self adjust, forcing it to operate at a lower h_{micro}/h^* level.

Although the cooling system was not sufficient over the full range of the tets, it did reduce the temperature in the earlier stages. In the 3:1 tests starting in ehl regime, which failed soon after entering the mixed lubrication regime, successful cooling throughout would increase the load carrying capacity.

Conversely, cooling tests in the micro-ehl regime may not be so beneficial as would first seem. Whilst reducing the temperature and hence nominal d_o/h^* levels for a given load group it may force the system to run at a lower h_{micro}/h^* level.

We still cannot answer the question "Why does scuffing occur?". The results of the tests and in subsequent developments have indicated conditions where scuffing is more probable by whatever mechanism.

Verification of these problem areas is needed and the work extended to cover a wider range of conditions, i.e. different surface roughness, oils, sliding speeds. By judiscious design, i.e. operation within the 'safer' regions and by careful considerations of cooling and heating aspects of machinery it may be possible to avoid the problem areas where scuffing occurs.

References

Archard, J.F. (1959). The temperature of rubbing surfaces. Wear. Vol.2. pp.438-455

Archard, J.F. & Baglin, K.P. (1986). Elastohydrodynamic lubrication - improvements in analytical solutions. Proc. Inst. Mech. Engrs. 200, No.C4, pp.281-291

Archard, J.F., Hunt, R.T. & Onions, R.A. (1975). Stylus profilometry and the analysis of the contact of rough surfaces. Proc. of the I.U.T.A.M. Symposium on the Mechanics of the Contact of Deformable Bodies. Delft University Press. pp.282-303

Archard, J.F. & Kirk, M.T. (1961). Lubrication at point contacts. Proc. Roy. Soc. London. A261. pp.532-550

Baglin, K.P. (1975). Elastohydrodynamic lubrication of materials of low elastic modules. M.Phil. thesis, University of Leicester

Baglin, K.P. (1986a). Elastohydrodynamic pressure rippling in cylinders finished with a circumferential lay. Proc. Inst. Mech. Engrs. 1986, 200, No.C5, pp.335-347

Baglin, K.P. (1986b). Microelastohydrodynamic lubrication and its relationship with running-in. Proc. Inst. Mech. Engrs. 200, No.C6, pp.415-424

Baglin, K.P. (1988). Rough surface lubrication, running-in and scuffing failure. Q.E.T. Fellowship Report to the I.Mech.E.

Bailey, M.W. & Cameron, A. (1973). The influence of temperature and metal pairs on the scuffing of a commercial lubricant. Proc. Instn. Mech. Eng. 187. pp.757-761

Baragan de Ling, F.D.M., Evans, H.P., Snidle, R.W. (1989). Micro-elastohydrodynamic lubrication of circumferentially finished rollers : the influence of temperature and roughness. To be presented at ASME Conference. Fort Lauderdale Oct. 1989

Barwell, F.T. & Milne, (1957). Some studies of scuffing with a crossed cylinder machine. Proc. Instn. Mech. Engrs. Conference on Lubrication and Wear. London (1957). pp.735-741

Bell, J.C. & Dyson, A. (1972a). The effect of some operating factors on the scuffing of hardened steel discs. Proc. Symp. on Elastohydrodynamic Lubrication. Inst. Mech. Engrs. No.C11. pp.61-67

Bell, J.C. & Dyson, A. (1972b). Mixed friction in an elastohydrodynamic system. Proc. Symp. on Elastohydrodynamic Lubrication. Inst. Mech. Engrs. No.C12, pp.68-76

Bell, J.C., Dyson, A. & Hadley, J.W. (1975).The effects of rolling and sliding speeds on the scuffing of lubricated steel discs. A.S.L.E. Trans. Vol.18, 1, pp.62-73

Berthe, D. & Godet, M. (1974). Elastohydrodynamic lubrication of surfaces in pure rolling. Tribology 1974, 7, pp 67-69

Bishop, I.F. (1981). Running-in and its relevance to scuffing failure. Ph.D. Thesis. University College Wales

Blok, H. (1937). Theoretical study of temperature rise in surfaces of actual contact of lubricated conditions. General discussion on lubrication. Inst. Mech. Engrs. London, 1987, p.222

Blok, H. (1939). Seizure delay method for determining the protection against scuffing afforded by extreme pressure lubricants, J. Society of Auto Engrs. Vol.44, No.5, pp.193-210 and 220.

Bodensiek, E.J. (1967). How film thickness affects gear tooth scoring. Power Transmission, Nov. 1967, pp.53-56

Boness, R.J. (1966). Isoviscous lubrication of rigid cylinders. Jnl. Mech. Engn. Sci. 8 (No.3), p.276

Campany, R.G. & Wilson, R.W. (1982). The metallurgy of scoring and scuffing failure. Proc. Symp. Tribology of Recriprocating Engines. Inst. Mech. Engrs. pp.201-211

Carper, H.T. & Ku, P.M. (1974). Thermal and scuffing behaviour of discs in sliding-rolling contact. A.S.L.E. Trans. Vol.18, 1, pp.39-41

Carper, H.T., Ku, P.M. & Anderson, E.L. (1972). Effect of some material and operating variables on scuffing. ASME-AGMA-IFTMM Symposium on Gearing and Transmissions, San Fransisco, California, U.S.A. October 1972.

Carslaw, H.S. & Jaegar, J.C. (1947). The conduction of heat in solids. Oxford University Press, London.

Castle, P. & Dowson, D. (1972). A theoretical analysis of the starved elastohydrodynamic lubrication problem for cylinders in line contact. Inst. Mch. Engrs. Proc. 2nd Symposium on Elastohydrodynamic Lubrication. pp.131-137

Cheng, H.S. (1967). Calculations of elastohydrodynamic film thickness in high sliding and rolling contact. Mechanical Technology Inc. Technical Report, MTI 67TR24

Cheng, H.S. (1983). Microelastohydrodynamic Lubrication. International Conference, Tribology in the 80s, NASA Lewis Research, Cleveland, Ohio, pp.161-170

Chow, L.S.H. & Cheng, H.S. (1976). The effect of surface roughness on the average film thickness between lubricated rollers. Trans A.S.M.E., J. Lubric. Tech., 98, pp.117-124

Christensen, H. (1965). Nature of metallic contact in mixed lubrication, Symposium on Elastohydrodynamic Lubrication. Proc. Inst. Mech. Engrs. Vol.180, Part 3B, p.147

Christensen, H. (1969-70). Stochastic models for hydrodynamic lubrication of rough surfaces. Proc. Inst. Mech. Engrs. Vol.184, Pt.1, No.55, pp.1013-1025

Christopherson, D.G. & Dowson, D. (1959). An example of minimum energy dissipation in viscous flow. Proc. Roy. Soc. A251

Conry, T.F., Johnson, K.L. & Owens, (1979). Viscosity in the thermal region in elastohydrodynamic traction. Proc. 6th Leeds-Lyon Symposium. Lyon 1979. (Mech.Eng. publication)

Crook, A.W. (1957). Simulated gear-tooth contacts - some experiments upon their lubrication and subsurface deformations. Proc. Inst. Mech. Engrs. Vol.171, pp.187-196

Crook, A.W. (1961). The lubrication of rollers - II. Film thickness with relation to viscosity and speed. Phil. Trans. Roy. Soc. 1961, Ser.A, 254, 223

Crook, A.W. & Shotter, B.A., (1957). Some scuffing experiments in a disc machine. Conference on Lubrication and Wear. Inst. Mech. Engrs. London,. pp.205-209

Des Riusseaux, N.R. & Zerkle, R.D. (1970). Temperature in semi-infinite and cylindrical bodies subjected to moving heat sources and surface cooling. Trans. A.S.M.E. Jour. of Heat Transfer. Vol.92, No.3, pp.456-464

Dowson, D. & Higginson, G.R. (1961). New roller bearing lubrication formula. Engineering (London), Vol.192, pp.158-159.

Dowson, D. & Higginson, G.R. (1966). Elastohydrodynamic lubrication. Pergamon Press, Oxford.

Dowson, D., Saman, W.Y. & Toyoda, S. (1979). A study of starved elastohydrodynamic line contacts. 5th Leeds/Lyon Symposium. Elastohydrodynamics and Related Topics. pp.92-103. Mech. Eng. Pub. Ltd.

Dowson, D. & Wholmes, T.L. (1967). Side leakage factors rigid cylinder lubrication with isoviscous fluids. Proc. Inst. Mech. Engrs. 181, Pt.30, p.165

Dowson, D. & Wholmes, T.L. (1971). The effect of surface roughness upon the lubrication of rigid cylindrical rollers. Wear 18, p.129

Dowson, D. & Whitaker, A.V. (1965). A numerical procedure for the solution of the elastohydrodynamic problem of rolling and sliding contacts lubricated by a Newtonian fluid. Proc. Inst. Mech. Engrs. 1965, 180, Pt.3B, p.57.

Dyson, A. (1975). Scuffing - a review. Tribology. April 1975

Dyson, A. (1975). Scuffing - a review. Part II. The mechanism of scuffing. Tribology, June 1975

Dyson, A. (1976). The failure of elastohydrodynamic lubrication of circumferentially ground discs. Proc. Inst. Mech.Engrs. Vol.190. No.52/76, pp.699-711

Dyson, A., Naylor, A. & Wilson, A.R. (1965). The measurement of oil film thickness in elastohydrodynamic contacts. Symposium on EHL. Proc. Inst. Mech. Engrs. 180. Pt.3B, pp.119-134

Evans, C.R. & Johnson, K.L. (1986a). The rheological properties of ehd lubricants. Proc. Inst. Mech. Engrs. Part C, 200, pp.303-312

Evans, C.R. & Johnson, K.L. (1986b). Regimes of traction in ehd lubrication. Proc. Inst. Mech. Engrs. Part C, 200, pp.313-324

Evans, C.R. & Johnson, K.L. (1987). The influence of surface roughness on elastohydrodynamic traction. Proc. Inst. Mech. Engrs. Part C, 201. pp.145-150

Fein, R.S. (1960). Transition temperatures with four ball machine. ASLE Trans 3, pp.34-39

Fein, R.S. (1965). Effect of lubricant on transition temperatures. Trans. A.S.L.E., Vol.8, No.2, pp.59-65

Fein, R.S. (1967). Operating procedure effcts on critical temperatures. Trans. A.S.L.E., Vol.10, No.4, pp.373-385

Finnis, M.P. (1984). The evaluation of two disc scuffing test differences in calculated film thicknesses for fully-flooded and zero reverse flow-starved inlet conditions, and the measurement of disc surface temperature by embedded thermocouples and infra-red scanner. First year report. Department of Engineering, University of Leicester.

Gecim, B. & Winer, W.O. (1984). Steady temperature in a rotating cylinder subject to surface heating and convective cooling. Trans. A.S.M.E., Vol,10, Jan. 1984. pp.120-127

Gecim, B. & Winer, W.O. (1986a). Effect of a surface film on the surface temperature of a rotating cylinder. Trans. A.S.M.E., Vol. 108, Jan. 1986. pp.92-97

Gecim, B. & Winer, W.O. (1986b). Steady temperature in a rotating cylinder - some variations in the geometry and the thermal boundary conditions. Trans. A.S.M.E., Vol. 108, July 1986. pp.446-454

Goksem, P.G. & Hargreaves, R.A. (1978a). The effect of viscous shear heating on both film thickness and rolling traction in an ehl line contact. Part I - Fully flooded conditions. pp.346-352. Part II - Starved conditions. pp.352-358. Trans. A.S.M.E. J.Lub.Tech.100.

Grubin, A.N. (1949). In the Proceedings of Symposium on Investigation into the contact of machine components. Book 30 (DSIR Translation 377), Central Scientific Institute for Technology and Mechanical Engineering, Moscow.

Halling, J. & Nuri, K.A. (1985). The elastic contact of rough surfaces and its importance in the reduction of wear. Proc. Inst. Mech. Engrs. 199, pp.139-144

Haltoff, B. (1970). An investigation into the breakdown of elastohydro-dynamic lubrication using the resistance breakdown counter. Third year project report. Department of Engineering, University of Leicester

Heat Transfer and Fluid Flow Data Book (1984). Genium Publishing Corporation, New York

Hertz, H. (1882). On the contact of elastic solids. J. reine und angewandte Mathematik 92, pp.156-171

Hirst, W. & Moore, A.G. (1980). The effect of temperature on traction in ehl. Phil. Trans. Roy. Soc. Ser.A. 1980. 298, pp.183-208

Institute of Mechanical Engineers (1957). Conference on Lubrication and Wear. Proc. Inst. Mech. Engrs. London, p.4.

Institute of Petroleum (1968). Load carrying capacity test for oils. IAE Gear Machine Method No. IP166/68

Jaegar, J.C. (1944). Some problems involving line sources in conduction of heat. Philosophical Magazine. Ser.7, Vol.35, pp.169-179

Kays, V.M., & Bjorkland, I.S. (1958). Heat transfer from a rotating cylinder with and without cross flow. Trans. A.S.M.E., Vol.80, No.1, pp.70-77

Karami, G., Evans, HP. & Snidle, R.W. (1986). Elastohydrodynamic lubrication of grooved rollers. 13th Leeds/Lyon Symposium on Tribology

Karami, G., Evans, H.P. & Snidle, R.W. (1987). Elastohydrodynamic lubrication of circumferentially finished rollers having sinusoidal roughness. Proc. I.Mech.E. 201, (C1), pp.29-36

Ku, P.M.. & Li, K.Y. (1977). Effect of surface topography on sliding-rolling disc scuffing. Proc. 4th Leeds/Lyon Symposium on Surface roughness effect in lubrication. Sept. 1977. (Pub. I.Mech.E. 1978). pp.210-217.

Ku, P.M., Staph, H.E. & Carper (1978). On the critical contact temperature of lubricated sliding rolling disks. A.S.L.E. Trans. Vol.21, 2, pp.161-180

Lauder, W. (1965). Hydrodynamic lubrication of proximate cylindrical surfaces of large relative curvature. Proc. Inst. Mech. Engrs. 180, Pt.3B, pp.101-106

Leach, E.F. & Kelly, B.W. (1965). Temperature - the key to lubricant capacity. Trans. A.S.L.E., Vol.8, pp.271-285

Ling, F.F. (1973). Surface Mechanics. Pub. John Wiley & Sons.

Matveesky, R.M. (1965). The critical temperature of oil with point and line contacts. Trans. A.S.M.E. Jour. of Basic Engineering, Vol.89, pp.754-760

Meng, V.V. (1960). Investigation of steel seizure on a roller testing machine (in Russian). Friction and Wear in Machinery, Vol.14 (1960). English translation, A.S.M.E. pp.202-217

Myers, G.E. (1971). Analytical methods in conduction heat transfer. Pub. McGraw-Hill Inc.

Neale, M.J. (1971). Piston ring scuffing - a broad survey of problems and practice. Proc. Inst. Mech. Engrs. Vol.188, pp.21-32

Neimen, G. & Lechner, G. (1967). Die Fressyrenzlast bei Stirnradern aus stahl. Elrod und Kohle Erdgas, Petrochemice. Vol.20, No.2, pp.96-106

Neimen, G. & Seitzinger, A. (1971). Temperature rise as the criterion for scuffing resistance of case-hardened gear teeth. Verein der Deutsche Ingenieure Zeitung, Vol.13, No.2, pp.97-172

O'Donoghue, J.P., Manton, S.M. & Askwith, T.C. (1967-68). An experimental determination of the temperature at scuffing. Proc. Inst. Mech. Engrs. Vol.182, Part 3N, pp.18-23

Orcutt, F.K. & Cheng, H.S. (1966). Lubrication of rolling contact instrument bearings. Gyro-spin-axis Hydrodynamic Bearing Symposium (M.I.T. Instrumentation Laboratory)

Padmoore, E.L. & Ruston, S.C. (1964/65). Effects of loading procedure on surface failure in spur gears. Proc. Instn. Mech. Engrs. Vol.179, Part 3J, pp.278-289

Remezova, N.E. (1959). Experimental investigation of crossed-helicar gear transmission using the roller analogy. Vestnik Machinostr. No.9, p.19 (English translation. Russ. Eng. J. Vol.9, p.17)

Reynolds, O. (1886). On the theory of lubrication and its application to Mr. Beauchamp Tower's experiments, including an experimental determination of the viscosity of olive oil. Phil. Trans. Roy. Soc. 1886, 177, pp.187-234

Rogers, M.D. (1969). Metallographic characterisation of transformation phases in scuffed cast iron diesel engine components. Tribology, Vol.2, No.2, pp.123-127

Rogers, M.D. (1970). The mechanism of scuffing in diesel engines. Wear,No.15, pp.105-116

Rossides, S.D. (1980). Surface topography and scuffing failure. Ph.D. Thesis University of Wales

Sakman, B.W. (1947). Geometrical and metallurgical changes in steel surfaces under conditions of boundary lubrication. Jour. Applied Mechanics, Vol.14, Part 1, A-43-S2

Saman, W.Y. (1974). A study of starved elastohydrodynamic lubrication with particular reference to gyroscope bearings. Ph.D. Thesis, University of Leeds.

Snidle, R.W., Rossides, S.D. & Dyson, A. (1984). The failure of elastohydrodynamic lubrication. Proc. Roy. Soc. Lond. Ser.A, 395, pp.291-311

Sparrow & Gregg (1959). Heat transfer from a rotating disc to fluids of any Prandtl. A.S.M.E. Trans. Jour. of Heat Transfer 81, Ser.C, 1959, pp.249-251

Staph, H.E., Ku, P.M. & Carper, H.J. (1973). Effect of surface roughness and surface texture on scuffing. Mechanisms and Machine Theory, Vol.8, pp.197-208

Story, D.L. (1984). A reassessment of scuffing failure of discs. Ph.D. Thesis (not submitted). Department of Engineering, University of Leicester

Story, D.L., Archard, J.F. & Baglin, K.P. (1980). A reassessment of scuffing failure data of discs. Symposium on Performance and Testing of Gear Oils and Transmission Fluids, Inst. of Petroleum, London.

Tallian, T.E. (1972). The theory of partial elastohydrodynamic contacts. Wear, Vol.2, No.1, pp.49-101

Tzeng, S.T. & Saibel, E. (1967). Surface roughness effect on slider bearing lubrication. A.S.L.E. Trans. Vol.10, pp.334-338

Vindograv, G.V. & Podolsky, I.I. (1960). High speed friction machine for the investigation of lubricants and plastics. USSR ZNITI Vol.8, No.II-60-S1/8

Westergaard, H.M. (1939). Bearing pressure and Cracks. Jour. Appl. Mech. 6, A49.

Whitehouse, D.J. & Phillips, M.J. (1978). Discrete properties of random surfaces. Phil. Trans. Roy. Soc. London, Vol.290, No.1369, pp.267-298

Williams, P.A., Finnis, M.P. & Kelly, D.A. (1988). Effects of test procedure and oil additives on scuffing in two-disc machines. Proc. Inst. Mech. Engrs. Part C, 202 (C3), pp.211-218

Wolveridge, P.E. & Archard, J.F. (1972). Temperature distributions in elastohydrodynamic films; a new analytical solution. Proc. Symp. Elastohydrodynamic lubrication. Inst. Mech. Engrs. C9, pp.48-54

Wolveridge, P.E., Baglin, K.P. & Archard, J.F. (1971). The starved lubrication of cylinders in line contact. Proc. Inst. Mech. Engrs. 185, pp.1159-1169.

Appendix 1

To integrate I_a and $I_{a\tau}$

I_a was given by equation (4.8) as

$$I_a = \int_{\tau=0}^{\tau=\alpha} \left[\frac{\tau^{3/2}}{(1+\tau^{3/2})^3 + 3\left(\frac{\sigma}{h_a^*}\right)^2 (1+\tau^{3/2})} \right] d\tau \qquad (A1.1)$$

and $I_{a\tau}$ by equation (4.16) as

$$I_{a\tau} = \int_{\tau=0}^{\tau=\tau_i} \left[\frac{\tau^{3/2}}{(1+\tau^{3/2})^3 + 3\left(\frac{\sigma}{h_{a\tau}^*}\right)^2 (1+\tau^{3/2})} \right] d\tau \qquad (A1.2)$$

Both integrals have the same form, eqn.(A1.1) being the fully flooded case ($\tau_i=\alpha$) and eqn.(A1.2) the starved case. Both expressions are functions of the prevailing film thickness h_a^* and $h_{a\tau}^*$ respectively. The solution for both cases can be obtained from the more general form of eqn.(A1.2).

Factorization of eqn.(A1.2) gives

$$I_{a\tau} = \frac{1}{3}\left(\frac{h_{a\tau}^*}{\sigma}\right)^2 \int_{\tau=0}^{\tau=\tau_i} \left[\frac{-1}{(1+\tau^{3/2})} + \frac{1}{2(1+m^3\tau^{3/2})} + \frac{1}{2(1+n^3\tau^{3/2})} \right] d\tau \quad (A1.3)$$

where $m = \left(1 + \frac{i\sqrt{3}\sigma}{h_{a\tau}^*}\right)^{-1/3}$ and $n = \left(1 - \frac{i\sqrt{3}\sigma}{h_{a\tau}^*}\right)^{-1/3}$

Each term in eqn.(A1.3) has the form $\int_0^{\tau=\tau_i} \frac{d\tau}{1+K^3\tau^{3/2}}$ where K=1, m,n respectively.

Using the substitution $z = \frac{1}{K\tau^{1/2}}$, this becomes $\frac{2}{K^2}\int_{1/K\tau_i^{1/2}}^{\alpha} \frac{dz}{1+z^3}$

This integral is a standard form

$$\frac{2}{K^2}\left[\frac{1}{3}\left\{\frac{1}{2}\,\ell n\left(\frac{(1+z)^2}{1-z+z^2}\right) + \sqrt{3}\,\tan^{-1}\left(\frac{2z-1}{\sqrt{3}}\right)\right\}\right]_{1/K\tau_i}^{\alpha}$$

which, on inserting the limits, becomes

$$\frac{\pi}{K^2\sqrt{3}} - \frac{2}{K^2}\left[\frac{1}{3}\left\{\frac{1}{2}\,\ell n\left(\frac{(1+K\tau_i^{1/2})^2}{K^2\tau_i - K\tau_i^{1/2}+1}\right) + \sqrt{3}\tan^{-1}\left(\frac{2-K\tau^{1/2}}{\sqrt{3}\;K\tau_i^{1/2}}\right)\right\}\right] \quad (A1.4)$$

Fully flooded solution

As $\tau_i \rightarrow \alpha$, $h^*_{a\tau} \rightarrow h^*_a$, equation (A1.4) reduces to

$$\frac{\pi}{K^2\sqrt{3}} - \frac{2}{K^2}\cdot\frac{1}{3}\sqrt{3}\left(-\frac{\pi}{6}\right) = \frac{4\,\pi}{3K^2\sqrt{3}}$$

Returning this expression to eqn.(A1.3) for K = 1, m and n gives

$$I_a = \frac{1}{3}\left(\frac{h^*_a}{\sigma}\right)^2 \cdot \frac{4\pi}{3\sqrt{3}}\left[-1 + \frac{1}{2m^2} + \frac{1}{2n^2}\right] \quad (A1.5)$$

m and n are complex numbers. $\frac{1}{m^2}$ and $\frac{1}{n^2}$ can be written in their polar forms.

$$\frac{1}{m^2} = \left(1 + 3\left(\frac{\sigma}{h^*_a}\right)^2\right)^{1/3} \cdot \left(\cos\frac{2\theta}{3} + i\sin\frac{2\theta}{3}\right)$$

$$(A1.6)$$

and

$$\frac{1}{n^2} = \left(1 + 3\left(\frac{\sigma}{h^*_a}\right)^2\right)^{1/3} \cdot \left(\cos\frac{2\theta}{3} - i\sin\frac{2\theta}{3}\right)$$

where $\theta = \tan^{-1}\dfrac{\sqrt{3}\sigma}{h^*_a}$

Substitution for m^2 and n^2 in eqn.(A1.5) gives

$$I_a = \frac{4\sqrt{3}\pi}{27}\left(\frac{h^*_a}{\sigma}\right)^2\left[\left(1 + 3\left(\frac{\sigma}{h^*_a}\right)^2\right)^{1/3} \cdot \cos\left(\frac{2}{3}\tan^{-1}\left(\frac{\sqrt{3}\sigma}{h^*_a}\right)\right) - 1\right] \quad (A1.7)$$

Starved solution

Substituting for each term in equation (A1.3) by equation (A1.4) gives

$$I_{a\tau} = \frac{1}{3}\left(\frac{h^*_{a\tau}}{\sigma}\right)^2\left\{\left[-\frac{\pi}{\sqrt{3}} + \frac{1}{2m^2}\frac{\pi}{\sqrt{3}} + \frac{1}{2n^2}\frac{\pi}{\sqrt{3}}\right]\right.$$

$$+ \frac{1}{3}\left[\ell n\left(\frac{(1+\tau_i^{1/2})^2}{\tau_i - \tau_i^{1/2}+1}\right) - \frac{1}{2m^2}\cdot\ell n\left(\frac{(1/m + \tau_i^{1/2})^2}{\tau_i - \tau_i^{1/2}\,1/m - 1/m^2}\right) - \frac{1}{2n^2}\cdot\ell n\left(\frac{(1/n + \tau_i^{1/2})^2}{\tau_i - \tau_i^{1/2}\,1/n - 1/n^2}\right)\right]$$

$$\left. + \frac{2}{\sqrt{3}}\left[\tan^{-1}\left(\frac{2-\tau_i^{1/2}}{\sqrt{3}\tau_i^{1/2}}\right) - \frac{1}{2m^2}\tan^{-1}\left(\frac{2/m - \tau_i^{1/2}}{\sqrt{3}\tau_i}\right) - \frac{1}{2n^2}\tan^{-1}\left(\frac{2/n - \tau_i^{1/2}}{\sqrt{3}\tau_i^{1/2}}\right)\right]\right\} \quad (A1.8)$$

Equation (A1.8) has three main parts (each enclosed by square brackets). m and n are complex numbers. The imaginary part can be removed by replacing m^2, n^2, m and n by their polar forms.

The polar form of $\frac{1}{m^2}$ and $\frac{1}{n^2}$ are given by eqn.(A1.6).

The polar form of $\frac{1}{m}$ is

$$r.\left(\cos\frac{\theta}{3} + i\sin\frac{\theta}{3}\right)$$

where

$$r = \left(1 + 3\left(\frac{\sigma}{h^*_{a\tau}}\right)^2\right)^{1/6}, \ \theta = \tan^{-1}\frac{\sqrt{3}\,\sigma}{h^*_{a\tau}}$$

and $\frac{1}{n}$ is

$$r.\left(\cos\frac{\theta}{3} - i\sin\frac{\theta}{3}\right) \quad .$$

A. Replacing $\frac{1}{m^2}$ and $\frac{1}{n^2}$ in the first part of eqn.(A1.8) gives

$$\frac{\pi}{\sqrt{3}}\left[\left(1 + 3\left(\frac{\sigma}{h^*_{a\tau}}\right)^2\right)^{1/3} \cos\left(\frac{2}{3}\tan^{-1}\frac{\sqrt{3}\sigma}{h^*_{a\tau}}\right) - 1\right] \tag{A1.9}$$

B. Replacing $\frac{1}{m^2}$, $\frac{1}{n^2}$, $\frac{1}{m}$ and $\frac{1}{n}$, the second set of terms - the 'ℓn' terms of eqn.(A1.8) becomes

$$\ell n\left(\frac{(1+\tau_i^{1/2})^2}{1-\tau_i^{1/2}+\tau_i}\right) - \frac{r^2}{2}\left(\cos\frac{2\theta}{3} + i\sin\frac{2\theta}{3}\right)\ell n\left(\frac{(M+iN)^2}{S+iT}\right) - \frac{r^2}{2}\left(\cos\frac{2\theta}{3} - i\sin\frac{2\theta}{3}\right)\ell n\left(\frac{(M-iN)^2}{S-iT}\right) \tag{A1.10}$$

where $M = \tau_i^{1/2} + r\cos\frac{\theta}{3}$

$N = r\sin\frac{\theta}{3}$

$S = \tau_i - \tau_i^{1/2} r\cos\frac{\theta}{3} + r^2\cos\frac{2\theta}{3}$

and $T = -\tau_i^{1/2}\, r\sin\frac{\theta}{3} + r^2\sin\frac{2\theta}{3}$

The complex numbers $M \pm iN$ and $S \pm iT$ can be expressed in polar form as

$$M \pm iN = \sqrt{M^2+N^2}\; e^{\pm ic} \quad \text{and} \quad S \pm iT = \sqrt{S^2+T^2}\; e^{\pm id}$$

where $c = \tan^{-1} \frac{N}{M}$ and $d = \tan^{-1} \frac{T}{S}$

Substituting these polar forms into eqn.(A1.10) gives

$$\ln \left(\frac{(1+\tau_i^{1/2})^2}{1-\tau_i^{1/2}+\tau_i}\right) - r^2 \cos\frac{2\theta}{3} \ln \left(\frac{M^2+N^2}{\sqrt{S^2+T^2}}\right) - \frac{r^2}{2}\left(\cos\frac{2\theta}{3} + i\sin\frac{2\theta}{3}\right)\ln\left(\frac{e^{i2c}}{e^{id}}\right)$$

$$- \frac{r^2}{2}\left(\cos\frac{2\theta}{3} - i\sin\frac{2\theta}{3}\right)\ln\left(\frac{e^{-i2c}}{e^{-id}}\right)$$

which reduces to

$$\ln \left(\frac{(1+\tau_i^{1/2})^2}{1-\tau_i^{1/2}+\tau_i}\right) - r^2 \cos\frac{2\theta}{3} \ln \left(\frac{M^2+N^2}{\sqrt{S^2+T^2}}\right) + r^2 \sin\frac{2\theta}{3}\left(2\tan^{-1}\left(\frac{N}{M}\right) - \tan^{-1}\left(\frac{T}{S}\right)\right) \quad \text{(A1.11)}$$

C. Substituting for m and n, the third part of equation (A1.8) the '$\tan^{-1}$' terms become

$$\tan^{-1}\left(\frac{2-\tau_i^{1/2}}{\sqrt{3}\;\tau_i^{1/2}}\right) - \frac{r^2}{2}\left(\cos\frac{2\theta}{3} + i\sin\frac{2\theta}{3}\right)\tan^{-1}(f+ig) - \frac{r^2}{2}\left(\cos\frac{2\theta}{3} - i\sin\frac{2\theta}{3}\right)\tan^{-1}(f-ig)$$

where $f = \dfrac{2r\cos\theta/3 - \tau_i^{1/2}}{\sqrt{3}\;\tau_i^{1/2}}$ and $g = \dfrac{2r\sin\theta/3}{\sqrt{3}\;\tau_i^{1/2}}$

Using the identify $\tan^{-1}(f+ig) = \frac{1}{2}\tan^{-1}\frac{2f}{1-f^2-g^2} + \frac{1}{4}\ln\left(\frac{f^2+(g+1)^2}{f^2+(g-1)^2}\right)$

the real and imaginary parts of the $\tan^{-1}$ terms can be separated to give

$$\tan^{-1}\left(\frac{2-\tau_i^{1/2}}{\sqrt{3}\;\tau_i^{1/2}}\right) - r^2\cos\frac{2\theta}{3}\cdot\frac{1}{2}\tan^{-1}\left(\frac{2f}{1-f^2-g^2}\right) + r^2\sin\frac{2\theta}{3}\cdot\frac{1}{4}\ln\left(\frac{f^2+g^2+2g+2}{f^2+g^2-2g+1}\right)$$

(A1.12)

Equations (A1.9), (A1.11) and (A1.12) when returned to equation (A1.8) gives the full solution for $I_{a\tau}$. Using the full expressions for M, N, S, T, f and g this becomes

$$I_{a\tau} = \frac{1}{3}\left(\frac{h^*_{a\tau}}{\sigma}\right)^2 \Big\langle \frac{\pi}{\sqrt{3}}\left[r^2\cos\left(\frac{2\theta}{3}\right) - 1\right]$$

$$+ \frac{1}{3}\left[\ell n\left(\frac{(1+\tau_i^{1/2})^2}{\tau_i-\tau_i^{1/2}+1}\right) - r^2\cos\frac{2\theta}{3}.\ell n\left(\frac{\tau_i + 2\tau_i^{1/2}.r\cos\theta/_3+r^2}{(\tau_i^2+r^4-2\tau_i^{3/2}.r\cos\theta/_3+\tau_i r^2(1+2\cos2\theta/_3)-2\tau_i^{1/2}r^3\cos\theta/_3)^{\frac{1}{2}}}\right)\right.$$

$$\left.+ r^2\sin\frac{2\theta}{3}.\left(2\tan^{-1}\left(\frac{r\sin\theta/_3}{r\cos\theta/_3+\tau_i^{1/2}}\right) - \tan^{-1}\left(\frac{-\tau_i^{1/2}r\sin\theta/_3 + r^2\sin2\theta/_3}{\tau_i-\tau_i^{1/2}r\cos\theta/_3+r^2\cos2\theta/_3}\right)\right)\right]$$

$$+ \frac{2}{\sqrt{3}}\left[\tan^{-1}\left(\frac{2-\tau_i^{1/2}}{\sqrt{3}\ \tau_i^{1/2}}\right) - r^2\cos\frac{2\theta}{3}.\frac{1}{2}\tan^{-1}\left(\frac{\sqrt{3}\tau_i^{1/2}(2r\cos\theta/_3-\tau_i^{1/2})}{\tau_i+2\tau_i^{1/2}.r\cos\theta/_3-2r^2}\right)\right.$$

$$\left.+ r^2\sin\frac{2\theta}{3}.\frac{1}{4}\ell n\left(\frac{r^2+\tau_i+\tau_i^{1/2}.r(-\cos\theta/_3+\sqrt{3}\sin\theta/_3)}{r^2+\tau_i+\tau_i^{1/2}\ r(-\cos\theta/_3-\sqrt{3}\sin\theta/_3)}\right)\right]\Big\rangle$$

where $\theta = \tan^{-1}\frac{\sqrt{36}}{h^*_{a\tau}}$ and $r = \left(1 + 3\left(\frac{\sigma}{h^*_{a\tau}}\right)^2\right)^{1/6}$

This expression for $I_{a\tau}$ can be substituted into Eqn.(4.16) to give the full expression for $\bar{q}_{a\tau}$.

$I_{a\tau}$ is a function of τ_i and $\left(\frac{\sigma}{h^*_{a\tau}}\right)$ and consists of eight terms. The first is a function of $\frac{\sigma}{h^*_a}$ only and has the same form as I_a . The second and sixth terms are functions of τ_i only and have the same form as terms in the solution given by Wolveridge et al for I_Γ

i.e.
$$I_\Gamma = \frac{(2\tau^{3/2}-1)\tau_i}{9(1+\tau_i^{3/2})^2} - \frac{2}{27}\left[\frac{1}{2}\ln\left\{\frac{(1+\tau_i^{\frac{1}{2}})^2}{\tau_i-\tau_i^{\frac{1}{2}}+1}\right\} + \sqrt{3}\tan^{-1}\left\{\frac{(2-\tau_i^{\frac{1}{2}})}{\sqrt{3}\ \tau_i^{\frac{1}{2}}}\right\}\right]$$

The remaining terms are functions of both parameters.

By expanding the θ and r terms in Eqn.(A1.14), as series of $\frac{\sigma}{h^*_{a\tau}}$, the expression can be shown after much tedius algebra to tend in the limit as $\frac{\sigma}{h^*_{a\tau}} \to 0$, to the expression for I_τ. By the same process, I_a given by Eqn.(A1.7) tends to $I = \frac{4\pi}{27\sqrt{3}}$ and this case is detailed below.

As $\tau_i \to \alpha$, $I_{a\tau}$ can be shown to tend to the expression for I_a, (Eqn.A1.7).

<u>Limiting case for $I_a \to I$ as $\sigma/h^*_a \to 0$</u>

I_a is given by Eqn.(A1.7) as

$$I_a = \frac{4\sqrt{3}\pi}{27}\left[\frac{h^*_a}{\sigma}\right]^2 \left[\left(1 + 3\left(\frac{\sigma}{h^*_a}\right)^2\right)^{1/3}.\cos\left[\frac{2}{3}\tan^{-1}\left(\frac{\sqrt{3}\sigma}{h^*_a}\right)\right] - 1\right]$$

Expanding as a series with $(\sigma/h^*_a)^2$ replaced by a' gives

$$(1 + 3a^2)^{1/3} = 1 + a^2 - a^4 + \frac{5}{3}a^6 + \ldots\ldots \text{(where } a = \left(\frac{\sigma}{h^*_a}\right)$$

$$\tan^{-1}\sqrt{3}a = \sqrt{3}a - \sqrt{3}a + \frac{9\sqrt{3}}{5}a^5 + \ldots$$

$$\cos\left(\frac{2}{3}\tan^{-1}\sqrt{3}a\right) \quad 1 - \frac{\left(\frac{2}{3}(\sqrt{3}a - \sqrt{3}a^3 + \ldots.)\right)^2}{2} + \ldots..$$

$$= 1 - \frac{2}{3}a^2 - \frac{4}{9}a^4 + \ldots$$

$$I_a = \frac{4\sqrt{3}\pi}{27}\left[\frac{1}{a^*}\right]^2 \left[(1+a^2-a^4)\left(1 - \frac{2}{3}a^2 - \frac{4}{9}a^4 + \ldots\right) - 1\right]$$

$$= \frac{4\sqrt{3}\pi}{27}\left[\frac{1}{a^2}\right]\left[\frac{a^2}{3} - \frac{19}{9}a^4 + \ldots.\right]$$

$$= \frac{4\sqrt{3}\pi}{27}\left[\frac{1}{3} - \frac{19}{9}a^2 + \ldots\ldots\right]$$

as $\frac{\sigma}{h^*_a} \to 0$ $a \to 0$ and

$$I_a \to \frac{4\sqrt{3}\pi}{27\sqrt{3}} \to \frac{4\pi}{27\sqrt{3}} = I .$$

Appendix 2

The zero reverse flow inlet boundary condition

In a starved contact, the position in the inlet region at which pressure generation begins can be determined using the zero reverse flow inlet boundary condition. This condition assumes that the oil film meniscus forms in a position where the condition

$$u = \frac{du}{dz} = 0 \qquad \text{(A2.1)}$$

is satisfied.

Using this condition and initially following the method used by Dowson, Saman and Toyoda (1979), the inlet position can be determined for the tests discussed in Section 4.

For the configuration shown in Fig.A2.1, the surface velocities are u_1 and u_2 and $h(x)$ is local film thickness at a distance x from the contact in the inlet zone. The fluid film velocity in the direction of entrainment u at a position x, varies with the height z above surface 2 according to

$$u = u_2 + \frac{z}{h}\ (u_1 - u_2) - \left[\frac{zh - z^2}{2\eta}\right]\frac{\partial p}{dx} \qquad \text{(A2.2)}$$

The integrated form of Reynolds Equation gives

$$\frac{\partial p}{dx} = 12\eta\bar{u}\ \left[\frac{h - h^*}{h^3}\right] \qquad \text{(A2.3)}$$

Combining equations (A2.2) and (A2.3) at the inlet meniscus position, x_i, where the film thickness is h_i and when $u = 0$, gives

$$\left[\frac{z}{h_i}\right]^2 - \left[\frac{z}{h_i}\right]\left[1 - \frac{u^*}{3\left(1 - \frac{h^*}{h_i}\right)}\right] + \frac{u_2}{6\bar{u}\ \left(1 - \frac{h^*}{h_i}\right)} = 0 \qquad \text{(A2.4)}$$

where $u^* = \left(\frac{u_1 - u_2}{u_1 + u_2}\right)$.

The roots of this equation give the values of $\frac{z}{h_i}$ at which $u = 0$.

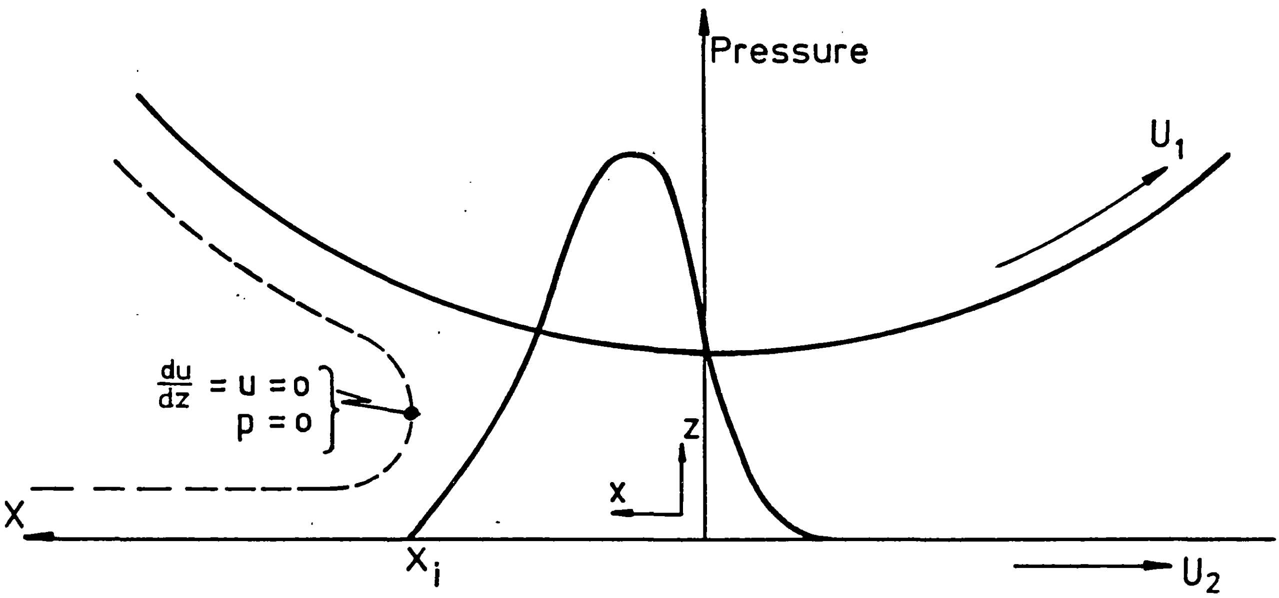

Fig.A2.1a Zero reverse flow inlet boundary condition

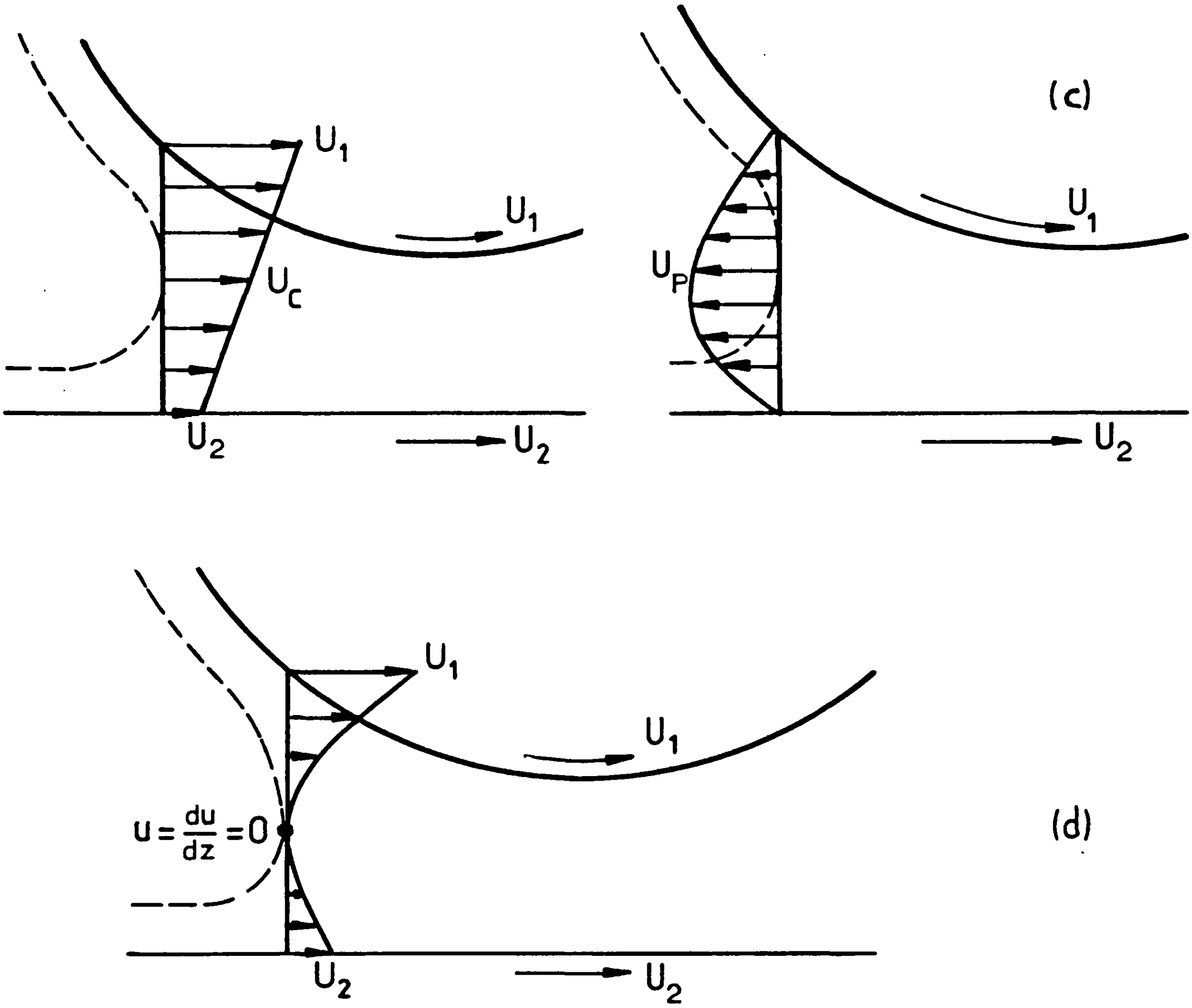

Fig.A2.1(b) & (c) Couette & Poiseuille flow components (d) resultant velocity profile at $X = X_i$ for zero reverse flow inlet condition

Combining the first derivative of eqn.(A2.2) with eqn.(A2.3) gives, when $\frac{du}{dz} = 0$,

$$\left[\frac{z}{h_i}\right] = \frac{1}{2}\left[1 - \frac{u^*}{3\left(1 - \frac{h^*}{h_i}\right)}\right] \tag{A2.5}$$

Combining equations (A2.4) and (A2.5) gives the ratio of the film thickness at the inlet position to that at the pressure maximum h^* , as a function of the surface speeds.

$$\left[\frac{h_i}{h^*}\right] = \frac{3}{2 \pm \sqrt{1-(u^*)^2}} \tag{A2.6}$$

The Crook approximation to the Hertz film shape in the inlet zone is

$$h = h^* \left(1+\tau^{3/2}\right) \qquad \text{(Section 4.2.2.2)}$$

where τ is the non-dimensional form of x

when $\tau = \tau_i$, $h = h_i$

and

$$h_i = h^* \left(1 + \tau_i^{3/2}\right) \tag{A2.7}$$

Equating eqn.(A2.6) and (A2.7) gives τ_i as a function of the surface speeds

$$\tau_i = \left\{\left(\frac{3}{2 \pm \sqrt{1-(u^*)^2}}\right) - 1\right\}^{2/3} \tag{A2.8}$$

Values of τ_i for the surface speeds of the 2:1 and 3:1 tests are given in Table A2.1.

Either Fig.4.7, which gives the starvation and roughness parameters in terms of the reduced film thickness ($h^*_{a\tau}$) or Fig.4.9, in which the parameters are in terms of the ideal film thickness (h^*) can be used to find the film thickness ratio $\left(\frac{h^*_{a\tau}}{h^*}\right)$.

The ideal film thickness can be found using the Dowson and Higginson film thickness formula to give the roughness parameter (σ/h^*) . Eqn.(A2.8) gives the inlet position τ_i in terms of $h^*_{a\tau}$. To use either Fig.4.7 or Fig.4.9, both parameters must be in terms of the same film thickness.

An approximate conversion can be made from τ_i to $\bar{\Psi}_i$ using the relationship between the equivalent parameters for smooth surfaces found by Wolveridge et al (1972). This gives the relationship between $\bar{\Psi}_i$ and τ_i as

$$\bar{\Psi}_i = \left(\frac{h^*_{a\tau}}{h^*}\right)^{3/4} \times \tau_i$$

The values of $\bar{\psi}_i$ thus found for the surface speeds of the 2:1 and 3:1 tests are also given in Table A2.1. The $\pm$ option in Eqn.((A2.6) gives two possible values for the inlet position. In Section 4.5 the least severe condition has been used to show the possible effects of roughness and starvation on film thickness for the two disc tests.

Appendix 3

To find the series of constants A_{mp} and B_{mp}

Equation (5.10b) was given by

$$\sum_{m=1}^{\alpha} \sum_{p=0}^{\alpha} (A_{mp}\cos p\theta + B_{mp}\sin p\theta).\cos(\Gamma_m z).[H_r+p)J_p(i\sqrt{s+\gamma_m^2}) - (i\sqrt{s+\gamma_m^2}).J_{p+1}(i\sqrt{s+\gamma_m^2})] = G'(1,\theta,s) \qquad (A3.1)$$

The unknown series' A_{mp} and B_{mp} can be found from this equation using the orthogonal functions. The method is first examined with a simpler example. The general solution to a problem is

$$X(x) = \sum_{m=1}^{\alpha} D_m \zeta_m(x) \qquad (A3.2)$$

where $X(x)$ is a known function, D_m is an unknown series of constants and $\zeta_m(x)$ is a series of functions which have arisen from a homogeneous boundary condition to the problem. $\zeta_M(x)$ is an orthogonal function to $\zeta_m(x)$ if

$$\int_a^b \zeta_M(x).\zeta_m(x).dx = 0$$

when $M \neq m$ and if

$$\int_a^b \zeta_M(x).\zeta_m(x) \neq 0$$

when M = m, a-b is the orthogonal interval.

These functions can be used to isolate the M^{th} term in the series $\sum_{m=1}^{\alpha} D_m$.
Multiplying both sides of eqn.(A3.2) by the orthogonal function $\zeta_M(x)$ and integrating over the interval a-b gives

$$\int_a^b \zeta_M(x).X(x).dx = \int_a^b \sum_{m=1}^{\alpha} D_m.\zeta_m(x).\zeta_M(x).dx .$$

The right-hand side of this expression = 0 , by definition of orthogonal functions, except for the term m=M . The expression therefore reduces to

$$\int_a^b \zeta_M(x)\cdot X(x)dx = \int_a^b D_M\cdot\zeta_M^2\cdot(x)\cdot dx$$

which, on rearranging, gives

$$D_M = \frac{\int_a^b \zeta_M(x).X(x)dx}{\int_a^b \zeta_M^2(x)dx}$$

When evaluated this gives the expression for D_M from the series $\sum_{m=1}^{\alpha} D_m$. However M could be replaced by any value of m in the series so the expression for D_M can be used as the general expression for D_m in eqn.(A3.2) to give

$$X(x) = \sum_{m=1}^{\alpha} \left(\frac{\int_a^b \zeta_m(x)\cdot X(x)\cdot dx}{\int_a^b \zeta_m^2(x).dx} \right) \zeta_m(x) .$$

Returning to the original problem, in eqn.(A3.1) $\sum_{m=1}^{\alpha}\sum_{p=0}^{\alpha} A_{mp}$ and $\sum_{m=1}^{\alpha}\sum_{p=0}^{\alpha} B_{mp}$ are double series of constants that are to be evaluated. The orthogonal function to $\cos(\Gamma_m z)$ is first used to isolate the terms $\sum_{p=0}^{\alpha} A_{Mp}$ and $\sum_{p=0}^{\alpha} B_{Mp}$.

The orthogonal function to $\cos(\Gamma_m z)$ is $\cos(\Gamma_M z)$ over the interval $0 \to 1$.

Multiply both sides of eqn.(A3.1) by $\cos(\Gamma_M z)dz$ gives

$$\int_0^1 \sum_{m=1}^{\alpha}\sum_{p=0}^{\alpha} (A_{mp}\cos p\theta+B_{mp}\sin p\theta).\cos(\Gamma_m z).\cos(\Gamma_M z).[(H_r+p).J_p(i\sqrt{s+\gamma_m^2}) - (i\sqrt{s+\gamma_m^2}).J_{p+1}(i\sqrt{s+\gamma_m^2})] = \int_0^1 G'(1,\theta,s).\cos(\gamma_M z)dz$$

By the properties of orthogonal functions, the left-hand side of this equation = 0 , except when $m = M$. On rearranging this becomes

$$\sum_{p=0}^{\alpha} (A_{Mp}\cos p\theta+B_{Mp}\sin p\theta)[(H_r+p).J_p(i\sqrt{s+\gamma_M^2}) - (i\sqrt{s+\gamma_M^2}).J_{p+1}(i\sqrt{s+\gamma_M^2})]$$

$$= \frac{\int_0^1 G'(1,\theta,s).\cos(\Gamma_M z)dz}{\int_0^1 \cos^2(\Gamma_M z)dz} = \frac{4\sin\Gamma_M}{2\Gamma_M + \sin 2\Gamma_M} . G'(1,\theta,s) \qquad (A3.3)$$

In the $\sum_{p=0}^{\alpha}$ series of terms the p=0 term must be dealt with separately as the integrands are different. Separating the p=0 and $\sum_{p=1}^{\alpha}$ terms in eqn.(A3.3) and using the full expression for $G'(1,\theta,s)$ from eqn. gives

$$A_{Mo}[H_r\, J_0(i\sqrt{s+\gamma_M^2}) - (i\sqrt{s+\gamma_M^2})J_1(i\sqrt{s+\gamma_M^2})]$$

$$+ \sum_{p=1}^{\alpha} (A_{Mp}\cos p\theta+B_{Mp}\sin p\theta)[(H_r+p)J_p(i\sqrt{s+\gamma_M^2})-(i\sqrt{s+\gamma_M^2}).J_{p+1}(i\sqrt{s+\gamma_M^2})]$$

$$= \frac{1}{\nu}\;\frac{4\sin\Gamma_M}{2\Gamma_M+\sin 2\Gamma_M}\cdot\left[\frac{\theta^*}{s\pi}+\frac{2}{\pi}\sum_{q=1}^{\alpha}\left\{\frac{\sin(q\theta^*)(s\cos(q\theta)+q\Omega\sin(q\theta))}{q(s^2+q^2\Omega^2)}\right\}\right] \qquad \text{(A3.4)}$$

Orthogonal functions are used to isolate A_{Mo}, A_{Mp} and B_{Mp} in turn from this expression.

(i) $\underline{A_{Mo}}$

To evaluate A_{Mo}, the function $\int_0^{2\pi} 1.d\theta$ is used. Noting that

$$\int_0^{2\pi}\cos(p\theta)d\theta = 0 \quad \text{and} \quad \int_0^{2\pi}\sin(p\theta)d\theta = 0 ,$$

multiplying both sides of eqn.(A3.4), by $\int_0^{2\pi} 1.d\theta$, all the sin and cos terms = 0 and the expression becomes

$$\int_0^{2\pi} A_{Mo}[H_r J_0(i\sqrt{s+\gamma_M^2})-(i\sqrt{s+\gamma_M^2})J_1(i\sqrt{s+\gamma_M^2})] =$$

$$\int_0^{2\pi}\left(\frac{4\sin\Gamma_M}{2\Gamma_M+\sin 2\Gamma_M}\right)\cdot\frac{1}{\nu}\cdot\frac{\theta^*}{s\pi}\,.\,d\theta\,.$$

Evaluating the integrals and rearranging gives

$$A_{Mo} = \frac{1}{\nu}\cdot\frac{\theta^*}{s\pi}\cdot\left(\frac{4\sin\Gamma_M}{2\Gamma_M+\sin 2\Gamma_M}\right)\cdot\left(\frac{1}{H_r J_0(i\sqrt{s+\gamma_M^2})-(i\sqrt{s+\gamma_M^2}).J_1(i\sqrt{s+\gamma_M^2})}\right) \qquad \text{(A3.5)}$$

(ii) $\underline{A_{MP}}$

To evaluate A_{MP}, the orthogonal function to $\cos p\theta$ is used with eqn.(A3.4). The orthogonal function to $\cos p\theta$ is $\cos P\theta$ over the interval $0 - 2\pi$.

As $\int_0^{2\pi} \cos(p\theta).d\theta = 0$, $\int_0^{2\pi} \sin p\theta \cos P\theta = 0$ and $\int_0^{2\pi} \sin q\theta \cos P\theta = 0$

and $\int_0^{2\pi} \cos P\theta.\cos p\theta = 0$ if $p \neq P$ and $\int_0^{2\pi} \cos q\theta.\cos P\theta = 0$ $q \neq P$

then eqn.(A3.4), when multiplied by the orthogonal function, reduces to

$$\int_0^{2\pi} A_{MP} \cos^2(P\theta).[(H_r+P)J_P(i\sqrt{s+\gamma_M^2})-(i\sqrt{s+\gamma_M^2})J_{P+1}(i\sqrt{s+\gamma^2})]$$
$$= \frac{1}{\nu}\left(\frac{4\sin\Gamma_M}{2\Gamma_M+\sin 2\Gamma_M}\right)\left[\frac{2}{\pi}\ \frac{\sin P\theta^*}{P}\ .\ \frac{1}{s^2+P^2\Omega^2}.\int_0^{2\pi}\cos^2(P\theta).d\theta\right.$$

Evaluating the integrals and rearranging gives

$$A_{MP} = \frac{1}{\nu}\ \frac{4\sin\Gamma_M}{2\Gamma_M+\sin 2\Gamma_M}\left[\frac{2}{\pi}\ .\ \frac{\sin P\theta^*}{P}\left(\frac{s}{s^2+P^2\Omega^2}\right)\left\{\frac{1}{(H_r+P)J_P(i\sqrt{s+\gamma_M^2})-(i\sqrt{s+\gamma_M^2})J_{P+1}(i\sqrt{s+\gamma_M^2})}\right\}\right]$$

(A3.6)

(iii) $\underline{B_{MP}}$

B_{MP} is evaluated by a similar process to that for A_{PM} but, using the orthogonal function to $\sin p\theta, \sin P\theta$, over the interval $0-2\pi$, again with eqn.(A3.4). This results in

$$B_{MP} = \frac{1}{\nu}\ .\left(\frac{4\sin\Gamma_M}{2\Gamma_M+\sin 2\Gamma_M}\right).\left[\frac{2}{\pi}\ .\ \frac{\sin P\theta^*}{P}\left(\frac{P\,\Omega}{s^2+P^2\Omega^2}\right)\left\{\frac{1}{(H_r+P)J_P(i\sqrt{s+\gamma_M^2})-(i\sqrt{s+\gamma_M^2})J_{P+1}(i\sqrt{s+\gamma_M^2})}\right\}\right]$$

(A3.7)

or $B_{MP} = A_{MP}\ .\ \frac{P\Omega}{s}$.

The expression for A_{MO}, A_{MP} and B_{MP} given by eqns. (A3.5), (A3.6) and (A3.7) are single values of the series' $\sum_{m=1}^{\alpha} A_{mo}$, $\sum_{m=1}^{\alpha}\sum_{p=1}^{\alpha} A_{mp}$ and $\sum_{m=1}^{\alpha}\sum_{p=1}^{\alpha} B_{mp}$. M and P could be any value of m and n in this series so the specific expressions for A_{MO}, A_{MP} and B_{MP} can be used as general expressions for A_{mo} , A_{mp} and B_{mp} in eqn.(5.10b), when M and P are replaced by m and p .

Appendix 4

To find the inverse Laplace Transforms of F_2 and F_3

The full expression for F, the transformed temperature, (Eqn.(5.11)), consisted of three parts F_1, F_2 and F_3. The inverse Laplace transform of F_1 was given in Section 5.3.2 and resulted in the bulk temperature terms. The inverse Laplace transform of F_2 and F_3 which is more complex, is given here.

The expressions for F_2 and F_3 were

$$F_2 = \frac{1}{\nu}\sum_{m=1}^{\alpha}\frac{4\sin\Gamma_m}{2\Gamma_m+\sin 2\Gamma_m}.\cos\Gamma_m z\sum_{p=1}^{\alpha}\frac{2}{\pi}\,\frac{\sin p\theta^*}{p(s^2+p^2\Omega^2)}.s\cos p\theta.\frac{J_p(y\,S_m)}{(H_r+p)J_pS_m-S_m.J_{p+1}(S_m)}$$

where $S_m = i\sqrt{s+\gamma_m{}^2}$

$$F_3 = \frac{p\Omega\sin p\theta}{s.\cos p\theta}\times F_2\ .$$

The inverse Laplace transform of a function $F(s)$ is defined as

$$\Sigma\,\text{residues of } e^{s\tau}.F(s) \text{ at the poles of } F(s)$$

where a pole is the value of the Laplace operator which makes the denominator of the function $F(s)$ equal zero. The residue of $F(s).e^{s\tau}$ at pole $s = a'$ is

$$\underset{s=a'}{\text{Residue}} = \underset{s\to a'}{\text{Limit}}\ (s-a').F(s)e^{s\tau}$$

For the inverse transform only the parts of F_2 and F_3 which are functions of s need be considered, i.e.

From F_2 we require the inverse of F_2' where

$$F_2' = \frac{s}{s^2+p^2\Omega^2}\cdot\frac{J_p(y\,S_m)}{(H_r+p)J_p(S_m)-S_mJ_{p+1}(S_m)}$$

and for F_3 the inverse of F_3' where

$$F_3' = \frac{1}{s}.F_2'\ .$$

The poles of both functions are

(i) $s = +ip\Omega$

(ii) $s = -ip\Omega$, and

(iii) $s = a'$ such that $\sqrt{a' + \gamma_m^2} = \Lambda$ and $H_r + p = \dfrac{\Lambda J_{p+1}(\Lambda)}{J_p(\Lambda)}$

<u>The residue for F_2' for the pole $s = +ip\Omega$ is</u>

$$\underset{s=ip\Omega}{\text{Residue}} = \lim_{s\to ip\Omega} \cdot \frac{(s-ip\Omega)}{s^2+p^2\Omega^2} \cdot s \cdot \frac{J_p(y\,S_m)}{(H_r+p).J_p(S_m)-S_m J_{p+1}(S_m)}$$

In the limit as $s \to ip\Omega$

$$S_m = i\sqrt{s+\gamma_m^2} \to i\sqrt{ip\Omega+\gamma_m^2} \;;\quad e^{s\tau} \to e^{ip\Omega\tau}$$

and using L'hopitals rule

$$\frac{s-ip\Omega}{s^2+p^2\Omega^2} \to \frac{1}{2ip\Omega}$$

Inserted this limits the residue for F_2' for the first pole becomes

$$\underset{s=ip\Omega}{\text{Residue}}\,(F_2') = \frac{1}{2}\,\frac{J_p(yi\sqrt{ip\Omega+\gamma_m^2})}{(H_r+p)J_p(i\sqrt{ip\Omega+\gamma_m^2}) - i\sqrt{ip\Omega+\gamma_m^2}\,J_{p+1}(i\sqrt{ip\Omega+\gamma_m^2})}\,.e^{ip\Omega\tau}$$

$$= A.e^{ip\Omega\tau} \qquad \text{(A4.1)}$$

<u>Similarly the residue of F_3' for the first pole</u>

$$\underset{s=ip\Omega}{\text{Residue}}\,(F_3') = \frac{1}{ip\Omega}.A.e^{ip\Omega\tau} \qquad \text{(A4.2)}$$

<u>For F_2' the residue for the second pole $s = -ip\Omega$ is</u>

$$\underset{s=-ip\Omega}{\text{Residue}}\,(F_2') = \frac{1}{2}\,\frac{J_p(yi\sqrt{-ip\Omega+\gamma_m^2}).e^{-ip\Omega\tau}}{(H_r+p)J_p.(i\sqrt{-ip\Omega+\gamma_m^2})-(i\sqrt{-ip\Omega+\gamma_m^2})J_{p+1}(i\sqrt{-ip\Omega+\gamma_m^2})}$$

$$= B.e^{-ip\Omega\tau} \qquad \text{(A4.3)}$$

<u>and for F_3' the residue for the second pole is</u>

$$\underset{s=-ip\Omega}{\text{Residue}}\,(F') = \frac{1}{-ip\Omega}\,.B.e^{-ip\Omega\tau} \qquad \text{(A4.4)}$$

For F_2' the residue for the third pole $s = a'$

$$\underset{s=a'}{\text{Residue}}\,(F_2') = \underset{s\to a'}{\text{Limit}} \cdot \frac{(s-a')}{s^2+p^2\Omega^2}\cdot s\cdot \frac{J_p(y\,S_m)}{(H_r+p)J_p(S_m)-S_m J_{p+1}(S_m)}$$

In the limit as $s \to a'$

$$(i\sqrt{s+\gamma_m^2}) \to (i\sqrt{a'+\gamma_m^2}) = \lambda \quad \text{where} \quad \lambda = \text{roots of } H_r+p = \frac{\lambda J_{p+1}(\lambda)}{J_p(\lambda)} \;;$$

$$s \to -\,(\lambda^2+\gamma_m^2) \;;\quad e^{s\tau} \to e^{-(\lambda^2+\gamma_m^2)\tau}$$

$\underset{s\to a'}{\text{Limit}} \quad \dfrac{(s-a')}{(H_r+p)J_p(S_m)-S_m J_{p+1}(S_m)}$ is indeterminate. Using L'hopitals rule

and standard Bessel function relationships, this limit can be shown to tend to

$$\frac{-\,2\lambda^2}{J_p(\lambda)(H_r^2+\lambda^2-p^2)}$$

and the residue becomes

$$\underset{s\to a'}{\text{Residue}}\quad F' = \frac{-(\lambda^2+\gamma_m^2)}{(\lambda^2+\gamma_m^2)^2+p^2\Omega^2}\cdot\frac{J_p(y\lambda)}{J_p(\lambda)}\cdot\frac{-2\lambda^2}{(H_r^2+\lambda^2-p^2)} = C \qquad \text{(A4.5)}$$

Similarly for F' the residue for the third root is

$$\underset{s\to a'}{\text{Residue}}\,(F_3') = \frac{C}{(\lambda^2+\gamma_m^2)} \qquad \text{(A4.6)}$$

The residues for F_2' and F_3' (eqns.(A4.1,2,3,4,5 and 6)) can be combined to give the inverse to F_2 and F_3.

$$\text{Inverse } F_2 + \text{Inverse } F_3 = T_2+T_3$$

$$= \frac{1}{\nu}\sum_{m=1}^{\alpha}\frac{4\sin\Gamma_m}{2\Gamma_m+\sin 2\Gamma_m}\cdot\cos\Gamma_m z\cdot\sum_{p=1}^{\alpha}\frac{2}{\pi}\cdot\frac{\sin p\theta^*}{p}\cdot$$

$$\times\left(\cos p\theta(A.e^{ip\Omega\tau}+B.e^{-ip\Omega\tau}) + p\Omega\sin p\theta\left(\frac{A.e^{ip\Omega\tau}}{ip\Omega}+\frac{B.e^{ip\Omega\tau}}{-ip\Omega}\right)\right.$$

$$\left. + C\left[\cos p\theta + \frac{p\Omega\sin p\theta}{-(\lambda^2+\gamma_m^2)}\right]\right)$$

This complex expression gives the periodic flash temperature terms. The third term is the periodic steady state term and represents the space variation of the temperature with the rotating heat source. The first and second term is the associated transient.

Due to the complex nature, and as we are concerned with the bulk temperature, this expression has not been evaluated. The expressions A and B include terms of the form $J_p(1\sqrt{1p\Omega+\gamma_m^2})$.

To evaluate this term the series approximation is

$$J_p(\chi z) = \chi \underline{+} p \sum_{k=0}^{\infty} \frac{(\bar{+})^K(\chi^2-1)^K(\frac{1}{2}z)^K}{!} \quad J_{p\underline{+}K}(z)$$

This will furnish expressions of $J_p(re^{i\theta})$ in terms of $J_{p\underline{+}K}(r)$.

Appendix 5

Bulk Temperature at $\tau = 0$

The expression for the bulk temperature in the cylinder at $\tau=0$ was given by eqn.(5.14) in shortened notation as

$$T^* = \sum_{m=1}^{\alpha} C_m - \sum_{m=1}^{\alpha} \sum_{n=1}^{\alpha} D_{mn} .$$

To satisfy the initial condition to the problem, that before the application of the heat source the temperature in all parts of the cylinder is uniform and equal to the ambient temperature, this expression must equal zero at any position y, θ, z in the cylinder, i.e.

$$\sum_{m=1}^{\alpha} C_m - \sum_{m=1}^{\alpha} \sum_{n=1}^{\alpha} D_{mn} = 0 \qquad \text{(A5.1)}$$

This is difficult to prove arithmetically because of the complex nature of the terms and the inaccuracies inherent with extrapolating values of Bessel functions from tables. The identity can be proved by use of a Dini series.

The Fourier Bessel expansion of a function $f(y)$, is given by

$$f(y) = \sum_{n=1}^{\alpha} a_n . J_p(\varepsilon_n y) \qquad \text{(A5.2)}$$

where ε_n are the roots of $J_p(\varepsilon_c) = 0$ (A5.3)

and a_n is a series of coefficients given by

$$a_n = \frac{2}{C^2 (J_{p+1}(\varepsilon_n . C))^2} . \int_o^c y.f(y).J_p(\varepsilon_n . y).dy \qquad \text{(A5.4)}$$

Similarly a Dini Series is also a Fourier Bessel expansion of a function f(y) again given by

$$f(y) = \sum_{n=1}^{\alpha} a_n . J_p(\varepsilon_n . y) \qquad \text{(A5.5)}$$

but ε_n are now the roots of $\varepsilon.c.J'_p(\varepsilon_c)+d.J_p(\varepsilon_c) = 0$ (A5.6)

and a_n is a series of coefficients given by

$$a_n = \frac{2\,\varepsilon_n^2}{(d^2+\varepsilon_n^2.c^2 - p^2)(J_p(\varepsilon_n.c))^2} . \int_o^c y.f(y).J_p(\varepsilon_n y).dy \qquad \text{(A5.7)}$$

A Fourier Bessel expansion and Dini Series can be used to prove identities which contain summations of Bessel functions of the zero roots of associated identities. A simple example of this method can be found in "Bessel Functions and their Physical Application".

<u>To prove the identity given by eqn.(A5.1)</u>

The full expression for the temperature in a cylinder at $\tau=0$ (eqn.(5.14) when rearranged is

$$\sum_{m=1}^{\alpha} \frac{4\sin\Gamma_m}{2\Gamma_m+\sin 2\Gamma_m} . \frac{I_o(\gamma_m y)}{HrI_o(\gamma_m)+\gamma_m.I_1(\gamma_m)} = \sum_{m=1}^{\alpha}\sum_{n=1}^{\alpha} \frac{4\sin\Gamma_m}{2\Gamma_m+\sin 2\Gamma_m} .$$

$$\frac{2\,\Lambda_n^2}{(Hr^2+\Lambda_n^2)\left(\Lambda_n^2+\frac{R^2\Gamma_m^2}{L^2}\right)} . \frac{J_o(\Lambda_n y)}{J_o(\Lambda_n)} \text{ , for } 0<y<1 \qquad \text{(A5.8)}$$

where Λ_n are the roots of $Hr = \dfrac{\Lambda_n J_1(\Lambda_n)}{J_o(\Lambda_n)}$ (A5.9)

To express a function as a Fourier Bessel expansion or Dini Series, the root condition must take the form of eqn.(A5.3) or (A5.6).

Rearranging and using standard Bessel function relationships and the root condition eqn.(A5.9), gives

$$\Lambda_n J'_o(\Lambda_n) + Hr.J_o(\Lambda_n) = 0$$

This has the same for m as eqn.(A5.6) with $c=0$, $p=0$, $d=Hr$, $n=n$ and $\varepsilon_n=\Lambda_n$. It is assumed therefore that the function given by the left-hand side of eqn.(A5.8) can be expressed as a Dini Series with the form given by eqn.(A5.5).

The coefficients a_n can be found using eqn.(A5.7). The function $f(y)$, the left-hand side of eqns.(A5.8), is itself a series solution over m .

Therefore

$$a_n = \frac{2\,\Lambda_n^2}{(Hr^2+\Lambda_n^2)(J_o(\Lambda_n))^2} \cdot \int_o^1 y \cdot \sum_{m=1}^{\alpha} \frac{4\sin\Gamma_m}{2\Gamma_m+\sin 2\Gamma_m} \cdot \frac{I_o(\gamma_m y)}{Hr\, I_o(\gamma_m)+\gamma_m\, I_1(\gamma_m)} \cdot J_o(\Lambda_n y)dy \qquad \text{(A5.10)}$$

The y dependent terms in this integral are $\int_o^1 y\,.I_o(\gamma_m y).J_o(\Lambda_n y)dy$. To evaluate the integral the $I_o(\gamma_m y)$ term is converted to $J_o(i\gamma_m y)$ using the standard Bessel function relationship $i^p I_p(y) = J_p(iy)$. The integral becomes $\int_o^1 y.J_o(i\gamma_m y).J_o(\Lambda_n y)dy$ which can be evaluated using the identity

$$\int y\, J_p(\bar{a}y).J_p(\bar{b}y)dy = y\left\{\frac{\bar{a}\,J_p(\bar{b}y).J_{p+1}(\bar{a}y) - \bar{b}\,J_p(\bar{a}y).J_{p+1}(\bar{b}y)}{\bar{a}^2 - \bar{b}^2}\right\}$$

and the identity $i^p I_p(y) = J_p(iy)$ to give

$$\int_o^1 y\, J_o(i\gamma_m y).J_o(\Lambda_n y)dy = \frac{J_o\,\Lambda_n[(Hr.I_o(\gamma_m)+(\gamma_m)I_1(\gamma_m)]}{\Lambda_n^2+\gamma_m^2}$$

When this expression is returned to eqn.(A5.10), I_o terms cancel to give

$$a_n = \sum_{m=1}^{\alpha} \frac{4\sin\Gamma_m}{2\,\Gamma_m+\sin 2\Gamma_m} \cdot \frac{2\,\Lambda_n^2}{(Hr^2+\Lambda_n^2)} \cdot \frac{1}{\Lambda_n^2+\gamma_m^2} \cdot \frac{1}{J_o(\Lambda_n)}$$

Using this expression for a_n and the values of the coefficients $c=0$, $p=0, \epsilon_n=\Lambda_n$ in the Dini series expression (eqn.(A5.5)) gives

$$f(y) = \sum_{n=1}^{\alpha} a_n\, J_p(\epsilon_n y)$$

$$f(y) = \sum_{m=1}^{\alpha}\sum_{n=1}^{\alpha} \left\{\frac{4\sin\Gamma_m}{2\Gamma_m+\sin 2\Gamma_m}\right\} \cdot \frac{2\,\Lambda_n^2}{(Hr^2+\Gamma_n^2)\left(\Lambda^2+\frac{R^2\Gamma_m^2}{L^2}\right)} \cdot \frac{J_o(\Lambda_n y)}{J_o\,\Lambda_n}$$

which is the required solution. The identity therefore satisfies the initial condition to the problem.

Appendix 6

Limit of Bulk Temperature as $h_a \to 0$

Eqn.(5.12) gives the steady state and the transient of the bulk temperature in a finite length cylinder with both axial and radial heat flow and convective losses. Eqn.(5.16) gives the equivalent expression from the solution by Story for an 'infinite' length cylinder, or one in which there is no axial heat flow or temperature gradient. Eqn.(5.12) can be shown to tend to eqn.(5.16) in the limit as $h_a \to 0$.

Eqn.(5.12), the bulk temperature in a finite disc, was

$$T^* = \frac{\theta^*}{\nu\pi}\left[\sum_{m=1}^{\alpha} \frac{4\sin\Gamma_m}{2\Gamma_m+\sin2\Gamma_m} \cdot \cos\Gamma_m \dot{z}\left\{\frac{I_o(\gamma_m y)}{Hr.I_o(\gamma_m)+\gamma_m I_1(\gamma_m)}\right.\right.$$

$$\left.\left.\sum_{n=1}^{\alpha} \frac{\Lambda_n^2 \; J_o(\Lambda_n y)}{(Hr^2+\Lambda_n^2)(\gamma_m^2+\Lambda_n^2)J_o(\Lambda_n)} \cdot e^{-(\Lambda_n^2+\gamma_m^2)\tau}\right\}\right] \qquad (A6.1)$$

(viz eqn.(5.12))

where $\gamma_m = \dfrac{R\Gamma_m}{L}$, $\Gamma_m \tan\Gamma_m = Ha$ and $Hr = \dfrac{\Lambda_n J_1(\Lambda_n)}{J_o(\Lambda_n)}$

The term $\displaystyle\sum_{m=1}^{\alpha}\left(\frac{4\sin\Gamma_m}{2\Gamma_m+\sin2\Gamma_m} \cdot \cos\Gamma_m z\right)$ is common to the steady state and is examined first.

As $h_a \to 0$, $Ha = \dfrac{h_a L}{k} \to 0$, and $\Gamma_m \to (m-1)\pi$.

<u>For m = 1</u> , $\Gamma_1 \to 0$, and the limit of $\dfrac{4\sin\Gamma_1}{2\Gamma_1+2\sin\Gamma_1}$ is indeterminate.

It can be shown using L'Hopitals rule, i.e.

$$\lim_{\Gamma_1\to0}\left(\frac{4\sin\Gamma_1}{2\Gamma_1+\sin2\Gamma_1}\right) = \left.\frac{\dfrac{\partial(4\sin\Gamma_1)}{d\Gamma_1}}{\dfrac{d(2\Gamma_1+\sin2\Gamma_1)}{\partial\Gamma_1}}\right|_{\Gamma_1=0} = \left.\frac{4\cos\Gamma_1}{2+2\cos\Gamma_1}\right|_{\Gamma_1=0} = 1$$

The limit of $\cos\Gamma_1 z$ as $\Gamma_1 \to 0 = 1$ for all z , i.e. there is no axial variation for the first term, $m = 1$.

For $m \neq 1$ $\quad \Gamma_m \to (m-1)\pi$

$$\underset{\Gamma_m \to (m-1)\pi}{\text{Limit}} \quad \frac{4\sin \Gamma_m}{2\Gamma_m + \sin 2\Gamma_m} \to \frac{4\sin(m-1)\pi}{2(m-1)\pi + \sin 2(m-1)\pi} \to 0$$

Therefore as $h_a \to 0$ only the first term, m=0 of the expression $\dfrac{4\sin \Gamma_m}{2\Gamma_m + \sin 2\Gamma_m} . \cos \Gamma_m z$ has a value and so the series over m can be replaced by its first term.

For the expression within the curved brackets,

for $m = 1$, as $h_a \to 0$, $\gamma_1 \to 0$ and

$I_o(\gamma_1 y) \to I_o(0) \to 1$ i.e. no radial variation in the steady state temperature,

$I_1(\gamma_1) \to I_1(0) \to 0$

and $\Lambda_n^2 + \gamma_m^2 \to \Lambda_n^2$.

The expression within the curved brackets in Eqn.(A6.1) then tends to

$$\left(\frac{1}{Hr} - \sum_{n=1}^{\alpha} \frac{2}{Hr^2 + \Lambda_n^2} \cdot \frac{J_o(\Lambda_n y)}{J_o \Lambda_n} \cdot e^{-\Lambda_n^2 \tau} \right)$$

With the series over m reducing to 1, the limit of eqn.(A6.1) with $h_a \to 0$ becomes

$$T^* = \frac{\theta^*}{\nu\pi} \left(\frac{1}{Hr} - \sum_{n=1}^{\alpha} \frac{2}{Hr^2 + \Lambda_n^2} \cdot \frac{J_o(\Lambda_n y)}{J_o(\Lambda_n)} \cdot e^{-\Lambda_n^2 \tau} \right)$$

which is the expression given by Story (eqn.(5.16)) for the bulk temperature in an infinite length cylinder.

Appendix 7

Bulk temperature terms for an insulated disc

The geometry of the disc is shown in Fig.A6.1. The disc is insulated at the centre and the side faces. It is assumed that there is no heat flow across these boundaries or in the axial direction.

The differential equation for heat flow in the discs is

$$\frac{1}{r}\frac{\partial}{\partial r}\left(r\frac{\partial T}{\partial r}\right) + \frac{1}{r^2} \cdot \frac{\partial^2 T}{\partial \theta^2} = \frac{1}{\kappa}\frac{\partial T}{\partial t} \tag{A7.1}$$

where T is a function of r , θ , t , and the initial and boundary conditions are

Initial condition: $T(r,\theta,0) = T_{amb}$

Boundary conditions: 1) $k\frac{\partial T}{\partial r}(r_1,\theta,t) = 0$

2) $T(r,\theta,t) = T(r,2\pi+\theta,t) \qquad R > r > r_1$

3) $\frac{\partial T}{\partial r}(R,\theta,t) = -\frac{h_r T(R,\theta,t)}{k} + g\,(R,\theta,t)$

The initial condition and boundary conditions 2) and 3) are similar to those of the original problem for a finite solid cylinder shown in Section . The first boundary condition is for no heat flow across the disc/insulated centre interface at $r=r_1$. The initial stages of the solution are as detailed in Sections 5.2.2, 5.2.3, 5.3.2 for the solid finite disc case.

The governing differential equation, eqn.(A7.1) and the boundary condition are normalised and Laplace transformed to give

$$\frac{\partial^2 F}{\partial y^2} + \frac{1}{y} \cdot \frac{\partial F}{\partial y} + \frac{1}{y^2} \cdot \frac{\partial^2 F}{\partial \theta^2} = sF \tag{A7.2}$$

and 1) $\frac{\partial F}{\partial y}(y,\theta,s) = 0$ where $y_1 = \frac{r_1}{R}$

2) $F(y,\theta,s) = F(y,\theta+2\pi,s) \quad 1 > y > y_1$

3) $\frac{\partial F}{\partial y}(1,\theta,s) = - H_r F(1,\theta,s) + G'(1,\theta,s)$ (where $G'(1,\theta,s)$ represents the heat source term)

Eqn.(A7.2) can be separated into functions $\Theta(\theta)$ and $Y(y)$ which have the general solutions

$$\Theta = c.\cos p\theta + d \sin p\theta \qquad (A7.3)$$

and

$$Y = eI_p(\sqrt{s}y) + FK_p(\sqrt{s}y) \qquad (A7.4)$$

The separated forms of boundary conditions 1) and 2) are

1) $\frac{\partial Y}{\partial y}(y_1,s) = 0$

and 2) $\Theta(\theta) = \Theta(2\pi+\theta)$.

The third boundary condition cannot be separated in this way.

Applying the second boundary condition to eqn.(A7.3) gives

$$\Theta = \sum_{p=o}^{\alpha} c_p \cos p\theta + d_p \sin p\theta \qquad (A7.5)$$

The first boundary condition is applied to eqn.(A7.4). Eqn.(A7.4) is differentiated with respect to y using the rule

$$\frac{\partial}{\partial y}(eI_p(\sqrt{s}y) + fK_p(\sqrt{s}y)) = \frac{\partial}{\partial(\sqrt{s}y)}(eI_p(\sqrt{s}y) + fK_p(\sqrt{s}y)) \cdot \frac{\partial(\sqrt{s}y)}{\partial y}$$

Applying the second boundary condition $\frac{\partial Y}{\partial y}(y_1) = 0$ gives

$$\frac{f}{e} = \frac{-(y_1\sqrt{s}\, I_{p+1}(\sqrt{s}y_1) + p\, I_p(\sqrt{s}y_1))}{(-y_1\sqrt{s}\, K_{p+1}\sqrt{s}y_1 + p\, K_p(\sqrt{s}y_1))} \qquad (A7.6)$$

The full expression for F, the transformed temperature, is found by combining eqn.(A7.4) and (A7.5) and gives, with the p=o terms separated from the series

$$F(y,\theta,s) = \Theta(\theta).Y(y,s) = a_o(eI_o(\sqrt{s}y) + fK_o(\sqrt{s}y)) +$$

$$\sum_{p=1}^{\alpha} (c_p\cos p\theta + d_p\sin p\theta)(eI_p(\sqrt{s}y) + fK_p(\sqrt{s}y) \qquad (A7.7)$$

where c_p, d_p, e and f are still unknown constants series.

This expression for F can now be combined with the third boundary condition, and the constants can then be found as before by using orthogonal functions.

Using the expression for F (eqn.(A7.7) in the third boundary conditions at $y=1$ gives

$$a_o[e(\sqrt{s}I_1(\sqrt{s}) + H_rI_o(\sqrt{s})) + f(-\sqrt{s}K_1(\sqrt{s}) + H_rK_o(\sqrt{s}))]$$

$$+ \sum_{p=1}^{\alpha}(a_p\cos p\theta+b_p\sin p\theta).[e(\sqrt{s}I_{p+1}(\sqrt{s}) + (H_r+p)I_p(\sqrt{s})) + f(-\sqrt{s}K_{p+1}\sqrt{s}) + (H_r+p)K_p(\sqrt{s}))]$$

$$= \frac{1}{\nu}\left(\frac{\theta^*}{s\pi} + \frac{2}{\pi}\sum_{q=1}^{\alpha}\left(\frac{\sin q\theta^*(s\cos q\theta+q\Omega\sin q\theta)}{q(q^2\Omega^2+s^2)}\right)\right) \qquad (A7.8)$$

In the finite solution the $p=o$ terms gave rise to both temperature terms - the steady state and the transient. In this solution only the bulk temperature terms will be considered. An expression for a_o can be found using the orthogonal function $\int_o^{2\pi} d\theta$ on eqn.(A7.8)

$$a_o = \frac{\theta^*}{s\nu\pi} \cdot \frac{1}{e(\sqrt{s}I_1(\sqrt{s})+H_rI_o(\sqrt{s})) + f(-\sqrt{s}K\ (\sqrt{s})+H_rK_o(\sqrt{s}))}$$

which, on substitution into the first part of eqn.(A7.7) gives the transformed bulk temperature as

$$F_{bulk} = \frac{\theta^*}{s\nu\pi}\left[\frac{I_o(\sqrt{s}y) + \left(\frac{f}{e}\right) K_o(\sqrt{s}y)}{(\sqrt{s}I_1(\sqrt{s}) + H_rI_o(\sqrt{s})) + \frac{f}{e}((-\sqrt{s}K_1(\sqrt{s}) + H_rK_o(\sqrt{s}))}\right] \qquad (A7.9)$$

The relationship $\frac{f}{e}$ was given as a function of y_1 in eqn.(A7.6). This arose from the first boundary condition.

At $p=o$ $\frac{f}{e}$ simplifies to

$$\frac{I_1(\sqrt{s}y_1)}{K_1(\sqrt{s}y_1)}$$

which makes eqn.(A7.9)

$$F_{bulk} = \frac{\theta^*}{s\nu\pi} \cdot \left[\frac{I_o(\sqrt{s}y) + \left(\frac{I_1(\sqrt{s}y_1)}{K_1(\sqrt{s}y_1)}\right) K_o(\sqrt{s}y)}{(\sqrt{s}I_1(\sqrt{s})+H_r I_o(\sqrt{s})) + \left(\frac{I_1(\sqrt{s}y_1)}{K_1(\sqrt{s}y_1)}\right). (-\sqrt{s}K_1(\sqrt{s})+H_r K_o(\sqrt{s}))} \right] \quad (A7.10)$$

This is the expression for the transformed bulk temperature. The inverse gives the required expression for T^* .

Inverse Laplace transform

The expression has two poles. The inverse Laplace transform is the sum of the residues at the poles. A pole is a value of the Laplace operator s at which the denominator of the expression = 0 .

The first pole is at $s = 0$

$$\underset{s=0}{\text{Residue}} = \lim_{s\to 0} (s-0)\, F(s)\, e^{s\tau}$$

where $F(s)$ is given by eqn.(A7.10) with $s\to 0$.

$$\therefore \quad \underset{s=0}{\text{Residue}} = \lim_{s\to 0} \left(\frac{(s-0)}{s}\right)\left(\frac{\theta^*}{\nu\pi}\right) \cdot \left[\frac{I_o(0) + \frac{I_1(0)}{K_1(0)} \cdot K_o(0)}{H_r I_o(0) + \frac{I_1(0)}{K_1(0)} \cdot H_r K_o(0)}\right] . e^{o\tau}$$

$I\ (0) = 1$, $I_1(0) = 0$, $K_1(0) = \alpha$ and $K_o(0) = \alpha$.

The $\lim_{s\to 0} \left(\frac{s-0}{s}\right)$ is indeterminate and is found using L'llopitaes rule to be = 1.

$$\underset{s=0}{\text{The residue}} \to \frac{\theta^*}{\nu\pi} \cdot \frac{1}{H_r} \quad (A7.11)$$

This is the bulk steady state temperature term T_s^* and is the same as for the infinite length cylinder.

The second pole is at s such that the denominator term within the brackets in eqn.(A7.10) = 0 . This part of the expression can be rearranged to give

$$H_r = \frac{\sqrt{s}(I_1(\sqrt{s}y_1) . K_1(\sqrt{s})) - (K_1(\sqrt{s}y_1). I_1(\sqrt{s}))}{K_1(\sqrt{s}y_1)I_o(\sqrt{s}) + I_1(\sqrt{s}y_1). K_o(\sqrt{s})} \qquad (A7.12)$$

The second pole is therefore at the values of s, which satisfy this condition. The equivalent term for the finite and infinite solid cylinder was $H_r = \dfrac{\Lambda n J_1(\Lambda n)}{J_o \Lambda n}$.

The I_o, I_1, K_o and K_1 terms in this expression can be converted to the equivalent J and Y forms using the standard Bessel function relationships

$$J_p(ix) = i^p I_p(x) \quad \text{and} \quad Y_p(ix) = i^p(iI_p(x) - \frac{2}{\pi}(-1)^p K_p(x))$$

which gives after much algebria

$$H_r = \frac{\Lambda n[(J_1(\Lambda n y_1).Y_1(\Lambda n)) - (Y_1(\Lambda n y_1).J_1(\Lambda n))]}{(J_1(\Lambda n y_1).Y_o(\Lambda n)) - Y_1(\Lambda n y_1).J_o(\Lambda n))} \qquad (A7.13)$$

where $\Lambda n = i\sqrt{s}$ = the successive roots of the identity.

Due to the complex nature of the pole the full inverse for the transient bulk temperature has not been attempted. The rate of decay is determined by $e^{s\tau}$, which at the roots of eqn.(A7.13) $e^{s\tau} \rightarrow e^{-\Lambda n^2 \tau}$, where Λn is given by eqn.(A7.13). Eqn.(A7.11) therefore gives the steady state temperature and eqn.(A7.13) determines the rate of change of the transient term, in a disc insulated at the side faces and in the centre at a radius $y = y_1$.

Appendix 8

Baglin, K.P., Finnis, M.P., Kelly, D.A. and Williams, P.A. (1987). Mixed and micro-elastohydrodynamic lubrication and the dependence on operating conditions. Proc. Inst. Mech. Engrs. Conference on Tribology, Friction, Lubrication and Wear - Fifty Years On. Vol.I, pp.61-70. (Mechanical Engineering Publications, London).*

Williams, P.A., Finnis, M.P. and Kelly, D.A. (1988). History dependence in two-disc scuffing tests. Proc. Inst. Mech. Engrs. Vol.202, pp.211-218.

*Awarded the BP Oil Tribology Award 1987 for the best paper in the category (Hydrodynamic, Elastohydrodynamic and Mixed Lubrication'.

The influence of machine thermal design and operating conditions on scuffing failure

ABSTRACT

Scuffing is a severe form of surface damage which limits the performance of lubricated sliding machine components. Empirical work has shown that failure either occurs under relatively mild elastohydrodynamic conditions with barely modified surfaces or under severe conditions with the surfaces well run-in. Two hypotheses exist which may explain these experimental differences. This thesis examines their relevance.

The first hypothesis is that, under elastohydrodynamic lubrication, the surface asperities either remain rigid or become elastically deformed - micro-elastohydrodynamic lubrication. A non-dimensional plot, developed by Baglin, predicts the occurrence of the regimes. An experimental study of running-in and scuffing for tests initially operating in the different regimes is described. Tests were run on a two disc machine with incremental loading. Running-in occurred both when tests started in the micro-ehl regime and when they apparently entered it during operation. High sliding prevented entry into micro-ehl; scuffing occurred with barely modified surfaces. This hypothesis discriminates between failure types but cannot alone predict scuffing.

The second hypothesis, by Crook and Shotter, is that scuffing represents an inbalance between the rate of film thinning with increasing load and the rate of running-in. Increasing load increases the temperature which, due to its effect on viscosity, controls film thinning. Knowledge of the machine's thermal behaviour is required. A model is developed to predict temperature in a finite length cylinder subject to a discrete rotating heat source and convective cooling. Steps to apply the theory to a two disc machine are detailed and the results compared to previous experimental temperatures. Methods of changing thermal response are considered and preliminary tests with the discs insulated to increase the temperature rise are described. A marked reduction in scuffing load emphasises the importance of thermal design. Further experimentation is necessary to determine whether the Crook and Shotter hypothesis can quantify scuffing failure.